LA--9101-T

DE82 007042

LA-9101-T
Thesis
UC-34c
Issued: November 1981

Measurement and Isobar-Model Analysis of the Doubly Differential Cross Section for the π^+ Produced in $\pi^-p \rightarrow \pi^+\pi^-n$

D. Mark Manley*

*Department of Physics, VPI and State University, Blacksburg, VA 24061.

Los Alamos National Laboratory
Los Alamos, New Mexico 87545

TABLE OF CONTENTS

Chapter		Page
	ABSTRACT	xvii
I.	INTRODUCTION	1
II.	EXPERIMENT AND APPARATUS	10
	Introduction	10
	Pion Beam	11
	Beam Monitors	12
	Liquid Hydrogen Target	15
	Spectrometer	18
	Particle Detection System	22
	Electronics	26
III.	DATA ACQUISITION	31
	Introduction	31
	Data Acquisition	32
	Replay of Events	35
	Criteria for Accepting Events	37
IV.	CALIBRATIONS WITH πp ELASTIC SCATTERING	62
	Channel Efficiencies and Dispersion	62
	Investigations of πp Elastic Spectra	71
V.	CALCULATION OF THE DOUBLY DIFFERENTIAL CROSS SECTION	107
	Event Rates and Backgrounds	107
	The Doubly Differential Cross Section and Matrix Element	127
	Error Analysis	132

Chapter Page

VI. EMPIRICAL ANALYSIS 153

The Integrated Reaction Cross Section 153

Comparison with Soft-Pion Theory 160

VII. ISOBAR-MODEL ANALYSIS 166

Introduction 166

Formalism 170

Comparison with the LBL-SLAC Analysis 178

The VPI Model 181

Results 185

VIII. SUMMARY AND CONCLUSIONS 222

ACKNOWLEDGEMENTS 225

REFERENCES 226

LIST OF TABLES

Table		Page
I.	Parameters for describing magnetic fields in the spectrometer	22
II.	Quantities scaled during a run	30
III.	Contents of an event block	33
IV.	Contents of header and trailer records	34
V.	Calibration parameters and distance Z of each wire chamber from the focal plane	42
VI.	Effective electron efficiency e_0 of the Cerenkov detector and minimum acceptable pulse height as a function of pion momentum p_π	60
VII.	Relative channel efficiencies	67
VIII.	Results from $\pi^+p\to\pi^+p$ spectra at 141 MeV (first beam)	81
IX.	Results from $\pi^+p\to\pi^+p$ spectra at 141 MeV (second beam)	82
X.	Results from $\pi^+p\to\pi^+p$ spectra at 141 MeV (third beam)	82
XI.	Results from the study of $\pi^+p\to\pi^+p$	83
XII.	Results from $\pi^-p\to\pi^-p$ spectra at 203 MeV (first beam)	91
XIII.	Results from $\pi^-p\to\pi^-p$ spectra at 203 MeV (second beam)	92

Table		Page
XIV.	Results from $\pi^-p \to \pi^-p$ spectra at 203 MeV (third beam)	92
XV.	Results from $\pi^-p \to \pi^-p$ spectra at 203 MeV (fourth beam)	93
XVI.	Results from $\pi^-p \to \pi^-p$ spectra at 203 MeV (fifth beam)	94
XVII.	Results from $\pi^-p \to \pi^-p$ spectra at 229 MeV (first beam)	96
XVIII.	Results from $\pi^-p \to \pi^-p$ spectra at 229 MeV (second beam)	97
XIX.	Results from $\pi^-p \to \pi^-p$ spectra at 229 MeV (third beam)	98
XX.	Results from $\pi^-p \to \pi^-p$ spectra at 256 MeV	100
XXI.	Results from $\pi^-p \to \pi^-p$ spectra at 358 MeV	102
XXII.	Results from the study of $\pi^-p \to \pi^-p$	104
XXIII.	Beam normalization factors and incident momentum distribution parameters corrected for energy loss in the target	106
XXIV.	The doubly differential cross section at 203 MeV	133
XXV.	The doubly differential cross section at 230 MeV	134
XXVI.	The doubly differential cross section at 254 MeV	135
XXVII.	The doubly differential cross section at 256 MeV	136
XXVIII.	The doubly differential cross section at 280 MeV	137
XXIX.	The doubly differential cross section at 292 MeV	138
XXX.	The doubly differential cross section at 331 MeV	139
XXXI.	The doubly differential cross section at 356 MeV	140

Table		Page
XXXII.	The doubly differential cross section at 358 MeV . . .	141
XXXIII.	Parameters and χ^2/ν obtained in fitting $\overline{\|M\|^2}$	156
XXXIV.	Integrated reaction cross section for $\pi^-p\to\pi^+\pi^-n$	157
XXXV.	Values of $\langle\|M_c\|^2\rangle$ for $\pi^-p\to\pi^+\pi^-n$	161
XXXVI.	$\pi N\to\pi\pi N$ charge reactions	166
XXXVII.	Intermediate isobars produced in $\pi N\to\pi\pi N$	167
XXXVIII.	Partial-wave amplitudes in modulus-phase form interpolated from the solutions of the LBL-SLAC analysis	179
XXXIX.	Barrier-penetration factors $B_{\ell_f}(p_\gamma)$	181
XL.	Elastic production phases (in radians)	184
XLI.	Partial-wave amplitudes in modulus-phase form interpolated from the EPP solutions of Arndt et al. .	184
XLII.	Partial-wave amplitudes in modulus-phase form interpolated from the SPP solutions of Arndt et al. .	185
XLIII.	Integrated reaction cross section for $\pi^-p\to\pi^+\pi^-n$ and normalization factor N determined by comparing LBL-SLAC solutions with spectrometer measurements . .	186
XLIV.	Preferred solutions for partial-wave amplitudes in modulus-phase form	191
XLV.	EPP Solutions at 292, 331, and 357 MeV in modulus-phase form	200
XLVI.	Alternate solutions at 292 and 331 MeV in modulus-phase form	201

Table Page

XLVII. Alternate solutions in modulus-phase form for the new measurement at 256 MeV and the previous measurements at 254 and 280 MeV 202

XLVIII. Integrated reaction cross section for $\pi^-p\to\pi^+\pi^-n$ as determined with the VPI model 202

XLIX. Values of $\langle|M_c|^2\rangle$ at 292, 331, and 358 MeV obtained from comparisons with the LBL-SLAC solutions 214

L. Values of $\langle|M_c|^2\rangle$ for $\pi^-p\to\pi^+\pi^-n$ as determined with the VPI model 215

LI. Cross-section predictions (in μb) for $\pi N\to\pi\pi N$ charge reactions at 292, 331, and 358 MeV obtained from comparisons with the LBL-SLAC solutions 218

LII. Cross-section predictions (in μb) for $\pi N\to\pi\pi N$ charge reactions 218

LIII. Elasticities $\eta_{\ell IJ}$ of the initial P11, D13, and D33 waves obtained from comparisons with the LBL-SLAC solutions 219

LIV. Elasticities $\eta_{\ell IJ}$ of the initial P11, D13, and D33 waves obtained with the VPI model 220

LV. Deviations of scattering angles observed by the spectrometer 233

LVI. Averages of path lengths in the liquid hydrogen target 234

LIST OF FIGURES

Figure		Page
1.	Experimental layout	14
2.	Piping schematic for the LH_2 target and refrigeration system	17
3.	Profile view of the spectrometer and the particle detection system	19
4.	The event trigger logic	27
5.	Data acquisition logic	28
6.	Sample efficiency curve for a wire chamber	39
7.	Sample histogram of a sum-difference distribution	41
8.	Sample histogram of a dX/dZ distribution	44
9.	Sample histogram of a dY/dZ distribution	45
10.	Sample histogram of $\Delta X = X_I - X_0$	46
11.	Sample histogram of a Y_0 distribution	47
12.	Scatterplot in the X-Y plane at the back of the Cerenkov detector for events that did not produce pulses in the Cerenkov detector	49
13.	Scatterplot in the X-Y plane at the back of the Cerenkov detector for events that produced pulses in the Cerenkov detector	50
14.	Sample histogram of the pulse height distribution in S1 when no lead absorber was used	52

Figure Page

15. Pulse height distribution in the solid-state detectors for 140 MeV/c events that did not produce pulses in the Cerenkov detector 54

16. Pulse height distribution in the solid-state detectors for 83 MeV/c events that did not produce pulses in the Cerenkov detector 55

17. Pulse height distribution in the solid-state detectors for 83 MeV/c events that produced pulses in the Cerenkov detector 56

18. Pulse height distribution in the Cerenkov detector . . . 58

19. Sample spectra for channel efficiencies 65

20. Relative detection channel efficiencies 68

21. Data used to determine the spectrometer dispersion . . . 70

22. Sample spectra for $\pi^+p \to \pi^+p$ at 141 MeV 80

23. Angular distribution of $\pi^+p \to \pi^+p$ at 141 MeV 85

24. Sample spectra for $\pi^-p \to \pi^-p$ at 203 MeV 87

25. Sample spectra for $\pi^-p \to \pi^-p$ at 229 MeV 88

26. Sample spectra for $\pi^-p \to \pi^-p$ at 256 MeV 89

27. Sample spectra for $\pi^-p \to \pi^-p$ at 358 MeV 90

28. Angular distribution of $\pi^-p \to \pi^-p$ at 203 MeV 95

29. Angular distribution of $\pi^-p \to \pi^-p$ at 229 MeV 99

30. Angular distribution of $\pi^-p \to \pi^-p$ at 256 MeV 101

31. Values of R_e/R_π at 203 MeV 111

32. Values of R_e/R_π at 230 MeV 112

33. Values of R_e/R_π at 256 MeV 113

34. Values of R_e/R_π at 280 MeV 114

Figure		Page
35.	Values of R_e/R_π at 292 MeV	115
36.	Values of R_e/R_π at 331 MeV	116
37.	Values of R_e/R_π at 358 MeV	117
38.	Values of $(R_\pi)_{empty}/R_\pi$ at 203 MeV	120
39.	Values of $(R_\pi)_{empty}/R_\pi$ at 230 MeV	121
40.	Values of $(R_\pi)_{empty}/R_\pi$ at 256 MeV	122
41.	Values of $(R_\pi)_{empty}/R_\pi$ at 280 MeV	123
42.	Values of $(R_\pi)_{empty}/R_\pi$ at 292 MeV	124
43.	Values of $(R_\pi)_{empty}/R_\pi$ at 331 MeV	125
44.	Values of $(R_\pi)_{empty}/R_\pi$ at 358 MeV	126
45.	Values of $\overline{\|M\|^2}$ at 203 MeV	142
46.	Values of $\overline{\|M\|^2}$ at 230 MeV	143
47.	Values of $\overline{\|M\|^2}$ at 254 MeV	144
48.	Values of $\overline{\|M\|^2}$ at 256 MeV	145
49.	Values of $\overline{\|M\|^2}$ at 280 MeV	146
50.	Values of $\overline{\|M\|^2}$ at 292 MeV	147
51.	Values of $\overline{\|M\|^2}$ at 331 MeV	148
52.	Values of $\overline{\|M\|^2}$ at 356 MeV	149
53.	Values of $\overline{\|M\|^2}$ at 358 MeV	150
54.	Integrated reaction cross section for $\pi^-p\to\pi^+\pi^-n$	159
55.	Measured values of $\langle\|M_c\|^2\rangle$	162
56.	Notation for the isobar model	172
57.	Best comparison of the measured $\overline{\|M\|^2}/(C_i\overline{C_f})$ at 292 MeV with the LBL-SLAC solutions	188
58.	Best comparison of the measured $\overline{\|M\|^2}/(C_i\overline{C_f})$ at 331 MeV with the LBL-SLAC solutions	189

Figure Page

59. Best comparison of the measured $\overline{|M|^2}/(C_i\overline{C_f})$ at 358 MeV with the LBL-SLAC solutions 190

60. Comparison of the measured $\overline{|M|^2}/(C_i\overline{C_f})$ at 203 MeV with the fitted results of the VPI model 192

61. Comparison of the measured $\overline{|M|^2}/(C_i\overline{C_f})$ at 230 MeV with the fitted results of the VPI model 193

62. Comparison of the measured $\overline{|M|^2}/(C_i\overline{C_f})$ at 256 MeV with the fitted results of the VPI model 194

63. Comparison of the measured $\overline{|M|^2}/(C_i\overline{C_f})$ at 280 MeV with the fitted results of the VPI model 195

64. Comparison of the measured $\overline{|M|^2}/(C_i\overline{C_f})$ at 292 MeV with the fitted results of the VPI model 196

65. Comparison of the measured $\overline{|M|^2}/(C_i\overline{C_f})$ at 331 MeV with the fitted results of the VPI model 197

66. Comparison of the measured $\overline{|M|^2}/(C_i\overline{C_f})$ at 358 MeV with the fitted results of the VPI model 198

67. Differential cross sections at 292 MeV obtained from our best comparison with the LBL-SLAC solutions 204

68. Differential cross sections at 331 MeV obtained from our best comparison with the LBL-SLAC solutions 205

69. Differential cross sections at 358 MeV obtained from our best comparison with the LBL-SLAC solutions 206

Figure Page

70. Differential cross sections at 203 MeV obtained with the VPI model 207

71. Differential cross sections at 230 MeV obtained with the VPI model 208

72. Differential cross sections at 256 MeV obtained with the VPI model 209

73. Differential cross sections at 280 MeV obtained with the VPI model 210

74. Differential cross sections at 292 MeV obtained with the VPI model 211

75. Differential cross sections at 331 MeV obtained with the VPI model 212

76. Differential cross sections at 358 MeV obtained with the VPI model 213

77. The $\langle|M_c|^2\rangle$ obtained with the VPI model 217

78. The pion-nucleon vertex diagram 245

79. Important tree diagrams that contribute to $\pi N \to \pi\pi N$ 253

CONTENTS OF APPENDICES

Appendix		Page
A.	MODEL FOR AN ELASTIC PEAK AT THE FOCAL PLANE	231
B.	REVIEW OF SOFT-PION THEORY	238
	Current Commutation Relations	238
	PCAC and the Goldberger-Treiman Relation	242
	Phenomenological πN Lagrangian	246
	Chiral-Symmetry Breaking	248
	Applications	249

MEASUREMENT AND ISOBAR-MODEL ANALYSIS OF THE DOUBLY DIFFERENTIAL CROSS SECTION FOR THE π^+ PRODUCED IN $\pi^-p \to \pi^+\pi^-n$

by

D. Mark Manley

ABSTRACT

The doubly differential cross section $\frac{d^2\sigma}{d\Omega dT}$ for π^+ mesons produced in the reaction $\pi^-p \to \pi^+\pi^-n$ was measured at 203, 230, 256, and 358 MeV with a single-arm magnetic spectrometer. A set of five previous measurements at 254, 280, 292, 331, and 356 MeV was reanalyzed with the new measurements. Integrated cross sections were calculated for the combined data set with unprecedented accuracy for this energy range. The chiral-symmetry-breaking parameter was determined to be $\xi = -0.03 \pm 0.26$ by extrapolating the mean square modulus of the matrix element to threshold and comparing the threshold matrix element with the prediction of soft-pion theory. This value of ξ is consistent with zero as required by the Weinberg Lagrangian. Measurements at the three highest energies were compared with the results of an isobar-model analysis of bubble-chamber events by an LBL-SLAC collaboration. After allowing for an overall normalization difference, the measurements at 331 and 358 MeV were in excellent agreement with the results of their analysis. The measurement at 292 MeV required variation of the PS11(εN) amplitude, as well as the overall normalization, which could be due to the limited number of bubble-chamber events available for the LBL-SLAC analysis at this energy. A partial-wave analysis of the measurements was also carried

out with the VPI isobar model. Within this model, the matrix element contains a background term calculated from a phenomenological πN Lagrangian that is consistent with the hypotheses of current algebra and PCAC. The reaction was found to be dominated by the initial P_{11} wave. Production of the Δ isobar from initial D waves was found to be significant at the two highest energies.

CHAPTER I

INTRODUCTION

In the past few years, considerable effort has been devoted to the experimental determination of the S-wave $\pi\pi$ amplitude. Because direct measurements of $\pi\pi$ scattering are not yet possible, the experimental work has had to depend on the use of reactions dominated by pion exchange. Reactions of the class $\pi N \to \pi\pi N$ are among the simplest types from which information about the $\pi\pi$ interaction can be extracted. Attempts at understanding this class of reactions from the viewpoint of soft-pion theory are fairly recent.[1,2] Soft-pion theory attempts to understand interactions involving pions of vanishing four-momenta. Older attempts at understanding $\pi N \to \pi\pi N$ reactions with non-soft-pion theories have been summarized by Chang.[1] The earliest calculations of soft-pion matrix elements made direct use of current commutation relations and PCAC, the partial conservation of the axial-vector current. Weinberg developed methods[3] of constructing phenomenological Lagrangians that are thought to reproduce the results of the current-algebra method. These methods have been of tremendous value in simplifying the calculation of matrix elements for processes involving soft pions.

Olsson and Turner calculated threshold matrix elements[2,4] for the different $\pi N \to \pi\pi N$ charge reactions using Weinberg's technique for constructing phenomenological Lagrangians. Their calculations did not take unitarity[5,6] and the formation of resonant states[7] properly into

account when the pion four-momentum was extrapolated to the physical threshold. Attempts to consider these effects more carefully have produced only slightly different results for the threshold predictions.[8] The threshold matrix elements for $\pi N \to \pi\pi N$, with all pions on the mass shell, contain a single free parameter ξ, which was introduced by Olsson and Turner.[2,4] ξ describes the departure from the type of symmetry breaking introduced in the Gell-Mann--Lévy σ model[9] and distinguishes among the various ways in which the chiral symmetry of the phenomenological πN Lagrangian can be broken as the soft pions are brought onto the mass shell.

This experiment measured the doubly differential cross section for the reaction $\pi^- p \to \pi^+ \pi^- n$ in the energy region near threshold by detecting only the outgoing π^+ meson. A previous experiment,[10] which used much of the same experimental apparatus, had measured the cross section at five incident kinetic energies: 254, 280, 292, 331, and 356 MeV. The present experiment, using the increased intensity of pion beams at the Clinton P. Anderson Meson Physics Facility (LAMPF) of the Los Alamos National Laboratory (LANL),[11] extended these measurements 50 MeV closer to the 172.4 MeV threshold by measuring the doubly differential cross section $\left(\frac{d^2\sigma}{d\Omega dp}\right)_{lab}$ at incident energies 203 and 230 MeV. As a consistency check of the previous measurements, the cross section was also remeasured at the extremes of the energy range for the previous experiment. The remeasured values, at 256 and 358 MeV, were more precise than the previous measurements at 254 and 356 MeV. Values of the cross section were combined at these two energies to give greater statistical accuracy. All reaction data from

the earlier experiment were reanalyzed together with the new data using an improved program.

This experiment was performed at the west leg of the High-Energy Pion Channel (P^3) at LAMPF. A double-focusing, 180° vertical bend, magnetic spectrometer selected the sign, momentum, and scattering angle of charged particles emanating from a liquid hydrogen target. The spectrometer assembly, including the cryostat, target, and scattering chamber could be rotated as a unit about the vertical axis of the cylindrical target flask for laboratory angles in the range 20.36° to 132°. Charged particles with momenta as high as 325 MeV/c and pions with momenta as low as 50 MeV/c could be detected. The upper momentum limit was determined by the maximum temperature allowed for the cooling water at output whereas the lower momentum limit was determined by the ability of our detection system to eliminate the background of "soft" electrons. An array of 18 solid-state transmission detectors, which spanned the focal plane of the spectrometer and covered a $\Delta p/p$ of 9.2%, determined the position of the particle in the focal plane and hence its momentum. The target flask, flight path in the spectrometer, and the array of detectors were in a common vacuum to minimize energy loss and multiple scattering at low momentum. An event was indicated by formation of the trigger pulse W1Y·W2Y·S1, which was the logical AND of signals from two multiwire proportional chambers and a scintillation detector located immediately behind the MWPC's. The timing of W1Y·W2Y·S1 was determined by the scintillation detector. A threshold Cerenkov detector distinguished between electrons and pions. For pions with momenta less than about 90 MeV/c, the dE/dx information from the solid-state detectors also

distinguished between pions and electrons. The solid-state detectors could also identify events caused by elastically scattered protons. For laboratory scattering angles greater than about 40°, the incident particle flux was measured by a scattering monitor. An ionization chamber checked the performance of the scattering monitor at these angles and determined the incident flux for scattering angles forward of 40°.

The doubly differential cross section $(\frac{d^2\sigma}{d\Omega dp})_{lab}$ of the produced π^+ meson was measured at 11 points at 203 MeV, 16 points at 230 MeV, 20 points at 256 MeV, and 21 points at 358 MeV. Measurements of $\frac{d^2\sigma}{d\Omega dT}$, the doubly differential cross section in the center-of-momentum (c.m.) system, were distributed fairly uniformly over the accessible portion of T-cosθ space. Here, T and cosθ refer to the c.m. kinetic energy and cosine of the production angle for the final-state π^+ meson. The $\frac{d^2\sigma}{d\Omega dT}$ were normalized to π^-p elastic scattering measured with the same apparatus for each incident beam. Each measurement of $\frac{d^2\sigma}{d\Omega dT}$ determined $\overline{|M|^2}$, the square modulus of the matrix element averaged over unobserved variables and divided by the square of the incident c.m. momentum.

The $\overline{|M|^2}$ varied much more slowly in T-cosθ space than the $\frac{d^2\sigma}{d\Omega dT}$, which were dominated by the density of phase space. Values of $\overline{|M|^2}$ corrected for Coulomb attraction in the initial and final states were fitted to an empirical function of the measured c.m. variables. At the lower energies, the function was taken to be a polynomial expansion in the c.m. variables p^2 and pcosθ, with p the momentum of the produced π^+. A contrived term was added to the expansion at 33' and 357 MeV to describe a sizable angular variation in $\overline{|M|^2}$ observed

for small T. At each incident energy, the fitted function was averaged over the measured variables to estimate $\langle|M_c|^2\rangle$, the square modulus of the matrix element corrected for Coulomb attraction in the initial and final states, averaged over all phase space, and divided by the square of the incident c.m. momentum. From this experiment and the previous one,[10] we obtained values of $\langle|M_c|^2\rangle$ at seven incident kinetic energies: 203, 230, 255, 280, 292, 331, and 357 MeV. These seven $\langle|M_c|^2\rangle$ were fitted to a linear function of the total c.m. energy. The extrapolated value of $\langle|M_c|^2\rangle$ at threshold was compared with the soft-pion calculation of Olsson and Turner[2,4] to determine $\xi = -0.03 \pm 0.26$. This value is consistent with $\xi = 0$ required for the Weinberg Lagrangian.[3] It is inconsistent with $\xi = 1$ or $\xi = -2$ required for the two Schwinger Lagrangians.[12] Assuming validity of the soft-pion result at threshold, this ξ establishes the S-wave isoscalar and isotensor $\pi\pi$ scattering lengths to be $a_0 = 0.178 \pm 0.016\ m_\pi^{-1}$ and $a_2 = -0.049 \pm 0.007\ m_\pi^{-1}$, respectively.

The measurements of $\overline{|M|^2}$ at 292, 331, and 358 MeV were compared with the solutions of an extensive, conventional, isobar-model analysis of bubble-chamber events for $\pi N \to \pi\pi N$ reactions performed by an LBL-SLAC collaboration.[13] In the standard isobar model, one assumes that the T matrix for $\pi N \to \pi\pi N$ can be written as a coherent sum of contributions from different isobars (resonant states). The LBL-SLAC analysis has indicated that production of only three isobars is important for incident kinetic energies less than about 600 MeV. These are the ε ($I = J = 0$) and ρ ($I = J = 1$) $\pi\pi$ resonances and the Δ ($I = J = 3/2$) πN resonance. Thus, in the standard isobar model, the T matrix for $\pi^- p \to \pi^+\pi^- n$ can be written as $T_{IM} = T_\varepsilon + T_\rho + T_{\Delta^+} + T_{\Delta^-}$,

where each term in the sum is a production amplitude for a particular isobar. In general, several partial waves can contribute to each isobar production amplitude, even at low energy. The notation for a partial-wave amplitude is $[\ell_i,\ell_f,2I,2J]$, where ℓ_i is the initial orbital angular momentum, ℓ_f is the orbital angular momentum between the isobar and the spectator particle, I is the total isospin, and J is the total angular momentum. Each partial-wave amplitude was an undetermined complex number, hence two undetermined real numbers. To compare with our measurements, we linearly interpolated partial-wave amplitudes from the LBL-SLAC solutions to 292, 331, and 358 MeV. Since the overall normalization of the LBL-SLAC solutions was not well established, we also renormalized their amplitudes to our cross sections by averaging the absolute square of the total amplitude over the unobserved spin and kinematic variables, correcting for Coulomb attraction in the initial and final states, and comparing with the measured $\overline{|M|^2}$. The renormalized amplitudes were in excellent agreement with the measurements at 331 and 358 MeV. To obtain good agreement at 292 MeV, at least one partial-wave amplitude had to be varied, as well as the overall normalization, which could be a result of the limited number of events available to the LBL-SLAC analysis at this energy. The solution most similar to that obtained when only the normalization was varied was obtained by varying both the normalization and the PS11(εN) amplitude, which is large at these energies. A good χ^2/ν was obtained and the normalization was only slightly different from that obtained when no additional parameters were varied. The modulus of the PS11(εN) wave decreased by about 8% whereas the phase increased by about 60°.

At each incident energy, the measured $\overline{|M|^2}$ were also compared with the isobar model for $\pi N \to \pi\pi N$ reactions as modified by Virginia Polytechnic Institute and State University (VPI&SU) and collaborating institutions.[14] The modified model of Arndt et al.,[14] which we call the VPI model, includes a background term T_{CA} in the amplitude so that the total R-matrix amplitude is $T = T_{IM} + T_{CA}$. T_{CA} is the current-algebra amplitude calculated from the phenomenological πN Lagrangian and is discussed in Appendix B. Some part of the background term potentially contributes to each partial wave. In our calculations with the VPI model, we neglected the term T_ρ in T_{IM} and set $\xi = 0$ in T_{CA}. Hence, the entire contribution to partial waves by ρ production was assumed to be adequately described by the background term. Our analysis, like that of Arndt et al.,[14] considered all final-state S waves and all final-state P waves that arise from resonant initial states (P11, P33, D13). The partial-wave amplitudes were established by fitting to measurements of $\overline{|M|^2}$ at each incident energy. Initial guesses for our partial-wave amplitudes at the two highest energies were interpolated from the solutions of Arndt et al. which those authors had normalized to our cross-section data. Initial guesses at the lower energies were obtained by propagating our solutions from the higher energies. The resulting amplitudes varied fairly uniformly from one incident energy to the next. At 331 and 357 MeV, they were in reasonable agreement with the solutions of Arndt et al. although we found slightly more Δ production and slightly less ε production. At each incident energy, we also calculated the elasticity $\eta_{\ell IJ}$ for the initial P11, D13, and D33 waves from our solutions to the VPI model. Previous determinations[15] of the $\eta_{\ell IJ}$

near single pion production threshold have been based on sparse measurements of integrated reaction cross sections that were several times less accurate than the present measurements.

We determined the integrated reaction cross section σ_R where possible from the empirical and both isobar-model analyses. The several values of σ_R calculated by all methods agreed well at each energy except 292 MeV. At this energy, the values calculated with the VPI model and from our best comparison with the LBL-SLAC solutions were respectively about 10% and 4% lower than the empirical result. Of the values, the isobar-model results are considered to be the more reliable; the empirical function had difficulty fitting a sizable variation with energy observed in $\overline{|M|^2}$ near the maximum allowed π^+ kinetic energy. The uncertainty in σ_R was about 11% at 203 MeV, about 5% at 230 MeV, and about 4% at all higher energies except 292 MeV, where the uncertainty was about 6%. At 331 and 358 MeV, the largest source of uncertainty was a 4% error associated with our normalization to π^-p elastic scattering.

Additional estimates of the chiral-symmetry-breaking parameter ξ were found by extrapolating the $\langle|M_c|^2\rangle$ determined from the isobar models to threshold. The values obtained, $\xi = 0.08 \pm 0.27$ and $\xi = 0.03 \pm 0.27$, were again consistent with zero.

Our experimental procedure and apparatus are described in Chapter II. The manner in which the raw data were collected and processed in preparation for subsequent analysis is discussed in Chapter III. Various calibrations that involved measurements of πp elastic scattering are discussed in Chapter IV. Our calculations of $\frac{d^2\sigma}{d\Omega dT}$ and $\overline{|M|^2}$ are described in Chapter V. The empirical analysis in

which we determined σ_R at each incident energy as well as the chiral-symmetry-breaking parameter ξ is discussed in Chapter VI. Finally, the isobar-model analysis is described in Chapter VII. A review of the model is included and our results are compared with the solutions of other isobar-model analyses.

CHAPTER II

EXPERIMENT AND APPARATUS

Introduction

This experiment measured the doubly differential cross section $\frac{d^2\sigma}{d\Omega dT}$ for the π^+ meson produced in the reaction $\pi^-p \rightarrow \pi^+\pi^-n$ at four incident energies: 203, 230, 256, and 358 MeV. Measurements at the highest energy were essentially at the 357.4 MeV threshold for the double pion production reaction $\pi^-p \rightarrow \pi^+\pi^-\pi^\circ n$. Hence, the π^+ provided a unique signature for single pion production from pions in the energy range of our measurements. All of our single pion production measurements were in the low-energy region. Our 203 MeV cross section, at just 31 MeV above threshold, is the closest measurement to single pion production threshold in existence.

The High-Energy Pion Channel at the Clinton P. Anderson Meson Physics Facility (LAMPF) designated "Pion and Particle Physics" (P^3) could provide an intense beam of either π^+ or π^- mesons in the energy range 100 to 600 MeV with a $\Delta p/p$ of 0.25% to 10%.[16] The incident beam of π^- mesons impinged on a liquid hydrogen (LH_2) target enclosed in a mylar flask. Beam flux was measured by both a scattering monitor downstream of the LH_2 target and an ionization chamber upstream. A beam profile monitor insured that the beam was on target. The elastically scattered π^- mesons and the produced π^+ mesons were observed by a magnetic spectrometer that selected the charge, the angle, and the momentum of the pions.

Pions were transported from the target to the top of the spectrometer where they were focused onto a vertical array of solid-state transmission detectors. The LH_2 target, flight path in the spectrometer, and the solid-state detectors were in a continuous vacuum to minimize energy loss and small-angle scattering. The pions continued past the solid-state detectors to a trigger telescope that consisted of two multiwire proportional chambers (MWPC's) followed by a 1.6 mm-thick scintillation detector designated S1. Since the MWPC's determined particle trajectories, we could eliminate background events that resulted from particles which had not passed through the correct solid-state detector. A 0.8 mm lead absorber was placed immediately before S1 for most measurements to eliminate background caused by protons and "soft" electrons. Located behind S1, a threshold Cerenkov detector identified events that resulted from high velocity electrons.

Pion Beam

The P^3 channel consists of three bend sections, each of which contains a 30° dipole bending magnet and two quadrupole doublets. The first bend determines the momentum and charge of the pion beam. A variable horizontal slit upstream of the first bending magnet and a variable vertical slit downstream define the solid angle acceptance of the channel. The beam comes to a dispersed double focus midway between the fourth and fifth quadrupole magnets where a variable momentum acceptance slit is located. A variable thickness graphite degrader is located immediately downstream of the momentum slit to give pions and protons in π^+ beams different momenta. The second bend brings the pion beam into a second double focus within the third

bending magnet and spatially separates the pions from the energy-degraded protons. Immediately before the third bending magnet, a movable proton absorber placed just off the beam axis could remove the protons from π^+ beams. A variable slit was located before the third bending magnet to clean up the beam. The third bending magnet steered the pion beam into one of two spatially separated experimental areas. After the third bending magnet, the pion beam was designed to be achromatic. Two sets of quadrupole doublets located after the third bending magnet were tuned to match the phase space of the pion beam to the phase space required for our experiment.

The P^3 channel was tuned primarily from the results of a computer simulation. Magnetic fields required for producing a beam of specified energy were determined from the program TRANSPORT.[17] The results of TRANSPORT were used by the program SHUNT, which determined the shunt voltages for the channel. Some final steering adjustments to the second and third bending magnets were made on the basis of an oscilloscope display of the horizontal position of the beam spot at the target. The beam spot at the target had 1.5 cm horizontal by 1.3 cm vertical full widths at half maximum (FWHM), as measured by a profile monitor discussed below.

Beam Monitors

The size and position of the beam spot were monitored continuously during the experiment with a profile monitor. Flux of the incident beam was monitored by a scattering experiment downstream of the LH_2 target and by an ionization chamber upstream. As shown in Fig. 1, the upstream end of the ionization chamber connected to a

flange on the P^3 channel valve whereas the downstream end connected to a 72.4 cm-long, 20.3 cm-diameter aluminum cylinder. This cylinder supported the profile monitor at its other end. The centroid and width of the incident momentum distribution were inferred from measurements of πp elastic scattering, which we discuss in Chapter IV.

The profile monitor located immediately upstream of the scattering chamber was a small wire chamber that had 64 vertical wires and 64 horizontal wires with 1 mm wire spacing. It operated at about -4 kV and was filled with "magic gas," discussed below. The current output from each wire was integrated over several beam pulses, buffered, sampled with a multiplexer, and displayed on an oscilloscope to produce histograms. These histograms determined the horizontal and vertical profile of the beam near the target and aided in steering the beam onto the target.

The scattering monitor, which has been described by Walter,[10] was the principal monitor of the incident beam flux. It consisted of a polyethylene (CH_2) target and two counter telescopes as shown in Fig. 1. The CH_2 target was 23 cm wide, 15 cm high, and 1.3 cm thick. It was oriented in a vertical plane at a 45° angle to the beam line and the line of the telescopes. Each telescope consisted of three plastic scintillation detectors that measured 15 cm × 15 cm × 0.3 cm and were observed through Lucite light pipes by RCA 6199 phototubes. These were labeled S1W, S2W, and S3W for the west telescope and S1E, S2E, and S3E for the east telescope. Valid events in the scattering monitor consisted of threefold coincidences in either telescope, S1W•S2W•S3W or S1E•S2E•S3E, which were scaled in CAMAC scalers.

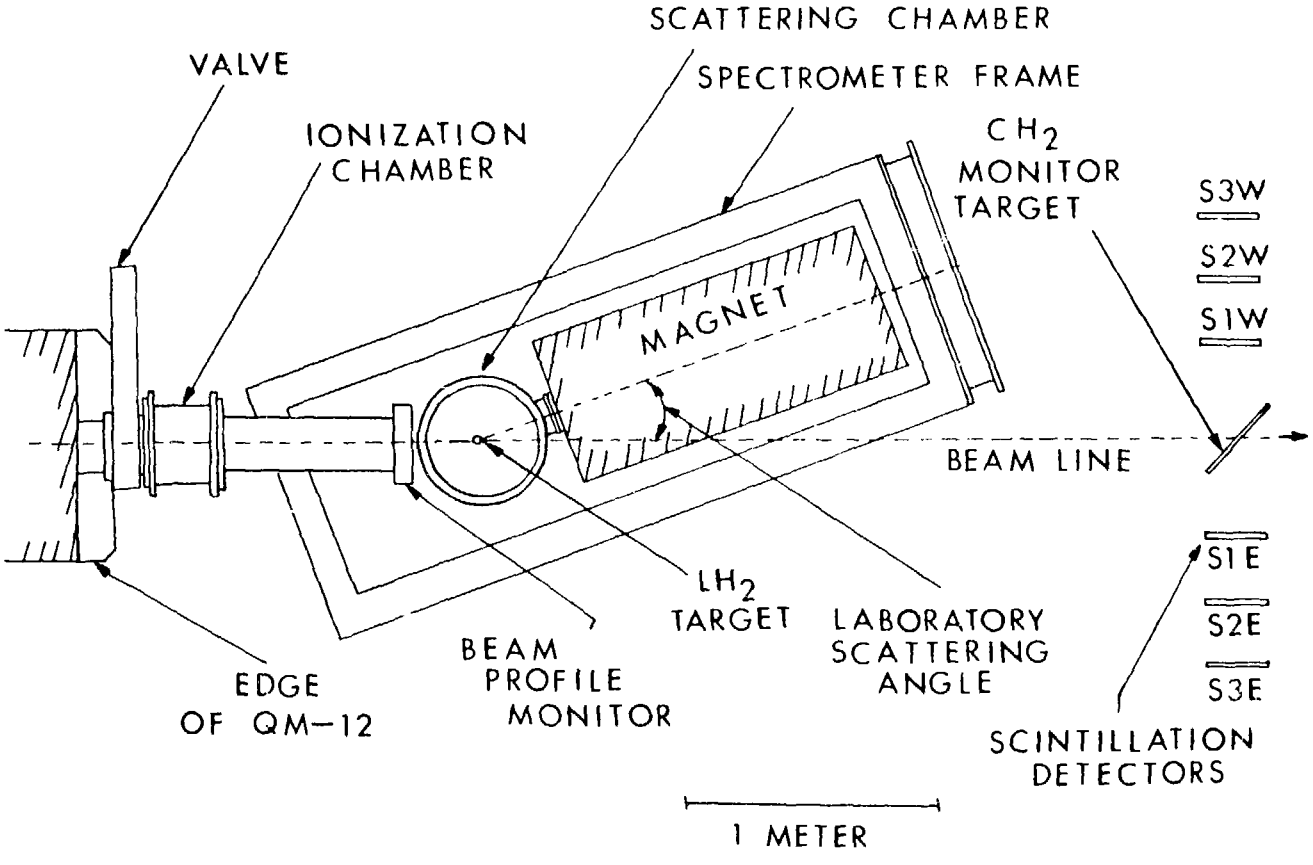

Figure 1. Experimental layout. QM-12 is the last quadrupole magnet in the west leg of the channel.

Coincidences in the two arms were summed to reduce the sensitivity of the monitor to beam steering.

The ionization chamber consisted of eleven 20 cm-diameter plates of stretched aluminized mylar spaced 2.54 cm apart. An argon-filled, 25.4 cm-long, 31.1 cm-diameter aluminum cylinder contained the nine 6 μm-thick internal plates and was sealed by the two 25 μm-thick end windows. The five alternating internal plates were maintained at 900 V by a battery power supply. The remaining four internal plates, which were near ground and interconnected, produced the output current. An Ortec 439 current digitizer produced a logic pulse for every 100 pC of charge collected from the ionization chamber. The output of the current digitizer drove a preset scaler that determined the duration of experimental runs in which data were collected, as well as a CAMAC scaler discussed below. For laboratory scattering angles forward of about 40°, the scattering monitor was blocked by the field clamp on the lower spectrometer magnet. Hence, the ionization chamber was necessary for monitoring the beam flux at forward angles. It also provided redundance at backward angles.

Liquid Hydrogen Target

The scattering target was boiling liquid hydrogen held at 14.6 psi absolute. It was contained in a cylindrical flask of 50 μm mylar, 12.7 cm long and 2.54 cm in diameter, and mounted coaxially with the vertical rotation axis of the spectrometer. An epoxy resin bonded the two ends of the flask to stainless steel end caps. Liquid hydrogen was supplied by a CTI model 1022 helium expansion refrigerator with a 1.5 liter LH_2 reservoir located above the scattering

chamber. The spectrometer and the hydrogen system, which consisted of the refrigerator, reservoir, and target, were enclosed in a continuous vacuum and could be rotated as a unit. A piping schematic of the LH_2 target and refrigeration system is shown in Fig. 2.

The process of filling the target flask with liquid hydrogen began by evacuating and then purging the reservoir and flask with gaseous hydrogen. Room temperature helium from the compressor cooled the refrigerator's surroundings as the helium did work on an engine. The helium then returned to the compressor to be recompressed and recooled. We cooled the refrigerator down to about 20° K with the hydrogen system pressurized to about 3 psi above atmospheric pressure by means of a regulated supply of hydrogen. Hydrogen condensed on the cold end of the refrigerator, dripped down, and cooled the rest of the hydrogen system. Although the liquid hydrogen initially vaporized when it touched the warm parts of the flask and connecting tubes, after all of the hydrogen system had cooled to the boiling point of hydrogen, the hydrogen remained liquid and began to fill the flask. A 1 kΩ carbon resistor at the bottom of the target flask acted as a remote level sensor to indicate when the bottom of the flask was immersed in liquid hydrogen and a similar level sensor at the top indicated when the flask was full. After the reservoir had partially filled, the supply of hydrogen gas was shut off. Hydrogen pressure in the target was kept stable by measuring the pressure and feeding back power to a resistive heater on the cold head of the refrigerator. The hydrogen system was insulated against radiative heat transfer by a layer of 6 μm aluminized mylar wrapped around the flask. A vertical

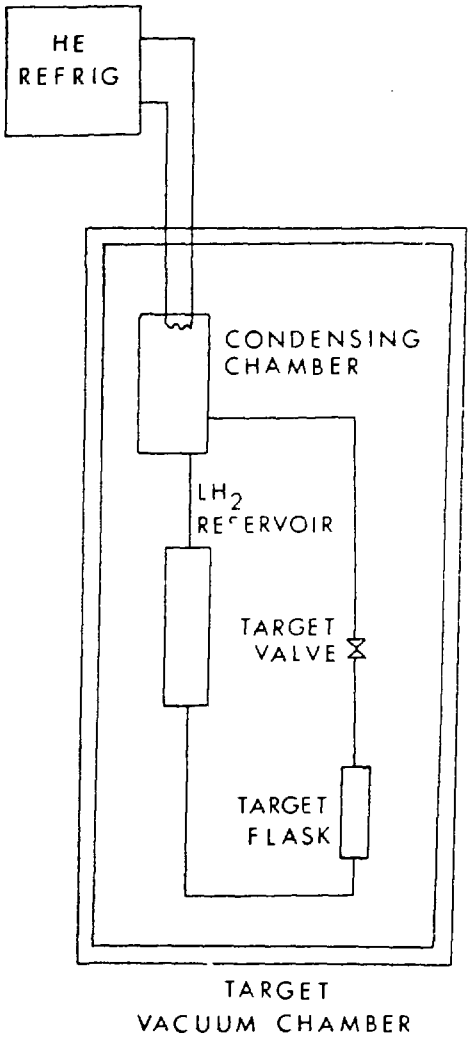

Figure 2. Piping schematic for the LH_2 target and refrigeration system.

slit in the insulation enclosing the flask permitted a visual inspection of the level of liquid hydrogen it contained.

Data were accumulated with the target flask empty as well as full of liquid hydrogen so that background not associated with the hydrogen

could be subtracted. To empty the flask, we simply closed the target valve, a helium-driven valve in the tube connecting the top of the target flask to the reservoir. Gaseous hydrogen boiling from the liquid hydrogen became trapped beneath the target valve forcing the liquid hydrogen out of the flask and up into the reservoir. The reservoir had more than adequate volume to store all of the liquid hydrogen during a data run with the target flask empty. Of course, the empty target flask still contained gaseous hydrogen at somewhat above 20° K, but this was accounted for in the analysis.

Spectrometer

A schematic profile view of the double-focusing, 180° vertical bend, magnetic spectrometer and the particle detection system is displayed in Fig. 3. The same spectrometer was used in a previous experiment that also measured the doubly differential cross section for the π^+ meson produced in the reaction $\pi^-p \rightarrow \pi^+\pi^-n$.[10] Its design has been discussed by Oyer.[18] The vacuum chamber that passes through the two 90° bending magnets has a rectangular cross section which measures 23.7 cm × 9.8 cm. This gap defines a solid angle acceptance of about 16 msr at the center of the focal plane. If desired, a smaller acceptance could be defined by a set of variable slits at the entry of the first magnet. The entry and exit faces of the magnets were at an angle of 26.6° to the direction of the central trajectory. Hence, each magnet acted like a sector magnet with a thin lens superimposed at each end. This configuration resulted in "edge focusing" so that the spectrometer focused in the nonbend plane as well as in the bend plane. Estimates of the magnification and momentum dispersion of the

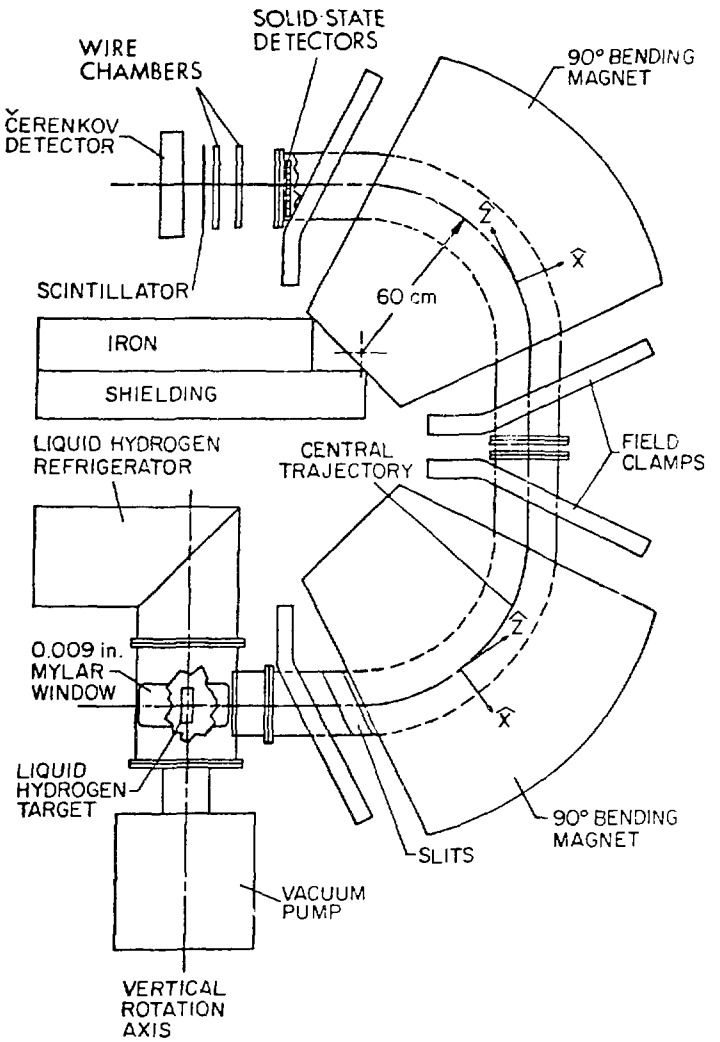

Figure 3. Profile view of the spectrometer and the particle detection system.

spectrometer are -0.96 and 4.26×10^{-3}/cm, respectively, as obtained from a Monte Carlo simulation.[10,18]

The spectrometer assembly, including the cryostat, LH_2 target, and scattering chamber, was mounted on a Navy surplus 5 inch gun

mount. This assembly could be rotated freely about the vertical axis of the cylindrical target flask for laboratory scattering angles between 20.36° and 132°. For the previous experiment,[10] the spectrometer could be rotated only as forward as 32°. The increased range for this experiment was obtained by building a larger scattering chamber. Scattering angles were measured from an angular reference system surveyed and painted on the floor of the experimental area. The reference system consisted of a series of radial lines at 5° intervals that were centered at the spectrometer's rotation axis. To measure at scattering angles that were an integral multiple of 5°, we rotated the spectrometer until we had aligned a plumb bob suspended from the front of the spectrometer with the reference line for the desired angle. For other scattering angles, it was necessary to interpolate between the two reference lines that most nearly approximated the desired angle. Since the plumb bob was 1.84 m from the axis of rotation, we could calculate the necessary arc length through which we needed to move the plumb bob to obtain the desired angle. This distance was measured with a ruler and marked. We then rotated the spectrometer until the plumb bob was aligned with the marked position.

The central momentum of the spectrometer was determined by the uniform fields of the two bending magnets. For a particle of unit electronic charge, the central momentum is assumed to be given by

$$p_c = \frac{a}{2} [H_1(x) + H_2(x)] ,$$

where $H_i(x)$ is the field in the ith magnet, x, the spectrometer shunt

voltage, is the potential difference across a metal alloy shunt in series with the two magnets, and a = 18.119 ± 0.012 (MeV/c)/kG is a conversion factor determined experimentally.[10] Since it can be shown that a = eR, with e the electronic charge and R the average bending radius, the measured value of a corresponds to R = 60.4 cm, in good agreement with the 60 cm for which the spectrometer's geometry was designed. The factor a had been previously determined by mounting an ^{241}Am source on beam line in place of the LH_2 target to provide a spectrum of alpha particles with well-known energies. A counting rate was acquired for several settings of the shunt voltage in the ninth and tenth of 19 surface barrier detectors located at the focal plane for the previous experiment.[10] This counting rate was maximum at the shunt voltage that corresponded to the primary peak in the alpha particle spectrum. The homogeneous field in each magnet was well represented by an integrated Fermi distribution[18]:

$$H(x) = A + B\sigma \left[1 + \exp\left(-\frac{\mu}{\sigma}\right)\right] \ln\left\{\left[1 + \exp\left(\frac{\mu}{\sigma}\right)\right]/\left[1 + \exp\left(\frac{\mu - x}{\sigma}\right)\right]\right\} ,$$

where values of the parameters are given in Table I. For small shunt voltage, the fields are approximately linear: $H(x) \approx A + Bx$. For large shunt voltage and $\mu/\sigma \gg 1$, the fields approach constant saturation levels: $H(x) \approx A + B\mu$. In practice, the upper momentum limit of the spectrometer is limited to about 325 MeV/c by the maximum allowed temperature for the cooling water at output.

A particle that entered the spectrometer along its central trajectory with momentum p_c would be transported through the internal

TABLE I. Parameters for describing magnetic fields in the spectrometer.

	A(G)	B(G/mV)	μ(mV)	σ(mV)
Magnet 1	12.55 ± 8.98	278.9 ± 0.42	74.02 ± 1.13	7.436 ± 0.54
Magnet 2	19.65 ± 3.45	277.8 ± 0.15	72.34 ± 0.39	6.484 ± 0.19

vacuum chamber and out through the center of the focal plane. At the focal plane of the spectrometer was located a vertical ladder of 18 solid-state transmission detectors, each of which defined a channel. The momentum of a particle that entered the spectrometer along its central trajectory and emerged through the center of the Ith detector is given by

$$p_I = p_c[1 + \delta(I - 9.5)] \ .$$

Since the spectrometer dispersion δ was measured to be $(5.132 \pm 0.011)\times10^{-3}$/channel, the solid-state detectors covered a $\Delta p/p$ of 9.2%.

Particle Detection System

The particle detection system for this experiment consisted of 18 solid-state detectors, two multiwire proportional chambers, a scintillation detector, and a Cerenkov detector. A particle that emerged from the spectrometer passed through one of the solid-state detectors, both MWPC's, the scintillation detector, and the Cerenkov detector. A

coincidence among both wire chambers and the scintillation detector signaled the on-line computer to record pulse heights from all the solid-state detectors, timing of pulses from the MWPC's, and pulse heights from the Cerenkov detector. The details of data acquisition and the criteria that had to be satisfied by valid events are discussed in Chapter III.

The solid-state detectors were of the Si(Li) variety, each of which measured 1 cm × 4 cm × 0.06 cm. They were arranged in a vertical ladder at the focal plane of the spectrometer with the 1 cm dimension spanning the vertical (x) direction and the 4 cm dimension spanning the horizontal (y) direction. The detectors were in a staggered arrangement, being positioned alternately 2 mm on either side of the focal plane. Since the detectors each spanned 1.0 cm in the direction of dispersion and were spaced with centers 1.186 cm apart, they indicated the momentum distribution at the focal plane.

The signal from each solid-state detector was a current pulse with a total charge proportional to the energy lost by a particle that had passed through the detector. A preamplifier located near the detector produced a current pulse whose amplitude was proportional to the integrated charge of the initial pulse with a long exponential decay. After traveling the length of a connecting cable, the output pulse was amplified, integrated once, and differentiated twice, all with 250 ns time constants. The resulting bipolar pulse had an amplitude proportional to the energy lost in the detector. This amplitude was digitized by a peak-detecting 11-bit CAMAC analog-to-digital converter (ADC).

Two wire chambers designated W1 and W2 and a thin scintillation detector designated S1 formed the trigger system. The fast timing of S1 defined the fiducial time of an event. The plastic scintillator of S1 measured 29.8 cm × 5.7 cm × 0.16 cm. An RCA 6199 phototube enclosed by mumetal and iron magnetic shields observed the scintillator through a Lucite light pipe. S1 was located 3.5 cm behind W2 such that its scintillator covered the 31.8 cm × 7.2 cm mylar window of the chamber. The signal from S1 was also digitized by an 11-bit CAMAC ADC.

The wire chambers W1 and W2, located respectively 15.9 cm and 24.8 cm behind the solid-state detectors, were based on a design developed at LAMPF by Morris.[19] Each chamber measured 48.9 cm × 23.1 cm × 2.4 cm and contained an anode plane and a parallel cathode plane, which were separated by 4.8 mm. The vertically oriented anode wires were spaced 2 mm apart and consisted of 20 μm gold-plated tungsten. The cathode wires were oriented horizontally with 1 mm wire spacing and consisted of 80 μm gold-plated aluminum. Ions produced when a charged particle passed through a chamber induced pulses on the wires nearest the position crossed by the particle. The wires for the anode and cathode fed into separate delay lines, each of which provided signals at both ends. The time required for the pulses to travel along the delay lines from the point of ionization was measured by CAMAC time-to-digital converters (TDC's).

A high efficiency gas mixture known as "magic gas" filled the chambers. This mixture was developed at CERN and consisted of 67.8% argon, 32.1% isobutane, and 0.1% freon 13 B-1, by volume. The argon was bubbled through 0° C isopropyl alcohol before mixing with the

other gases. Free radicals from dissociation of the freon and isobutane could polymerize on the wires forming an insulating layer. The isopropyl alcohol provided neutralizing electric charges to prevent migration of the radicals to the wires and hence to increase the lifetime of the chambers.

The efficiencies of W1 and W2 were measured regularly throughout the experiment by inserting a scintillation detector, designated S0, immediately before W1. Efficiencies were then calculated as a function of high voltage on the chambers as discussed in Chapter III. Each chamber typically operated with almost 100% efficiency at about 3.7 kV.

A liquid fluorochemical (FC-88) Cerenkov detector was the final element of the detection system. The back of the Cerenkov detector was located 19.05 cm behind W2. Fluid for the detector was held in a container of 1.6 mm aluminum that was 35.6 cm high, 10.5 cm wide, and 7.9 cm thick. A 0.4 mm sheet of alzak lined the container to provide high reflectivity. Amperex 58 DVP phototubes, which operated at about 2.3 kV, were located at the top and bottom of the container to detect Cerenkov radiation produced in the medium. Signals from the top and bottom phototubes, denoted CT and CB, respectively, were digitized by 11-bit CAMAC ADC's. The index of refraction for the fluorochemical was 1.238 at 25° C for the sodium D line. Averaged over the entire spectrum of Cerenkov radiation, the effective index was somewhat higher and corresponded to a velocity threshold of about 0.79 c. Thus, for momenta less than about 180 MeV/c, pions were too slow to produce Cerenkov radiation and the Cerenkov detector provided a means to identify most electron events.

For most measurements of single pion production, a 0.8 mm lead absorber was placed immediately before S1. This absorber substantially eliminated events resulting from protons and "soft" electrons. The absorber was removed whenever we tried to detect pions with momenta between 60 and 72 MeV/c. At low momentum, the background of soft electrons was often as large, or larger, than the number of pions we were trying to detect. These electrons did not always produce pulses in the Cerenkov detector and hence, another method was required to reduce the background. The thin detector S1 was removed and replaced with a 1.3 cm-thick counter that could stop pions below 72 MeV/c and yet easily pass electrons. A second counter that measured 31.1 cm × 7.0 cm × 0.3 cm was inserted between the thick counter and the Cerenkov detector to veto these electrons.

Electronics

The usual trigger for an event, denoted W1Y•W2Y•S1, was formed by a threefold coincidence among the wire chambers W1 and W2 and the scintillation detector S1. A schematic diagram of the trigger logic is displayed in Fig. 4. W1Y was a 35 ns standard NIM logic pulse produced from a logic fan-in whenever pulses were received from either end of the anode delay line of W1, and similarly for W2Y. The trigger used pulses from the anode delay line, rather than from the cathode, because it was shorter and thus provided signals with less time jitter. We delayed the pulse from S1 by about 15 ns to allow time for both W1Y and W2Y to be present in the logic box that formed the trigger pulse. The wire chamber pulses were sufficiently wide that,

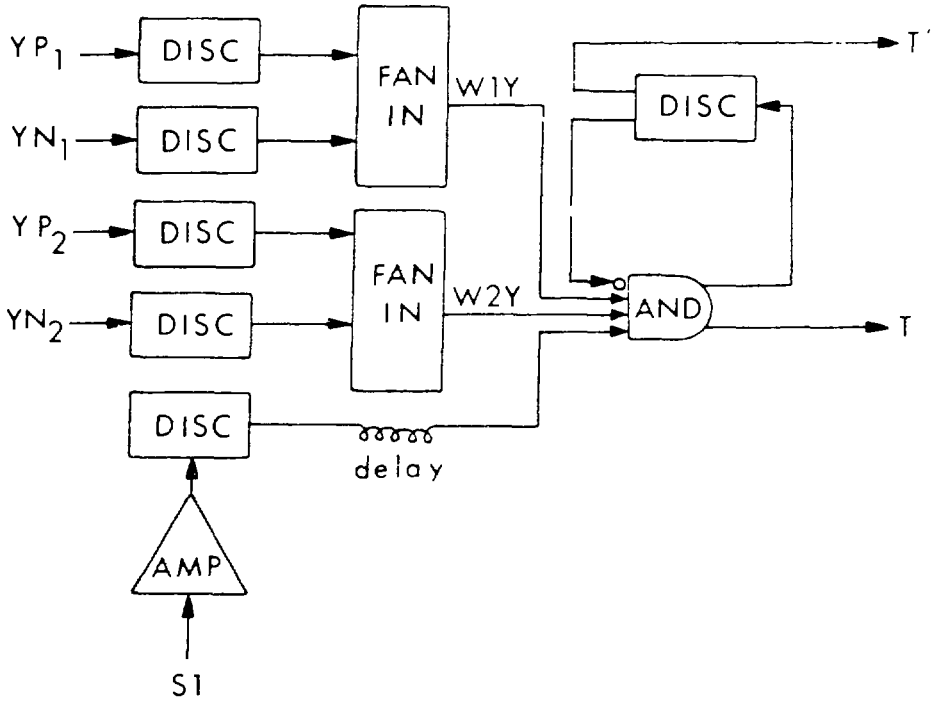

Figure 4. The event trigger logic. The arrival times of pulses from the positive and negative ends of the anode delay line for W1 are denoted by YP_1 and YN_1, respectively, and similarly for W2.

when the pulse from S1 arrived, all three pulses overlapped and formed a trigger pulse T.

A schematic diagram for the data acquisition logic is shown in Fig. 5. The rise of the trigger pulse initiated an output pulse T'

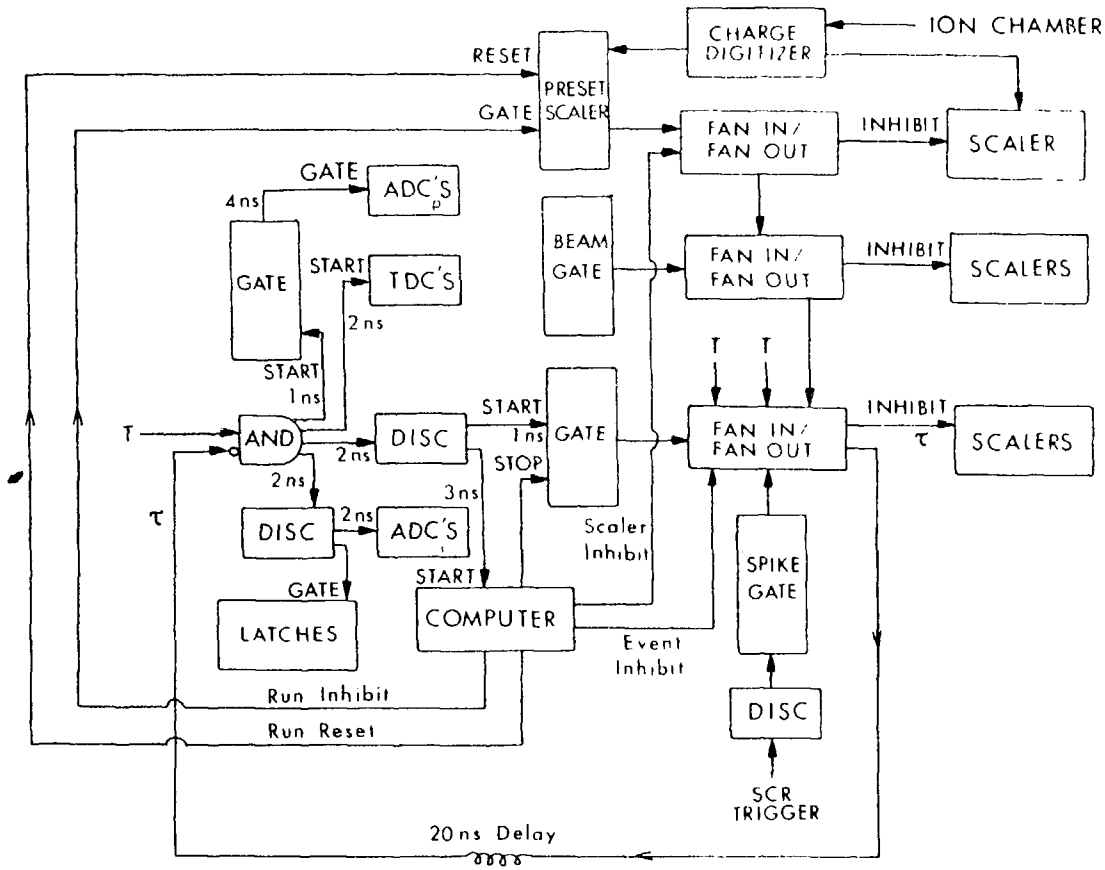

Figure 5. Data acquisition logic. The peak-detecting ADC's for the solid-state detectors are denoted by ADC_p whereas the integrating ADC's for the Cerenkov detector and the scintillation detectors are denoted by ADC_i.

from a discriminator, which provided a fast inhibit of further triggers and allowed sufficient time for signals from the detection system to reach the CAMAC registers: a set of peak-detecting ADC's to measure pulse heights in the signals from the solid-state detectors; a set of integrating ADC's to measure pulse heights from the Cerenkov detector and the scintillation detectors; a set of TDC's to measure the timing of pulses from the MWPC's; and a coincidence latch used in measurements of MWPC efficiencies. We delayed a 150 ns gate pulse for the peak-detecting ADC's to allow time for their preamplifiers to integrate the current pulses from the solid-state detectors. The trigger pulse notified the on-line PDP-11/45 computer to read and clear the various CAMAC registers and initiated a dead-time pulse τ, which inhibited further triggers until the event had been read into core. The trigger pulse also initiated a pulse from a gate generator that prolonged the dead time until the computer was ready for a new event. When it was ready, the computer lifted its event inhibit and produced a reset pulse that terminated the gate pulse.

Several quantities of interest, which we list in Table II, were scaled in CAMAC scalers during each run. The computer read and cleared the scalers periodically. If the digital volt meter that measured the spectrometer shunt voltage were not busy digitizing, the shunt voltage was read at the same time. The recording of events was inhibited by the computer during scaler reads. For the scalers, there were three levels of inhibit. The digitized charge from the ionization chamber was scaled only during an interval gate which indicated that a run had started and was in progress. Total-time scalers for the event trigger and coincidences in either arm of the scattering

TABLE II. Quantities scaled during a run.

q_{IC}	digitized charge from the ionization chamber
T_ℓ	the number of event triggers during live time
T_t	the number of event triggers during total time
$(S1W \cdot S2W \cdot S3W)_\ell$	triple coincidences in the west arm of the scattering monitor during live time
$(S1W \cdot S2W \cdot S3W)_t$	triple coincidences in the west arm of the scattering monitor during total time
$(S1E \cdot S2E \cdot S3E)_\ell$	triple coincidences in the east arm of the scattering monitor during live time
$(S1E \cdot S2E \cdot S3E)_t$	triple coincidences in the east arm of the scattering monitor during total time

monitor required the presence of the LAMPF beam gate as well as the interval gate. The primary proton beam and hence the pion beam had a macropulse structure of 500 μs duration and a repetition rate of 120 Hz. Finally, live-time scalers for the event trigger and coincidences in either arm of the scattering monitor required both the interval gate and the beam gate but were inhibited by the dead-time pulse τ. Significant spikes were periodically produced in the signals from the solid-state detectors by silicon control rectifiers (SCR's) turning on in the power supply for the spectrometer. To avoid this source of accidentals and a long uncontrolled dead time, the triggers and the live-time scalers were inhibited for a period of 210 μs covering the period when the spikes occurred. This "spike" gate was primarily a precaution since the spikes were usually outside the beam gate.

CHAPTER III

DATA ACQUISITION

Introduction

This chapter discusses the procedure used during the experiment to collect, record, and, to some extent, analyze the data. Data were collected in a series of runs in which the spectrometer was adjusted to detect particles of the desired charge, momentum, and scattering angle. Each data run was started by an operator command from a Tektronix 4010 terminal. Many quantities, such as the run number, the status of the target flask, the approximate beam energy, the laboratory scattering angle, and general run comments, were entered from the terminal at the start of a run. For successive runs, the run number incremented automatically, whereas an operator was required to change other quantities. Runs normally terminated automatically when a predetermined amount of charge was accumulated from the ionization chamber on the preset scaler. It was possible, however, to interrupt or terminate a run at any time by the appropriate commands.

A sample of the detected events were analyzed during data acquisition. This on-line analysis served several useful functions: it allowed us to estimate the relative sizes of our measured cross sections and to generally check our experimental technique, it enabled us to establish cuts that could be used to identify and later eliminate unsatisfactory events, and it provided a means to estimate when we had obtained a desirable statistical accuracy for each

measurement. In special cases to be described later, it also allowed us to periodically check the efficiencies of the wire chambers and the Cerenkov detector. After the data had been collected, we more carefully analyzed all of the recorded events. The criteria for accepting events were refined, a quantitative estimate of the efficiency of the Cerenkov detector for detecting electrons was established, and finally, a set of magnetic tapes were produced that contained histograms for each run of the number of acceptable events in each solid-state detector. One histogram was for events that produced pulses in the Cerenkov detector and one was for events that did not.

Data Acquisition

At the beginning of a run, the computer was initialized, the spectrometer shunt voltage was read, and a 128-word header record, which contained general information about the run and identified its start was written on magnetic tape. The computer stored information for each event and each scaler read in blocks of 16-bit words that formed a 1024-word buffer. When the buffer was full, it was written on tape. Thus, many 1024-word records usually followed the header record on tape. The information recorded for each event is summarized in Table III. At the end of the run, the scalers and shunt voltage were read a final time and a trailer record, which was similar to the header record, was created. The buffer containing the last scaler block was then written on tape followed by the trailer record and an end of file. In Table IV, the contents of header and trailer records are summarized.

TABLE III. Contents of an event block.

EVENT NUMBER	the number of the event in the run
SSD_I	the digitized pulse height for the Ith solid-state detector (I = 1,•••,18)
CT	the digitized pulse height for the top phototube of the Cerenkov detector
CB	the digitized pulse height for the bottom phototube of the Cerenkov detector
S1	the digitized pulse height for the scintillation detector located immediately after W2
XP_1,XN_1	the arrival times of pulses from the cathode delay line of W1
YP_1,YN_1	the arrival times of pulses from the anode delay line of W1
XP_2,XN_2	the arrival times of pulses from the cathode delay line of W2
YP_2,YN_2	the arrival times of pulses from the anode delay line of W2

Several histograms were formed by the computer during each run. The quantities to be histogrammed were specified in a file at the start of the data acquisition program.[20] Histograms were created for such quantities as the number of events in each of the solid-state detectors, pulse heights, and particle locations extrapolated from wire chamber data. Creating histograms and selecting cuts for the data were major parts of the on-line data analysis. Events that contributed to the histograms were analyzed when the computer was not busy recording data or writing tapes. Four histograms were always

TABLE IV. Contents of header and trailer records.

LABEL (-1 for header, -9 for trailer)
RUN NUMBER
STATUS OF TARGET FLASK (full or empty)
INCIDENT KINETIC ENERGY (MeV)
INCIDENT MOMENTUM (MeV/c)
LABORATORY SCATTERING ANGLE (deg)
INITIAL SHUNT VOLTAGE (mV)
FINAL SHUNT VOLTAGE (mV)[a]
DATE
TIME
GENERAL RUN COMMENTS

[a]For header records, the value of the final shunt voltage was zeroed.

included in the histogram file, each of which had 18 bins, one for each solid-state detector. Events in which exactly one solid-state detector produced a pulse, without a coincident pulse in the Cerenkov detector, were added to the first histogram. Events in which exactly one solid-state detector produced a pulse with a coincident Cerenkov pulse were added to the second histogram. Events with exactly two solid-state detectors producing pulses were added to the third histogram and events with more than two were added to the fourth histogram. The third and fourth histograms ignored the Cerenkov detector. Much longer lists of histograms were generated whenever we investigated the performance of detectors such as the wire chambers or the Cerenkov

detector. Any or all of the histograms could be plotted at the end of the run.

After a run had ended, the computer produced a hard-copy summary of pertinent information about the run that included the four histograms discussed above of the analyzed events in each solid-state detector, most of the data in the trailer record, and the total accumulation of counts in each scaler. These summaries also included calculations of the live-time fraction and an account of the number of events that failed various cuts which are discussed below.

Whenever we measured single pion production, data were collected with the LH_2 target flask both empty and full so that background could be subtracted. For measurements of elastic scattering, data were usually collected only with the target flask full, although data were collected at a few scattering angles with the flask empty to estimate the size of the background elastic peak.

The finished product of data acquisition was a set of magnetic tapes, each of which contained several files, one for each data run. These tapes formed a permanent record of all events detected during the experiment.

Replay of Events

The events recorded on tapes during data acquisition were replayed for off-line analysis on a PDP-11/70 computer. Replaying the data allowed us to analyze several runs together to develop more stringent cuts for eliminating unsatisfactory events. After the best cuts had been established, they were employed to reanalyze all events.

The data tapes were read and controlled by a set of FORTRAN-callable subroutines developed at LAMPF.[21] All runs for a particular measurement were analyzed as a set. The header record, which indicated the start of a run, was identified by two means. First, the 128-word length of the header record was unique. Second, the first element of the array into which the data were read was a label that for header records had the value -1. Several 1024-word records followed the header record. These were divided into 16 blocks, each of which contained information either from a scaler read or about an individual event. Data from each block were read into an array, the first element of which was again a label. This label was zero for scaler blocks and the event number for event blocks. The trailer record was the last record on tape for a run and it was identified by a label with value -9. When a scaler block was encountered on tape, the replay program incremented and stored running sums of the number of counts in each scaler. The program also calculated a mean spectrometer shunt voltage by arithmetically averaging all values of the shunt voltage that were read during a run. This mean shunt voltage determined the central momentum p_c of the spectrometer for the run. Measurements of the shunt voltage during a run varied by about 0.02% to 0.08%. When an event block was encountered, up to 15 criteria could be selected to eliminate undesired events. These criteria are discussed in the next section. As many as 70 histograms and five scatterplots of the analyzed events could be incremented and stored.

After all runs for a measurement had been read and analyzed, we could select any or all of the histograms and/or scatterplots to be plotted. Summaries containing important information about each run

were stored on disk. Each summary contained the approximate incident momentum, the nominal laboratory scattering angle, the mean spectrometer shunt voltage, the total accumulation of counts in each scaler, and, for identification purposes, the run number. They also contained histograms of the analyzed events in each solid-state detector, one histogram for events that produced pulses in the Cerenkov detector and one for events that did not. These run summaries were copied to magnetic tape for subsequent analysis carried out with CDC 6600 and CDC 7600 computers at the laboratory and discussed in the next four chapters.

Criteria for Accepting Events

The raw data tapes contained information about every event for which a threefold coincidence had been produced among both MWPC's and S1. Since this was a very unrestrictive trigger, many of these events were undesirable. This section primarily describes the cuts that identified and eliminated unacceptable events. It also discusses efficiency studies of the Cerenkov detector and wire chambers. For each acceptable event, we required that one and only one solid-state detector had a pulse above its discrimination level, that the wire chambers functioned properly, and that the trajectory reconstructed from information furnished by the wire chambers agreed with the solid-state detector that had produced a pulse. Events that did not satisfy these criteria were not analyzed.

All events required a coincidence between both MWPC's and, therefore, it was important during data acquisition that both operated as efficiently as possible. We periodically measured their efficiencies

during the experiment by installing a scintillation detector called S0 immediately before W1, the first MWPC. Any particle that passed through the spectrometer, S0, and S1 would pass through both wire chambers. For the efficiency measurements, the event trigger was changed to a coincidence among three or more of the logic pulses S0, S1, W1Y, and W2Y and several short runs of πp elastic scattering were made with different high voltages on the chambers. For these runs, the computer used a latch module to determine which detectors had produced signals. The computer subsequently scaled several coincidences: S0•S1, S0•W1Y•S1, S0•W2Y•S1, S0•W1Y•W2Y, S1•W1Y•W2Y, and S0•W1Y•W2Y•S1. The efficiency of W1 was calculated as the ratio of the number of events that produced the coincidence S0•W1Y•W2Y•S1 to the number of events that produced S0•W2Y•S1, and similarly for W2. An efficiency curve was plotted for each MWPC, a sample of which is displayed in Fig. 6. Stability was insured by selecting the high voltage for an efficiency well above the knee of the curve. Operating efficiencies were typically about 99.9% for each chamber.

We analyzed only those events for which the wire chambers operated properly. The sum of the arrival times of pulses from both ends of a delay line would be constant if not for variation in the drift time of ions to reach the signal wires through the chamber gas. In a chamber that operates properly, this drift time is canceled when the sum of arrival times from the anode delay line is subtracted from the sum from the cathode delay line. Thus, if each chamber was operating properly, the sum-difference (chamber indices 1 and 2 have been dropped in the display equation)

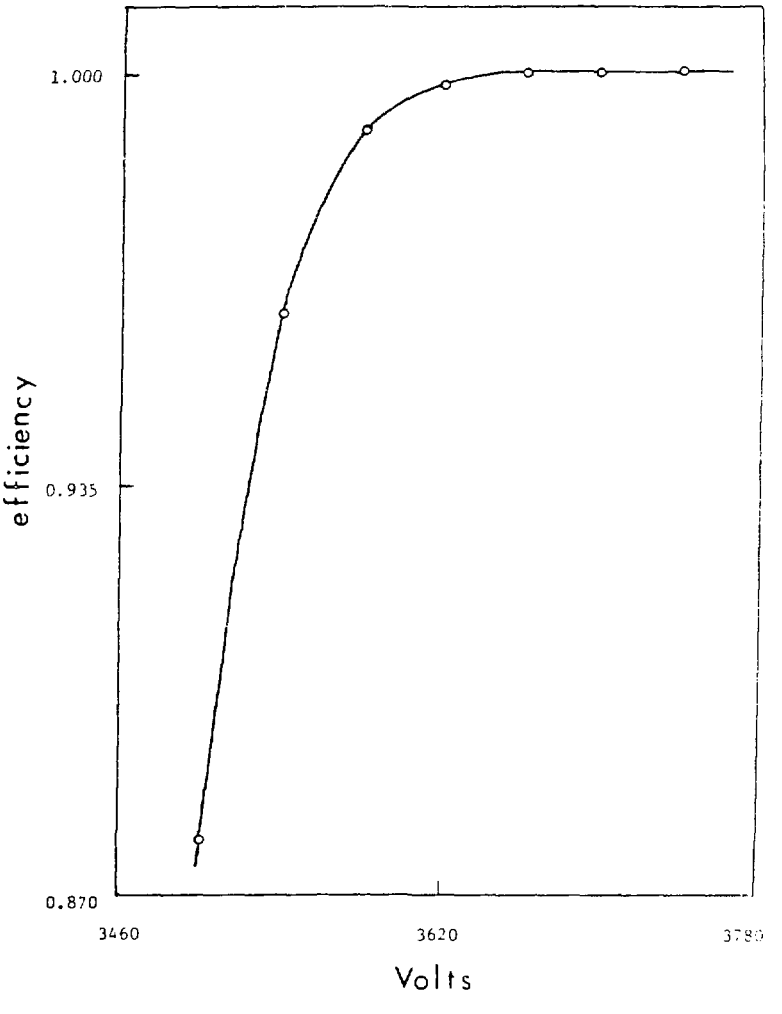

Figure 6. Sample efficiency curve for a wire chamber.

$$\Delta = (YP + YN) - (XP + XN)$$

should be constant. A sample histogram of a sum-difference distribution is displayed in Fig. 7. The distribution is sharply peaked, as expected, with a FWHM of 20 channels or 2 ns. Measurements of πp elastic scattering provided many events to establish reasonable ranges for Δ_1 and Δ_2. Usually, less than 0.5% of events were outside of these ranges and were rejected.

Locations in the wire chambers were described by the TRANSPORT[17] coordinates for the spectrometer. The direction of beam propagation defined the Z axis, the magnetic field for positively charged particles defined the Y axis, and the requirement of an orthogonal right-handed coordinate system defined the X axis. As Fig. 3 indicates, the X axis pointed vertically upward at the wire chambers. We defined the origin of the coordinate system as that position in the focal plane of the spectrometer through which a particle traveling along the central trajectory with momentum p_c would pass. The coordinates of a particle at each wire chamber were calculated from the arrival times of pulses from the anode and cathode delay lines. These coordinates are given by (chamber indices 1 and 2 have been dropped in the display equations)

$$X = A_x + B_x(XN - XP) ,$$

$$Y = A_y + B_y(YN - YP) ,$$

$$Z = \text{constant} .$$

Table V presents a summary of the channel-to-position conversion

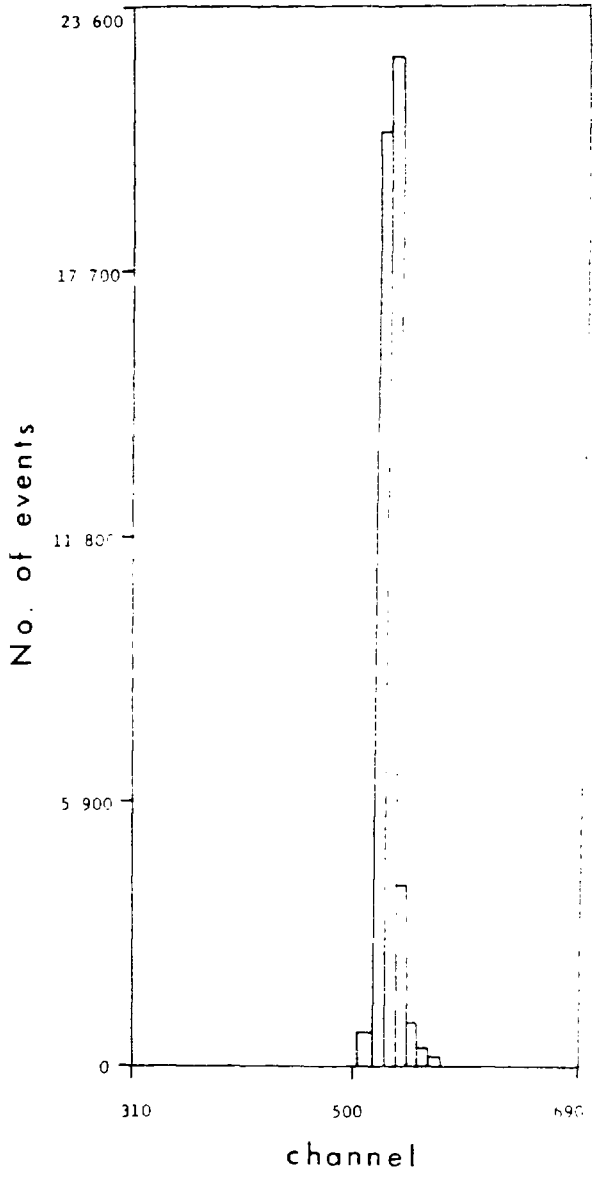

Figure 7. Sample histogram of a sum-difference distribution.

parameters and distance Z of each MWPC from the focal plane. The conversion parameters were determined by calibrating each MWPC and the system as a whole with an ^{55}Fe electron capture source. To calibrate a chamber, histograms of the difference distributions were formed with the source positioned on the chamber at (X,Y) locations: (0,0), (5.08,0), (-5.08,0), and (0,-2.54), with X and Y in cm. The channel for the centroid of a distribution was associated with the position (in cm) of the source at the chamber. Two different positions in both X and Y were sufficient to determine the conversion parameters. The widths of the distributions established the X resolution to be ±0.4 mm and the Y resolution to be ±1 mm for each chamber.

We parametrized the mean trajectory of the ionizing particle in the form:

$$X = X_1 + \frac{dX}{dZ}(Z - Z_1) ,$$

$$Y = Y_1 + \frac{dY}{dZ}(Z - Z_1) .$$

TABLE V. Calibration parameters and distance Z of each wire chamber from the focal plane.

	A_x(cm)	B_x(cm/channel)	A_y(cm)	B_y(cm/channel)	Z(cm)
W1	-0.1875	0.02083	0.0466	0.01866	15.90
W2	-0.1992	0.01992	0.0050	0.01848	24.79

Histograms of dX/dZ and dY/dZ are displayed in Figs. 8 and 9, respectively. These histograms were formed from several measurements of π^+p elastic scattering at 141 MeV. If only the Ith solid-state detector had produced a pulse above threshold, we could compare X_0, the vertical position of the particle extrapolated to the focal plane, with X_I, the vertical position calculated from the spatial dispersion relation

$$X_I = \delta X \, (I - 9.5) \, ,$$

with δX = 1.186 cm the distance between solid-state detectors. A histogram of the quantity $\Delta X = X_I - X_0$ is displayed in Fig. 10. Since X_I represents the vertical position of the center of the Ith detector, we expect X_I and X_0 to agree within about 0.5 cm. This value is consistent with the 0.52 cm width of the ΔX distribution shown in Fig. 10. In Fig. 11, we display a histogram of Y_0, the horizontal position of the particle extrapolated to the focal plane. From measurements of πp elastic scattering, we constructed histograms of the distributions of dX/dZ, dY/dZ, ΔX, and Y_0. These histograms determined a reasonable range of values for each quantity at the momentum of the measurement. Their nominal ranges were increased as a function of the momentum of the produced pion to allow for multiple small-angle scatterings at low momentum. Contributions to the ranges from each scattering medium in the particle detection system were added in quadrature. Each contribution to the width of the distribution of deflection angles was calculated from the relation[22]

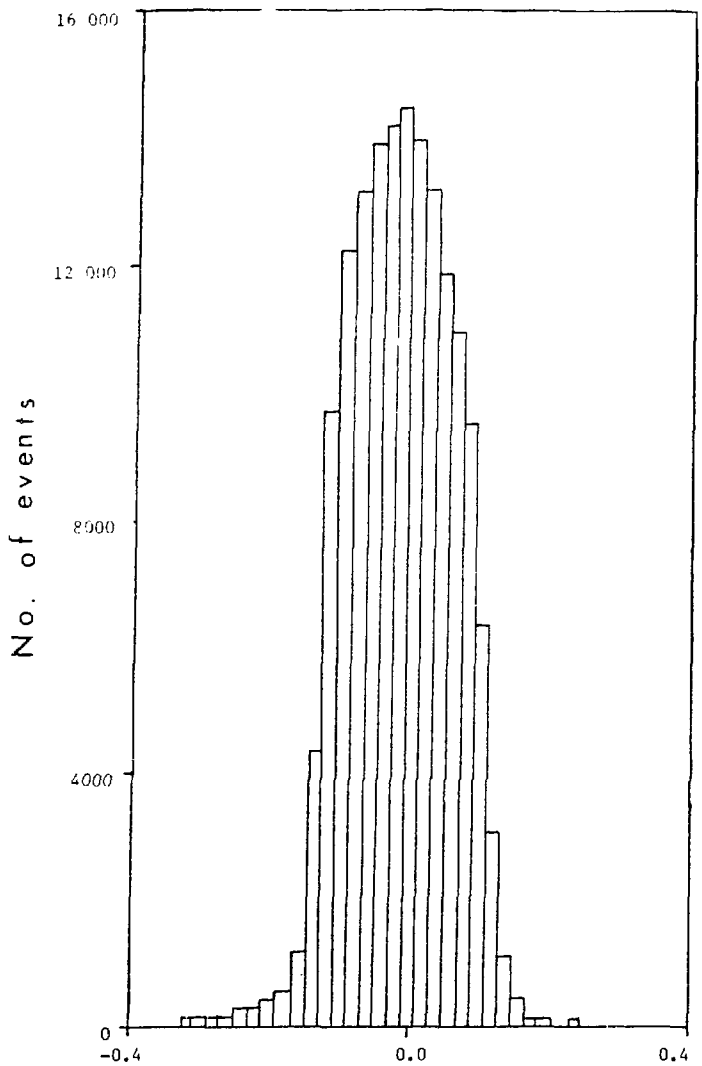

Figure 8. Sample histogram of a dX/dZ distribution.

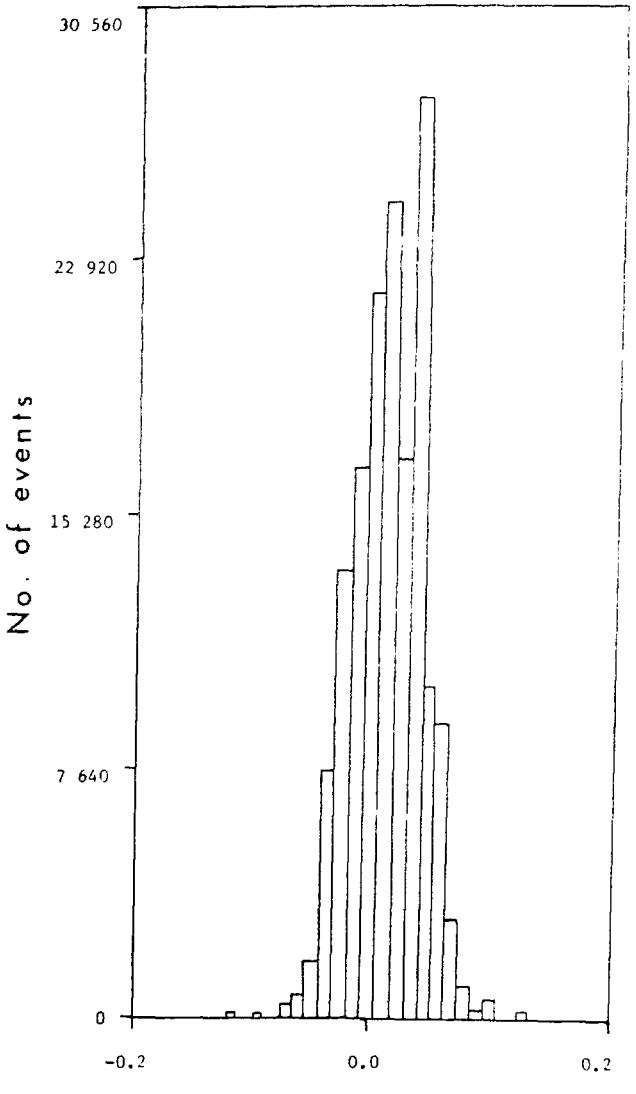

Figure 9. Sample histogram of a dY/dZ distribution.

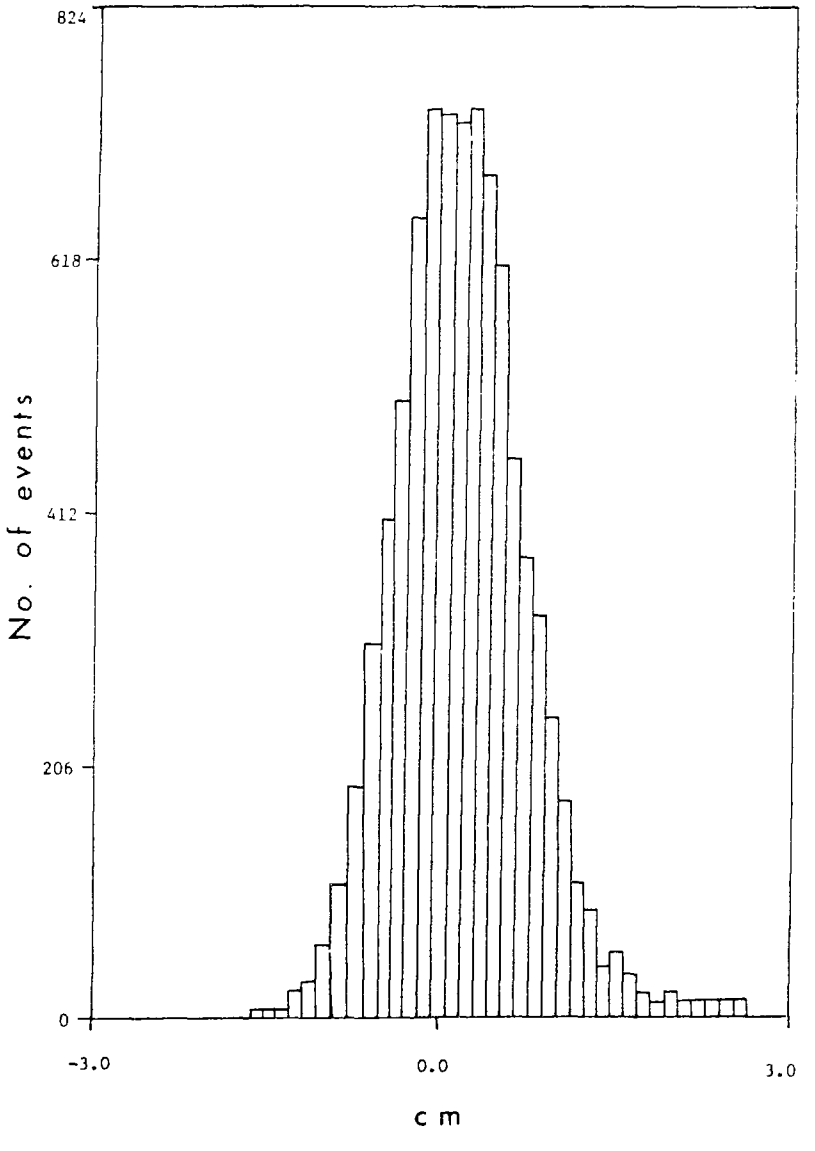

Figure 10. Sample histogram of $\Delta X = X_I - X_0$.

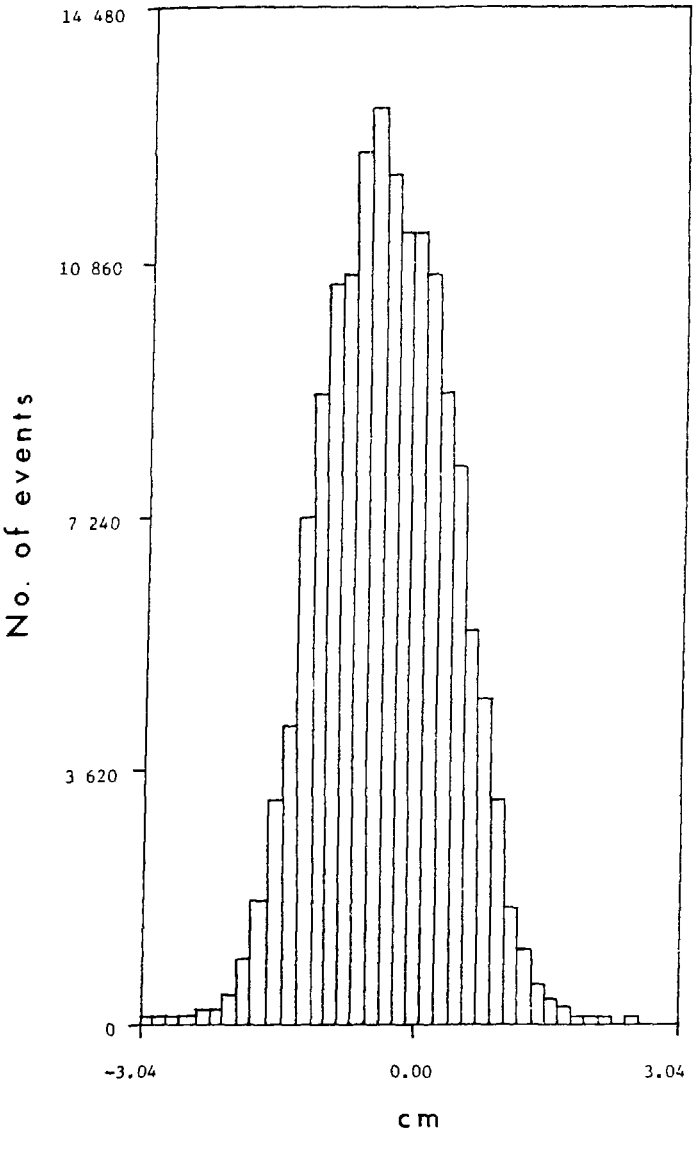

Figure 11. Sample histogram of a Y_0 distribution. Y_0 is the horizontal position of a particle extrapolated to the focal plane.

$$\theta = \frac{15 \text{ MeV/c}}{p_\pi \beta} \left(\frac{L}{L_R}\right)^{1/2} ,$$

where p_π is the pion momentum, β is its speed, L is the thickness of the medium, and L_R is the radiation length of the medium. We considered the following scattering media: the solid-state detectors with L = 0.06 cm, L_R = 9.3 cm, and L/L_R = 0.0064; an aluminum window that sealed the vacuum path through the spectrometer with L = 0.025 cm, L_R = 8.9 cm, and L/L_R = 0.0030; components of the first wire chamber with an effective L/L_R = 0.0092; and the air space between the solid-state detectors and the second wire chamber with L = 24.8 cm, L_R = 39100 cm, and L/L_R = 0.0006. The contributions to the ranges of the dX/dZ and dY/dZ distributions were proportional to θ whereas the contributions to the ranges of the ΔX and Y_0 distributions were proportional to both θ and the distance of the scattering medium from the focal plane. Very loose cuts were established to eliminate events in which values fell outside their expected ranges.

Particle trajectories were also extrapolated forward to the far side of the Cerenkov detector at Z = 43.84 cm. Scatterplots of the distribution of events in the X-Y plane were calculated both for events that produced pulses in the Cerenkov detector and for events that did not. These were compared to insure that both types of events had equal spatial distributions. Sample scatterplots for both kinds of events are displayed in Figs. 12 and 13. These scatterplots show the results of several measurements of π^-p elastic scattering at an incident kinetic energy of 256 MeV. Events that contributed to the scatterplots satisfied all criteria for acceptable events. Although

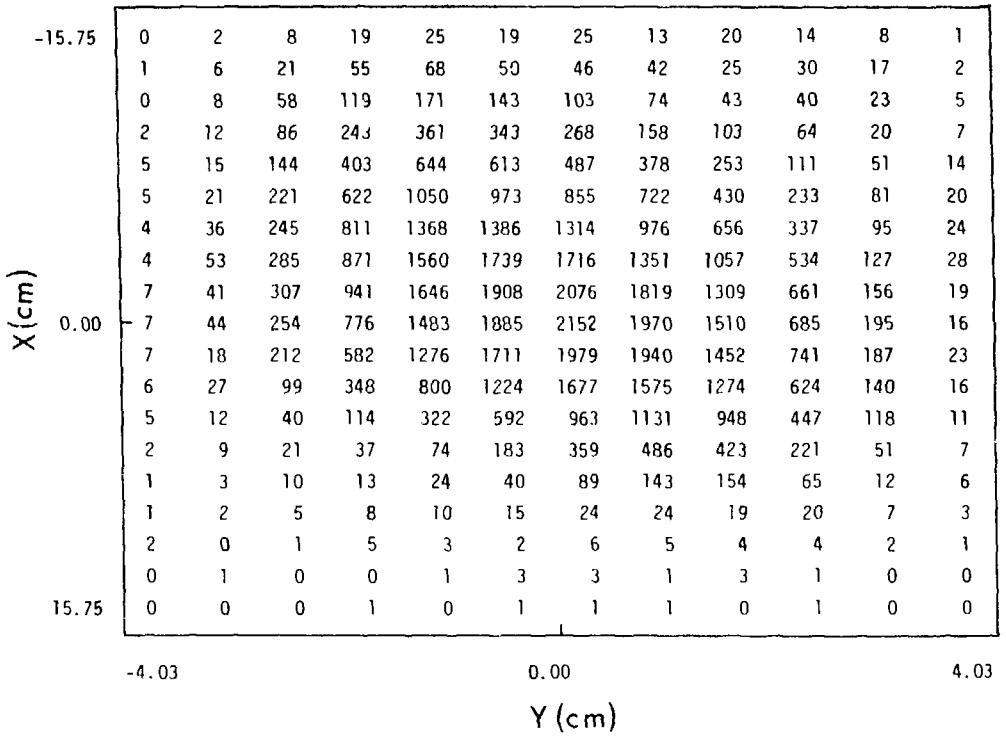

Figure 12. Scatterplot in the X-Y plane at the back of the Cerenkov detector for events that did not produce pulses in the Cerenkov detector.

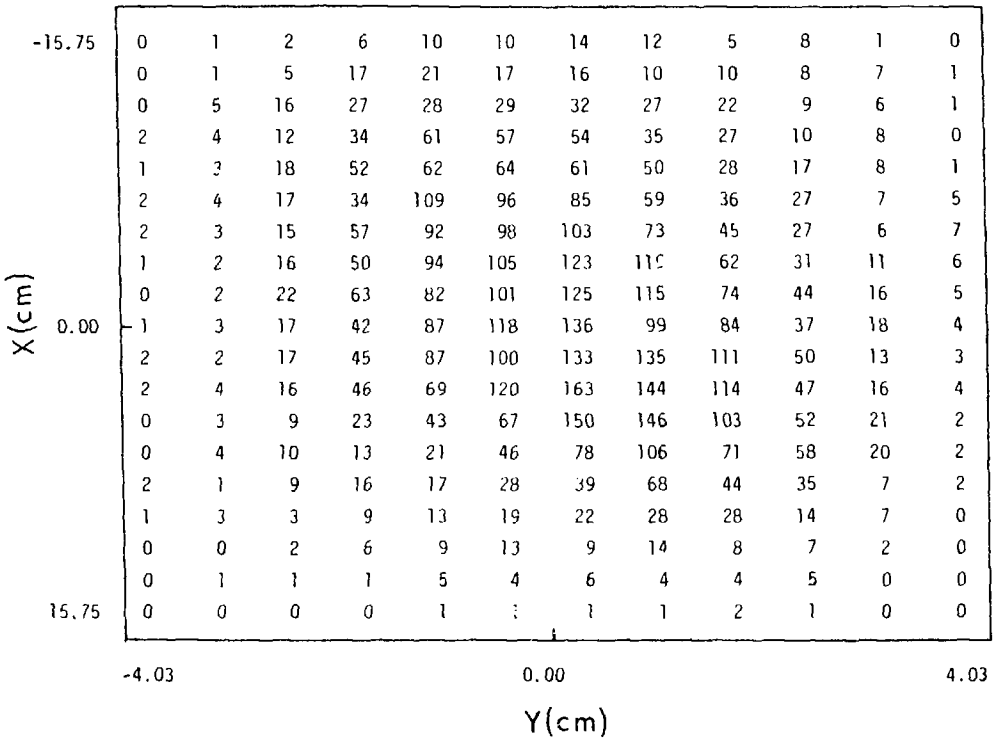

Figure 13. Scatterplot in the X-Y plane at the back of the Cerenkov detector for events that produced pulses in the Cerenkov detector.

the sample scatterplots do not show locations for the edges of the Cerenkov detector, there were extremely few events in which particles passed through those positions.

Since pulses from the scintillation detector S1 formed part of the trigger for events, we monitored the pulse height distribution in S1 throughout the experiment. For almost all measurements, the pulse height in S1 was not required as a means for eliminating unsatisfactory events. However, for three production measurements at 203 MeV in which the π^+ momentum was less than 72 MeV/c, a small peak that we associated with protons appeared in the S1 pulse height distribution. Proton events for most measurements were eliminated by the 0.8 mm lead absorber placed immediately before S1. For these three low-momentum measurements, this absorber was not used. Fig. 14 shows a histogram of the S1 pulse height distribution for one of the three measurements. Events that contributed to this histogram satisfied all other criteria for acceptable events and did not produce pulses in the Cerenkov detector. The events that produced the proton peak were rejected by selecting a pulse height cut-off at channel 300.

Only those events in which exactly one solid-state detector produced a pulse above the discrimination level were accepted. This test eliminated about 20% of the events detected during measurements of elastic scattering, about 60% of the events detected during production measurements at 358 MeV, and about 80% of the events detected during production measurements at 203 MeV. To eliminate background from noise and electrons, we varied the minimum acceptable pulse height for each solid-state detector as a function of the momentum p_π of the detected pions. The pulse height cut-off was determined by inspecting

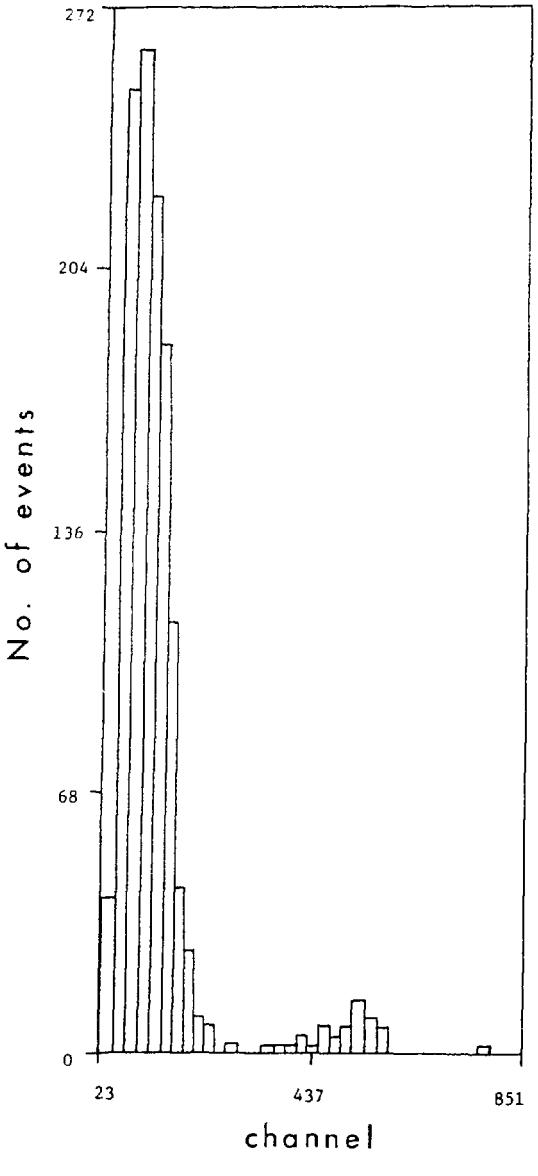

Figure 14. Sample histogram of the pulse height distribution in S1 when no lead absorber was used.

histograms of the pulse height distribution in the solid-state detectors. For most production measurements, the detected π^+ mesons had momenta greater than 100 MeV/c. Fig. 15 shows a typical histogram of the pulse height distribution in the solid-state detectors for a production measurement in which the spectrometer was set to accept 140 MeV/c particles. Events that contributed to this histogram did not produce pulses in the Cerenkov detector. Only a single peak is evident because the dE/dx for pions is close to minimum ionizing above about 100 MeV/c. At this momentum, the number of events that produced pulses in the Cerenkov detector was a small fraction of all acceptable events, which indicated that the electron background was small. The number of electron events that did not produce pulses in the Cerenkov detector was estimated from the assumed momentum dependence of the efficiency of the Cerenkov detector, which is discussed below. For our sample measurement, we eliminated noise by selecting a pulse height cut-off in the solid-state detectors at ADC channel number 110. Events caused by elastically scattered protons were eliminated by selecting an upper pulse height cut-off at channel number 1200. At lower momenta, the upper cut-off was increased to channel number 1950 so that pion events in the tails of the distribution would not also be eliminated. Figs. 16 and 17 display two histograms that correspond to the same measurement of single pion production with the spectrometer set for 83 MeV/c. Only events that did not produce pulses in the Cerenkov detector contributed to the histogram in Fig. 16, which shows peaks for both electron and pion events. These peaks were partially resolved because of differences in dE/dx for the two kinds of particle at this momentum. Only events that had produced a pulse in the

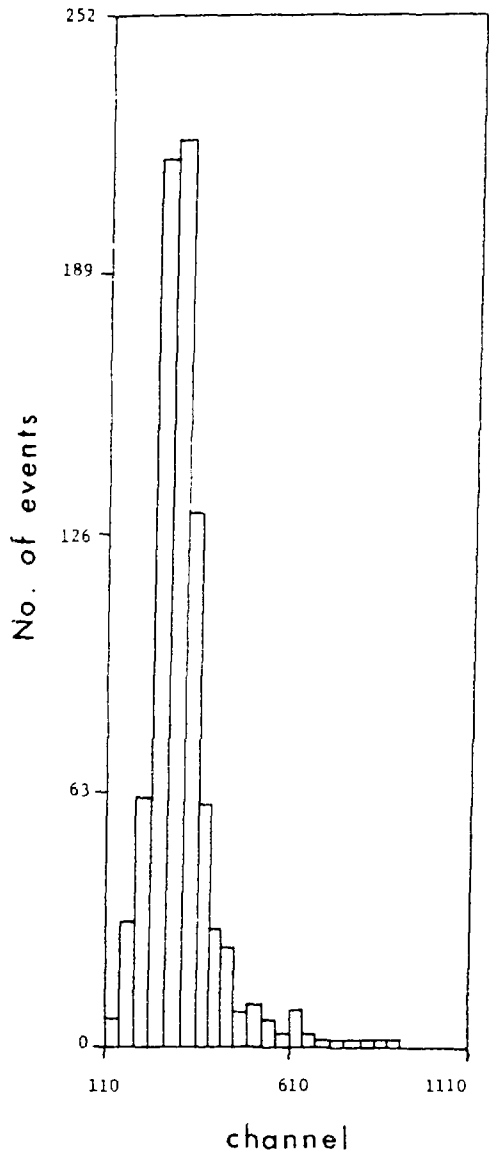

Figure 15. Pulse height distribution in the solid-state detectors for 140 MeV/c events that did not produce pulses in the Cerenkov detector.

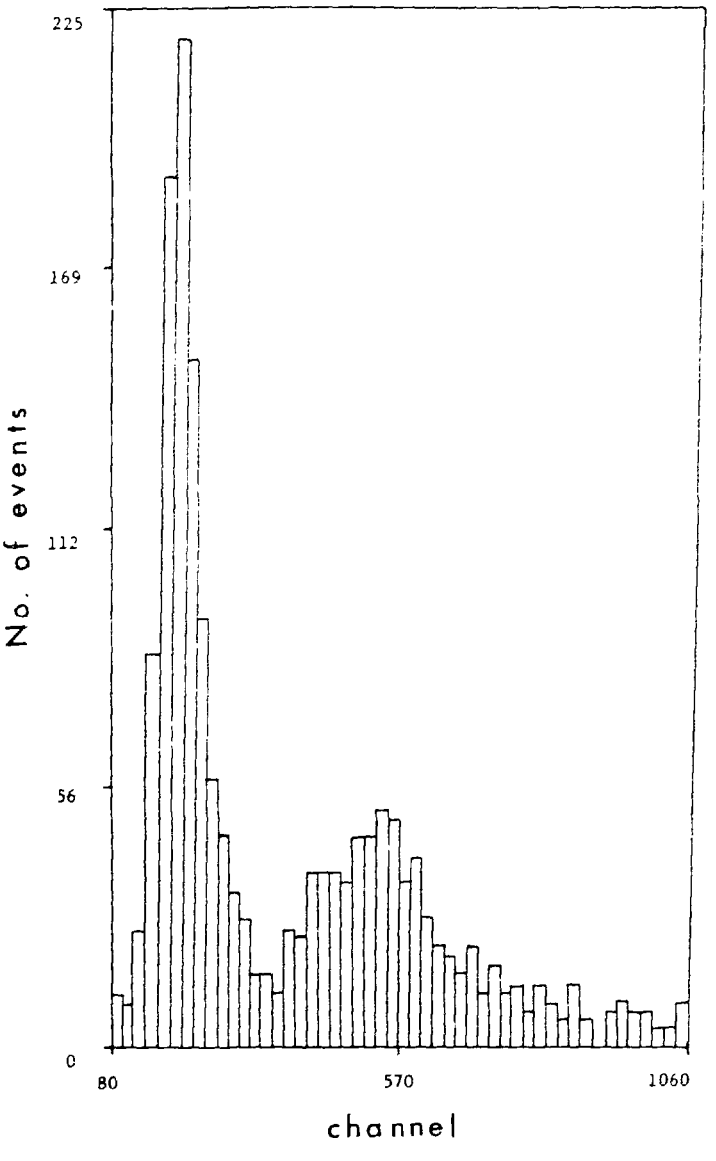

Figure 16. Pulse height distribution in the solid-state detectors for 83 MeV/c events that did not produce pulses in the Cerenkov detector.

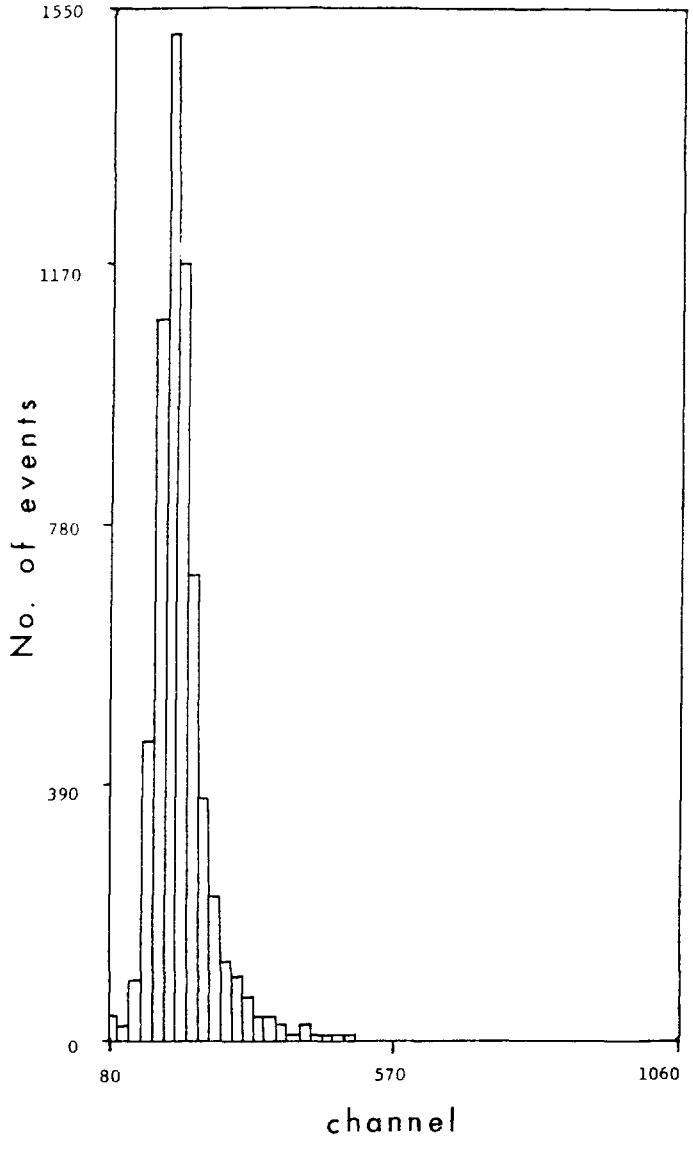

Figure 17. Pulse height distribution in the solid-state detectors for 83 MeV/c events that produced pulses in the Cerenkov detector.

Cerenkov detector contributed to the histogram in Fig. 16, which shows only a peak for electrons because pions were too slow to produce Cerenkov radiation. For this measurement, we selected ADC channel number 300 for the minimum acceptable pulse height for each solid-state detector. As Figs. 16 and 17 indicate, this cut-off eliminated most electron events and, hopefully, no pion events. A correction was made for the few remaining electron events by estimating the electron efficiency of the Cerenkov detector.

As the discussion above indicates, we also sorted events by whether or not they produced pulses in the Cerenkov detector. Since the Cerenkov detector was our principal means of identifying electrons, it was important to establish its efficiency. The pulse height distribution in the Cerenkov detector was monitored periodically throughout the experiment. We rotated the spectrometer to a laboratory scattering angle of 20.5° and set the P^3 beam for an incident momentum of 145 MeV/c. Data were briefly collected for $e^{+}p$ elastic scattering and histograms of the pulse height distribution in the Cerenkov detector were plotted for the sum of pulses from the top and bottom phototubes as well as from the individual phototubes. The shape of the distribution was important since it could reveal a loss of gain or a leak in the Cerenkov detector.

Fig. 18 is a typical histogram of the pulse height distribution in the Cerenkov detector. It was produced for the same 83 MeV/c production measurement discussed earlier. For momenta less than about 180 MeV/c, only electrons were fast enough to produce pulses in the Cerenkov detector. Noise was eliminated by requiring a minimum pulse height for the Cerenkov detector corresponding to ADC channel number

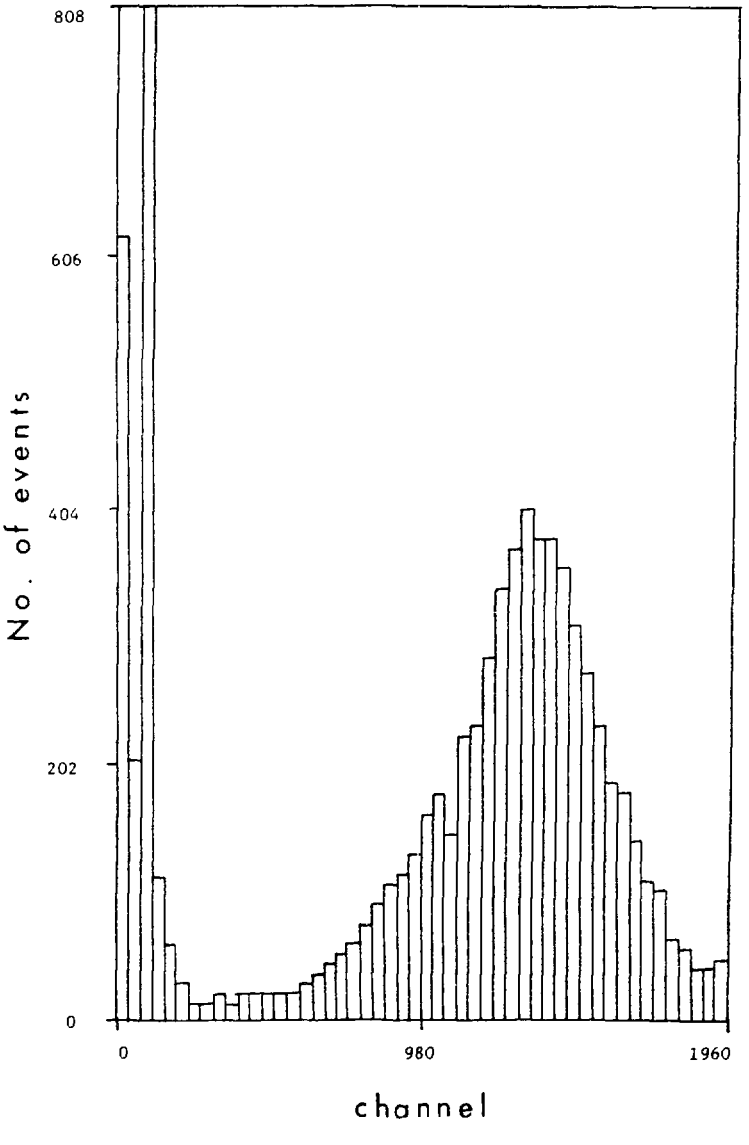

Figure 18. Pulse height distribution in the Cerenkov detector.

470. With this discrimination level, we assumed that the Cerenkov detector was perfectly efficient. At momenta greater than 180 MeV/c, a bump appeared in the Cerenkov pulse height histogram that we identified with high-velocity pions. Such pions were produced only for six measurements of single pion production at 358 MeV. At the expense of decreasing the efficiency of the Cerenkov detector for detecting electrons, we increased the cut-off for those measurements until a negligible number of pions produced pulses above the increased cut-off. The efficiency of the Cerenkov detector for detecting pions ε_π was taken to be zero and no error was assigned. To estimate the efficiency of the Cerenkov detector for detecting electrons, we used the pulse height histogram for e^+p elastic scattering observed just before acquiring the 358 MeV production data. We initially made the approximation that all electron events produced pulses in the Cerenkov detector. The effective electron efficiency e_0 for a given cut-off was defined as the ratio of the number of electron events that produced pulses above the cut-off to the number of electron events that produced pulses above the noise level of the Cerenkov detector. Table VI summarizes the minimum pulse heights and effective efficiencies used for various momenta p_π of the detected pions. At the higher momenta where the pulse height cut-offs were increased, the electron background was small.

A small number of electrons did not produce pulses in the Cerenkov detector regardless of how low the cut-off level was set. The presence of an electron peak in Fig. 16 is evidence of this fact. Presumably, such electrons lost enough energy by bremsstrahlung either in the 0.8 mm lead absorber placed immediately before S1 or in the

TABLE VI. Effective electron efficiency e_0 of the Cerenkov detector and minimum acceptable pulse height level as a function of pion momentum p_π.

e_0 (%)	Minimum Pulse Height (channel)	p_π (MeV/c)
100.0	470	60 - 180
96.4	800	180 - 210
87.0	1000	210 - 260

Cerenkov detector that they failed to trigger the Cerenkov detector. As a result, the actual electron efficiency ϵ_e was always less than unity. The fraction of electrons that did not trigger the Cerenkov detector was estimated by studying measurements of single pion production in which the momentum of the detected pion was less than about 100 MeV/c. Histograms were formed of the pulse height distributions in the solid-state dE/dx detectors and a minimum acceptable pulse height was established to eliminate noise and electrons. The fraction of electrons $(1 - e_1)$ not eliminated by the Cerenkov detector was estimated by taking the ratio of events in the electron peak formed without a Cerenkov pulse to those formed with a Cerenkov pulse. Values for e_1 were parametrized in the form

$$e_1 = 1 - \frac{p_0}{p_c} ,$$

with p_c the central momentum of the spectrometer calculated from the

mean spectrometer shunt voltage. This parametrization was suggested from calculations of energy loss resulting from bremsstrahlung.[23] The parameter p_0 was determined by a least squares analysis to be $p_0 = 2.53 \pm 0.24$ MeV/c. The actual efficiency of the Cerenkov detector for detecting electrons is given by $\varepsilon_e = e_0 e_1$ and its uncertainty by

$$\Delta\varepsilon_e = \varepsilon_e \left[\left(\frac{\Delta e_0}{e_0}\right)^2 + \left(\frac{\Delta p_0}{p_c - p_0}\right)^2\right]^{1/2},$$

with Δe_0 and Δp_0 the respective uncertainties in e_0 and p_0. No error was assigned to e_0 for this experiment.[24] The fraction of electrons that did not trigger the Cerenkov detector was significant only for measurements at very low momentum. For the two or three measurements at the lowest energies in which the momenta of the detected pions was less than about 70 MeV/c, e_1 was about 0.96. At 203 MeV, e_1 was typically about 0.97, whereas for most measurements at energies above 203 MeV, e_1 was about 0.98 or higher. The inefficiency of the Cerenkov detector for detecting electrons was unimportant for most measurements because the fraction of all events that were identified as electrons was small, except for one production measurement at 203 MeV.

CHAPTER IV

CALIBRATIONS WITH πp ELASTIC SCATTERING

We determined the relative efficiency of each detection channel and the momentum dispersion of the spectrometer with a 141 MeV π^+ beam by sweeping the spectrum of elastically scattered pions successively across each solid-state detector. At the same energy, we measured the angular distribution of the elastically scattered pions and compared it with the known differential cross section to check for possible systematic deviations in acceptance with angle. The differential cross section for π^+p elastic scattering is known accurately enough at 141 MeV that we could compare at the 1% level. We also measured the angular distributions of elastically scattered pions for each incident π^- beam employed in the measurement of the doubly differential cross section for $\pi^-p \rightarrow \pi^+\pi^-n$. The angular distributions for the π^- mesons were normalized to the known elastic cross section so we could calibrate our measurements of the reaction cross section. These distributions also checked less critically for a variation of acceptance with angle and determined the width and centroid of each incident momentum distribution.

Channel Efficiencies and Dispersion

We determined the relative efficiency of each detection channel and the momentum dispersion of the spectrometer from measurements of π^+p elastic scattering at 141 MeV with a scattering angle of 90°. The

elastic scattering peak was marched across the focal plane of the spectrometer in 44 small steps of 0.005 fractional change in central momentum of the spectrometer. An initial shunt voltage for which the elastically scattered pions had insufficient momentum to be detected by the spectrometer was selected and events were collected in each channel. Then the shunt voltage was slightly decreased and the procedure was repeated until the scattering peak had moved across each channel and was once again undetectable by the spectrometer. At each setting of the shunt voltage, a total charge of 1 μC was collected from the ionization chamber.

The number of events N in each solid-state detector was normalized by the number of live-time counts M_ℓ in the scattering monitor and adjusted for the known variation in momentum acceptance with central momentum p_c. Since the electron background was small, we considered events that produced pulses in the Cerenkov detector as well as those that did not. Measurements of the π^+ spectrum for each channel consisted of the set of points:

$$Y(p_c) = \frac{N}{M_\ell p_c} ,$$

with statistical uncertainties:

$$\Delta Y = Y\left(\frac{N + 1}{N^2} + \frac{M_\ell + 1}{M_\ell^2}\right)^{1/2} .$$

For the Ith channel, the $Y(p_c)$ were fitted to a skewed Gaussian peak with constant and error function background terms (the channel index I is suppressed in the display formula):

$$F(p_c) = \frac{P_1}{\sqrt{2\pi}\, P_2}\left[1 - \frac{P_4}{2}\left(x - \frac{x^3}{3}\right)\right] \exp\left(-\frac{x^2}{2}\right) + P_5$$

$$+ \frac{P_6}{\sqrt{2\pi}} \int_x^\infty \exp\left(-\frac{t^2}{2}\right) dt \ ,$$

with

$$x = \frac{p_c - P_3}{P_2} \ .$$

Here, $P_{2,I}$ is the width of the elastic peak and $P_{3,I}$ is the mean value of the central momentum when the scattering peak was centered on the Ith channel. The parameters $P_{i,I}$ and their errors $\Delta P_{i,I}$ were determined by PACKALG,[25] a nonlinear least squares fitting algorithm. χ^2/ν between two and three were typical with most of the χ^2 due to poor fitting of the tails of the distributions. These χ^2 may also reflect a known instability in the measured shunt voltage that ranged approximately from 0.02% to 0.08% and was neglected by the fitting algorithm. In Fig. 19, we show some sample spectra with the fitted curves.

The relative efficiency of the Ith detection channel was proportional to $P_{1,I}$, the area of the scattering peak in the Ith detector. We arbitrarily chose to scale the efficiencies relative to the tenth detector. Thus, the relative efficiency of the Ith channel was

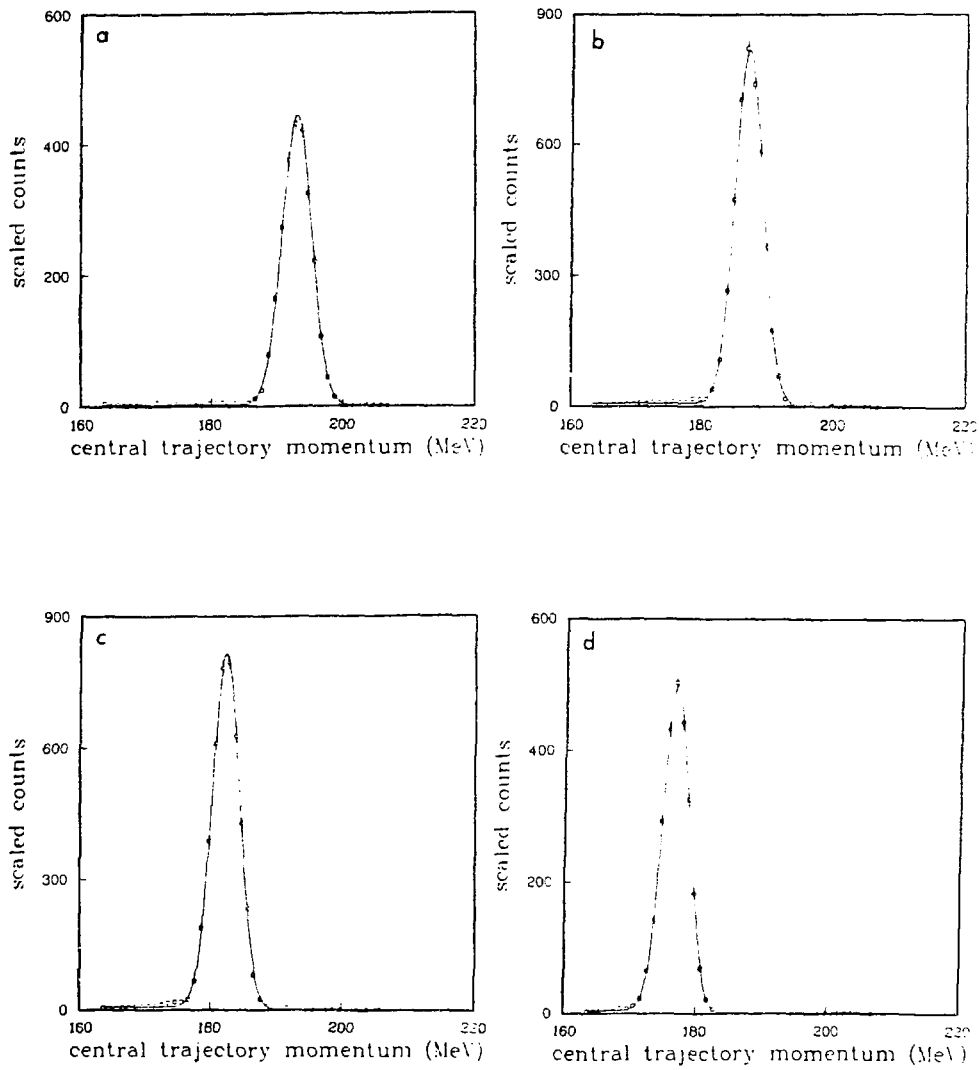

Figure 19. Sample spectra for channel efficiencies. Spectra are for (a) channel 1, (b) channel 7, (c) channel 12, and (d) channel 18. The curves show the results of the least squares fitting procedure.

$$\varepsilon_I = \frac{P_{1,I}}{P_{1,10}} ,$$

with statistical uncertainty

$$\Delta\varepsilon_I = \frac{\Delta P_{1,I}}{P_{1,10}} .$$

The ε_I and their statistical uncertainties are presented in Table VII and a plot is shown in Fig. 20. It is evident from the figure that the efficiencies of the central channels were nearly equal. The approximately linear decrease in efficiency for the extreme channels is attributed to a decreasing solid angle acceptance that resulted from shadowing by the walls of the vacuum chamber in the spectrometer. Small irregularities in the channel efficiencies might have resulted from variations in the active areas of individual detectors, such as for numbers 7 and 12.

The momentum of a particle that entered the spectrometer along its central trajectory and emerged through the center of the Ith channel is given by

$$p_I = p_c[1 + \delta(I - 9.5)] ,$$

with p_c the central momentum calculated from the spectrometer shunt voltage, δ the dispersion, and I the channel number. We determined δ by fitting the 18 values of $P_{3,I}$ to the function

TABLE VII. Relative channel efficiencies.

Channel	ε	$\Delta\varepsilon$
1	0.5667	0.0065
2	0.7077	0.0074
3	0.8018	0.0080
4	0.8922	0.0085
5	0.9735	0.0090
6	1.0007	0.0092
7	0.9946	0.0093
8	1.0017	0.0094
9	1.0032	0.0094
10	1.0000	0.0094
11	0.9953	0.0094
12	0.9672	0.0092
13	0.9694	0.0092
14	0.8723	0.0087
15	0.8084	0.0083
16	0.7311	0.0080
17	0.6564	0.0074
18	0.5692	0.0068

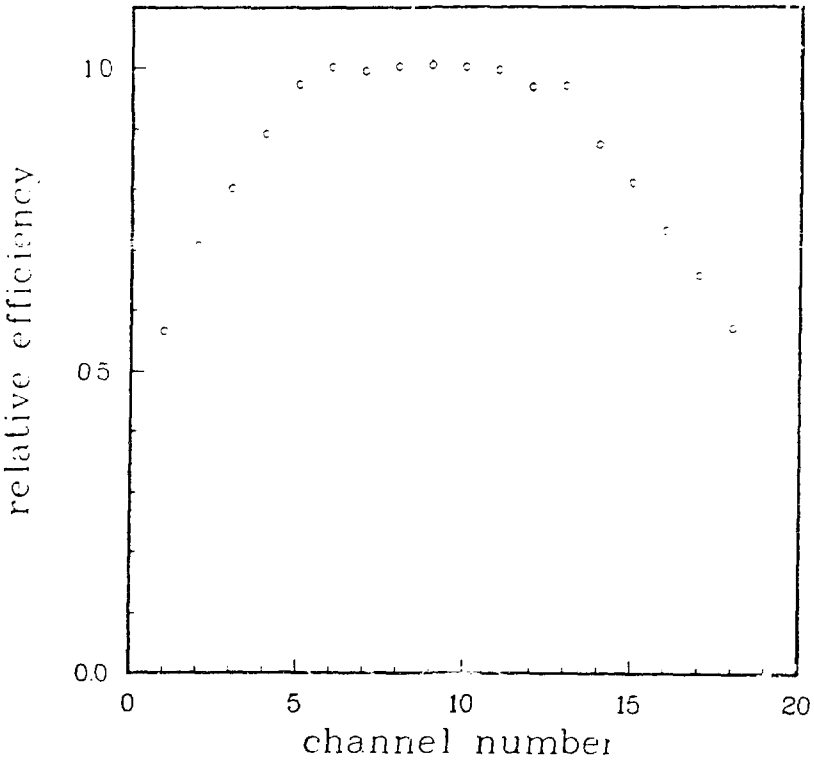

Figure 20. Relative detection channel efficiencies.

$$G(I) = p/[1 + \delta(I - 9.5)] ,$$

with both p and δ treated as free parameters. To include the contribution from a ± 0.5 mm uncertainty in the positions of detector centers or, equivalently, an uncertainty in I of $\Delta I = 0.0422$, we minimized a χ^2 defined by

$$\chi^2 = \sum_I \frac{(G(I) - P_{3,I})^2}{(\Delta P_{3,I})^2 + \left(\frac{\partial G(I)}{\partial I}\Delta I\right)^2} .$$

We obtained $\chi^2 = 1.67$ to establish $\delta = (5.132 \pm 0.011)\times10^{-3}$/channel. The $P_{3,I}$ are shown with the fitted curve in Fig. 21. Error bars were smaller than the markers for the points. Since the distance between detector centers was 1.186 cm, the momentum dispersion of the spectrometer was $(4.327 \pm 0.010)\times10^{-3}$/cm. This value is in good agreement with the previous measurements, $(4.351 \pm 0.004)\cdot10^{-3}$/cm[10] and $(4.376 \pm 0.021)\times10^{-3}$/cm,[18] where the uncertainty ΔI has been neglected. The dispersion obtained by a Monte Carlo simulation that traced particles through the spectrometer was 4.26×10^{-3}/cm.[18]

We repeated the entire procedure for determining the channel efficiencies and dispersion at a laboratory scattering angle of 45°. This study consisted of 51 runs in which successive runs differed by 0.004 fractional change in central momentum. The incident beam was tuned for 141 MeV π^+ mesons like for the previous study but the amount of charge collected from the ionization chamber for each run was only

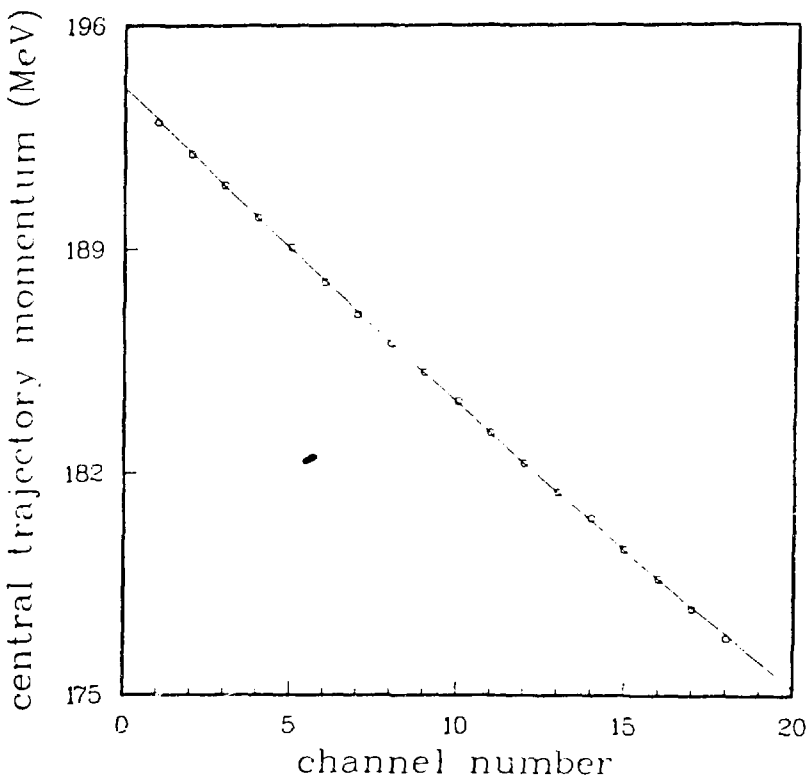

Figure 21. Data used to determine the spectrometer dispersion. The curve shows the results of the least squares fitting procedure.

0.5 μC. We redetermined the spectrometer dispersion to be $(5.127 \pm 0.012)\times10^{-3}$/channel or $(4.323 \pm 0.010)\times10^{-3}$/cm with $\chi^2/\nu = 1.19$. The redetermined channel efficiencies were in overall good agreement with those previously determined.

Investigations of πp Elastic Spectra

Angular distributions were measured for πp elastic scattering and compared with the known differential cross section to search for systematic angular variations in the solid angle acceptance of the spectrometer. We established calibrations for all π^- beams involved in our production measurements by normalizing our measured angular distributions for π^-p elastic scattering to the known differential cross sections. The elastic spectra also determined the centroid and width of the momentum distribution for each incident beam. Data were usually collected at 10° intervals for laboratory scattering angles as far backward as 130° and as far forward as permitted by the 325 MeV/c limit of the spectrometer. Most spectra were measured only with the target flask filled with liquid hydrogen although a few were measured with the flask empty to estimate the size of the background elastic peak. Since the πp elastic cross section was much larger than the electron background, we included events that produced pulses in the Cerenkov detector as well as those that did not.

We normalized the number of events N_I in the Ith detector by the number of counts M_ℓ in the scattering monitor during live time, by the momentum acceptance $p_c\delta$, and by the channel efficiency ε_I. The normalized number of counts in the Ith channel is given by

$$Y_I = \frac{N_I}{M_\ell \varepsilon_I p_c \delta}$$

and its uncertainty by

$$\Delta Y_I = Y_I \left[\left(\frac{\Delta \varepsilon_I}{\varepsilon_I} \right)^2 + \frac{(N_I + 1)}{N_I^2} \right]^{1/2} .$$

We neglected contributions to ΔY_I from the comparatively small uncertainties in M_ℓ and δ, which were the same for each channel. For scattering angles forward of about 40° in the laboratory, the spectrometer blocked part of the pion beam from reaching the scattering monitor. When this occurred, M_ℓ was replaced by M_ℓ', the projected number of counts in the monitor during live time:

$$M_\ell' = \left(\frac{M_\ell}{M_t} \right) q_{IC} \left\langle \frac{M_t}{q_{IC}} \right\rangle .$$

Here, q_{IC} is the amount of charge collected from the ionization chamber and $\langle M_t/q_{IC} \rangle$ is a factor determined from preceding or following measurements in which the beam was not blocked. M_ℓ/M_t is the live-time fraction with M_t the number of counts in the scattering monitor ignoring the dead-time inhibit. At 20.5°, the live-time fraction calculated by this method usually differed by less than 0.6% from the live-time fraction T_ℓ/T_t calculated from the number of event triggers during live and total time.

At each angle, the Y_I were fitted to a skewed Gaussian distribution with a constant background:

$$H(p_I) = \frac{P_1}{\sqrt{2\pi}\sigma}\left[1 - \frac{P_4}{2}\left(x - \frac{x^3}{3}\right)\right]\exp\left(-\frac{x^2}{2}\right) + P_5 ,$$

with

$$x = \frac{p_I - \mu}{\sigma} .$$

The centroid μ and width σ of the momentum distribution for the scattered pions were parametrized in terms of the centroid $P_3 = \mu_b$ and width $P_2 = \sigma_b$ of the incident momentum distribution. This form for the elastic peak was based on the assumption that a large number of effects combine to give a distribution that is approximately Gaussian near the peak. The centroid of the distribution for scattered pions was calculated as

$$\mu = p_{lab} - p_{loss} ,$$

with p_{lab} the mean momentum of the scattered pions calculated from kinematics and p_{loss} the momentum loss caused by collisions with atomic electrons in the target. p_{loss} is given by

$$-p_{loss} = \overline{S_{in}}\,\frac{d\mu_b}{dx}\,\frac{dp_{lab}}{d\mu_b} + \overline{S_{out}}\,\frac{dp_{lab}}{dx} ,$$

where the first term on the righthand side gives the effect of

momentum loss by the incident beam before it interacted in the target and the second term is the momentum loss after the interaction. $\overline{S_{in}}$ and $\overline{S_{out}}$ are the average path lengths traveled into and out of the target, before and after scattering, respectively. The calculation of p_{lab}, and hence p_{loss}, took into account that $\overline{\cos\theta_{lab}}$, the mean cosine of the scattering angle, differed from $\cos\theta_{lab}$, the cosine of the nominal scattering angle. $\overline{S_{in}}$, $\overline{S_{out}}$, and $\overline{\cos\theta_{lab}}$ were calculated, together with higher-order terms, with a Monte Carlo program. Further details of how p_{lab} and p_{loss} were calculated are discussed in Appendix A. The width of the momentum distribution of scattered pions can be written as[10]

$$\sigma = \left[\left(\sigma_b \frac{dp_{lab}}{d\mu_b}\right)^2 + \sigma_{ang}^2 + \sigma_{loss}^2 + \sigma_{spot}^2 + \sigma_{coul}^2 + \sigma_{strag}^2\right]^{1/2},$$

where we have assumed that the many small contributions to the width can be added in quadrature. The first term represents the contribution from the incident beam, σ_{ang} is a contribution due to the variation in the scattering angle caused by the finite angular acceptance of the spectrometer, σ_{loss} is a contribution due to variation in the path length in the target, σ_{spot} is a contribution due to the height of the beam spot at the target, σ_{coul} is a contribution to the width from the variation in the scattering angle caused by multiple small-angle scattering, and σ_{strag} is a contribution from straggling in the target. A discussion of each of the terms in the quadrature sum is also presented in Appendix A. The optimum value for

the centroid of the incident momentum distribution was determined by forming a weighted average of the μ_b:

$$\mu_{beam} = \frac{\sum \mu_b (\Delta\mu_b)^{-2}}{\sum (\Delta\mu_b)^{-2}} ,$$

with the sum running over all angles. The optimum value of the width σ_{beam} of the incident momentum distribution was found in the same manner from the σ_b and their uncertainties.

The differential cross section in the c.m. system for a given scattering angle was proportional to P_I, the area under the skewed Gaussian peak:

$$\frac{d\sigma}{d\Omega} = P_I T D J .$$

Here, J is the Jacobian required for effecting the transformation from the laboratory to the c.m. system:

$$J = \left|\frac{d\cos\theta_{lab}}{d\cos\theta}\right| = \frac{p(E E_{lab} - \gamma m_\pi{}^2)}{p_{lab}{}^3} ,$$

where p and E are respectively the momentum and total energy of the scattered pions in the c.m. system and E_{lab} is the total energy of the scattered pions in the laboratory. The factor D corrects for pion decay and is given by

$$D = \exp\left(\frac{\Lambda\, m_\pi}{\tau_\pi\, p_{lab}}\right) ,$$

with Λ = 355 cm the average path length from the LH_2 target to the focal plane of the spectrometer, m_π the mass of the charged pion, and $\tau_\pi c$ = 780.4 cm, where τ_π is the mean lifetime of the charged pion. This decay correction was checked by a Monte Carlo program called DECAY TURTLE[26] that traced pions and muons arising from the decay of pions through the spectrometer and detector system. The quantity T is a normalization factor for the system as a whole that was determined by requiring values of the measured cross section to agree on the average with values of the known cross section. More precisely, T was chosen to minimize the quantity

$$\chi^2 = \sum_i \frac{(y_i - f_i)^2}{(\Delta y_i)^2 + (\Delta f_i)^2} ,$$

where y_i is the ith value of the measured cross section, f_i is the corresponding value of the known cross section, and Δy_i and Δf_i are their respective uncertainties. The sum runs over all angles for a given beam. The subroutine SCATPI,[27] which was based upon the phase shift analysis of Carter, Bugg, and Carter,[15] generated values and uncertainties for the known differential cross section at incident kinetic energies below 300 MeV. SCATPI used, as input, the incident beam momentum estimated for loss of momentum at the center of the

target and $\cos\theta$, the cosine of the scattering angle in the c.m. system. The uncertainty in $\frac{d\sigma}{d\Omega}$ was calculated as

$$\Delta\left(\frac{d\sigma}{d\Omega}\right) = \frac{d\sigma}{d\Omega}\left[\left(\frac{\Delta P_1}{P_1}\right)^2 + \left(\frac{\Delta M_\ell}{M_\ell}\right)^2\right]^{1/2},$$

with ΔP_1 the uncertainty in P_1 obtained from the least squares analysis and $\Delta M_\ell = \sqrt{M_\ell + 1}$ the statistical uncertainty in M_ℓ.

Most of our data for πp elastic scattering were collected with the target flask full of liquid hydrogen although we collected data at a few angles with the flask empty to estimate the size of the elastic background. We always collected data with the flask empty immediately before or after collecting data at the same scattering angle with the flask full. Only half as much charge was collected from the ionization chamber with the flask empty as with the flask full. Hence, elastic spectra measured when the flask was empty generally had rather poor statistics. When we fitted elastic spectra measured with the flask empty, only P_1, the area under the elastic peak, and P_5, the constant background term, were allowed to vary. The width P_2, centroid P_3, and coefficient of skewing P_4 were held fixed at the values established for the spectrum measured at the same angle with the target flask full of liquid hydrogen. The width and centroid of the momentum distribution of scattered pions were calculated from P_2 and P_3 as before except that momentum loss in the target was neglected. The relative size of the background elastic peak was provided by the ratio $(P_1)_{empty}/(P_1)_{full}$, where the subscripts full and empty indicate the status of the target flask. This ratio depended

weakly on the temperature of the target since the ratio tended to be slightly smaller whenever we measured a spectrum with the flask empty before we had measured the spectrum at the same angle with the flask full. In such cases, hydrogen gas in the target had warmed above the boiling point, which resulted in a lower proton density. On the other hand, when a spectrum was measured with the flask empty after the spectrum had been measured at the same angle with the flask full, hydrogen gas in the target flask was still near the boiling point and relatively dense. Although the temperature dependence was poorly determined, we estimated that it was only about a 20% effect. Thus, we averaged results of all spectra measured with the target flask both empty and full to obtain $\langle (P_l)_{empty}/(P_l)_{full} \rangle = 0.01$. From estimates of the density of protons in gaseous hydrogen at 20° K and in the mylar target walls, we expected $\langle (P_l)_{empty}/(P_l)_{full} \rangle \leq 0.02$, with most of the background due to scattering from the gaseous hydrogen. Thus, our measured ratio is probably a reasonable estimate of the size of the background elastic peak. Since our production measurements involved the difference between the pion production rates with the flask full and empty, their appropriate normalization is

$$T' = T \left[1 - \langle (P_l)_{empty}/(P_l)_{full} \rangle\right]^{-1},$$

rather than simply T.

Our study of π^+p elastic scattering involved three separate measurements at 141 MeV in which each π^+ beam had $\Delta p/p = 2.2\%$ (FWHM). π^+p elastic scattering was measured at several angles for which 2 μC of charge was usually collected from the ionization chamber.

Elastically scattered π^+ mesons were observed by the spectrometer as forward as 20.36° in the laboratory. Only measurements as forward as 30° were included in the analysis because of a sizable background of π^+ mesons that were scattered from ^{12}C in the mylar target flask. At 30°, this background produced events in the upper four or five solid-state detectors that were also not analyzed. Measurements of the angular distribution of the elastically scattered π^+ mesons were compared to the prediction of SCATPI.[27] At 141 MeV, the cross section for π^+ mesons is known with two or three times the accuracy as that for π^- mesons. The predictions of SCATPI at this energy allowed comparisons with the known differential cross section at the 1% level. Thus, each π^+ beam provided an individual test for a possible systematic variation in the solid angle acceptance of the spectrometer with angle. The use of three separate measurements also provided a means to check the reproducibility of a given beam tune.

Sample spectra for π^+p elastic scattering are presented in Fig. 22 for several laboratory scattering angles. The results of the spectra are presented in Table VIII for the first beam, in Table IX for the second, and in Table X for the third. The quoted errors in μ_b and σ_b are the root mean square (r.m.s.) deviations predicted by the fitting algorithm. χ^2/ν for the fitted spectra ranged from 0.99 to 5.63. It was evident from the plots of the fitted spectra that the functional form of $H(p_I)$ was not entirely sufficient for describing the present measurements with their 0.03% statistical accuracy. The largest contributions to χ^2 usually came from the region of a peak's centroid. In general, when fits were of poor quality, the fitted curve overestimated the area under the peak in the region of the

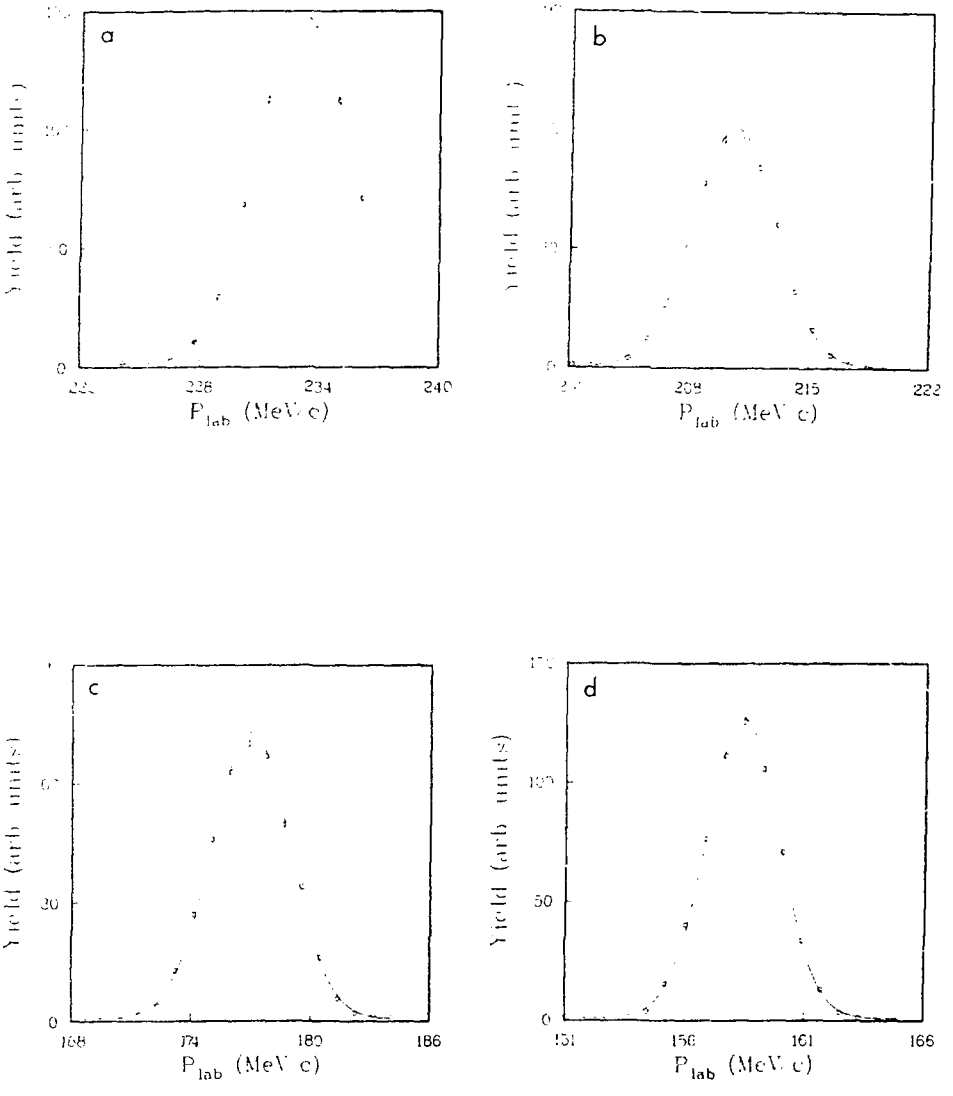

Figure 22. Sample spectra for $\pi^+p \to \pi^+p$ at 141 MeV. Spectra are for laboratory scattering angles (a) 30°, (b) 60°, (c) 100°, and (d) 130°. These sample spectra were all measured for the second beam. The curves show the results of the least squares fitting procedure.

TABLE VIII. Results from $\pi^+p\to\pi^+p$ spectra at 141 MeV (first beam).

θ_{lab}	cosθ	$\frac{d\sigma}{d\Omega}$(mb/sr)	μ_b(MeV/c)	σ_b(MeV/c)	χ^2/ν
40	0.642	11.490 ± 0.080	243.677 ± 0.018	2.210 ± 0.018	4.46
50	0.474	9.116 ± 0.068	243.631 ± 0.020	2.285 ± 0.023	5.63
60	0.292	7.420 ± 0.056	243.604 ± 0.022	2.274 ± 0.025	3.97
70	0.106	6.904 ± 0.054	243.674 ± 0.024	2.345 ± 0.029	2.11
80	-0.075	7.316 ± 0.058	243.650 ± 0.024	2.334 ± 0.030	2.94
90	-0.247	8.553 ± 0.066	243.612 ± 0.024	2.279 ± 0.030	3.57
100	-0.405	10.758 ± 0.080	243.613 ± 0.023	2.280 ± 0.028	3.41
110	-0.545	13.393 ± 0.095	243.596 ± 0.022	2.303 ± 0.026	1.68
120	-0.667	15.903 ± 0.111	243.728 ± 0.021	2.283 ± 0.024	3.67
130	-0.770	18.789 ± 0.128	243.561 ± 0.019	2.238 ± 0.021	2.65

centroid. This effect was always very small for π^+ spectra and the contribution to the area was estimated to be less than 1%. No systematic angular variation was apparent for measurements of the centroids of the momentum distributions. For the centroid of each beam, the r.m.s. deviations predicted by the fitting algorithm were about half the r.m.s. deviation from the mean of the measurements. The fitting algorithm included statistical errors for the number of scattering events in each solid-state detector but neglected uncertainties in the positions of the detectors, an instability of the measured shunt voltage, and reproducibility of the magnetic fields. Measurements of the momentum width tended to decrease slightly at forward angles, which is not understood. For the width of each beam,

TABLE IX. Results from $\pi^+p \to \pi^+p$ spectra at 141 MeV (second beam).

θ_{lab}	cosθ	$\frac{d\sigma}{d\Omega}$(mb/sr)	μ_b(MeV/c)	σ_b(MeV/c)	χ^2/ν
30	0.788	14.121 ± 0.098	243.648 ± 0.021	2.216 ± 0.020	3.11
40	0.642	11.504 ± 0.120	243.760 ± 0.027	2.208 ± 0.028	2.48
40	0.642	11.365 ± 0.081	243.748 ± 0.018	2.224 ± 0.018	2.81
50	0.474	9.029 ± 0.070	243.661 ± 0.021	2.262 ± 0.023	2.49
60	0.292	7.395 ± 0.057	243.754 ± 0.023	2.311 ± 0.026	1.98
70	0.106	6.886 ± 0.054	243.714 ± 0.024	2.298 ± 0.028	4.69
80	-0.076	7.204 ± 0.058	243.739 ± 0.025	2.349 ± 0.031	1.66
90	-0.247	8.638 ± 0.068	243.660 ± 0.025	2.345 ± 0.031	4.74
100	-0.405	10.699 ± 0.117	243.707 ± 0.035	2.334 ± 0.043	2.64
100	-0.405	10.798 ± 0.082	243.661 ± 0.024	2.349 ± 0.030	2.23
110	-0.545	13.525 ± 0.098	243.615 ± 0.023	2.332 ± 0.027	2.01
120	-0.667	16.100 ± 0.114	243.632 ± 0.021	2.316 ± 0.024	3.75
130	-0.770	18.912 ± 0.132	243.605 ± 0.020	2.269 ± 0.022	3.87

TABLE X. Results from $\pi^+p \to \pi^+p$ spectra at 141 MeV (third beam).

θ_{lab}	cosθ	$\frac{d\sigma}{d\Omega}$(mb/sr)	μ_b(MeV/c)	σ_b(MeV/c)	χ^2/ν
50	0.474	9.022 ± 0.177	243.576 ± 0.056	2.323 ± 0.063	0.99
50	0.474	8.886 ± 0.074	243.449 ± 0.023	2.241 ± 0.025	2.42
70	0.106	6.748 ± 0.070	243.511 ± 0.032	2.375 ± 0.038	1.25
90	-0.247	8.795 ± 0.118	243.369 ± 0.043	2.326 ± 0.054	1.18
110	-0.545	13.427 ± 0.160	243.543 ± 0.037	2.271 ± 0.046	2.46

r.m.s. deviations predicted by the fitting algorithm were also about half the r.m.s. deviation from the mean of the measurements, which again reflects the fitting algorithm's neglect of some uncertainties. Table XI summarizes the optimum centroid and width and their r.m.s. deviations from their mean values predicted by measurements at each angle for each π^+ beam. These values together with the results for the π^- beams discussed below suggest that beam tunes were reproducible to within about 0.2%. For our measurements of π^+p elastic scattering, we opened the momentum slit of the pion channel 3.81 cm. The 5.6×10^{-3}/cm dispersion[16] for the west leg of the channel predicted $\Delta p/p$ = 2.1% (FWHM) for this setting, in good agreement with our measured $\Delta p/p$ = 2.2%. Each measurement of μ_{beam} for the π^+ beams was about 2% lower than the 248.54 MeV/c predicted by the computer codes used to tune the channel. Table XI also presents the T′ and χ^2/ν that resulted by varying T for each beam until values of the measured cross

TABLE XI. Results from the study of $\pi^+p\to\pi^+p$. Each quoted uncertainty is the r.m.s. deviation from the mean of the measurements at each angle.

T (MeV)	μ_{beam} (MeV/c)	σ_{beam} (MeV/c)	T′ (mb/sr)(monitor counts/π)	χ^2/ν
141[a]	243.635 ± 0.051	2.272 ± 0.043	73.69 ± 0.91	2.12
141[b]	243.682 ± 0.057	2.279 ± 0.053	74.67 ± 0.57	0.64
141[c]	243.477 ± 0.069	2.288 ± 0.065	76.46 ± 0.75	0.70

[a]First beam.
[b]Second beam.
[c]Third beam.

section agreed on the average with values of the known cross section. Fig. 23 compares the angular distribution obtained for each beam with the cross section predicted by SCATPI. For the first measurement, we observed a variation from the predicted angular distribution of about 1.3% which gave $\chi^2/\nu = 2.12$ when we determined T. For the second and third measurements, we obtained χ^2/ν of 0.64 and 0.70, respectively, and any angular variation was estimated to be 1% or less. For π^+p elastic scattering at 141 MeV, SCATPI's predictions are not expected to be in better agreement with measurement. The first measurement had a larger χ^2/ν than the second or third because measurements of the angular distribution at 70° and 120° for that beam differed by about 2% from the predictions of SCATPI.

Angular distributions for π^-p elastic scattering were measured for each incident π^- beam employed in the measurement of the $\pi^-p \to \pi^+\pi^-n$ cross section. Data were usually accumulated at each angle until 20 μC of charge had been collected from the ionization chamber. At the lowest energies, only measurements as forward as 40° were analyzed because of a background of π^- mesons scattered from ^{12}C in the mylar target flask. At higher energies, the most forward angle at which elastically scattered π^- mesons could be detected was restricted by the upper momentum limit of the spectrometer. Our analysis of the elastic spectra yielded the relative π^-p elastic cross sections and the centroid and width of each incident momentum distribution. For incident kinetic energies less than 300 MeV, SCATPI also normalized angular distributions of the elastically scattered π^- mesons to measurements of the known differential cross section. For incident kinetic energies greater than 300 MeV, the angular distributions were

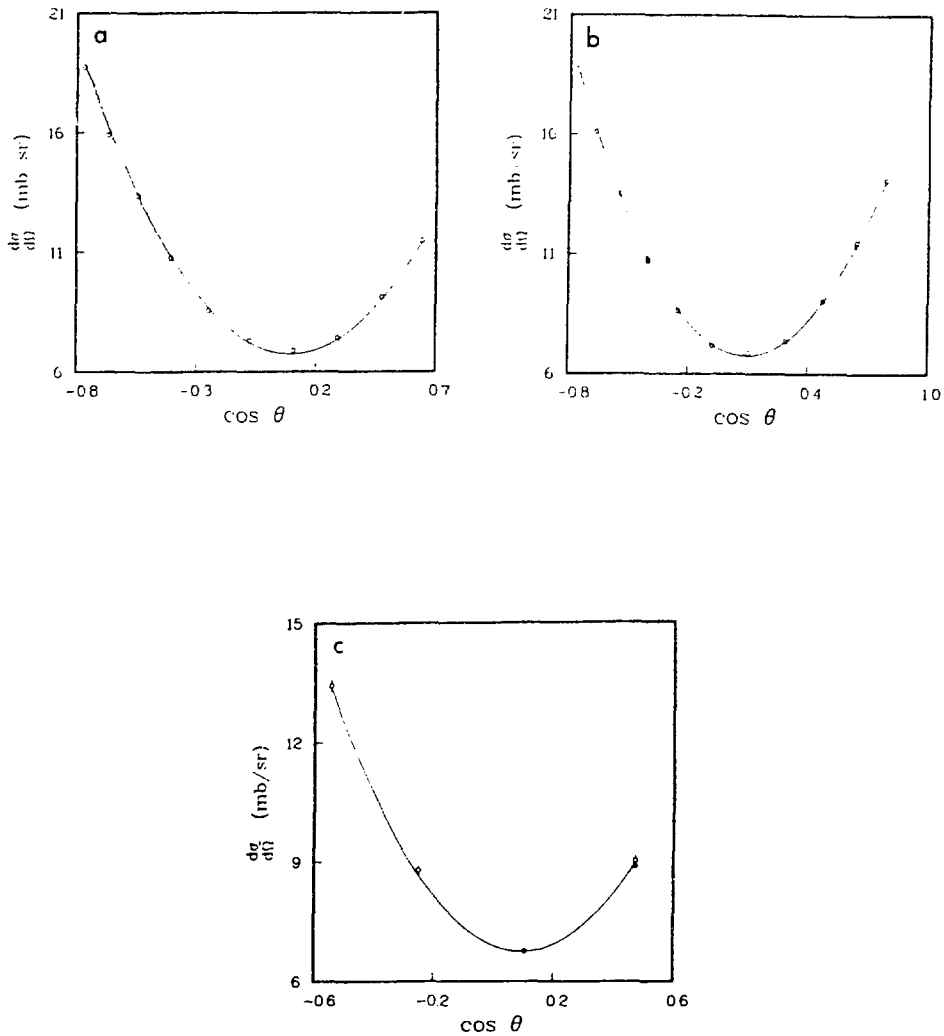

Figure 23. Angular distribution of $\pi^+p \to \pi^+p$ at 141 MeV. Measurements are for (a) first beam, (b) second beam, and (c) third beam. The curves represent the interpolation of SCATPI.

normalized to cross sections graphically interpolated from the 370 and 410 MeV measurements of Ogden et al.,[28] the 310 MeV measurements of Rugge and Vik,[29] and the 264 and 292 MeV measurements of Bussey et al.[30] The procedure for interpolating values and assigning uncertainties at incident kinetic energies greater than 300 MeV has been discussed by Walter.[10]

The π^- beams were studied five times at 203 MeV, three at 229 MeV, one at 256, and one at 358 MeV. Each incident π^- beam had a $\Delta p/p$ of about 4.1% (FWHM), so they were about twice as wide as the π^+ beams discussed above. Sample spectra at each energy are displayed in Figs. 24-27 and the results of the analyses of the spectra are presented in Tables XII-XVI and Fig. 28 for 203 MeV, Tables XVII-XIX and Fig. 29 for 229 MeV, Table XX and Fig. 30 for 256 MeV, and in Table XXI for 358 MeV. The quoted errors in μ_b and σ_b are the r.m.s. deviations predicted by the fitting algorithm. χ^2/ν for the fitted spectra tended to be quite large, particularly at forward and backward angles where the trial function poorly described the centroid region and skewing of the peaks. χ^2/ν of two were typical for measurements at 90° whereas χ^2/ν near ten were typical at 40°. These large χ^2/ν reflect the inadequacies of the function $H(p_I)$ for fitting the present measurements, for which the centroids were determined with a statistical accuracy of about 0.02%. Unfortunately, the structure of the measured spectra was sufficiently complex that we failed to conceive of a more satisfactory function. The problem of overestimating the area under the peak discussed above for π^+ beams was more serious for the wider π^- beams. For the worst cases, we estimate that the area under the elastic peak was overestimated by about 2%.

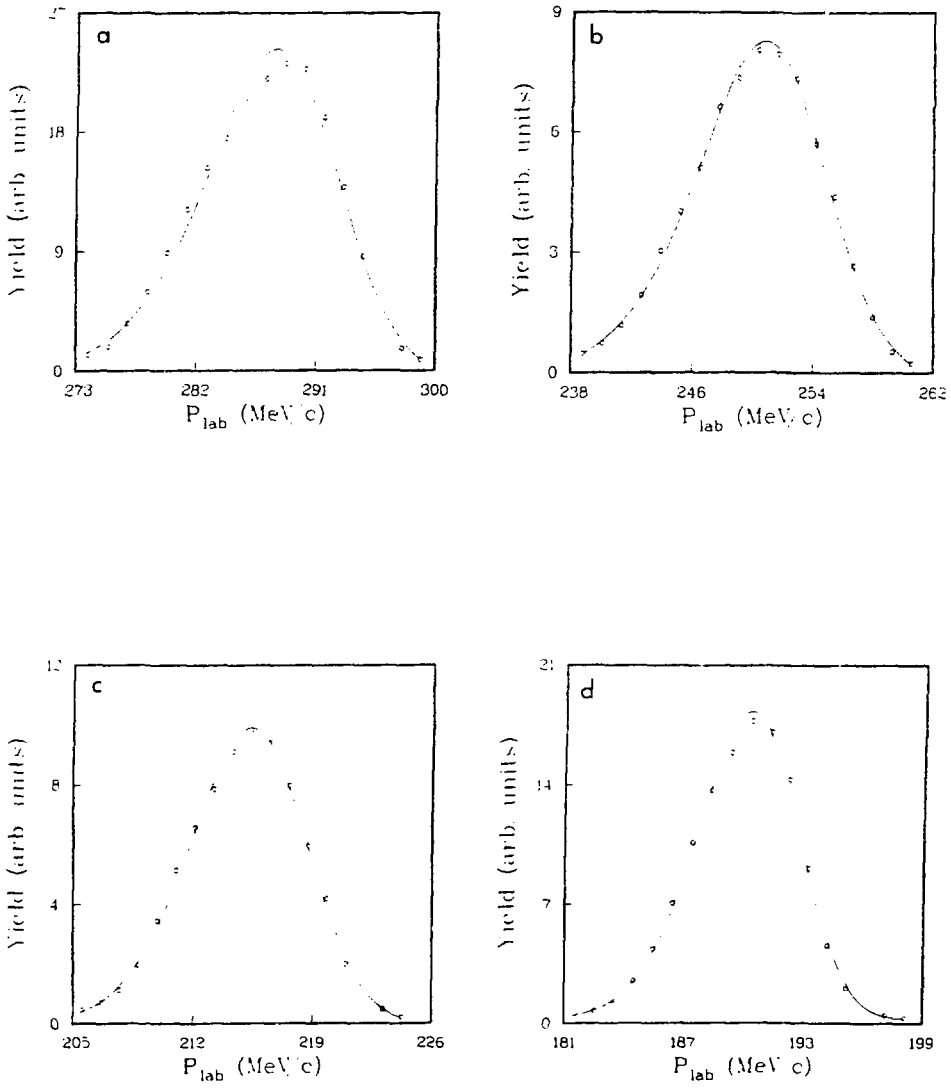

Figure 24. Sample spectra for $\pi^- p \to \pi^- p$ at 203 MeV. Spectra are for laboratory scattering angles (a) 40°, (b) 70°, (c) 100°, and (d) 130°. These sample spectra were all measured for the first beam except for that at 70°, which was measured for the fourth beam. The curves show the results of the least squares fitting procedure.

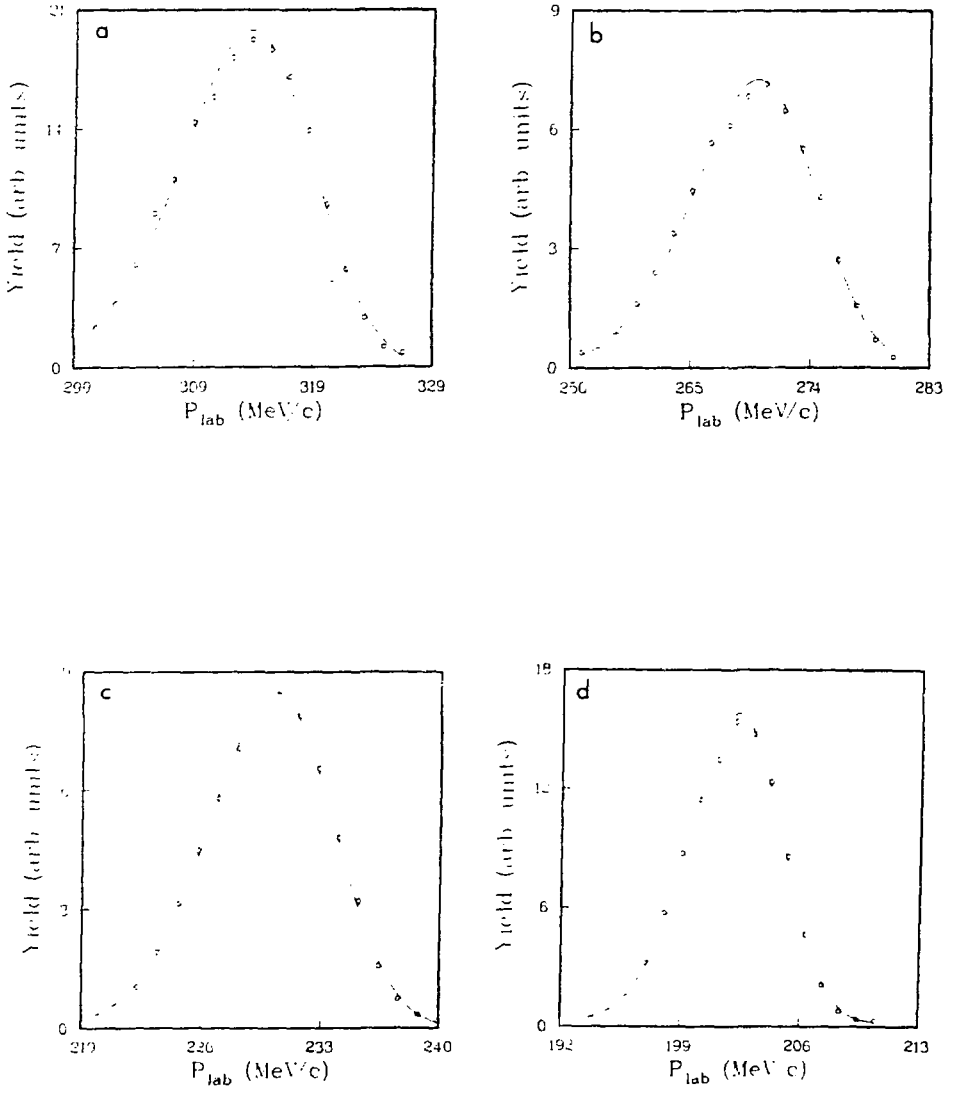

Figure 25. Sample spectra for $\pi^-p \to \pi^-p$ at 229 MeV. Spectra are for laboratory scattering angles (a) 40°, (b) 70°, (c) 100°, and (d) 130°. These sample spectra were all measured for the third beam. The curves show the results of the least squares fitting procedure.

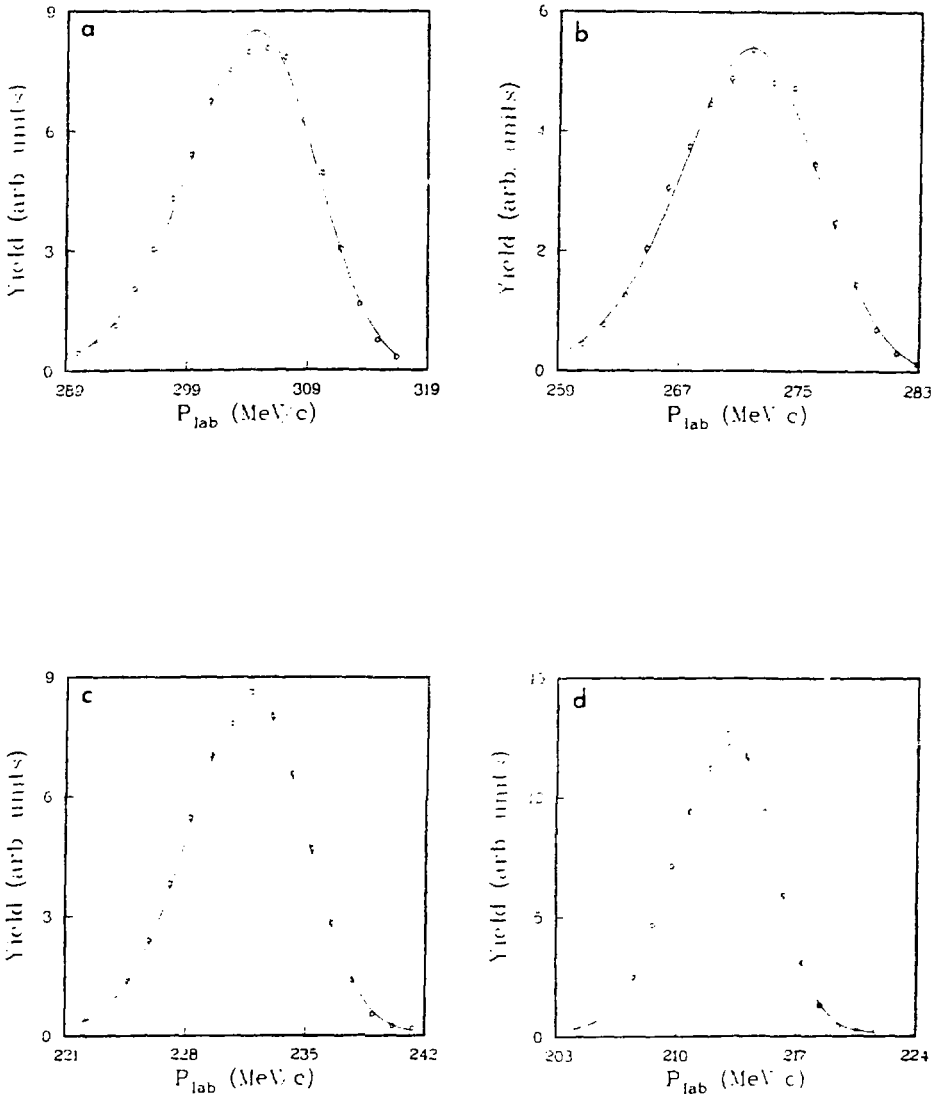

Figure 26. Sample spectra for $\pi^-p \to \pi^-p$ at 256 MeV. Spectra are for laboratory scattering angles (a) 60°, (b) 80°, (c) 110°, and (d) 130°. The curves show the results of the least squares fitting procedure.

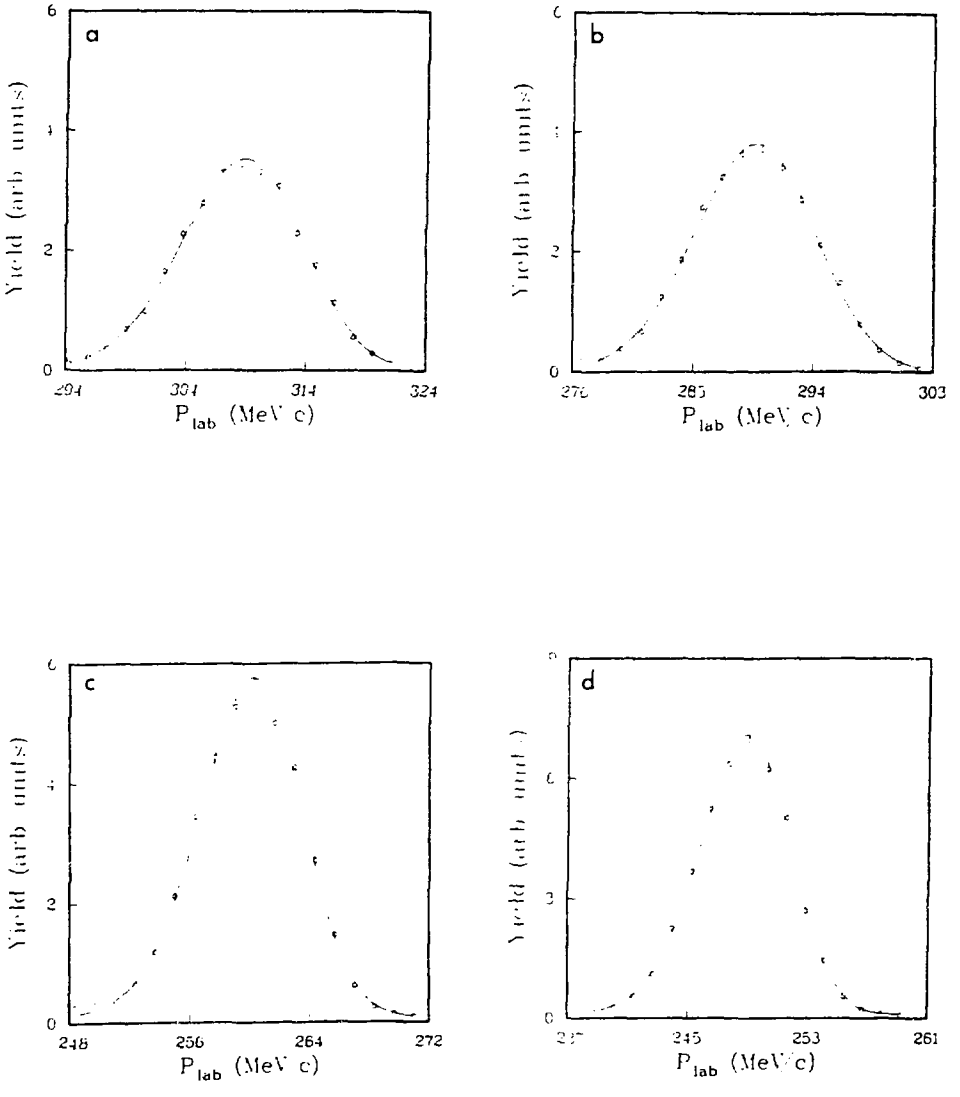

Figure 27. Sample spectra for $\pi^- p \to \pi^- p$ at 358 MeV. Spectra are for laboratory scattering angles (a) 90°, (b) 100°, (c) 120°, and (d) 130°. The curves show the results of the least squares fitting procedure.

TABLE XII. Results from $\pi^-p \to \pi^-p$ spectra at 203 MeV (first beam).

θ_{lab}	$\cos\theta$	$\frac{d\sigma}{d\Omega}$(mb/sr)	μ_b(MeV/c)	σ_b(MeV/c)	χ^2/ν
40	0.619	2.026 ± 0.027	312.688 ± 0.042	5.366 ± 0.076	11.46
50	0.443	1.489 ± 0.021	312.225 ± 0.047	5.526 ± 0.085	7.54
60	0.256	1.072 ± 0.016	312.256 ± 0.053	5.478 ± 0.097	1.38
70	0.068	0.843 ± 0.015	312.308 ± 0.064	5.673 ± 0.121	4.49
80	-0.114	0.789 ± 0.014	312.396 ± 0.067	5.686 ± 0.122	2.00
90	-0.284	0.876 ± 0.014	312.404 ± 0.068	5.773 ± 0.119	1.72
100	-0.437	1.086 ± 0.014	312.352 ± 0.059	5.622 ± 0.091	3.49
110	-0.572	1.403 ± 0.015	312.432 ± 0.052	5.667 ± 0.078	5.06
120	-0.688	1.694 ± 0.016	312.657 ± 0.049	5.478 ± 0.064	4.14
130	-0.785	1.965 ± 0.016	312.594 ± 0.047	5.327 ± 0.053	5.35

TABLE XIII. Results from $\pi^- p \to \pi^- p$ spectra at 203 MeV (second beam).

θ_{lab}	$\cos\theta$	$\frac{d\sigma}{d\Omega}$(mb/sr)	μ_b(MeV/c)	σ_b(MeV/c)	χ^2/ν
40	0.619	2.058 ± 0.024	311.988 ± 0.040	5.481 ± 0.065	18.16
50	0.443	1.493 ± 0.017	311.629 ± 0.046	5.584 ± 0.070	8.02
60	0.256	1.079 ± 0.014	311.713 ± 0.053	5.543 ± 0.082	4.88
70	0.068	0.849 ± 0.013	311.897 ± 0.060	5.594 ± 0.102	4.06
80	-0.114	0.791 ± 0.013	311.912 ± 0.065	5.680 ± 0.112	3.37
90	-0.283	0.889 ± 0.014	311.703 ± 0.067	5.871 ± 0.109	1.55
100	-0.437	1.110 ± 0.013	311.853 ± 0.056	5.732 ± 0.085	3.94
110	-0.572	1.390 ± 0.014	311.917 ± 0.050	5.645 ± 0.072	7.38
120	-0.688	1.684 ± 0.015	312.012 ± 0.048	5.668 ± 0.061	6.63
130	-0.785	1.948 ± 0.016	311.973 ± 0.045	5.403 ± 0.051	10.83

TABLE XIV. Results from $\pi^- p \to \pi^- p$ spectra at 203 MeV (third beam).

θ_{lab}	$\cos\theta$	$\frac{d\sigma}{d\Omega}$(mb/sr)	μ_b(MeV/c)	σ_b(MeV/c)	χ^2/ν
40	0.619	2.004 ± 0.026	312.752 ± 0.043	5.427 ± 0.074	9.39
60	0.256	1.070 ± 0.015	312.433 ± 0.052	5.443 ± 0.091	4.96
80	-0.114	0.769 ± 0.013	312.668 ± 0.064	5.534 ± 0.112	1.43
90	-0.284	0.868 ± 0.014	312.432 ± 0.065	5.723 ± 0.111	2.59
110	-0.572	1.371 ± 0.015	312.816 ± 0.052	5.679 ± 0.076	3.08

TABLE XV. Results from $\pi^-p \to \pi^-p$ spectra at 203 MeV (fourth beam).

θ_{lab}	$\cos\theta$	$\frac{d\sigma}{d\Omega}$(mb/sr)	μ_b(MeV/c)	σ_b(MeV/c)	χ^2/ν
40	0.619	2.047 ± 0.032	312.816 ± 0.053	5.295 ± 0.087	11.12
40	0.619	2.010 ± 0.028	312.794 ± 0.048	5.280 ± 0.079	8.47
50	0.443	1.462 ± 0.016	312.491 ± 0.041	5.290 ± 0.068	12.04
60	0.256	1.072 ± 0.014	312.446 ± 0.050	5.402 ± 0.086	4.86
70	0.068	0.845 ± 0.013	312.517 ± 0.058	5.510 ± 0.104	1.89
80	-0.114	0.792 ± 0.012	312.485 ± 0.061	5.522 ± 0.106	3.37
90	-0.284	0.898 ± 0.012	312.538 ± 0.058	5.579 ± 0.097	3.55
100	-0.437	1.089 ± 0.012	312.640 ± 0.052	5.512 ± 0.079	3.39
110	-0.572	1.395 ± 0.013	312.703 ± 0.046	5.386 ± 0.063	3.87
120	-0.688	1.669 ± 0.014	313.089 ± 0.044	5.209 ± 0.055	7.81
130	-0.785	1.960 ± 0.015	313.146 ± 0.042	5.143 ± 0.047	9.90

TABLE XVI. Results from $\pi^-p \to \pi^-p$ spectra at 203 MeV (fifth beam).

θ_{lab}	$\cos\theta$	$\frac{d\sigma}{d\Omega}$(mb/sr)	μ_b(MeV/c)	σ_b(MeV/c)	χ^2/ν
50	0.443	1.469 ± 0.017	312.536 ± 0.042	5.304 ± 0.070	9.00
60	0.256	1.059 ± 0.014	312.454 ± 0.050	5.404 ± 0.085	7.42
70	0.068	0.837 ± 0.013	312.585 ± 0.058	5.508 ± 0.102	3.28
80	-0.114	0.787 ± 0.011	312.544 ± 0.060	5.500 ± 0.100	1.85
90	-0.284	0.898 ± 0.012	312.732 ± 0.056	5.462 ± 0.094	4.09
100	-0.437	1.103 ± 0.012	312.748 ± 0.051	5.580 ± 0.081	2.36
110	-0.572	1.360 ± 0.013	312.790 ± 0.047	5.370 ± 0.065	4.53
120	-0.688	1.706 ± 0.014	313.203 ± 0.044	5.325 ± 0.056	7.66
130	-0.785	1.978 ± 0.015	313.136 ± 0.041	5.185 ± 0.048	9.87

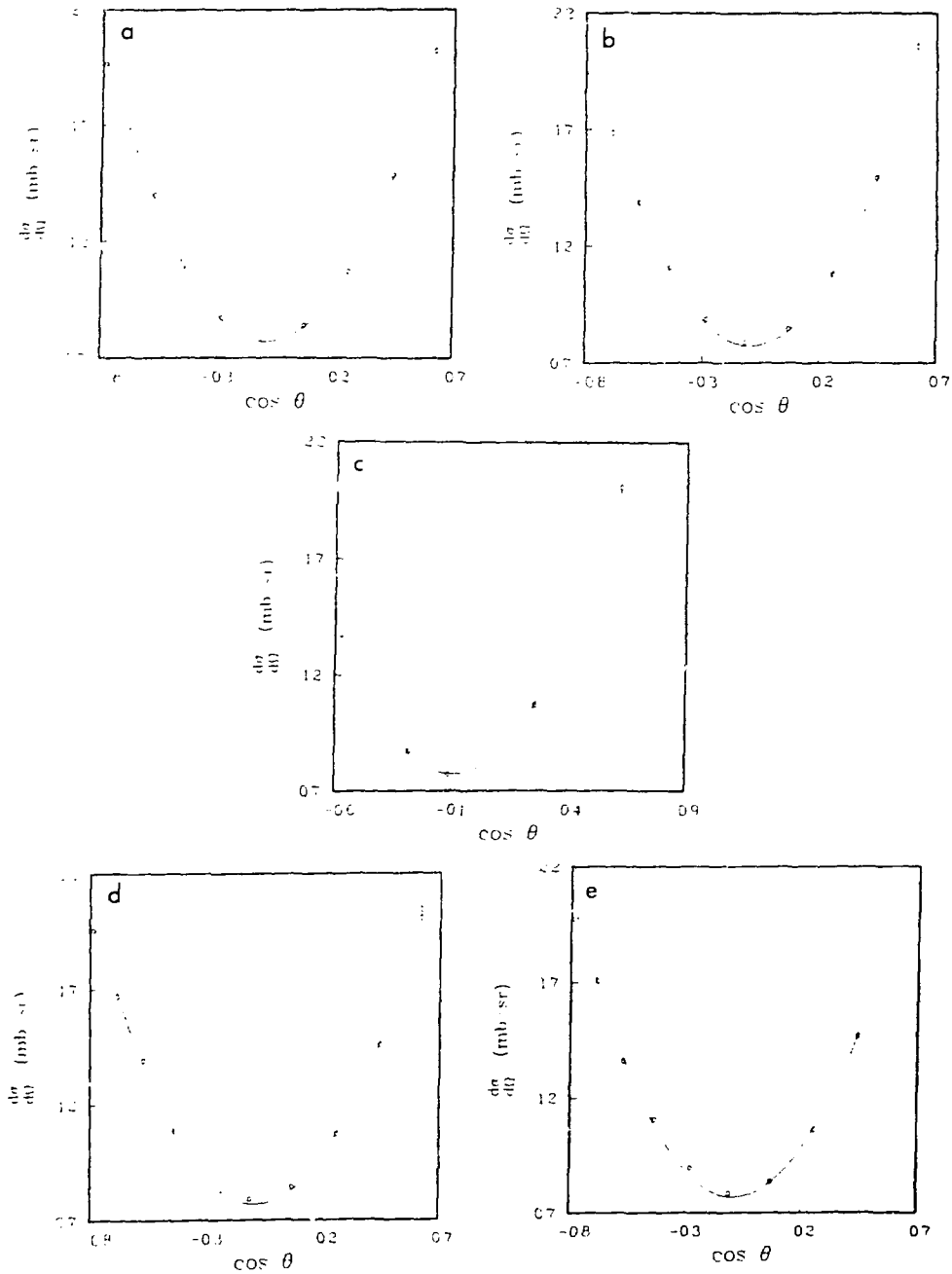

Figure 28. Angular distribution of $\pi^-p \to \pi^-p$ at 203 MeV. Measurements are for (a) first beam, (b) second beam, (c) third beam, (d) fourth beam, and (e) fifth beam. The curves represent the interpolation of SCATPI.

TABLE XVII. Results from $\pi^-p \to \pi^-p$ spectra at 229 MeV (first beam).

θ_{lab}	$\cos\theta$	$\frac{d\sigma}{d\Omega}$(mb/sr)	μ_b(MeV/c)	σ_b(MeV/c)	χ^2/ν
40	0.611	1.564 ± 0.090	336.558 ± 0.363	10.158 ± 0.351	2.83
40	0.609	1.575 ± 0.018	342.087 ± 0.055	6.106 ± 0.074	6.61
50	0.430	1.206 ± 0.018	341.661 ± 0.084	6.420 ± 0.104	3.96
50	0.430	1.187 ± 0.019	341.894 ± 0.083	6.234 ± 0.109	2.70
60	0.241	0.887 ± 0.010	341.292 ± 0.076	6.367 ± 0.086	1.87
70	0.052	0.701 ± 0.014	341.398 ± 0.075	6.286 ± 0.147	1.95
80	-0.129	0.637 ± 0.013	341.152 ± 0.082	6.249 ± 0.156	2.64
90	-0.298	0.703 ± 0.010	341.160 ± 0.078	6.289 ± 0.114	1.50
100	-0.450	0.912 ± 0.012	341.277 ± 0.071	6.256 ± 0.104	2.57
110	-0.583	1.144 ± 0.013	341.266 ± 0.063	6.236 ± 0.091	3.14
120	-0.697	1.384 ± 0.013	341.426 ± 0.057	6.018 ± 0.074	4.62
130	-0.791	1.634 ± 0.014	341.509 ± 0.051	5.914 ± 0.059	5.38

TABLE XVIII. Results from $\pi^-p \to \pi^-p$ spectra at 229 MeV (second beam).

θ_{lab}	cosθ	$\frac{d\sigma}{d\Omega}$(mb/sr)	μ_b(MeV/c)	σ_b(MeV/c)	χ^2/ν
40	0.609	1.631 ± 0.018	342.245 ± 0.045	5.975 ± 0.068	11.80
50	0.430	1.187 ± 0.011	341.570 ± 0.050	5.883 ± 0.062	6.61
60	0.241	0.885 ± 0.009	341.100 ± 0.064	6.091 ± 0.071	4.25
70	0.052	0.695 ± 0.012	341.181 ± 0.068	6.067 ± 0.129	2.61
80	-0.129	0.648 ± 0.011	341.060 ± 0.072	5.997 ± 0.132	2.71
90	-0.298	0.713 ± 0.009	340.912 ± 0.073	6.014 ± 0.104	2.03
100	-0.449	0.881 ± 0.011	341.118 ± 0.069	5.911 ± 0.097	2.51
110	-0.583	1.133 ± 0.012	341.296 ± 0.060	5.886 ± 0.083	4.54
120	-0.697	1.387 ± 0.013	341.533 ± 0.055	5.829 ± 0.069	3.44
130	-0.791	1.626 ± 0.014	341.509 ± 0.049	5.681 ± 0.057	8.17

TABLE XIX. Results from $\pi^-p \to \pi^-p$ spectra at 229 MeV (third beam).

ϑ_{lab}	$\cos\theta$	$\frac{d\sigma}{d\Omega}$(mb/sr)	μ_b(MeV/c)	σ_b(MeV/c)	χ^2/ν
40	0.609	1.629 ± 0.022	342.904 ± 0.047	6.036 ± 0.082	8.27
50	0.430	1.183 ± 0.012	342.178 ± 0.053	6.058 ± 0.071	6.10
60	0.241	0.884 ± 0.009	341.673 ± 0.058	6.118 ± 0.072	4.86
70	0.052	0.684 ± 0.012	341.722 ± 0.069	6.041 ± 0.132	2.89
80	-0.130	0.638 ± 0.012	341.472 ± 0.079	6.111 ± 0.145	2.87
90	-0.298	0.702 ± 0.010	341.490 ± 0.076	6.203 ± 0.112	1.78
100	-0.450	0.899 ± 0.012	341.711 ± 0.071	6.182 ± 0.109	1.79
110	-0.583	1.120 ± 0.013	341.639 ± 0.063	6.105 ± 0.091	3.83
120	-0.697	1.376 ± 0.013	341.915 ± 0.056	5.993 ± 0.073	3.59
130	-0.791	1.638 ± 0.014	342.042 ± 0.051	5.913 ± 0.061	5.89

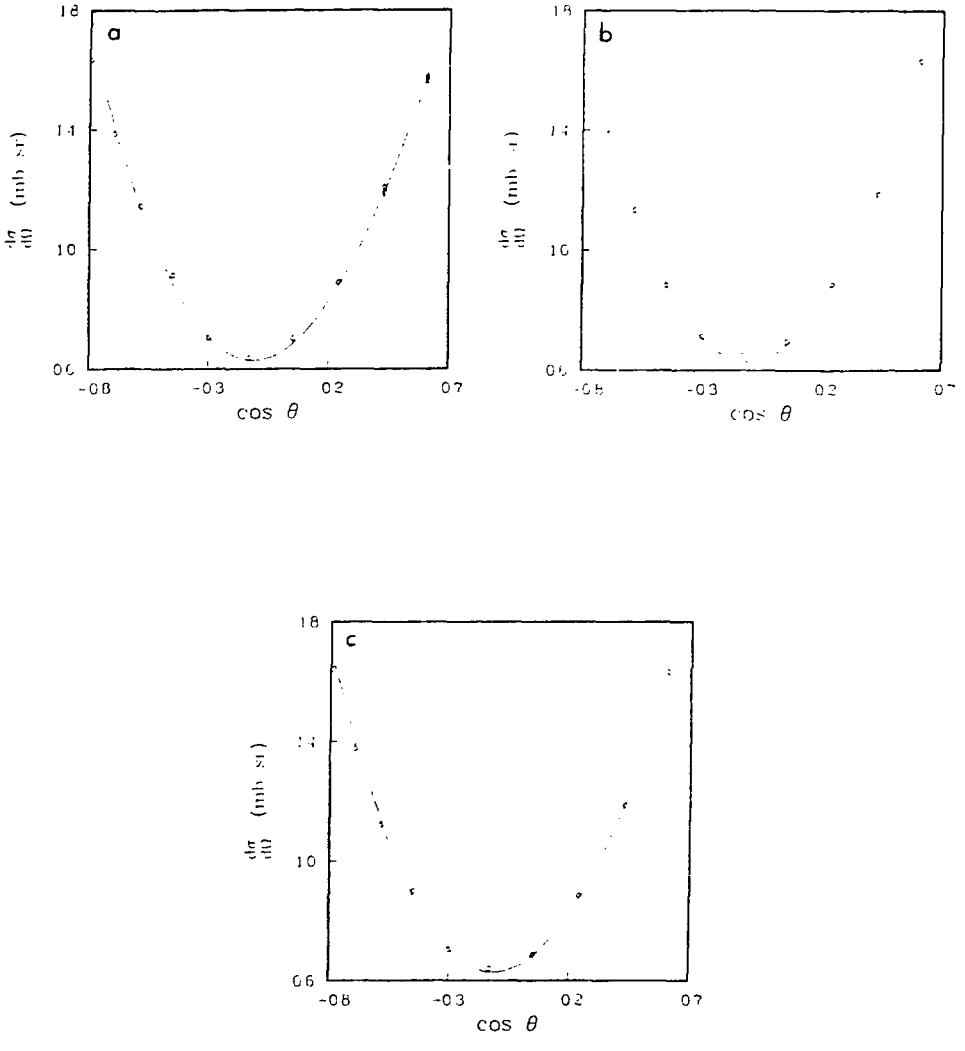

Figure 29. Angular distribution of $\pi^-p \to \pi^-p$ at 229 MeV. Measurements are for (a) first beam, (b) second beam, and (c) third beam. The curves represent the interpolation of SCATPI.

TABLE XX. Results from $\pi^-p \to \pi^-p$ spectra at 256 MeV.

θ_{lab}	$\cos\theta$	$\frac{d\sigma}{d\Omega}$(mb/sr)	μ_b(MeV/c)	σ_b(MeV/c)	χ^2/ν
60	0.227	0.7735 ± 0.0112	369.929 ± 0.058	6.432 ± 0.113	4.06
70	0.037	0.5975 ± 0.0087	369.655 ± 0.066	6.440 ± 0.123	1.89
80	-0.144	0.5442 ± 0.0090	369.185 ± 0.080	6.606 ± 0.143	3.31
90	-0.312	0.5885 ± 0.0087	369.113 ± 0.079	6.536 ± 0.133	2.31
100	-0.461	0.7144 ± 0.0091	369.085 ± 0.074	6.444 ± 0.117	3.75
110	-0.593	0.9019 ± 0.0100	369.447 ± 0.069	6.265 ± 0.098	2.74
120	-0.704	1.1149 ± 0.0105	369.877 ± 0.062	6.383 ± 0.080	3.93
130	-0.797	1.3062 ± 0.0109	369.846 ± 0.055	6.164 ± 0.063	7.21

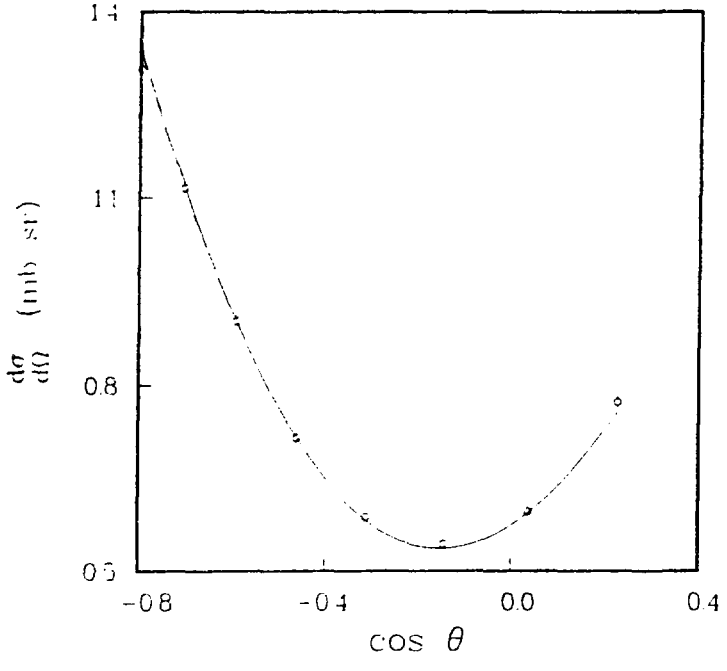

Figure 30. Angular distribution of $\pi^-p \to \pi^-p$ at 256 MeV. The curve represents the interpolation of SCATPI.

TABLE XXI. Results from $\pi^- p \to \pi^- p$ spectra at 358 MeV.

θ_{lab}	$\cos\theta$	$\frac{d\sigma}{d\Omega}$(mb/sr)	μ_b(MeV/c)	σ_b(MeV/c)	χ^2/ν
90	-0.361	0.3967 ± 0.0062	478.25 ± 0.11	8.57 ± 0.22	2.37
100	-0.504	0.4401 ± 0.0056	476.94 ± 0.10	8.59 ± 0.18	2.39
110	-0.627	0.5223 ± 0.0064	476.75 ± 0.12	8.43 ± 0.17	2.41
120	-0.731	0.6254 ± 0.0074	477.23 ± 0.11	7.97 ± 0.15	3.14
130	-0.816	0.7538 ± 0.0080	477.43 ± 0.10	7.96 ± 0.12	3.20

This effect was partially compensated by a failure of our trial function to properly describe skewing in the low-momentum sides of the elastic peaks.

The inadequacy of our trial function to fit the data suggests that the centroids and widths of the incident momentum distributions were less well defined than indicated by the fitting algorithm; hence, variations with angle might have been expected. Measurements of the momentum width decreased slightly at forward and backward angles with a corresponding increase in measurements of the centroid. The optimum centroid and width and the r.m.s. deviations from the mean centroid and width of the measurements are given in Table XXII for each incident momentum distribution. For the centroid of each beam, the r.m.s. deviation from the mean of the measurements was greater than the r.m.s. deviation predicted by the fitting algorithm by a factor of about two or three at 203 MeV and by a factor of about five at 358 MeV. For the width of each beam, the r.m.s. deviation from the mean of the measurements was about twice the r.m.s. deviations predicted by the fitting algorithm. These differences may be the result of the inadequate form assumed for $H(p_I)$, the neglected instability in the measured shunt voltage, or other causes. From the results in Table XXII, we estimate that the uncertainties in our measurements of μ_{beam} and σ_{beam} were about 0.1% and 3%, respectively.

For each π^- beam, we opened the momentum slit of the P^3 channel 7.67 cm. The dispersion for the west leg of the channel predicts $\Delta p/p = 4.3\%$ (FWHM) at this setting, in good agreement with our measured 4.1%. The centroids given in Table XXII were between 1.5%

TABLE XXII. Results from the study of $\pi^- p \to \pi^- p$. Each quoted uncertainty is the r.m.s. deviation from the mean of the measurements at each angle.

T (MeV)	μ_{beam} (MeV/c)	σ_{beam} (MeV/c)
203[a]	312.46 ± 0.18	5.50 ± 0.15
203[b]	311.87 ± 0.14	5.58 ± 0.13
203[c]	312.64 ± 0.18	5.55 ± 0.14
203[d]	312.73 ± 0.26	5.32 ± 0.15
203[e]	312.78 ± 0.28	5.35 ± 0.13
229[a]	341.48 ± 0.43	6.18 ± 0.38
229[b]	341.47 ± 0.43	5.90 ± 0.14
229[c]	342.00 ± 0.48	6.05 ± 0.09
256	369.60 ± 0.35	6.34 ± 0.15
358	477.33 ± 0.56	8.21 ± 0.32

[a]First beam.
[b]Second beam.
[c]Third beam.
[d]Fourth beam.
[e]Fifth beam.

and 1.6% lower than those predicted by the computer codes used to tune the channel.

In Table XXIII, we present values of the normalization factor T′ and the centroid and width of each incident π^- beam, corrected for energy loss after entering the target. These were used in the analysis of $\pi^-p\rightarrow\pi^+\pi^-n$ as discussed in Chapter V. Table XXIII also presents the χ^2/ν that were obtained by varying T as discussed earlier so that values of the measured cross section agreed on the average with values of the known cross section. χ^2/ν for the π^- beams varied from 0.05 to 3.82. The larger χ^2 reflect variations, which are not understood, of about 2% from the predicted angular distributions at forward and backward angles. Figs. 28-30 show that the measured angular distributions were lower than SCATPI's predictions at forward angles and higher at backward angles. The variation at backward angles is of the size and direction expected from our trial function's overestimation of the area under the elastic peaks. At forward angles, the variation is opposite to the expected direction. Some of the variation may reflect inconsistencies of the order of 2% in the measurements of Carter et al.[15] upon which SCATPI was based.

TABLE XXIII. Beam normalization factors and incident momentum distribution parameters corrected for energy loss in the target.

T (MeV)	T′ (mb/sr)(monitor counts/π)	μ_{beam} (MeV/c)	σ_{beam} (MeV/c)	χ^2/ν
202[a]	32.66 ± 0.14	312.09	5.50	2.00
202[b]	34.53 ± 0.14	311.50	5.58	3.82
202[c]	31.58 ± 0.20	312.28	5.55	0.05
202[d]	34.13 ± 0.13	312.36	5.32	3.35
202[e]	34.11 ± 0.14	312.42	5.35	2.59
229[a]	31.00 ± 0.15	341.12	6.18	1.28
229[b]	28.62 ± 0.13	341.11	5.90	2.09
229[c]	29.67 ± 0.14	341.64	6.05	1.56
255	28.71 ± 0.18	369.25	6.34	0.51
357	25.72 ± 0.51	477.00	8.21	0.12

[a]First beam.
[b]Second beam.
[c]Third beam.
[d]Fourth beam.
[e]Fifth beam.

CHAPTER V

CALCULATION OF THE DOUBLY DIFFERENTIAL CROSS SECTION

The doubly differential cross section $\frac{d^2\sigma}{d\Omega dT}$ for the π^+ mesons produced in the reaction $\pi^-p \rightarrow \pi^+\pi^-n$ was measured at four incident kinetic energies: 203, 230, 256, and 358 MeV. Measurements of $\frac{d^2\sigma}{d\Omega dT}$ were calculated in a similar, but improved, manner to that used to analyze a set of previous measurements.[10] These previous cross sections at incident energies 254, 280, 292, 331, and 356 MeV were recalculated by the new method. The improved analysis more properly handled the small statistical sampling in each detection channel. In addition, an error matrix, sometimes called a variance-covariance matrix, was calculated at each incident energy so that correlated errors in measurements of $\frac{d^2\sigma}{d\Omega dT}$ at different locations in T-cosθ space could be properly propagated.

Event Rates and Backgrounds

After adjusting the spectrometer for the desired charge, momentum, and production angle, two sets of data for calculating $\frac{d^2\sigma}{d\Omega dT}$ were accumulated, one with the target flask filled with liquid hydrogen and one with the flask empty. Each set was collected in one or more data runs in which, typically, 40-80 μC of charge were collected from the ionization chamber. Events in each of the solid-state detectors were binned according to whether or not there was a pulse above the cut-off

level of the Cerenkov detector. The rate of events from hydrogen that did not produce pulses in the Cerenkov detector is given by

$$R_{\bar{C}} = \left(\frac{N_{\bar{C}}}{M_\ell}\right)_{full} - \left(\frac{N_{\bar{C}}}{M_\ell S}\right)_{empty} ,$$

whereas the rate of events from hydrogen that did produce pulses in the Cerenkov detector is given by

$$R_C = \left(\frac{N_C}{M_\ell}\right)_{full} - \left(\frac{N_C}{M_\ell S}\right)_{empty} .$$

The subscripts full and empty refer to the status of the target flask. N_C and $N_{\bar{C}}$ refer respectively to the number of events with or without a pulse in the Cerenkov detector, summed over all functional solid-state detectors. Here, as before, M_ℓ is either the number of counts in the scattering monitor during live time or, for scattering angles forward of 40° in the laboratory, the projected number of counts during live time calculated from the charge collected from the ionization chamber. When the target flask was empty, the factor

$$S = \exp(-\sigma\, n\, L)$$

compensated for the reduced probability for a pion to be scattered out of the beam before reaching the monitor. Here, σ is the total $\pi^- p$ cross section generated with SCATPI,[27] n is the number density of protons in the target, and $L \approx 2.2$ cm is an average interaction length

for the beam in the target. The correction due to S varied from 0.5% at 203 MeV to 0.2% at 358 MeV. Since SCATPI's prediction for σ at 358 MeV agrees within 6% of measurement, the error introduced in S is negligible. For either $R_{\bar{c}}$ or R_c, the mean square deviation is given by (the subscripts c and $\bar{c}$ have been dropped in the display formula)

$$\overline{(\Delta R)^2} = \left[\frac{(N+1)}{M_\ell^2}\right]_{full} + \left[\frac{(N+1)}{M_\ell^2 S^2}\right]_{empty} .$$

The statistical uncertainty in M_ℓ, typically about 0.1%, was neglected.

If we denote as in Chapter III the efficiencies of the Cerenkov detector for detecting electrons and pions by ε_e and ε_π, respectively, then the rate of pion events from hydrogen can be written as

$$R_\pi = \frac{\varepsilon_e R_{\bar{c}} - (1-\varepsilon_e)R_c}{\varepsilon_e - \varepsilon_\pi} ,$$

with the corresponding rate of electron events from hydrogen given by

$$R_e = \frac{-\varepsilon_\pi R_{\bar{c}} + (1-\varepsilon_\pi)R_c}{\varepsilon_e - \varepsilon_\pi} .$$

Assume that $\Delta\varepsilon_e$ and $\Delta\varepsilon_\pi$ are the respective uncertainties in ε_e and ε_π, that $\overline{(\Delta R_{\bar{c}})^2}^{1/2}$ and $\overline{(\Delta R_c)^2}^{1/2}$ are the respective uncertainties in $R_{\bar{c}}$ and R_c, and that all uncertainties combine in quadrature. Then the respective mean square deviations in R_π and R_e are

$$\overline{(\Delta R_\pi)^2} = (\varepsilon_e - \varepsilon_\pi)^{-2}[(\varepsilon_e)^2\overline{(\Delta R_{\bar{c}})^2} + (1 - \varepsilon_e)^2\overline{(\Delta R_c)^2} + R_e{}^2(\Delta\varepsilon_e)^2 + R_\pi{}^2(\Delta\varepsilon_\pi)^2]$$

and

$$\overline{(\Delta R_e)^2} = (\varepsilon_e - \varepsilon_\pi)^{-2}[(\varepsilon_\pi)^2\overline{(\Delta R_{\bar{c}})^2} + (1 - \varepsilon_\pi)^2\overline{(\Delta R_c)^2} + R_e{}^2(\Delta\varepsilon_e)^2 + R_\pi{}^2(\Delta\varepsilon_\pi)^2] .$$

Since R_π and R_e were not statistically independent, they had a nonzero covariance:

$$\overline{(\Delta R_\pi)(\Delta R_e)} = -(\varepsilon_e - \varepsilon_\pi)^{-2}[\varepsilon_e\varepsilon_\pi\overline{(\Delta R_{\bar{c}})^2} + (1 - \varepsilon_\pi)(1 - \varepsilon_e)\overline{(\Delta R_c)^2} + R_e{}^2(\Delta\varepsilon_e)^2 + R_\pi{}^2(\Delta\varepsilon_\pi)^2] .$$

Plots of R_e/R_π at each incident energy, illustrating the importance of the e^+ background, are shown in Figs. 31-37. Values are plotted for each measurement in T-cosθ space. The r.m.s. deviation in R_e/R_π, which was calculated as

$$\Delta\left(\frac{R_e}{R_\pi}\right) = \frac{R_e}{R_\pi}\left[\frac{\overline{(\Delta R_e)^2}}{R_e{}^2} + \frac{\overline{(\Delta R_\pi)^2}}{R_\pi{}^2} - 2\,\frac{\overline{(\Delta R_e)(\Delta R_\pi)}}{R_eR_\pi}\right]^{1/2},$$

is given in parentheses beside the calculated ratio at each point. At a given incident energy, R_e/R_π increases at forward angles. When R_e/R_π exceeded unity, the electron background was large and the ability to accurately separate electron and pion events was extremely important. At the two lowest energies, 203 and 230 MeV, the e^+

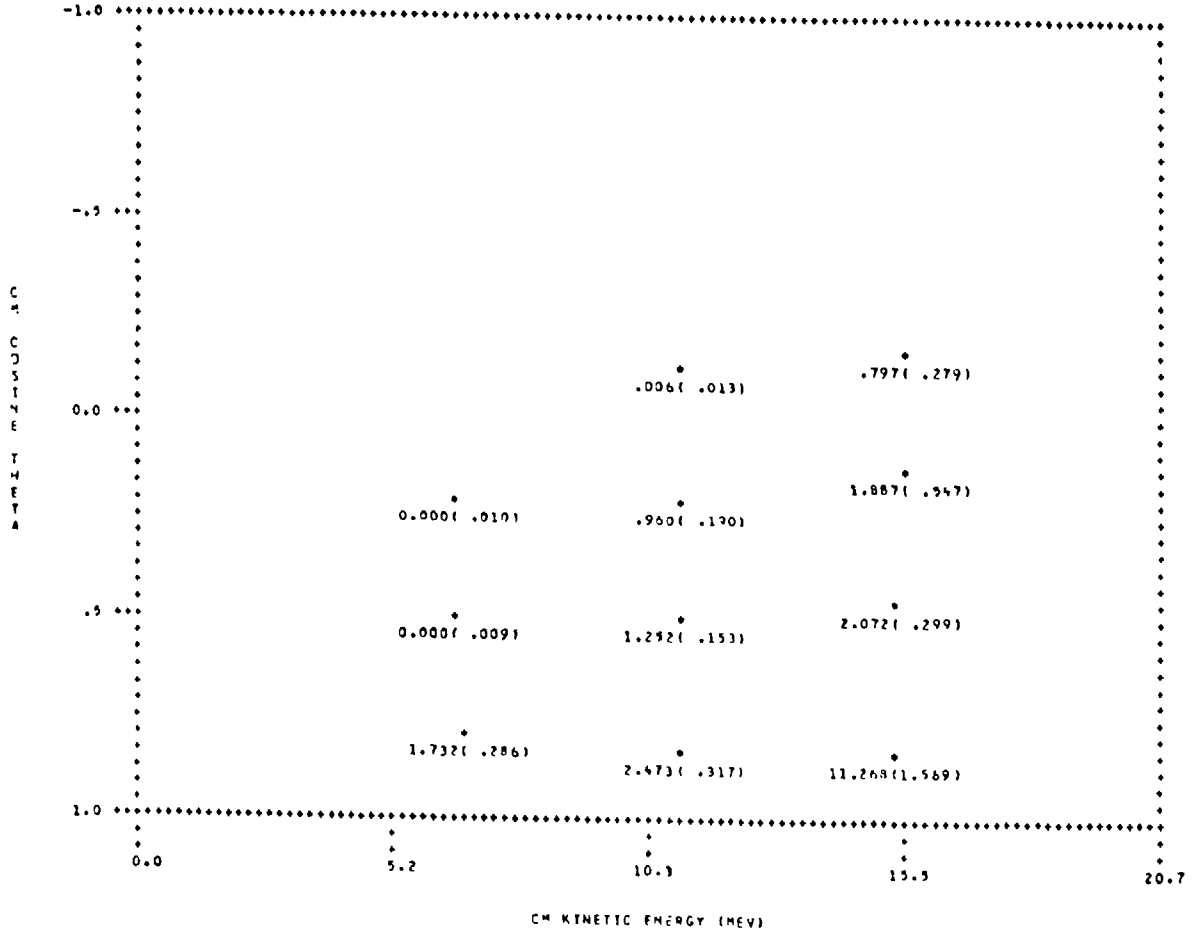

Figure 31. Values of R_e/R_π at 203 MeV.

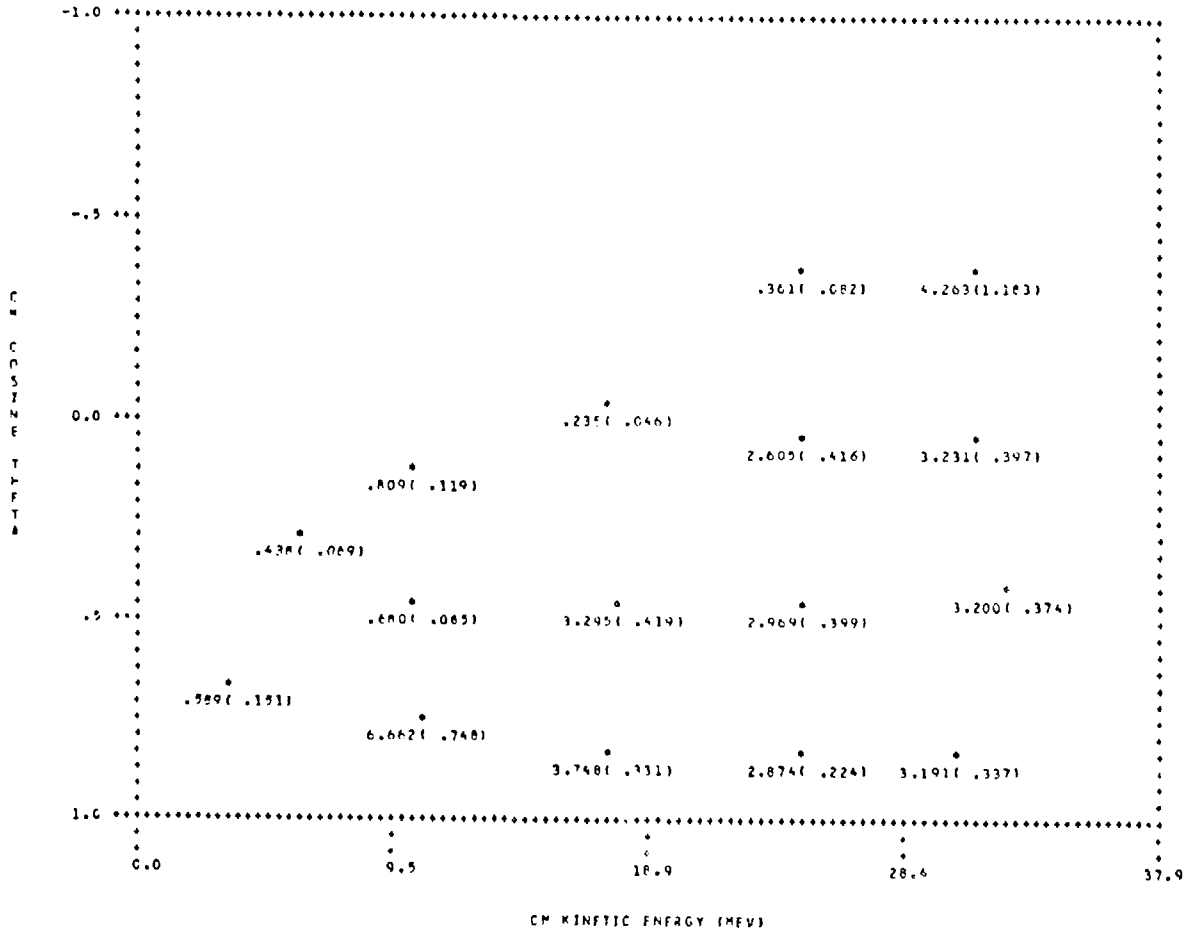

Figure 32. Values of R_e/R_π at 230 MeV.

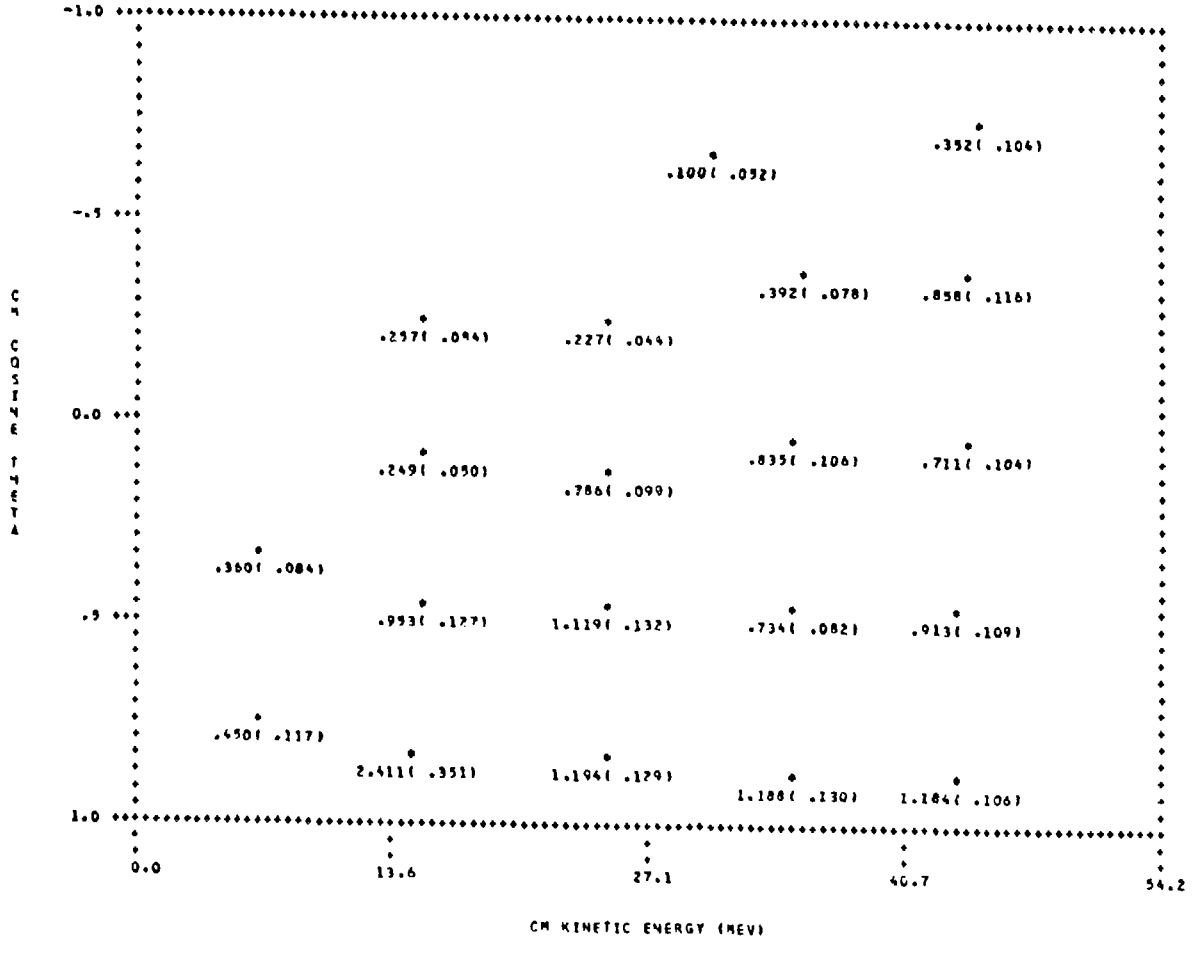

Figure 33. Values of R_e/R_π at 256 MeV.

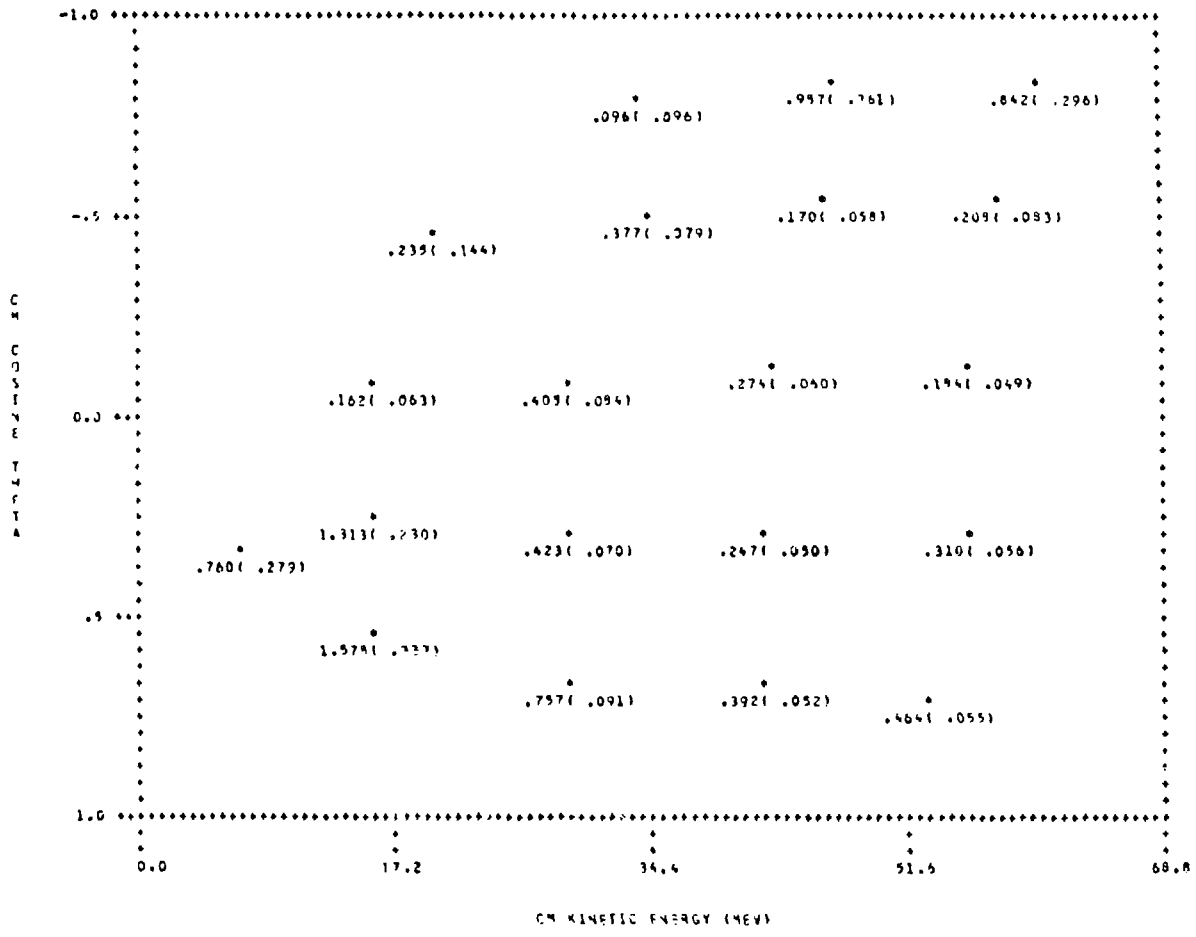

Figure 34. Values of R_e/R_π at 280 MeV. The data were obtained from a previous $\pi^-p \to \pi^+\pi^-n$ experiment.[10]

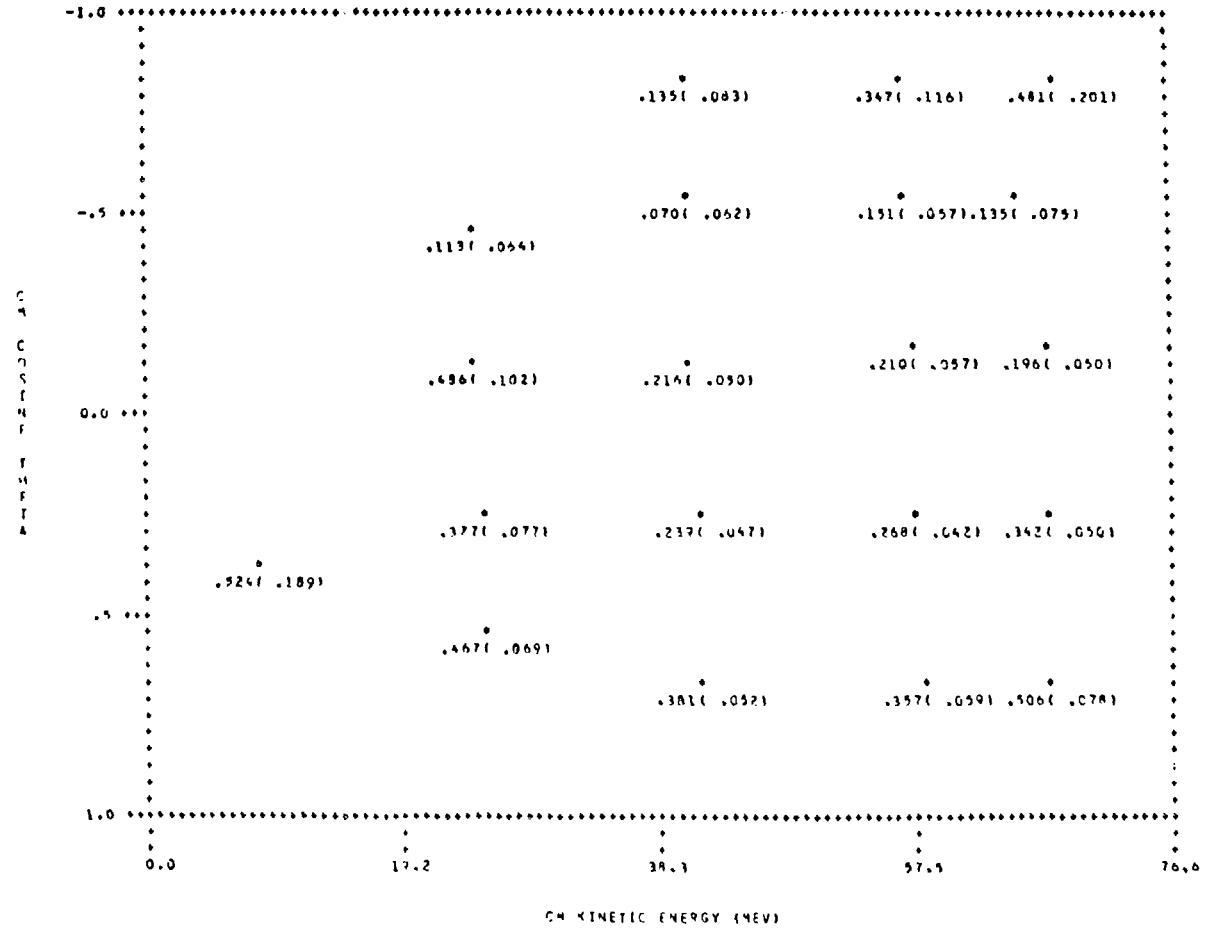

Figure 35. Values of R_e/R_π at 292 MeV. The data were obtained from a previous $\pi^- p \to \pi^+ \pi^- n$ experiment.[10]

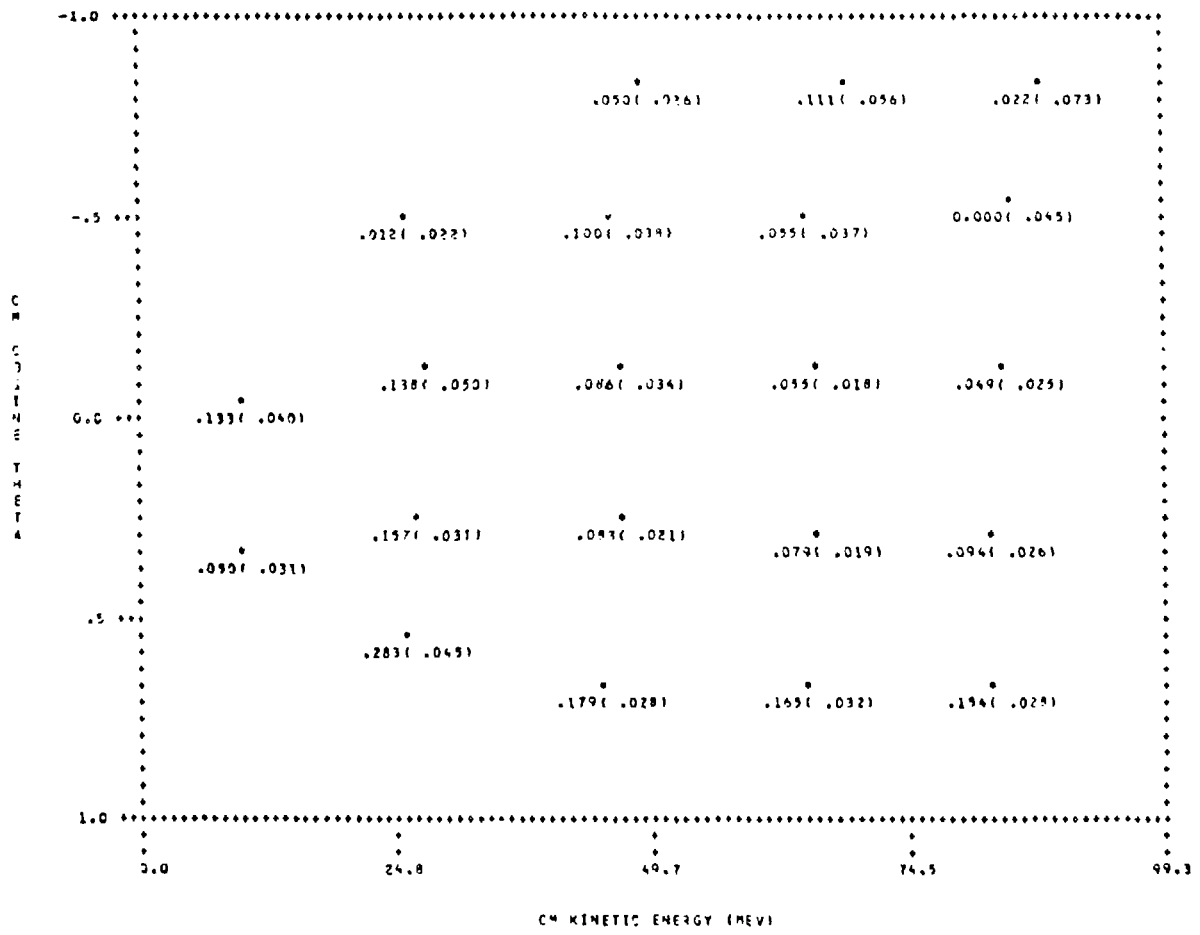

Figure 36. Values of R_e/R_π at 331 MeV. The data were obtained from a previous $\pi^-p \to \pi^+\pi^-n$ experiment.[10]

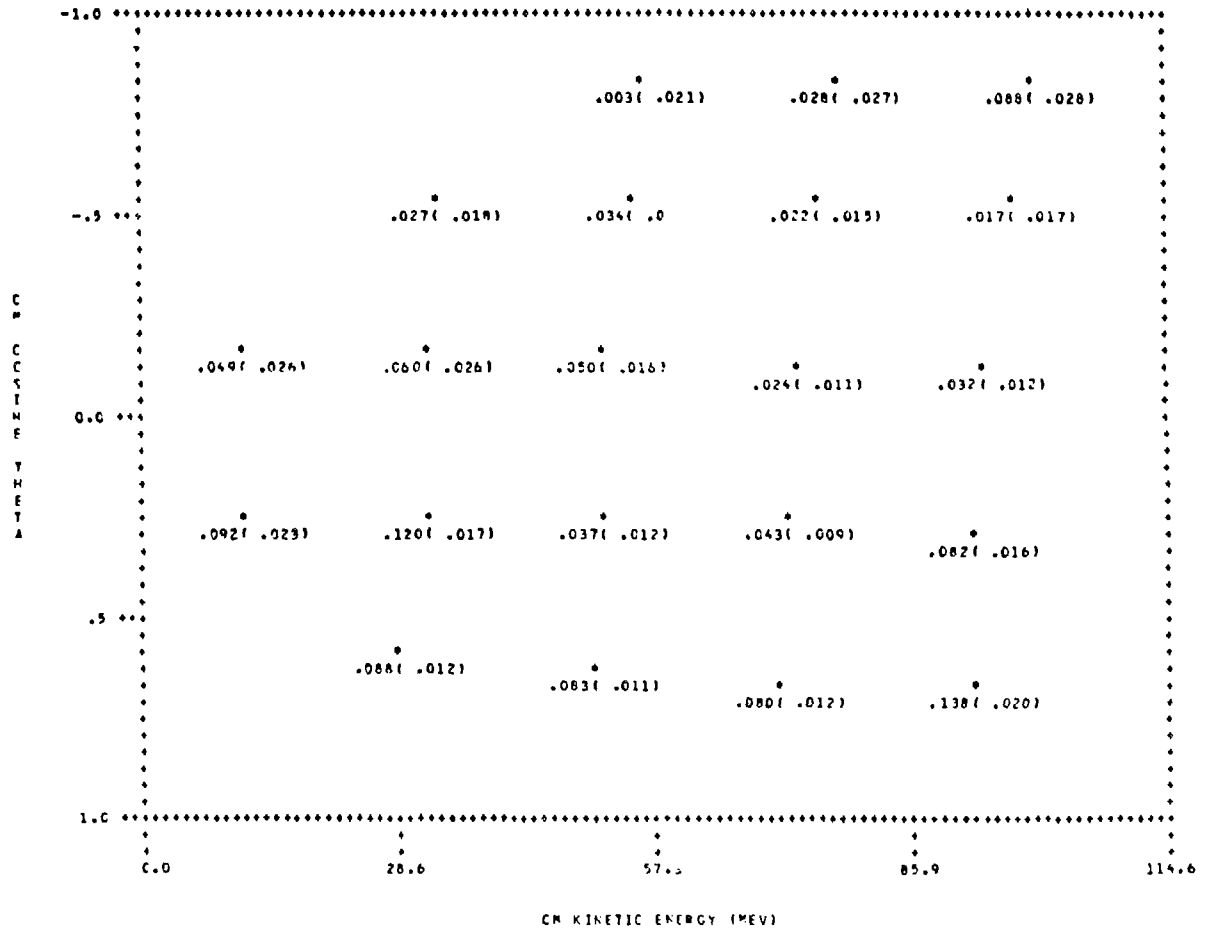

Figure 37. Values of R_e/R_π at 358 MeV.

background was quite large for most measurements, with an event rate for electrons several times that for pions. About 60% of the measurements at 256 MeV were sensitive to the e^+ background. At 280 MeV, the e^+ background was significant only for measurements at the most forward angles, whereas at the three highest energies, 292, 331, and 357 MeV, the background was almost negligible.

Another important quantity was the ratio $(R_\pi)_{empty}/R_\pi$, which measured the size of the background of events identified as pions that were unassociated with the liquid hydrogen. Here, $(R_\pi)_{empty}$ is the calculated rate of events identified as pions when the target flask was empty:

$$(R_\pi)_{empty} = \frac{\varepsilon_e(R_{\bar{c}})_{empty} - (1 - \varepsilon_e)(R_c)_{empty}}{\varepsilon_e - \varepsilon_\pi} .$$

The corresponding rate of events identified as electrons when the target flask was empty is given by

$$(R_e)_{empty} = \frac{-\varepsilon_\pi(R_{\bar{c}})_{empty} + (1 - \varepsilon_\pi)(R_c)_{empty}}{\varepsilon_e - \varepsilon_\pi} ,$$

where $(R_{\bar{c}})_{empty} = [N_{\bar{c}}/(M_\ell S)]_{empty}$ and $(R_c)_{empty} = [N_c/(M_\ell S)]_{empty}$. The quantity

$$\overline{(\Delta R_\pi)^2_{empty}} = (\varepsilon_e - \varepsilon_\pi)^{-2}[(\varepsilon_e)^2\overline{(\Delta R_{\bar{c}})^2_{empty}} + (1 - \varepsilon_e)^2\overline{(\Delta R_c)^2_{empty}}$$
$$+ (R_e)^2_{empty}(\Delta\varepsilon_e)^2 + (R_\pi)^2_{empty}(\Delta\varepsilon_\pi)^2]$$

is the mean square deviation in $(R_\pi)_{empty}$ and

$$\overline{(\Delta R_\pi)(\Delta R_\pi)_{empty}} = (\varepsilon_e - \varepsilon_\pi)^{-2}[-(\varepsilon_e)^2\overline{(\Delta R_c)^2_{empty}} - (1 - \varepsilon_e)^2\overline{(\Delta R_c)^2_{empty}} + (R_e)(R_e)_{empty}(\Delta\varepsilon_e)^2 + (R_\pi)(R_\pi)_{empty}(\Delta\varepsilon_\pi)^2] .$$

is the covariance in R_π and $(R_\pi)_{empty}$. To minimize the uncertainty in R_π, we apportioned the time spent on each production measurement according to the relation

$$\frac{t_{empty}}{t_{full}} = \left[\frac{(R_\pi)_{empty}/R_\pi}{1 + (R_\pi)_{empty}/R_\pi}\right]^{1/2},$$

where t_{full} and t_{empty} represent the amounts of time in which the target flask was respectively full or empty of liquid hydrogen. When $(R_\pi)_{empty}/R_\pi$ was large, it was necessary to measure for equal amounts of time with the flask empty and full so that the rate of events measured with the flask empty and full were established with equal accuracy. To reduce the uncertainties in such measurements was clearly difficult and required substantial amounts of time. Furthermore, the reliability of our technique of subtracting background in such cases was, at best, questionable. Plots of $(R_\pi)_{empty}/R_\pi$ at each incident energy are shown in Figs. 38-44 for each measurement in T-cosθ space. The r.m.s. deviation in $(R_\pi)_{empty}/R_\pi$,

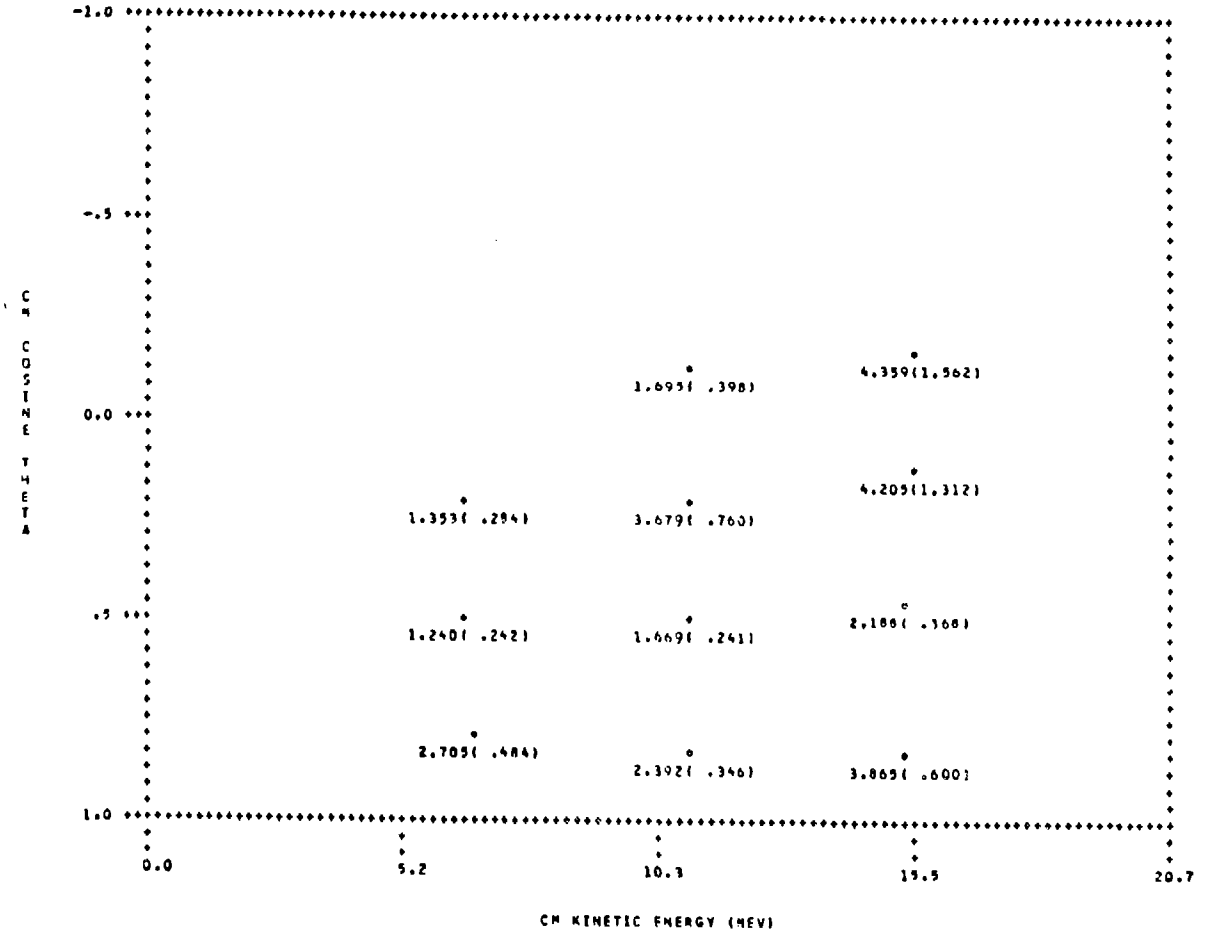

Figure 38. Values of $(R_\pi)_{empty}/R_\pi$ at 203 MeV.

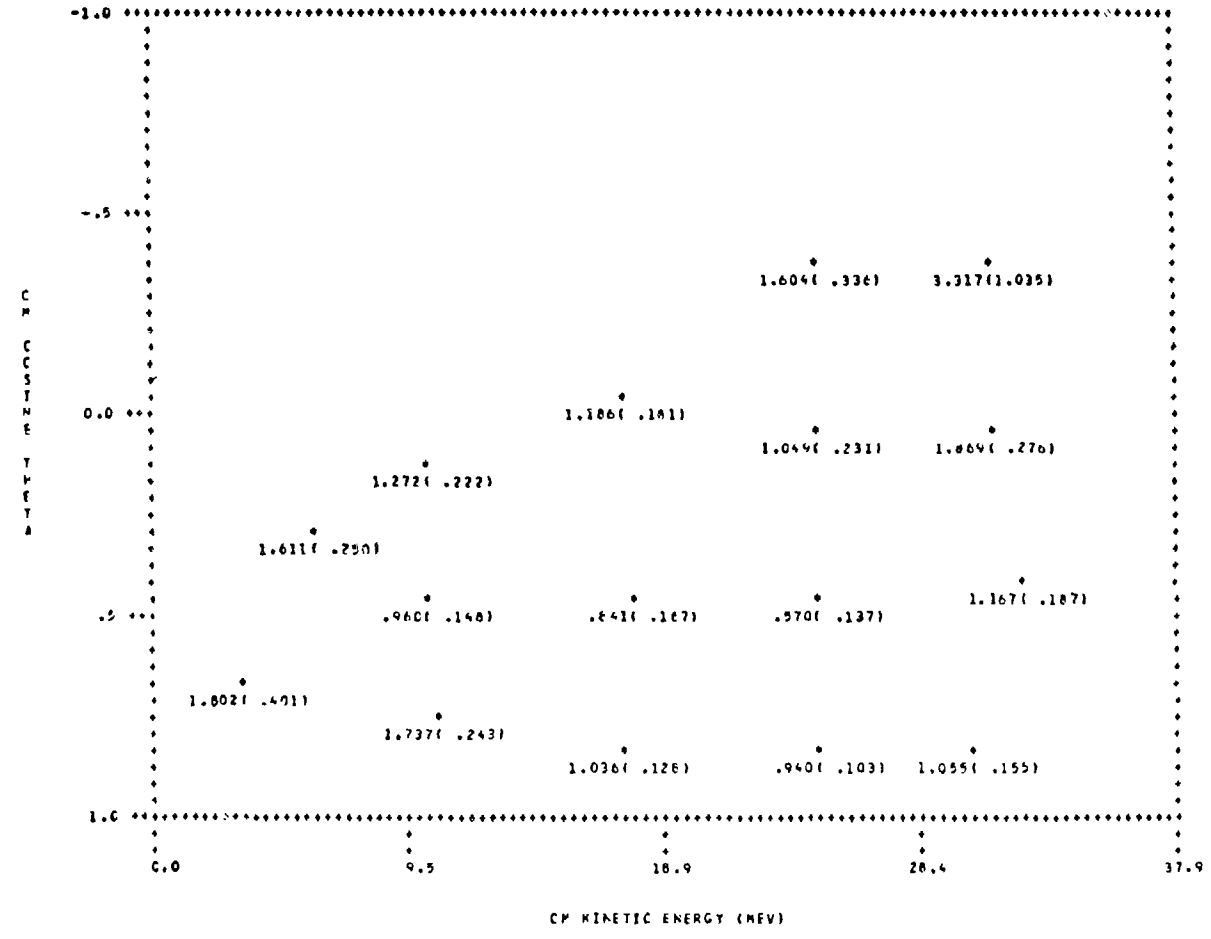

Figure 39. Values of $(R_\pi)_{empty}/R_\pi$ at 230 MeV.

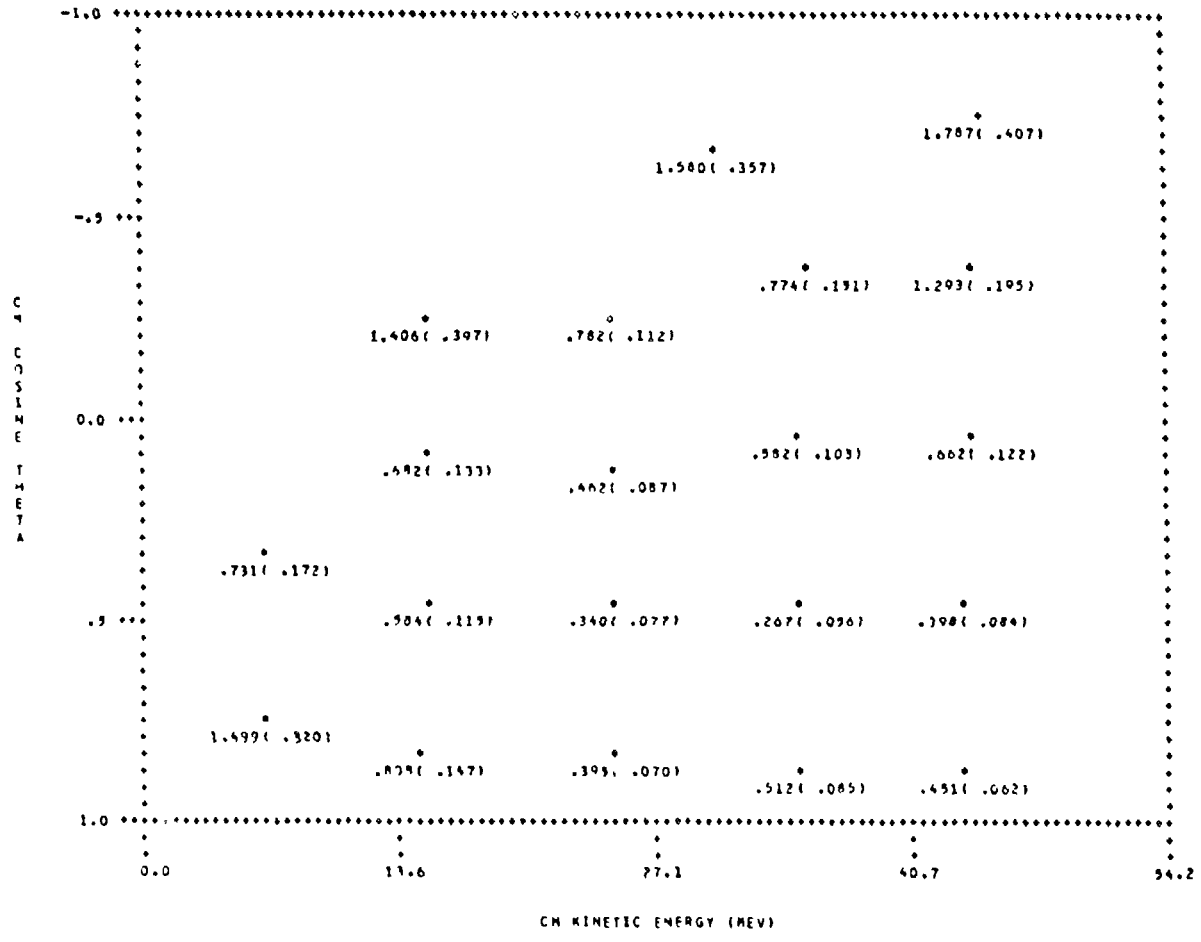

Figure 40. Values of $(R_\pi)_{empty}/R_\pi$ at 256 MeV.

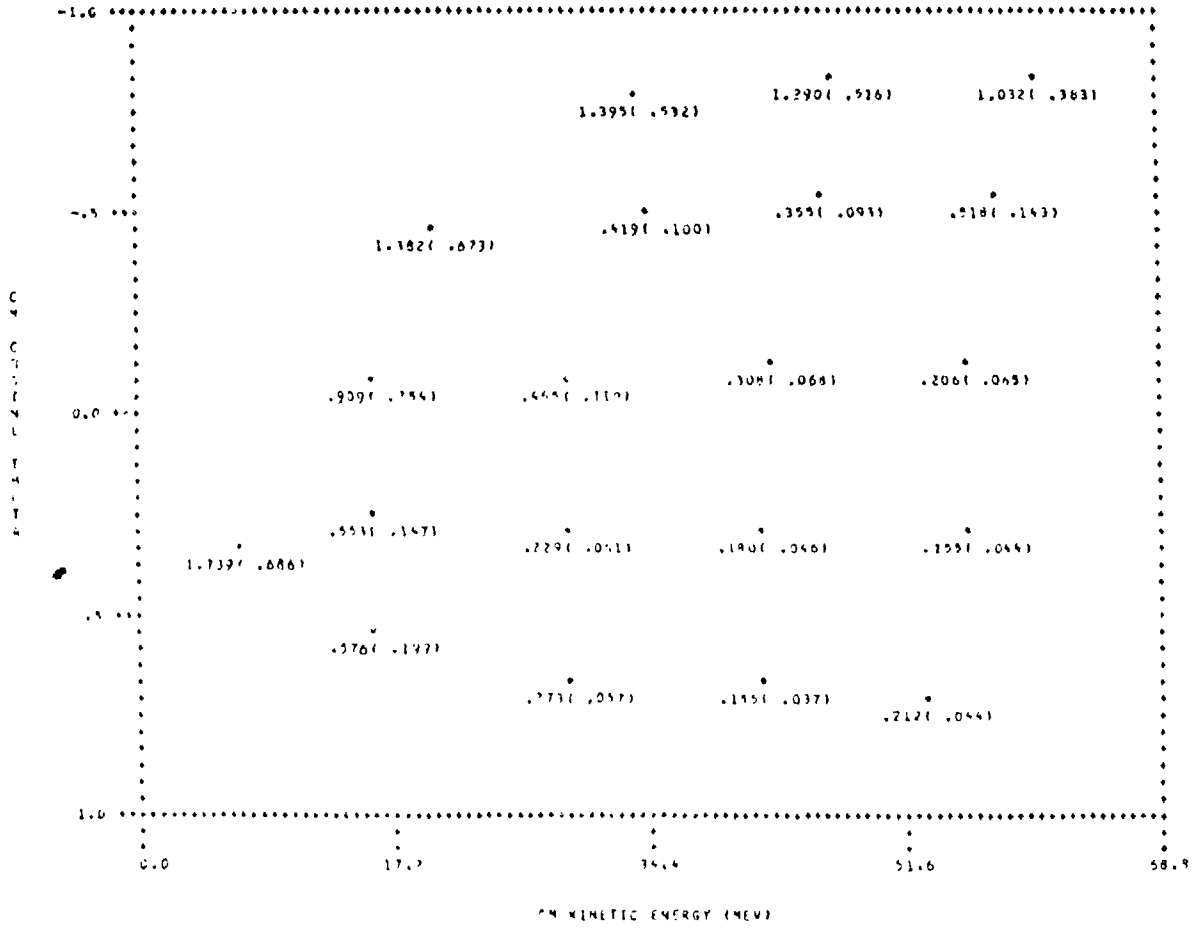

Figure 41. Values of $(R_\pi)_{empty}/R_\pi$ at 280 MeV. The data were obtained from a previous $\pi^-p\to\pi^+\pi^-n$ experiment.[10]

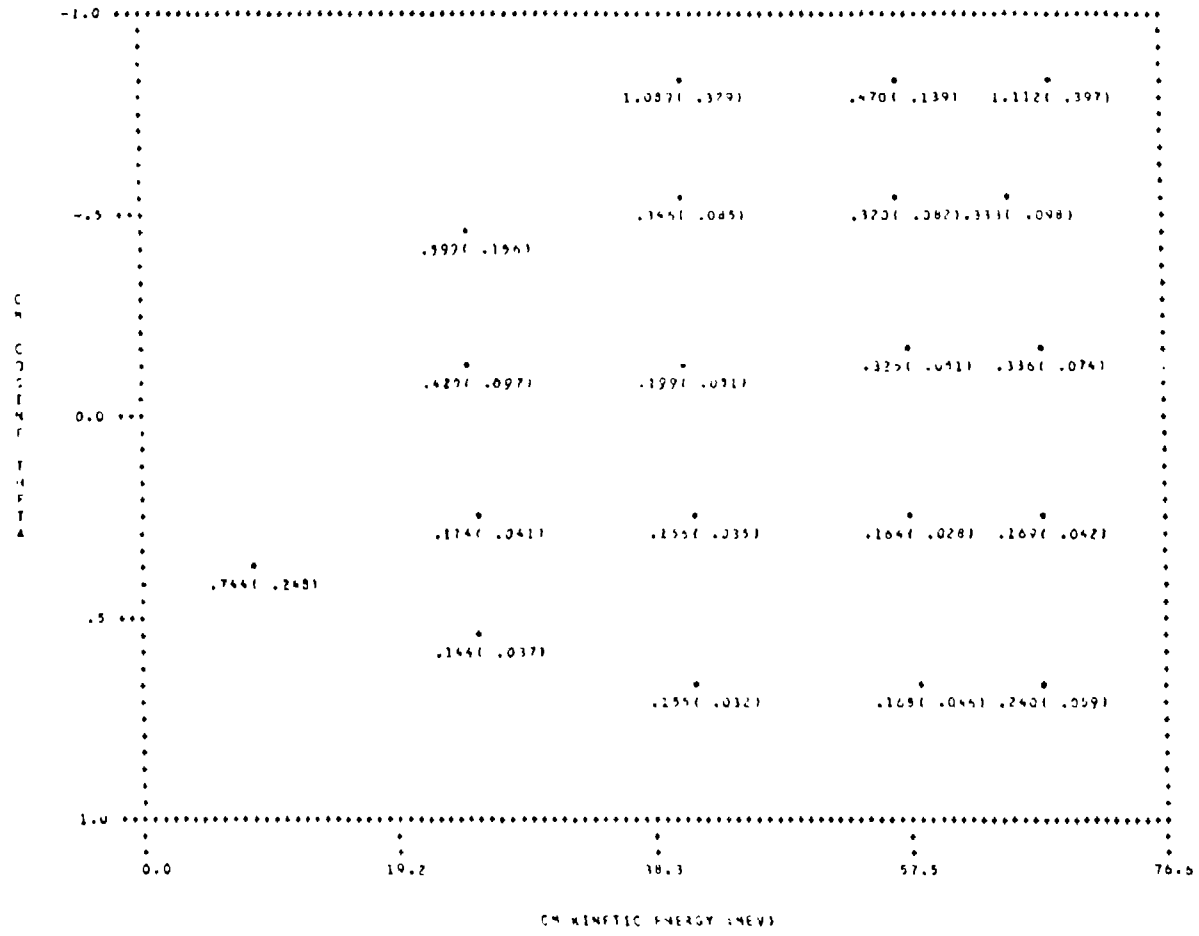

Figure 42. Values of $(R_\pi)_{empty}/R_\pi$ at 292 MeV. The data were obtained from a previous $\pi^- p \to \pi^+ \pi^- n$ experiment.[10]

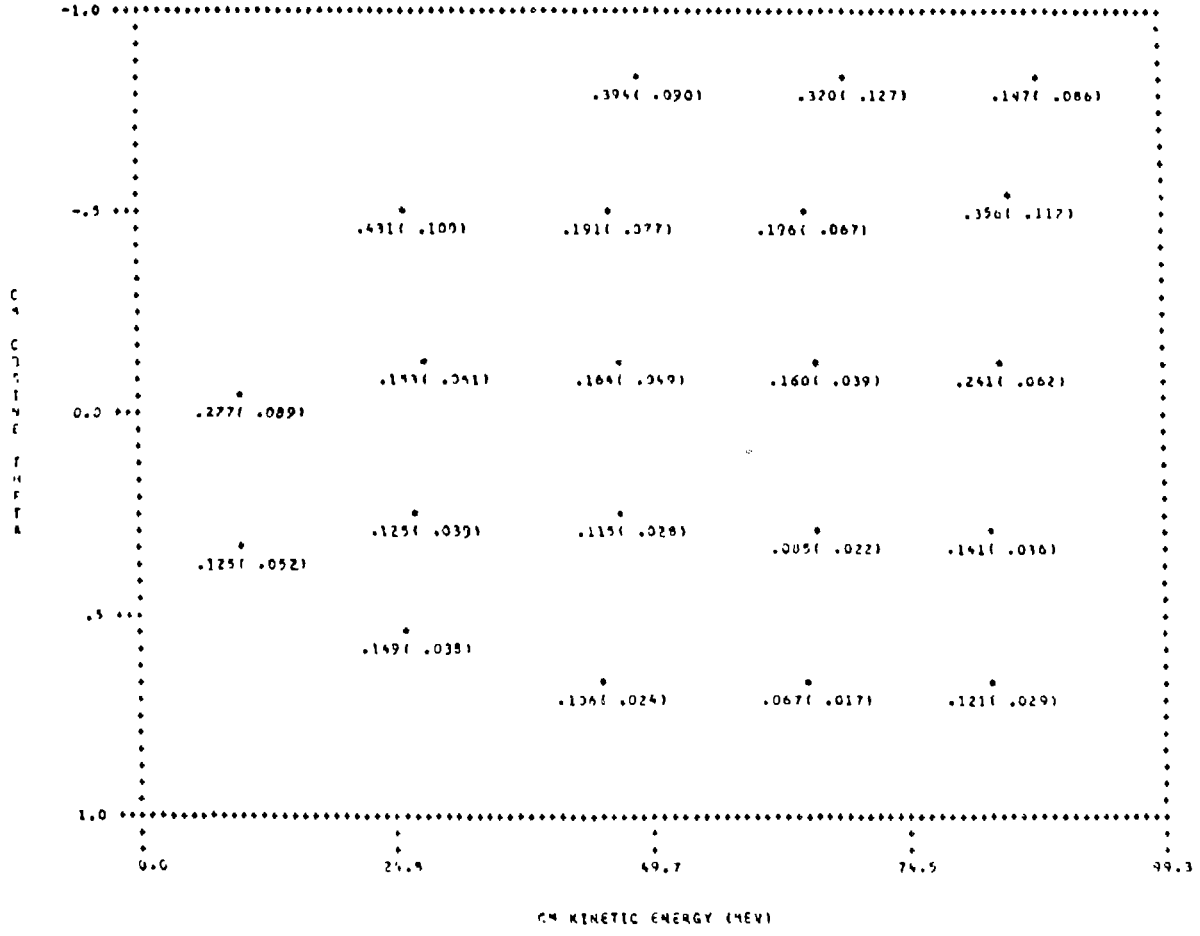

Figure 43. Values of $(R_\pi)_{empty}/R_\pi$ at 331 MeV. The data were obtained from a previous $\pi^-p \to \pi^+\pi^-n$ experiment.[10]

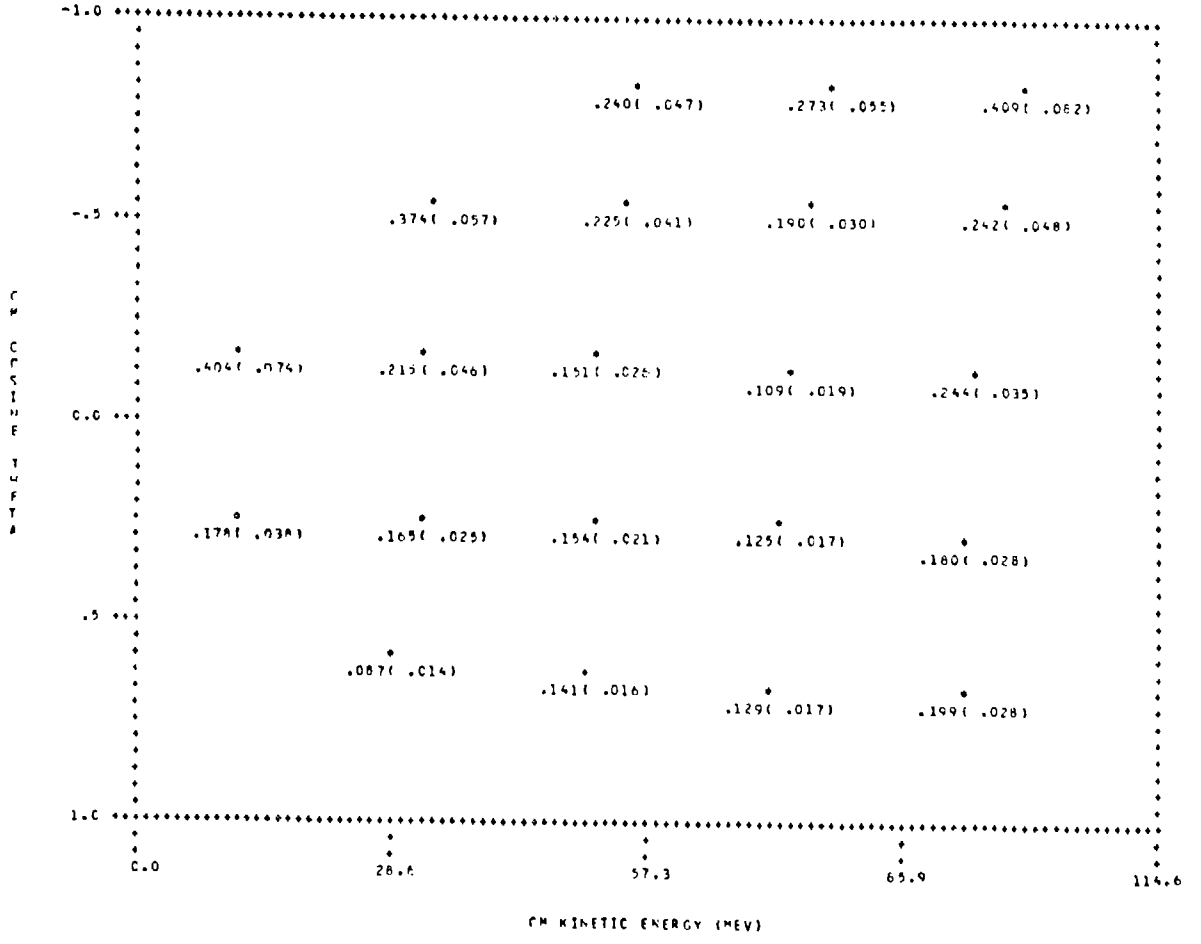

Figure 44. Values of $(R_\pi)_{empty}/R_\pi$ at 358 MeV.

$$\Delta\left[\frac{(R_\pi)_{empty}}{R_\pi}\right] = \frac{(R_\pi)_{empty}}{R_\pi}\left[\frac{\overline{(\Delta R_\pi)^2_{empty}}}{(R_\pi)^2_{empty}} + \frac{\overline{(\Delta R_\pi)^2}}{R_\pi{}^2}\right.$$

$$\left. - 2\,\frac{\overline{(\Delta R_\pi)(\Delta R_\pi)_{empty}}}{(R_\pi)(R_\pi)_{empty}}\right]^{1/2},$$

is given in parentheses beside the calculated ratio at each point. At a given incident energy, $(R_\pi)_{empty}/R_\pi$ increased as the π^+ momentum in the laboratory decreased. The pion background was significant when $(R_\pi)_{empty}/R_\pi$ was greater than unity. This was the case for all measurements at 203 MeV and for most at 230 MeV, which indicates the difficulty of those measurements. The $(R_\pi)_{empty}/R_\pi$, which varied from 1.2 to 4.4 at 203 MeV and from 0.6 to 3.3 at 230 MeV, decreased with incident energy until, at 358 MeV, the values varied from 0.1 to 0.4.

The Doubly Differential Cross Section and Matrix Element

The doubly differential cross section $\frac{d^2\sigma}{d\Omega dT}$ was proportional to R_π, the rate at which pions were produced from hydrogen in the target. Since these $\frac{d^2\sigma}{d\Omega dT}$ were strongly dominated by phase space, they varied rapidly with the kinetic energy of the final-state π^+ meson. To facilitate our efforts to model the production measurements, we reduced the doubly differential cross section to the mean square modulus of the matrix element, a quantity which varied relatively slowly in T-cosθ space.

Each measurement of the pion event rate represents an average over the momentum distribution of the incident beam and an integration (replaced by a summation) over the momentum of the detected pion:

$$R_\pi = \sum_I F_I \int \left(\frac{d^2\sigma}{d\Omega dp}\right)_I \omega(p_{in})\, dp_{in} \ .$$

The distribution function was assumed to be Gaussian:

$$\omega(p_{in}) = N \exp\left[-\frac{1}{2}\left(\frac{p_{in} - \mu_{beam}}{\sigma_{beam}}\right)^2\right] \ .$$

As discussed in Chapter IV, the beam centroid μ_{beam} and width σ_{beam} were inferred from measurements of π^-p elastic scattering with the incident beam. N is a normalization constant determined such that

$$\int \omega(p_{in})\, dp_{in} = 1 \ ,$$

with integration limits $\mu_{beam} - 2\sigma_{beam}$ and $\mu_{beam} + 2\sigma_{beam}$. The treatment of using a Gaussian distribution function with a finite domain is a convenient approximation to the true form of the distribution function, which is unknown.

The summation above includes all detection channels, which are indicated by the index I. The quantity $\left(\frac{d^2\sigma}{d\Omega dp}\right)_I$ represents the doubly differential cross section for π^+ mesons detected in the Ith channel when the incident momentum was p_{in}. F_I is an overall factor to normalize the Ith channel by its momentum acceptance and relative efficiency, to correct for pion decay, and to normalize the measurement to known cross sections. We can write

$$F_I = \frac{p_c \delta \varepsilon_I}{T' D_I} ,$$

where $p_c\delta$ is the momentum acceptance of a channel, ε_I is the relative channel efficiency, and T' is the normalization factor determined from measurements of $\pi^- p$ elastic scattering. Pion decay, which has been discussed earlier, is corrected for by the factor D_I:

$$D_I = \exp\left(\frac{\Lambda\, m_\pi}{p_I \tau_\pi}\right) .$$

The quantities m_π and τ_π are, respectively, the mass and mean lifetime of the charged pion. Λ was the mean path length from the target to the focal plane of the spectrometer and p_I was the momentum of particles detected in the Ith channel. We can transform $\left(\frac{d^2\sigma}{d\Omega dp}\right)_I\Big|_{lab}$ to $\left(\frac{d^2\sigma}{d\Omega dT}\right)_I\Big|_{c.m.}$ by introducing the Jacobian

$$J_I = (p_I^2 + m_\pi^2)^{-1/2}\, p_I^2/q_I ,$$

where q_I is the momentum p_I transformed to the c.m. system and

$$\left(\frac{d^2\sigma}{d\Omega dp}\right)_I\Big|_{lab} = \left(\frac{d^2\sigma}{d\Omega dT}\right)_I\Big|_{c.m.} J_I .$$

We can write[31]

$$\left(\frac{d^2\sigma}{d\Omega dT}\right)_I = \left(\frac{d^2\sigma_o}{d\Omega dT}\right)_I \langle |M|_I^2 \rangle ,$$

with $\langle|M|_I^2\rangle$ the quare modulus of the matrix element averaged over unobserved variables and divided by Q^2, the square of the incident c.m. momentum. The quantity

$$\frac{d^2\sigma_o}{d\Omega dT} = \frac{m_p m_n}{128\pi^4}\frac{Q}{W}\frac{2q\ \{W(T_{max}-T)\ [2m_\pi m_n + W(T_{max}-T)]\}^{1/2}}{(m_\pi + m_n)^2 + 2W(T_{max}-T)}$$

is the density in phase space integrated over unmeasured variables and multiplied by Q^2 and the usual flux factor.[32] In this expression, m_p and m_n are the respective masses of the proton and neutron, W is the total c.m. energy, q and T are, respectively, the momentum and kinetic energy of the π^+ in the c.m. system, and

$$T_{max} = \frac{(W - m_\pi)^2 - (m_\pi + m_n)^2}{2W}$$

is the maximum value of T allowed by kinematics. We assumed that $\langle|M|_I^2\rangle$ varied very slowly over the momentum distribution of the incident beam and that it did not change much from one detection channel to the next. Hence,

$$\overline{|M|^2} = R_\pi \left[\sum_I F_I \int \left(\frac{d^2\sigma_o}{d\Omega dT}\right)_I J_I\, \omega(p_{in})\, dp_{in}\right]^{-1},$$

where $\overline{|M|^2}$ represents $\langle|M|_I^2\rangle$ averaged over the momentum distributions of the incident beam and the detected pions. The error in $\overline{|M|^2}$ is given by

$$\Delta\overline{|M|^2} = \overline{|M|^2}\left[\frac{\overline{(\Delta R_\pi)^2}}{R_\pi^2} + \frac{(\Delta T')^2}{T'^2}\right]^{1/2}.$$

The average incident momentum in the laboratory associated with each measurement of $\overline{|M|^2}$ was calculated with the same weighting:

$$\overline{p_{in}} = \frac{\sum_I F_I \int p_{in} \left(\frac{d^2\sigma_o}{d\Omega dT}\right)_I J_I \, \omega(p_{in}) \, dp_{in}}{\sum_I F_I \int \left(\frac{d^2\sigma_o}{d\Omega dT}\right)_I J_I \, \omega(p_{in}) \, dp_{in}}.$$

The incident kinetic energy in the laboratory for a set of measurements was

$$T_\pi = (p_\pi^2 + m_\pi^2)^{1/2} - m_\pi ,$$

with p_π the average value of $\overline{p_{in}}$ weighted over each measurement in T-cosθ space:

$$p_\pi = \frac{\sum \overline{p_{in}} \, (\overline{|M|^2}/\Delta\overline{|M|^2})^2}{\sum (\overline{|M|^2}/\Delta\overline{|M|^2})^2}.$$

Since variations in the $\overline{p_{in}}$ were always less than 1%, the choice of how to average was not critical. The p_π obtained for our several production beams were always greater than the corresponding values of μ_{beam} by less than 1%. We estimated the error in T_π to be about 0.2%.

The kinetic energy $\overline{T}$ and cosine of the production angle $\overline{\cos\theta}$ in the c.m. system were found in a manner similar to that used to calculate $\overline{p_{in}}$. From p_π and $\overline{T}$, $\frac{d^2\sigma_o}{d\Omega dT}$ was calculated for each measurement of $\overline{|M|^2}$ in T-cosθ space to give the doubly differential cross section

$$\frac{d^2\sigma}{d\Omega dT} = \frac{d^2\sigma_o}{d\Omega dT}\,\overline{|M|^2}$$

in the c.m. system and its uncertainty

$$\Delta\left(\frac{d^2\sigma}{d\Omega dT}\right) = \frac{d^2\sigma_o}{d\Omega dT}\,\Delta\overline{|M|^2}\ .$$

In Tables XXIV-XXXII, we summarize the values calculated for $\frac{d^2\sigma}{d\Omega dT}$ and $\overline{|M|^2}$ at each incident energy. These tables give a statistical error, which includes only the errors for the counting statistics of the production measurements, and a total error, which includes, additionally, the contributions from $\Delta\varepsilon_e$ and $\Delta T'$. Our measured $\overline{|M|^2}$ are shown in Figs. 45-53 with their total errors given in parentheses.

Error Analysis

For a given incident energy, values of $\overline{|M|^2}$ measured at different locations in T-cosθ space often depended on quantities common to many or all of the measurements. Examples of such quantities are the electron efficiency of the Cerenkov detector ε_e and the normalization factor T′ determined from measurements of π^-p elastic scattering. To properly propagate their errors, an error matrix was calculated for all measurements of $\overline{|M|^2}$ at each incident energy.

TABLE XXIV. The doubly differential cross section at 203 MeV.

$\overline{T}$ (MeV)	$\overline{\cos\theta}$	$\overline{\lvert M\rvert^2}$ (m_π^{-6})	$\frac{d^2\sigma}{d\Omega dT}$ ($\mu b \cdot sr^{-1} \cdot MeV^{-1}$)	Statistical Error (%)	Total Error (%)
11.0	-0.106	18.22	0.0705	18.3	18.3
15.5	-0.148	21.61	0.0732	32.2	32.2
15.4	0.112	14.07	0.0479	28.2	28.2
6.5	0.193	20.83	0.0744	15.2	15.2
11.0	0.194	18.51	0.0716	18.3	18.3
6.4	0.493	16.68	0.0595	13.8	13.8
10.9	0.505	22.10	0.0855	11.0	11.0
15.3	0.474	21.36	0.0730	13.7	13.7
6.6	0.784	23.55	0.0845	15.0	15.0
10.9	0.822	22.33	0.0864	12.0	12.0
15.2	0.840	22.64	0.0778	13.8	14.0

TABLE XXV. The doubly differential cross section at 230 MeV.

$\overline{T}$ (MeV)	$\overline{\cos\theta}$	$\overline{\lvert M\rvert^2}$ (m_π^{-6})	$\frac{d^2\sigma}{d\Omega dT}$ ($\mu b \cdot sr^{-1} \cdot MeV^{-1}$)	Statistical Error (%)	Total Error (%)
24.5	-0.356	21.42	0.159	16.2	16.2
31.1	-0.357	16.08	0.096	27.1	27.1
17.4	-0.057	22.47	0.172	11.0	11.0
24.7	0.045	24.79	0.183	14.8	14.8
31.0	0.043	17.48	0.105	11.7	11.8
10.4	0.141	21.63	0.146	12.5	12.5
6.0	0.288	23.38	0.128	12.0	12.0
10.3	0.442	22.85	0.154	9.9	10.0
17.6	0.447	27.24	0.208	12.0	12.0
24.6	0.446	25.02	0.185	12.5	12.5
32.1	0.406	22.62	0.128	11..	11.1
3.3	0.665	22.54	0.096	16.8	16.8
10.5	0.748	23.84	0.162	10.9	11.1
17.5	0.819	27.43	0.210	8.3	8.3
24.6	0.849	27.42	0.203	7.2	7.2
30.5	0.849	25.41	0.158	9.9	9.9

TABLE XXVI. The doubly differential cross section at 254 MeV. The data were obtained from a previous $\pi^- p \to \pi^+ \pi^- n$ experiment.[a]

$\overline{T}$ (MeV)	$\overline{\cos\theta}$	$\overline{\lvert M \rvert^2}$ (m_π^{-6})	$\frac{d^2\sigma}{d\Omega dT}$ ($\mu b \cdot sr^{-1} \cdot MeV^{-1}$)	Statistical Error (%)	Total Error (%)
36.1	-0.751	23.92	0.263	32.7	32.8
46.2	-0.751	17.19	0.139	38.4	39.8
25.8	0.352	28.05	0.324	18.9	19.4
36.0	-0.352	28.84	0.317	13.4	13.7
44.6	-0.354	21.45	0.189	18.1	18.3
15.3	-0.198	23.80	0.245	29.5	29.5
24.2	-0.007	30.99	0.356	11.7	12.3
34.3	-0.005	32.62	0.366	9.7	10.1
43.9	-0.009	20.24	0.184	15.3	15.9
15.5	0.148	31.41	0.324	14.7	16.6
23.7	0.294	24.46	0.280	14.4	16.1
34.3	0.294	30.87	0.346	10.9	11.4
43.5	0.290	35.19	0.324	8.2	8.7
8.6	0.348	40.76	0.337	15.6	15.7
15.4	0.548	25.84	0.266	14.4	18.2
23.6	0.643	31.46	0.360	10.7	12.1
33.6	0.644	31.47	0.355	8.9	9.9
42.5	0.648	27.47	0.262	10.0	11.3

[a]Ref. 10.

TABLE XXVII. The doubly differential cross section at 256 MeV.

$\overline{T}$ (MeV)	$\overline{\cos\theta}$	$\overline{\lvert M\rvert^2}$ (m_π^{-6})	$\frac{d^2\sigma}{d\Omega dT}$ ($\mu b \cdot sr^{-1} \cdot MeV^{-1}$)	Statistical Error (%)	Total Error (%)
44.3	-0.753	18.36	0.172	17.9	17.9
30.6	-0.673	26.32	0.310	16.6	16.6
35.1	-0.356	27.43	0.313	12.2	12.2
44.0	-0.356	20.11	0.190	10.9	10.9
15.1	-0.257	24.84	0.258	20.5	20.5
25.1	-0.247	26.66	0.313	9.3	9.3
35.0	0.044	28.11	0.322	9.7	9.8
43.9	0.043	25.35	0.241	10.7	10.7
15.0	0.102	24.78	0.257	11.5	11.5
25.0	0.113	30.57	0.359	8.8	8.8
6.6	0.339	33.80	0.253	14.5	14.5
14.9	0.463	30.28	0.313	10.5	10.5
24.9	0.475	30.92	0.363	9.3	9.3
34.8	0.445	31.89	0.366	7.8	7.8
43.6	0.444	27.31	0.262	9.3	9.4
6.6	0.753	23.68	0.177	15.8	15.8
14.8	0.820	30.71	0.317	12.9	12.9
24.7	0.846	35.91	0.421	8.4	8.4
34.6	0.858	30.10	0.345	8.8	8.8
43.4	0.864	31.52	0.305	7.2	7.2

TABLE XXVIII. The doubly differential cross section at 280 MeV. The data were obtained from a previous $\pi^- p \to \pi^+ \pi^- n$ experiment.[a]

$\bar{T}$ (MeV)	$\overline{\cos\theta}$	$\overline{\lvert M \rvert^2}$ (m_π^{-6})	$\frac{d^2\sigma}{d\Omega dT}$ ($\mu b \cdot sr^{-1} \cdot MeV^{-1}$)	Statistical Error (%)	Total Error (%)
47.0	-0.850	21.36	0.322	27.5	27.8
60.3	-0.851	22.96	0.249	23.7	24.0
33.6	-0.790	29.81	0.473	28.1	28.1
34.4	-0.502	38.68	0.615	10.9	11.0
45.9	-0.528	38.40	0.585	10.2	10.3
57.7	-0.527	29.27	0.354	12.9	12.9
20.2	-0.451	24.60	0.348	33.0	33.0
15.8	-0.103	30.82	0.399	17.1	17.1
29.0	-0.097	34.18	0.532	11.2	11.3
42.7	-0.107	34.64	0.541	9.3	9.4
55.8	-0.108	36.35	0.467	8.8	8.8
15.7	0.248	32.06	0.414	14.0	15.0
29.1	0.290	44.05	0.686	9.2	9.4
42.2	0.299	42.03	0.658	7.7	7.7
55.4	0.296	37.34	0.485	7.9	8.0
6.7	0.348	21.85	0.197	29.3	29.5
15.7	0.548	28.71	0.371	16.7	17.9
29.0	0.648	35.93	0.559	8.0	8.6
41.9	0.648	42.40	0.666	6.5	6.7
52.7	0.688	37.25	0.515	7.0	7.2

[a]Ref. 10.

TABLE XXIX. The doubly differential cross section at 292 MeV. The data were obtained from a previous $\pi^- p \to \pi^+ \pi^- n$ experiment.[a]

$\overline{T}$ (MeV)	$\overline{\cos\theta}$	$\overline{\lvert M \rvert^2}$ (m_π^{-6})	$\frac{d^2\sigma}{d\Omega dT}$ ($\mu b \cdot sr^{-1} \cdot MeV^{-1}$)	Statistical Error (%)	Total Error (%)
40.5	-0.847	34.95	0.638	20.9	21.6
56.7	-0.848	36.24	0.594	14.0	20.0
68.0	-0.852	23.68	0.284	23.5	30.8
40.7	-0.543	44.34	0.809	10.6	11.0
57.0	-0.544	35.97	0.588	10.0	11.5
65.2	-0.557	30.97	0.417	10.8	12.1
24.5	-0.440	39.05	0.649	13.5	16.7
24.6	-0.138	37.38	0.622	11.6	23.2
40.9	-0.139	44.50	0.812	8.3	12.2
57.5	-0.146	29.85	0.484	10.1	13.3
67.5	-0.154	30.90	0.380	9.0	12.1
25.0	0.255	51.08	0.854	7.8	17.4
41.1	0.264	45.80	0.836	6.9	12.1
57.7	0.253	36.07	0.583	6.2	12.7
67.6	0.243	31.12	0.381	7.2	7.4
8.4	0.368	33.46	0.362	19.6	58.0
25.1	0.559	44.77	0.750	7.7	8.0
41.1	0.654	39.07	0.713	7.5	7.6
58.0	0.655	35.16	0.565	8.0	8.2
67.3	0.649	27.84	0.346	8.9	9.2

[a]Ref. 10.

TABLE XXX. The doubly differential cross section at 331 MeV. The data were obtained from a previous $\pi^- p \to \pi^+ \pi^- n$ experiment.[a]

$\overline{T}$ (MeV)	$\overline{\cos\theta}$	$\overline{\lvert M \rvert^2}$ (m_π^{-6})	$\frac{d^2\sigma}{d\Omega dT}$ ($\mu b \cdot sr^{-1} \cdot MeV^{-1}$)	Statistical Error (%)	Total Error (%)
48.7	-0.851	39.55	1.012	10.0	10.0
68.2	-0.851	37.93	0.926	12.5	12.5
87.4	-0.851	39.13	0.686	10.4	10.5
25.5	-0.496	39.82	0.857	10.6	10.6
45.6	-0.507	46.56	1.181	10.5	10.6
64.8	-0.501	41.89	1.045	9.2	9.2
84.4	-0.535	34.93	0.671	11.1	11.1
27.5	-0.122	57.15	1.263	8.5	8.5
46.7	-0.121	47.35	1.205	8.5	8.5
65.8	-0.120	51.24	1.272	6.9	7.0
83.1	-0.122	36.67	0.728	8.9	8.9
9.7	-0.054	43.39	0.616	10.7	10.8
27.2	0.244	59.74	1.315	6.7	6.7
46.6	0.270	57.62	1.467	5.8	5.8
65.3	0.276	49.67	1.236	5.3	5.3
82.7	0.276	36.12	0.724	6.8	6.8
9.7	0.346	63.71	0.905	8.2	8.2
25.7	0.553	59.67	1.287	7.0	7.1
45.0	0.647	53.10	1.345	5.1	5.2
64.3	0.650	47.06	1.177	6.3	6.3
82.8	0.653	35.27	0.706	5.8	5.9

[a]Ref. 10.

TABLE XXXI. The doubly differential cross section at 356 MeV. The data were obtained from a previous $\pi^- p \to \pi^+ \pi^- n$ experiment.[a]

$\overline{T}$ (MeV)	$\overline{\cos\theta}$	$\overline{\lvert M \rvert^2}$ (m_π^{-6})	$\frac{d^2\sigma}{d\Omega dT}$ ($\mu b \cdot sr^{-1} \cdot MeV^{-1}$)	Statistical Error (%)	Total Error (%)
56.0	-0.851	45.04	1.383	10.4	10.4
78.1	-0.851	45.18	1.329	9.1	9.1
100.1	-0.851	38.43	0.811	10.5	10.5
33.6	-0.552	46.50	1.256	10.5	10.5
55.8	-0.552	55.77	1.712	7.7	7.7
76.6	-0.533	46.05	1.367	6.9	6.9
97.7	-0.524	37.91	0.857	7.5	7.5
11.2	-0.153	51.25	0.868	13.4	13.4
32.4	-0.153	62.91	1.677	6.4	6.5
52.4	-0.143	58.41	1.778	6.1	6.2
74.3	-0.134	52.32	1.570	5.5	5.5
94.0	-0.110	41.33	1.012	6.2	6.3
11.2	0.246	76.03	1.287	9.5	9.5
31.9	0.251	70.92	1.881	6.0	6.0
52.6	0.234	59.70	1.818	4.8	4.9
73.0	0.270	56.67	1.711	4.1	4.2
93.7	0.291	39.98	0.985	5.4	5.4
29.5	0.588	88.40	2.279	4.3	4.4
51.0	0.635	67.66	2.050	4.5	4.5
72.3	0.656	54.95	1.663	4.3	4.4
93.3	0.668	39.59	0.982	4.9	4.9

[a]Ref. 10.

TABLE XXXII. The doubly differential cross section at 358 MeV.

$\bar{T}$ (MeV)	$\overline{\cos\theta}$	$\overline{\lvert M\rvert^2}$ (m_π^{-6})	$\frac{d^2\sigma}{d\Omega dT}$ ($\mu b \cdot sr^{-1} \cdot MeV^{-1}$)	Statistical Error (%)	Total Error (%)
55.6	-0.852	46.68	1.447	6.7	6.8
77.7	-0.852	46.96	1.405	7.4	7.4
99.2	-0.848	35.71	0.802	9.0	9.0
33.3	-0.555	48.46	1.315	7.1	7.1
55.4	-0.554	49.83	1.544	6.1	6.2
76.0	-0.534	48.24	1.457	4.9	4.9
97.0	-0.525	37.14	0.879	6.1	6.1
11.1	-0.160	56.26	0.954	8.8	8.8
32.1	-0.157	53.87	1.443	6.1	6.2
51.9	-0.146	56.75	1.742	4.8	4.8
73.7	-0.136	49.62	1.514	4.1	4.2
94.3	-0.129	45.72	1.142	5.1	5.1
11.0	0.239	79.22	1.339	6.4	6.4
31.6	0.248	76.62	2.040	4.5	4.5
51.2	0.251	60.98	1.867	3.8	3.9
72.3	0.268	53.86	1.652	3.4	3.4
92.7	0.289	42.10	1.080	4.7	4.7
29.2	0.585	84.54	2.185	3.3	3.4
50.4	0.633	64.83	1.979	3.1	3.1
71.6	0.655	52.43	1.612	3.4	3.4
92.3	0.666	38.24	0.988	4.6	4.6

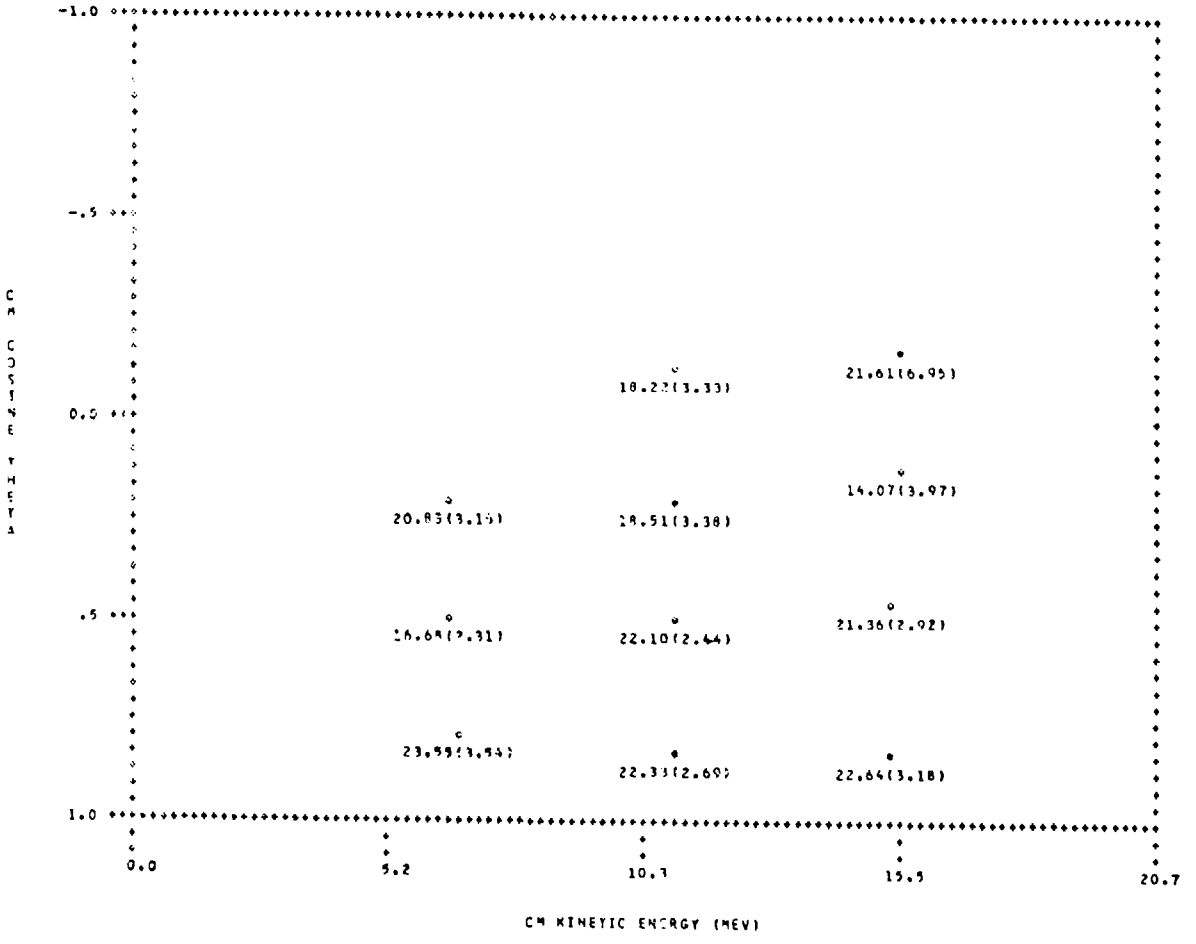

Figure 45. Values of $\overline{|M|^2}$ at 203 MeV.

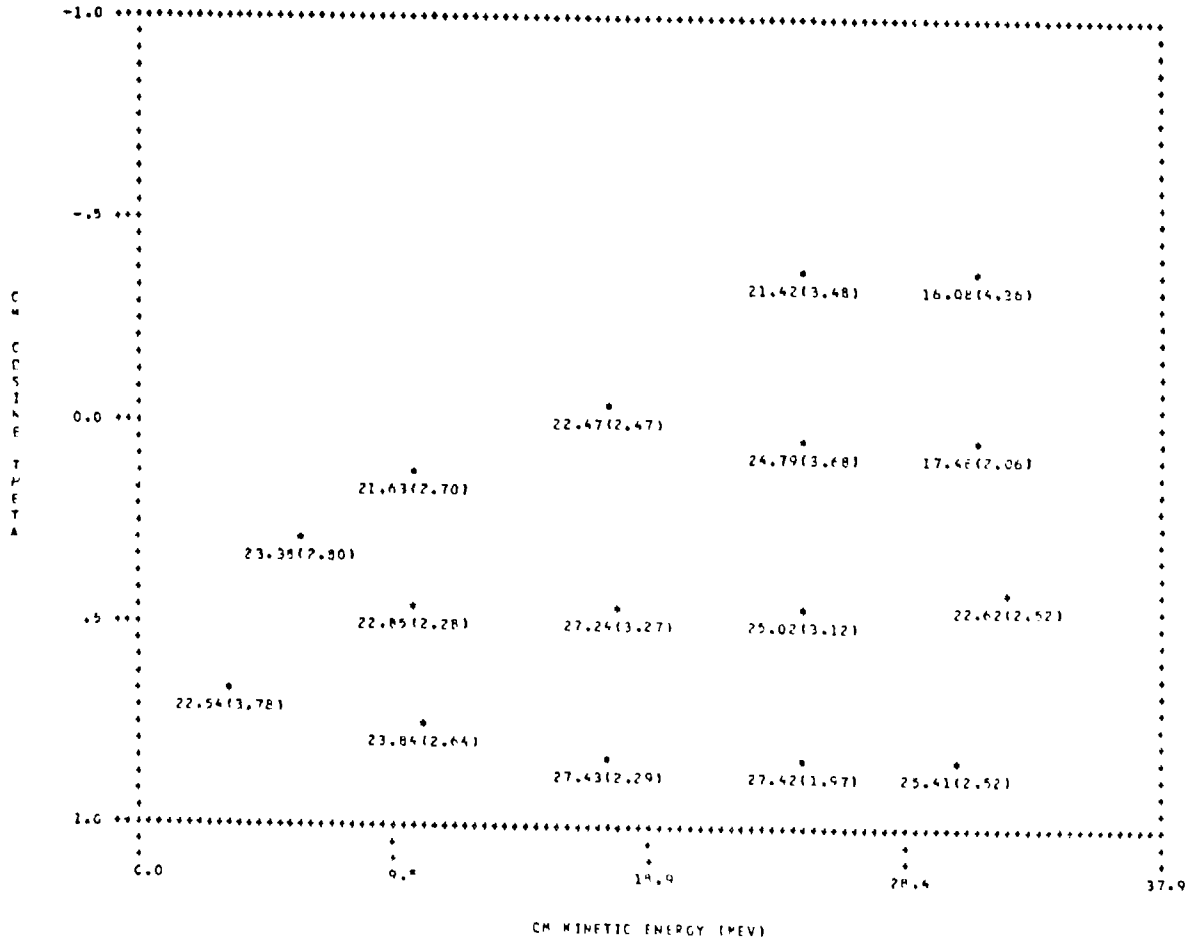

Figure 46. Values of $\overline{|M|^2}$ at 230 MeV.

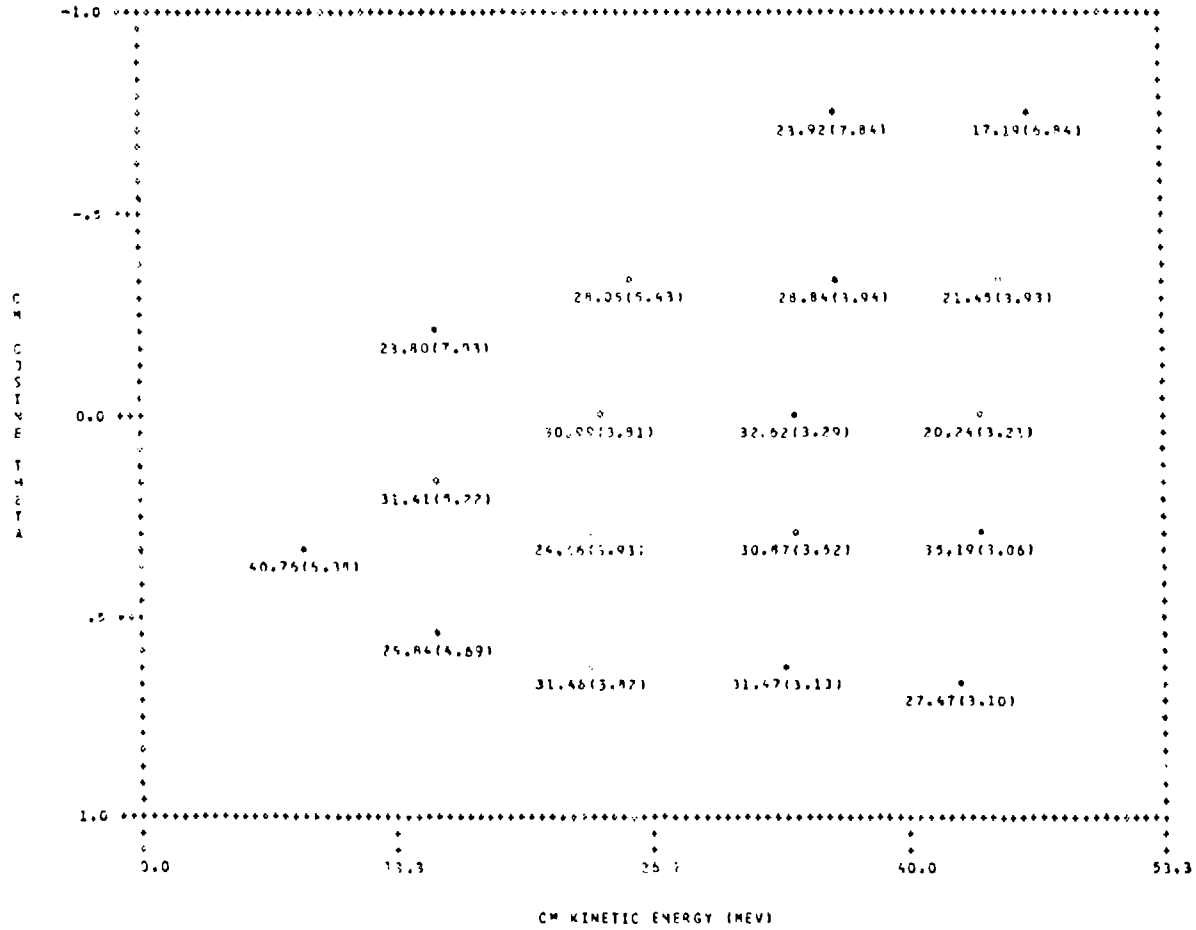

Figure 47. Values of $\overline{|M|^2}$ at 254 MeV. The data were obtained from a previous $\pi^- p \to \pi^+ \pi^- n$ experiment.[10]

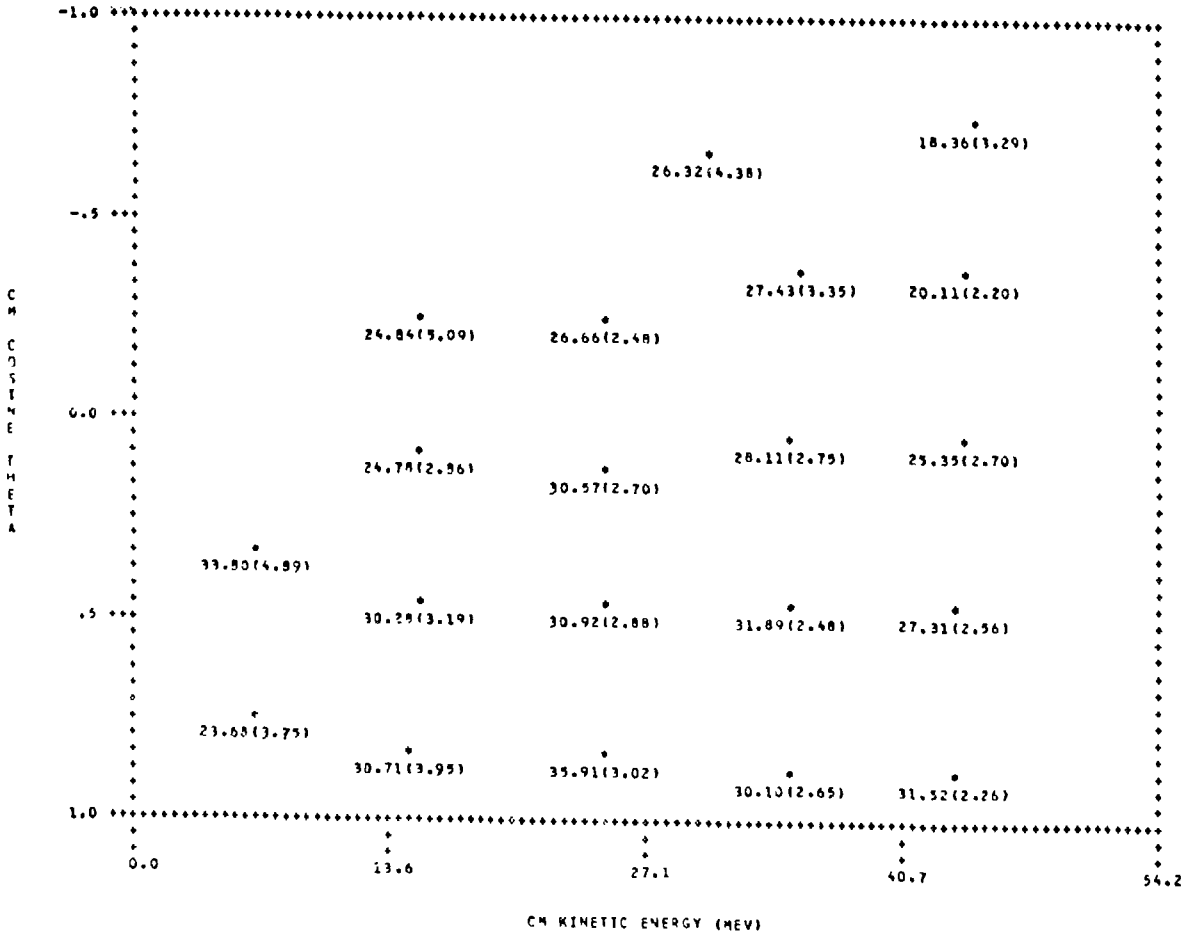

Figure 48. Values of $\overline{|M|^2}$ at 256 MeV.

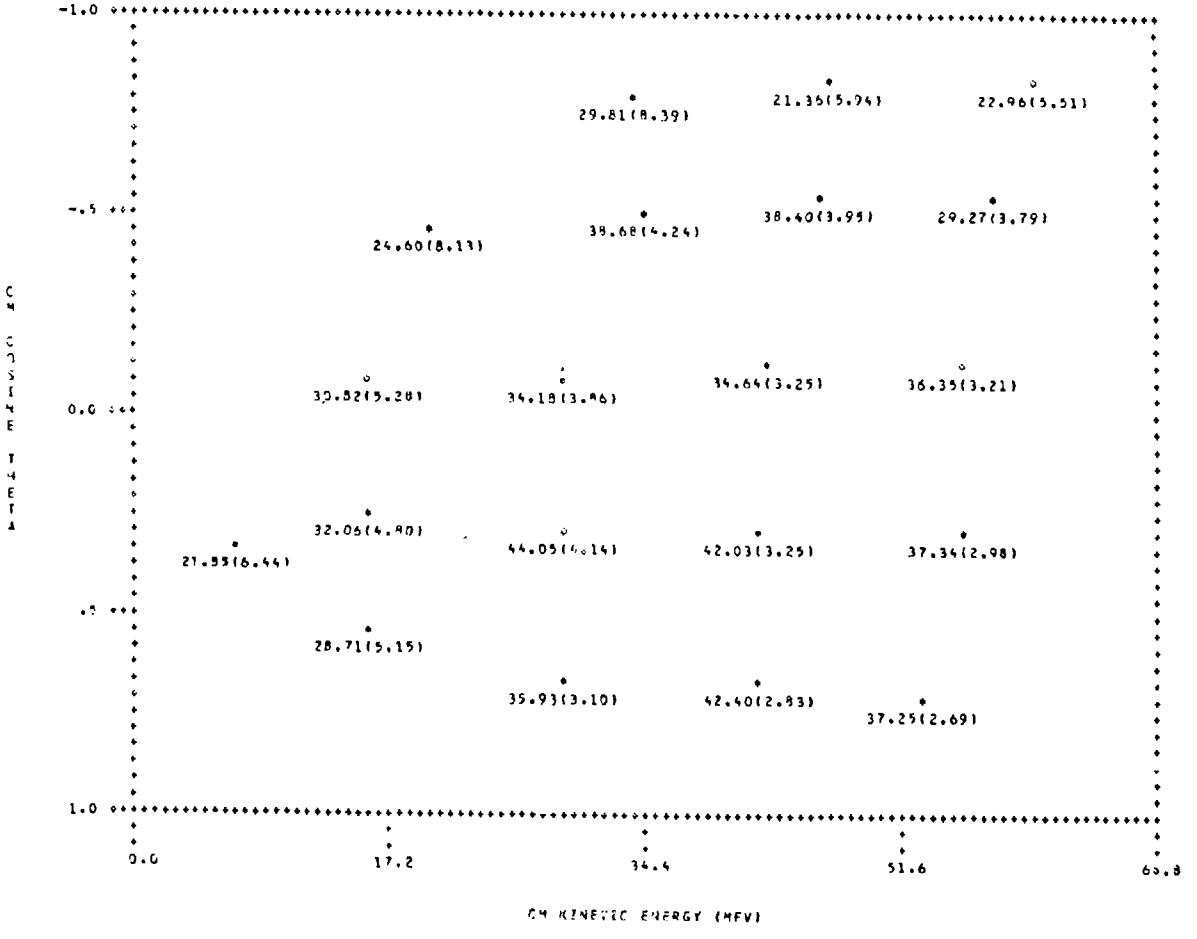

Figure 49. Values of $\overline{|M|^2}$ at 280 MeV. The data were obtained from a previous $\pi^- p \to \pi^+ \pi^- n$ experiment.[10]

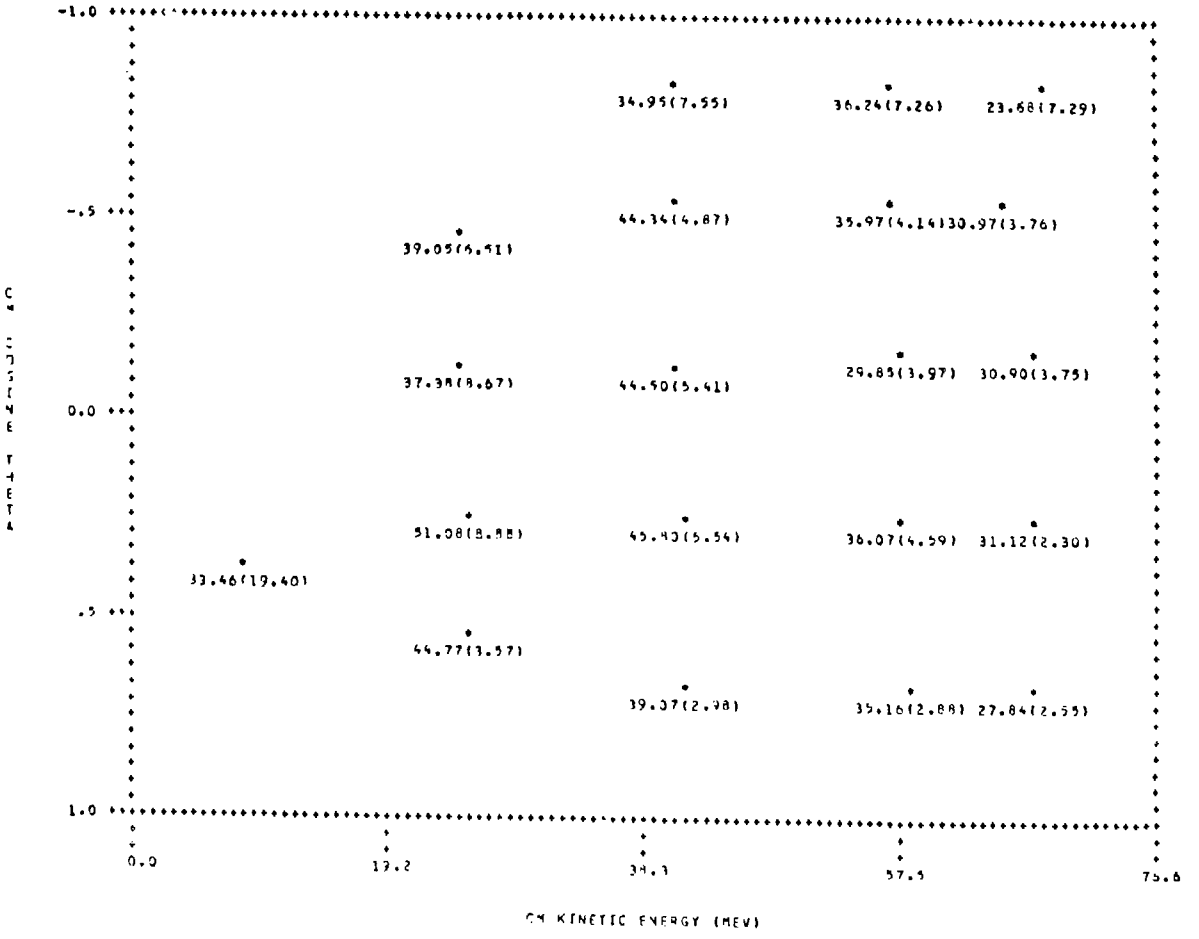

Figure 50. Values of $\overline{|M|^2}$ at 292 MeV. The data were obtained from a previous $\pi^- p \to \pi^+ \pi^- n$ experiment.[10]

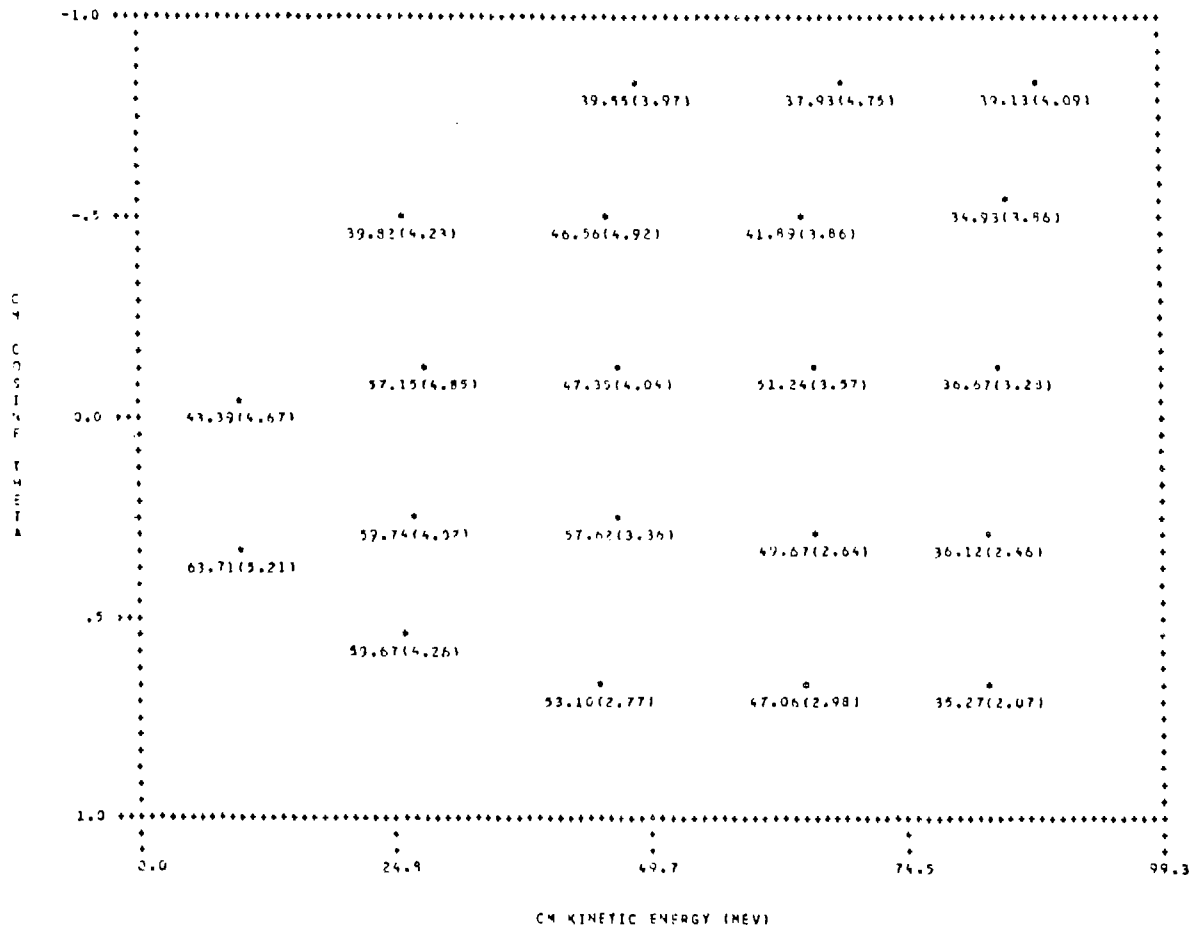

Figure 51. Values of $\overline{|M|^2}$ at 331 MeV. The data were obtained from a previous $\pi^- p \to \pi^+ \pi^- n$ experiment.[10]

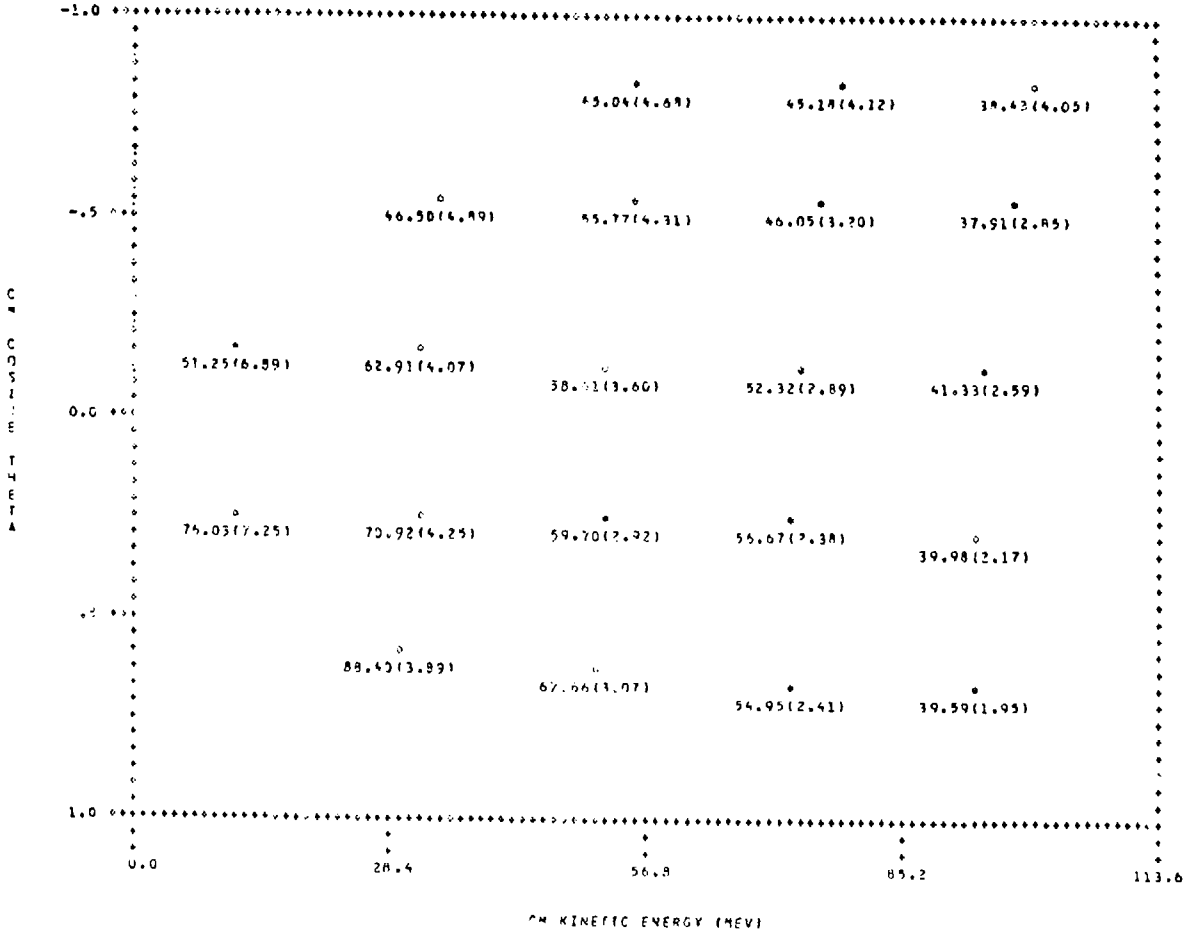

Figure 52. Values of $\overline{|M|^2}$ at 356 MeV. The data were obtained from a previous $\pi^- p \to \pi^+ \pi^- n$ experiment.[10]

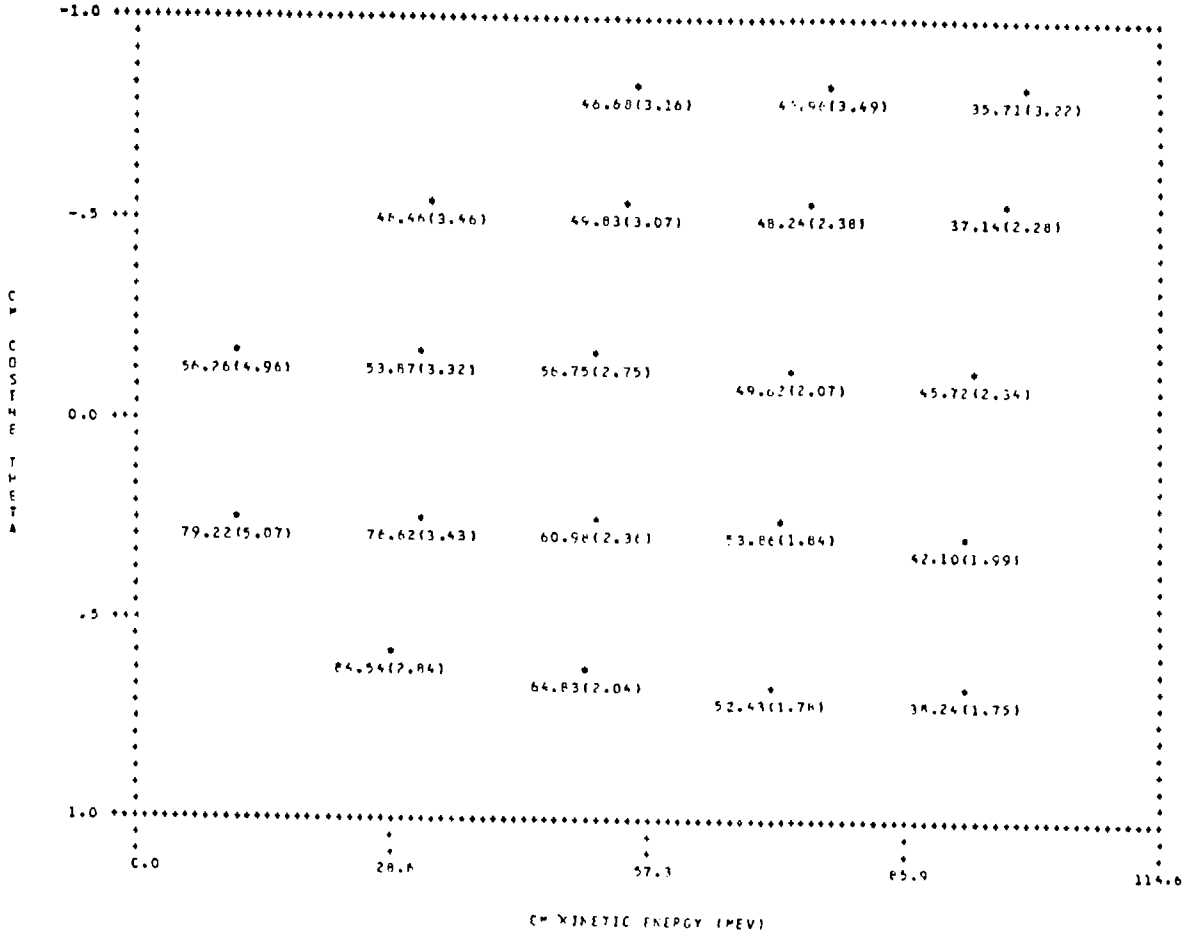

Figure 53. Values of $\overline{|M|^2}$ at 358 MeV.

For the ith measurement of $\overline{|M|^2}$ in T-cosθ space, we introduce the simpler notation: $\overline{\zeta_i} = \overline{|M|^2}$. Thus, we can write

$$E_{ij} = \overline{(\zeta_i - \overline{\zeta_i})(\zeta_j - \overline{\zeta_j})} \ ,$$

where

$$\zeta_i = \zeta_i(A) \simeq \zeta_i(\overline{A}) + \sum_k \left(\frac{\partial \zeta_i}{\partial A_k}\right)_{\overline{A}} (A_k - \overline{A_k}) \ .$$

Here, A_k represents the set of quantities e_0, p_0, T', $(N_c)_{full}$, $(N_c)_{empty}$, $(N_{\bar{c}})_{full}$, and $(N_{\bar{c}})_{empty}$, with e_0 and p_0 the parameters introduced in Chapter III to describe the electron efficiency of the Cerenkov detector. When the subscript on A is neglected, we refer to the entire set. The contributions from errors in the channel efficiencies ε_I were contained in the error assigned to T'. To calculate E_{ij}, we approximated the mean values with our best estimates:

$$\overline{\zeta_i} \simeq \zeta_i(\overline{A}) \ ,$$

$$\overline{A_k^2} \simeq \overline{A_k}^2 + \Delta A_k^2 \ ,$$

with ΔA_k the error associated with A_k. The only terms that could contribute to off-diagonal elements were e_0, p_0, and T'. The derivatives with respect to these quantities were calculated as

$$\frac{\partial \zeta_i}{\partial e_0} = \frac{\zeta_i}{e_0} \frac{\varepsilon_e}{\varepsilon_e - \varepsilon_\pi} \frac{R_e}{R_\pi} \ ,$$

$$\frac{\partial \zeta_i}{\partial p_0} = - \frac{\zeta_i}{p_c} \frac{e_0}{\varepsilon_e - \varepsilon_\pi} \frac{R_e}{R_\pi} ,$$

$$\frac{\partial \zeta_i}{\partial \pi'} = \frac{\zeta_i}{\pi'} .$$

For all of the new measurements and most of the previous ones,[10] contributions to $\Delta\overline{|M|^2}$ from the uncertainties in these quantities were very small. However, for most of the previous 292 MeV measurements gathered at backward angles, the uncertainty in the electron efficiency of the Cerenkov detector was 40%.[10] This uncertainty made a sizable contribution to $\Delta\overline{|M|^2}$ for those measurements and their errors were highly correlated with correlation coefficients among different measurements that ranged from 0.07 to 0.84. In Chapters VI and VII, we discuss parametrizations of the $\overline{|M|^2}$ in terms of the measured kinematic variables. At each incident energy, we defined χ^2 to incorporate the error matrix for the $\overline{|M|^2}$ so that our fitting procedure properly accounted for correlated errors in the measurements.

CHAPTER VI

EMPIRICAL ANALYSIS

At each incident energy, we wished to calculate the integrated reaction cross section σ_R and compare it with older measurements. We also wished to calculate $\langle|M_c|^2\rangle$, the square modulus of the matrix element corrected for Coulomb attraction in the initial and final states, divided by the square of the incident c.m. momentum, and averaged over all phase space. Calculations of both σ_R and $\langle|M_c|^2\rangle$ involved extrapolations and integrations that we wished to perform in an empirical manner. Thus, at each incident energy, we fitted our measured $\overline{|M|^2}$ to a plausible function of the measured kinematic variables. Estimates of $\langle|M_c|^2\rangle$ obtained at each incident energy were fitted to a function of the total c.m. energy and extrapolated to threshold. The threshold value of $\langle|M_c|^2\rangle$ was compared with the prediction of soft-pion calculations[2,4] to determine the chiral-symmetry-breaking parameter ξ. With the ξ obtained, the soft-pion calculations for the S-wave isoscalar and isotensor $\pi\pi$ scattering lengths were evaluated.

The Integrated Reaction Cross Section

At each incident energy, the measurements of $\overline{|M|^2}$ were fitted to a function $C_i\overline{C_f}\,F$, with

$$F = P_1 + P_2 q\cos\theta + P_3(q\cos\theta)^2 + P_4 q^2 + \frac{P_5 q\cos\theta}{P_6 + q^4} ,$$

$$C_i = \frac{2\pi n_i}{\exp(2\pi n_i) - 1} ,$$

$$\overline{C_f} = \left\langle \frac{2\pi n_f}{\exp(2\pi n_f) - 1} \right\rangle .$$

The first four terms of F represent an expansion in the measured c.m. variables q^2 and $q\cos\theta$, where q is the ratio of the π^+ momentum to the maximum momentum allowed by kinematics. The last term in F was contrived to describe a sizable angular variation in $\overline{|M|^2}$ observed for small q at 331 MeV and 357 MeV. The Coulomb barrier-penetration factors C_i and $\overline{C_f}$ corrected the measurements for enhancement caused by the initial- and final-state charged particles, respectively. Both factors were calculated in an S-wave approximation with $\eta = -\alpha/\beta$, where α is the fine-structure constant and β is the velocity of one charged particle in the rest frame of the other. $\overline{C_f}$ was calculated by a Monte Carlo program and represents an average over the unmeasured variables. The factor $\overline{C_f}$ varies slowly with the π^+ kinetic energy. It ranges between 1.04 and 1.06 at 203 MeV and between 1.026 and 1.031 at 358 MeV. The procedure of using an average correction factor was checked by comparing values of the quantities $\overline{\zeta}/\overline{C_f}$ and $\overline{\zeta/C_f}$. Here, $\overline{\zeta}$ represents a value of $\overline{|M|^2}$ computed from the isobar model discussed in Chapter VII and $\overline{\zeta/C_f}$ represents a value of $\overline{|M|^2}$ calculated in the same manner with a correction for final-state Coulomb attraction made before averaging over unobserved variables. We found that $\overline{\zeta}/\overline{C_f}$ was

consistently less than $\overline{\zeta/C_f}$ over the measured range of incident energies with the percent difference in the two quantities greatest for those measurements at backward angles. For most measurements at 203 MeV, the quantities differed by about 0.5% whereas for most measurements at 358 MeV, they differed by about 0.3%. Since the percent difference in the two quantities was always less than 1%, our procedure was suitably justified.

The $\overline{|M|^2}$ were fitted to the empirical function by minimizing

$$\chi^2 = \sum_{m,n} (\overline{|M|^2} - C_i\overline{C_f}\ F)_m\ E^{-1}{}_{mn}\ (\overline{|M|^2} - C_i\overline{C_f}\ F)_n\ ,$$

where E^{-1} is the inverse of the error matrix discussed in Chapter V and the summation includes all measurements of $\overline{|M|^2}$ at a given incident energy. We varied the smallest number of parameters P_i in F necessary for a satisfactory χ^2/ν and set the parameters not varied equal to zero. A summary of the fitted parameters and χ^2/ν is presented in Table XXXIII. Except at the highest three incident energies, only two parameters were needed to satisfactorily describe the measurements. The fact that one of those parameters describes an angular variation is evidence for production of pions in the P state very near the 172 MeV threshold. Since the measurements at 331 and 357 MeV were within the half width for production of the Δ isobar, a need for additional parameters at the higher energies could well be expected. Indeed, an isobar-model analysis discussed in Chapter VII required partial waves for Δ production to describe the angular variation observed for small q at 331 and 357 MeV.

TABLE XXXIII. Parameters and χ^2/ν obtained in fitting $\overline{|M|^2}$.

T_π (MeV)	P_1 (m_π^{-6})	P_2 (m_π^{-6})	P_3 (m_π^{-6})	P_4 (m_π^{-6})	P_5 (m_π^{-6})	P_6	χ^2/ν
203	16.5 ± 1.5	6.9 ± 3.9	•••	•••	•••	•••	0.57
230	19.9 ± 0.9	7.9 ± 2.2	•••	•••	•••	•••	0.63
254	26.7 ± 1.3	6.6 ± 2.9	•••	•••	•••	•••	1.54
256	25.0 ± 0.8	8.3 ± 1.7	•••	•••	•••	•••	0.95
280	33.6 ± 1.0	8.1 ± 2.2	•••	•••	•••	•••	1.52
292	50.5 ± 3.2	0.2 ± 2.1	•••	-24.5 ± 4.0	•••	•••	1.42
331	55.2 ± 2.0	-10.8 ± 5.8	- 8.6 ± 5.3	-21.0 ± 3.7	5.9 ± 3.5	0.071 ± 0.066	1.78
356	71.1 ± 2.0	- 8.5 ± 3.4	- 5.1 ± 4.8	-39.4 ± 3.6	5.0 ± 1.4	0.019 ± 0.014	1.01
358	68.8 ± 1.5	- 9.2 ± 2.5	-11.1 ± 4.0	-35.3 ± 2.9	4.5 ± 0.8	0.015 ± 0.008	0.97

The integrated reaction cross section was calculated at each incident energy as

$$\sigma_R = 2\pi \int_0^{T_{max}} \int_{-1}^{1} C_i \overline{C_f} \, F \, \frac{d^2\sigma_o}{d\Omega dT} \, d\cos\theta \, dT \, ,$$

where integration over cosθ was calculated analytically and integration over T was calculated numerically. Table XXXIV summarizes the σ_R and its total uncertainty at each incident energy as determined by this analysis. The total uncertainty in σ_R included a systematic uncertainty that was combined in quadrature with the error provided by the fitting algorithm. We assumed systematic uncertainties of 3% for measurements at 230, 255, and 280 MeV and 4% for measurements at 331

TABLE XXXIV. Integrated reaction cross section for $\pi^- p \to \pi^+ \pi^- n$. Systematic uncertainties are included in the errors.

T_π (MeV)	σ_R (μb)	Error (μb)
203	14.1	1.5
230	60.8	3.2
255	168.7	6.4
280	384	16
292	568	36
331	1168	52
357	1888	78

and 357 MeV to account for the uncertainty in the normalization to π^-p elastic scattering. We assumed a systematic uncertainty of 6% for the measurement at 203 MeV to account for the added difficulty of separating pion and electron events. A total contribution of 5% was assumed for the measurement at 292 MeV because of the difficulty the empirical function had fitting measurements of $\overline{|M|^2}$ near T_{max}. Fig. 54 shows the σ_R and the results of older measurements[33-40] with errors less than 40%. The curve in the figure was generated to guide the eye by fitting values of σ_R to the function

$$G = 2\pi(P_1 + P_2\, T_{total})\int_0^{T_{max}} \int_{-1}^{1} \frac{d^2\sigma_o}{d\Omega dT}\, d\cos\theta\, dT \ ,$$

where

$$T_{total} = W - (2m_\pi + m_n) \ ,$$

with W the total c.m. energy.

Our 203 MeV cross section is the closest existing measurement to $\pi^-p \to \pi^+\pi^-n$ threshold and is determined with twice the accuracy of the previous closest measurement.[33] The only prior measurements for this reaction below 290 MeV were from the early emulsion experiments of Batusov et al.[33,34] For most of these low-energy measurements, our cross sections were about five times more accurate and about a factor of 1.3-1.5 times larger. The earliest counter experiment[36] measured the reaction cross section with about 20% accuracy at 317 and 371 MeV and both measurements were about 20% lower than the values predicted by the curve in Fig. 54, which was fitted to our data. Above about 300 MeV, our cross sections were in excellent agreement with previous

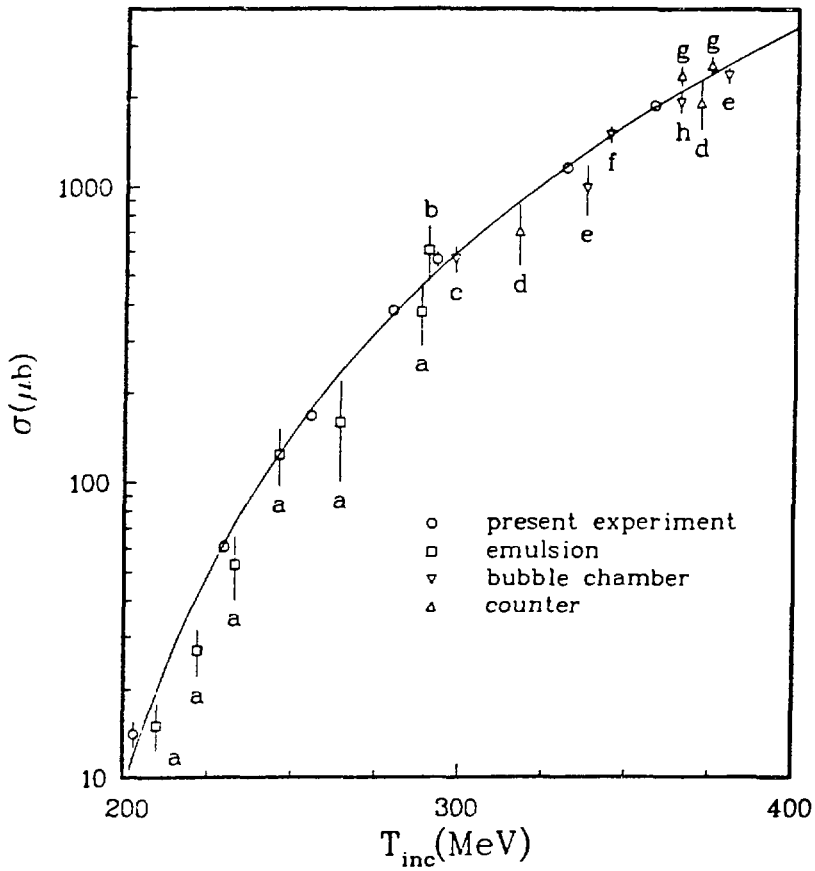

Figure 54. Integrated reaction cross section for $\pi^-p \to \pi^+\pi^-n$. The present measurements are shown together with a selection of previous measurements: (a) Ref. 33, (b) Ref. 34, (c) Ref. 35, (d) Ref. 36, (e) Ref. 37, (f) Ref. 38, (g) Ref. 39, and (d) Ref. 40.

measurements[35,37-40] and were roughly twice as accurate as the best of those measurements.

Comparison with Soft-Pion Theory

The square modulus of the matrix element corrected for Coulomb attraction in the initial and final states, divided by the square of the incident c.m. momentum, and averaged over all phase space, was calculated at each incident energy as

$$\langle |M_c|^2 \rangle = \frac{\int_0^{T_{max}} \int_{-1}^{1} F \frac{d^2\sigma_o}{d\Omega dT} d\cos\theta \, dT}{\int_0^{T_{max}} \int_{-1}^{1} \frac{d^2\sigma_o}{d\Omega dT} d\cos\theta \, dT} .$$

In Table XXXV, we present values of $\langle |M_c|^2 \rangle$ with total uncertainties at each incident energy that were calculated as those for the σ_R. To extrapolate the measured $\langle |M_c|^2 \rangle$ to threshold, they were fitted with $\chi^2/\nu = 1.41$ to the function

$$H = P_1 + P_2 \, T_{total} .$$

It was unnecessary to include higher-order powers of T_{total} to obtain a satisfactory χ^2/ν. Fig. 55 shows the $\langle |M_c|^2 \rangle$ with their total uncertainties and the fitted curve. From our extrapolation, we obtained the threshold value

$$\langle |M_c|^2 \rangle^{1/2} = 2.427 \pm 0.277 \, m_\pi^{-3}.$$

TABLE XXXV. Values of $\langle|M_c|^2\rangle$ for $\pi^-p\to\pi^+\pi^-n$. Systematic uncertainties are included in the errors.

T_π (MeV)	$\langle\|M_c\|^2\rangle$ (m_π^{-6})	Error (m_π^{-6})
203	16.5	1.8
230	19.9	1.1
255	25.4	1.0
280	33.6	1.4
292	39.0	2.5
331	44.2	2.0
357	51.4	2.1

In a two-component spinor notation, the threshold matrix element calculated by soft-pion theory is[4]

$$T_{thresh} = 2\sqrt{2}\, i \left(\frac{G}{2m_N}\right)^3 \left(\frac{g_V}{g_A}\right)^2 \left[\frac{m_N}{2(E_N + m_N)}\right]^{1/2} \chi_f^\dagger\, \vec{Q}\cdot\vec{\sigma}\, \chi_i$$

$$\times \left[\frac{\xi m_\pi - 2E_\pi}{E_\pi - m_\pi} - \frac{2m_\pi}{m_N} + 2 + \frac{2m_\pi}{2m_N + m_\pi} - \frac{2m_\pi}{2E_N - m_\pi}\right] ,$$

with $\vec{Q}$, as before, the incident (pion) momentum in the c.m. system, m_N the nucleon mass, $E_N = (Q^2 + m_N^2)^{1/2}$, and $E_\pi = (Q^2 + m_\pi^2)^{1/2}$. Here, $G = 13.4 \pm 0.1$ is the renormalized πN coupling constant[41] and $g_A/g_V = -1.254 \pm 0.007$ is the ratio of the renormalized axial-vector and vector coupling constants of the nucleon.[42] These values correspond to $f_\pi = 87.8$ MeV via the Goldberger-Treiman relation[43] for the

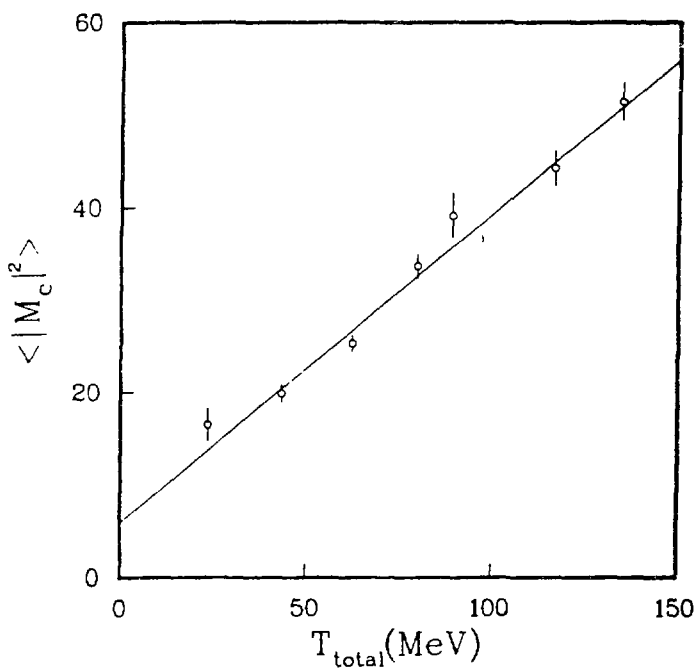

Figure 55. Measured values of $<|M_c|^2>$. The fitted curve indicates the extrapolation to threshold.

pion decay constant, which is discussed in Appendix B. The quantity ξ is the chiral-symmetry-breaking parameter introduced by Olsson and Turner,[2,4] χ_i and χ_f are nucleon spinors for the initial and final states, respectively, and $\vec{\sigma}$ is the usual Pauli spin matrix. T_{thresh} was calculated from a phenomenological πN Lagrangian that had been derived to be consistent with current algebra and PCAC, the partial conservation of the axial-vector current. The calculation of T_{thresh} included only contributions from "tree" diagrams that contained no more than two pion-nucleon vertices.

In terms of the mean square modulus of the T-matrix amplitude, we can write

$$\langle |M_c|^2 \rangle = \frac{\langle |T|^2 \rangle}{Q^2} .$$

Hence, at threshold

$$\pm \langle |M_c|^2 \rangle^{1/2} = -2.395 + 1.058\xi \, m_\pi^{-3}.$$

To determine ξ, this result was compared with the $\langle |M_c|^2 \rangle^{1/2}$ obtained by our extrapolation procedure. By choosing the negative root to determine the chiral-symmetry-breaking parameter, we obtained

$$\xi = -0.03 \pm 0.26 .$$

Comparisons of the sparse low-energy measurements available for the reactions $\pi^- p \to \pi^0 \pi^0 n$ and $\pi^+ p \to \pi^+ \pi^+ n$ with threshold predictions of

soft-pion calculations support this choice. The value of ξ determined by this analysis is consistent with $\xi = 0$ required for the Weinberg Lagrangian.[3] It is inconsistent with either $\xi = 1$ or $\xi = -2$ required for the two Schwinger Lagrangians.[12] If we had chosen the positive root rather than the negative, we would have obtained $\xi = 4.56 \pm 0.26$. Soft-pion calculations with this ξ predict a negative S-wave isoscalar $\pi\pi$ scattering length which, as discussed below, disagrees with the result of a measurement of K_{e4} decay.[44]

The S-wave isoscalar and isotensor $\pi\pi$ scattering lengths predicted by soft-pion theory are[2,4]

$$a_0 = \left(\frac{14 - 5\xi}{8}\right) L$$

and

$$a_2 = -\left(\frac{\xi + 2}{4}\right) L ,$$

where

$$L = \frac{m_\pi}{2\pi} \left(\frac{G}{2m_N}\right)^2 \left(\frac{g_V}{g_A}\right)^2 .$$

With the ξ found in this analysis, we obtain

$$a_0 = 0.178 \pm 0.016\ m_\pi^{-1} ,$$

$$a_2 = -0.049 \pm 0.007\ m_\pi^{-1} .$$

Although this a_0 has the same sign, it is somewhat smaller than the $a_0 = 0.28 \pm 0.05\ m_\pi^{-1}$ obtained from an analysis of K_{e4} decay.[44] If we

had chosen the positive root to determine ξ, we would have obtained $a_0 = -0.110 \pm 0.016\ m_\pi^{-1}$ and $a_2 = -0.165 \pm 0.007\ m_\pi^{-1}$, which clearly disagrees with the result of the K_{e4} analysis.

In all models of $\pi N \to \pi\pi N$ in which the reaction near threshold is dominated by the tree diagram involving $\pi\pi$ scattering, an expansion of the threshold matrix element in powers of m_π/m_N should be dominated by the $\pi\pi$ scattering lengths. For example, our expression above for $\langle|M_c|^2\rangle^{1/2}$ at threshold can be rewritten as

$$\pm\langle|M_c|^2\rangle^{1/2} = -7.021\ (2a_0 + a_2) - 0.279\ m_\pi^{-3},$$

where the leading term is of order unity and has the combination of $\pi\pi$ scattering lengths specified by isospin Clebsch-Gordan coefficients for $\pi^-\pi^+ \to \pi^-\pi^+$. The second term on the righthand side is of order m_π/m_N and represents the contribution from diagrams that do not involve $\pi\pi$ scattering. At threshold, the leading term should be approximately model independent although, above threshold, the leading term of such an expansion may vary according to how different models describe the $\pi\pi$ interaction. We expect a_2 to be smaller than a_0 since, experimentally, the $I = 3/2$ $\pi N \to \pi\pi N$ cross section is known to be much smaller near threshold than the $I = 1/2$ cross section, with I the total isospin. Hence, we expect

$$\pm\langle|M_c|^2\rangle^{1/2} \approx -14.04\ a_0\ m_\pi^{-3},$$

so that the a_0 determined by our experiment should be approximately independent of specific models.

CHAPTER VII

ISOBAR-MODEL ANALYSIS

Introduction

The phenomenological isobar model assumes that the reaction $\pi N \to \pi\pi N$ can proceed through several two-body intermediate channels consisting of a particle and an isobar.[13,14,45] This model is a useful method of analysis for three-body final states in which pair interactions are dominated by a few partial waves. Recent analyses[13,14] of $\pi N \to \pi\pi N$ bubble-chamber events have shown that the isobar model provides a very good description of single pion production in an energy range that overlaps our data.

The five $\pi N \to \pi\pi N$ charge reactions amenable to measurement and, therefore, to an isobar-model analysis are presented in Table XXXVI. It has been shown[13] that, with the present level of precision, each of

TABLE XXXVI. $\pi N \to \pi\pi N$ charge reactions.

$\pi^- p \to \pi^o \pi^o n$
$\pi^- p \to \pi^+ \pi^- n$
$\pi^- p \to \pi^o \pi^- p$
$\pi^+ p \to \pi^o \pi^+ p$
$\pi^+ p \to \pi^+ \pi^+ n$

the reactions is well described below 600 MeV by considering production of only the ε, ρ, and Δ isobars in the intermediate state. Properties of these isobars and others are summarized in Table XXXVII. Below 600 MeV, the isobar-model amplitude for production of all isobars in the reaction $\pi N \to 1+2+3$ is given by

$$T_{IM} = T_{\varepsilon} + T_{\rho} + T_{\Delta_1} + T_{\Delta_2} ,$$

with particles 1 and 2 the final-state pions and particle 3 the final-state nucleon. In this expression, T_{Δ_i} describes production of the Δ isobar and particle i in the intermediate state. The variable parameters of the isobar model are the partial-wave amplitudes, which are denoted by the quantum numbers $[\ell_i,\ell_f,2I,2J]$. Here, ℓ_i is the initial orbital angular momentum, ℓ_f is the final orbital angular

TABLE XXXVII. Intermediate isobars produced in $\pi N \to \pi\pi N$.[a]

Isobar	Mass (MeV)	Full Width (MeV)	ℓ	I	J^P	Principal Decay Products
ε	~1300	200-400	0	0	0^+	$\pi\pi$
ρ	776	158	1	1	1^-	$\pi\pi$
Δ	1232	115	1	3/2	$3/2^+$	πN
N	1470	200	1	1/2	$1/2^+$	πN
N	1520	125	2	1/2	$3/2^-$	πN

[a]Ref. 42.

momentum between the isobar and the spectator particle, I is the total isospin, and J is the total angular momentum. At a given incident energy, each partial-wave amplitude is assumed to be a complex constant.[46] Two notable isobar-model analyses of single pion production have been recently completed that partially overlap the energy range of our data.

In 1975, a collaboration of the Lawrence Berkeley Laboratory (LBL) and the Stanford Linear Accelerator Center (SLAC) completed a comprehensive partial-wave analysis of $\pi N \to \pi\pi N$ reactions.[13] Their study involved 163 000 bubble-chamber events for incident kinetic energies between 295 and 1500 MeV. In the energy range of our measurements, their solutions involved 11 partial waves. Too few bubble-chamber events were available for their fitting program to establish unique solutions below 396 MeV. Hence, unique solutions obtained at higher energies were propagated as starting guesses for the amplitudes at lower energies. Because of the large number of free parameters involved, we were unable to independently estimate their partial-wave amplitudes from our spectrometer measurements. We were, however, able to renormalize their amplitudes to our measurements and to vary the larger amplitudes until the resulting solutions agreed with our doubly differential cross sections.

In 1979, Arndt et al.[14] analyzed 4140 bubble-chamber events between 338 and 388 MeV with an isobar model that included a background term determined from soft-pion theory. At threshold, soft-pion theory is thought to determine the T matrix exactly with ξ the only free parameter. In the absence of narrow resonances near threshold, one might hope the T-matrix amplitude T_{CA} determined from soft-pion

theory to agree fairly well with experiment for energies slightly above threshold. T_{CA} is calculable from a phenomenological πN Lagrangian based upon PCAC and current algebra. A discussion of T_{CA} can be found in Appendix B. It is known from experiment that measurements of $\pi^-p\to\pi^+\pi^-n$ in the energy range 300 MeV < T_π < 470 MeV are within the half-width for Δ production. Furthermore, production of the ϵ isobar is expected to be important at low energies for both $\pi^-p\to\pi^+\pi^-n$ and $\pi^-p\to\pi^0\pi^0n$. Consequently, T_{CA} is inadequate for describing measurements in the energy range of this experiment. In their analysis, a collaboration of Virginia Polytechnic Institute and State University (VPI&SU), University of Texas, Northeastern University, and Brookhaven National Laboratory described low-energy $\pi^-p\to\pi^+\pi^-n$ measurements by treating T_{CA} as a background term, with the total T-matrix amplitude given by[14]

$$T = T_{IM} + T_{CA} .$$

We refer to their version of the isobar model as the VPI model. This model has certain advantages near threshold over the more conventional model since fewer partial waves need to be considered and the background term provides a means to establish the overall relative phase of the partial-wave amplitudes.

Only six partial waves were considered by Arndt et al.[14] and the term T_ρ for explicitly describing ρ production was neglected. Since the $I = J = 1$ $\pi\pi$ phase shift is almost negligible at 358 MeV,[47] production of the ρ isobar is expected to be small over the energy range of this experiment. This conclusion is supported by the

LBL-SLAC analysis,[13] which found that ρ production contributes only about 10% of the integrated reaction cross section at 338 MeV.

We borrowed the computer programs of Arndt et al. for generating T_{IM} and T_{CA} and employed them to analyze our doubly differential cross sections. Our procedure generally followed that of Arndt et al. We attempted to find solutions at our highest energies by starting with partial-wave amplitudes graphically interpolated from their solutions. Their solutions had been normalized to the previous $\pi^-p\to\pi^+\pi^-n$ spectrometer measurements[10] although no corrections for Coulomb interactions in the initial or final state had been considered.

Formalism

The isobar-model amplitude for production of pions through all isobars can be written as a coherent sum over all isobars and all partial waves[47]:

$$T_{IM} = \sum_{\gamma=1}^{3} \sum_{n_\gamma} A_{n_\gamma} X_{n_\gamma} .$$

Here, A_{n_γ} is a partial-wave amplitude and X_{n_γ} is a basis function that depends on four kinematic variables for describing the final state. The index n_γ denotes the nth partial wave in the γth representation, which, for $\pi N\to 1+2+3$, corresponds to the case where particle γ is a spectator particle and particles α and β form an isobar [$(\alpha\beta\gamma)=(123)$ et cycl.]. Contributions to the integrated reaction cross section from different X_{n_γ} with the same parity and total angular momentum generally overlap; that is, the X_{n_γ} are not orthogonal. We can write

$$X_{n_\gamma} = \left(\frac{C_{n_\gamma} K_{n_\gamma} B_{\ell_f}(p_\gamma)}{R}\right) D(q_\gamma) ,$$

where the quantity in parentheses describes the production of the particle γ and the (α,β) isobar from the πN initial state with C_{n_γ} an isospin coefficient, K_{n_γ} a kinematic factor, $B_{\ell_f}(p_\gamma)$ a barrier-penetration factor discussed below, and R a normalization integral. $D(q_\gamma)$ is a quasi-two-body amplitude that describes the propagation and decay of the isobar. $\vec{p}_\gamma$ is the c.m. momentum of particle γ and $\vec{q}_\gamma$ is the relative momentum of the (α,β) pair. The general notation for the isobar model is summarized in Fig. 56.

The isospin coefficients are given by (for $\gamma \neq 2$)[47]

$$C_{n_\gamma} = C(1,1/2,I;i_\pi i_N i)\ C(I_\alpha I_\beta \tilde{I};i_\alpha i_\beta \tilde{i})\ C(\tilde{I} I_\gamma I;\tilde{i} i_\gamma i)\ a_\gamma ,$$

where $C(j_1 j_2 j;m_1 m_2 m)$ is a Clebsch-Gordan coefficient. The isospin coefficient for $\gamma = 2$ is obtained by interchanging α and β in the above expression. Here, the total isospin and its z projection are respectively denoted by I and i; the isospin of the isobar and its z projection are respectively denoted by $\tilde{I}$ and $\tilde{i}$. The normalization coefficients a_γ have been discussed by Goradia and Arndt.[47] For $\pi^- p \to \pi^+ \pi^- n$, $a_1 = a_2 = 1$ and $a_3 = \sqrt{2}$.

INITIAL PION MOMENTUM $\vec{Q}$

TOTAL C.M. ENERGY W

FINAL MOMENTA $\begin{cases} \vec{p}_1, \vec{p}_2 & \text{pions} \\ \vec{p}_3 & \text{nucleon} \end{cases}$

SUBENERGIES W_1, W_2, W_3

SUBMOMENTA $\vec{q}_1, \vec{q}_2, \vec{q}_3$

ANGULAR MOMENTA

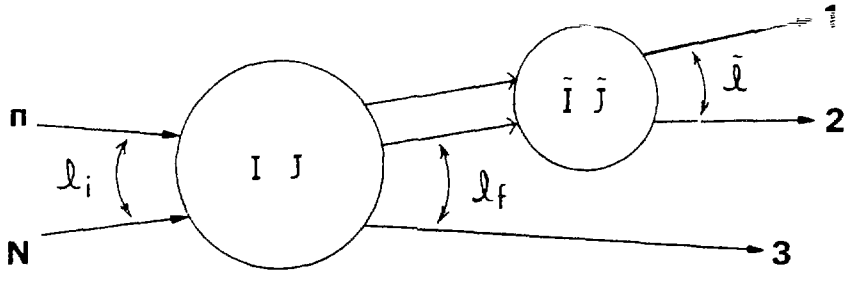

SPIN PROJECTIONS $\begin{cases} \mu_i & \text{initial} \\ \mu_f & \text{final} \end{cases}$

ISOSPIN PROJECTIONS $i_\pi, i_N, i_1, i_2, i_3$

Figure 56. Notation for the isobar model. W_i and $\vec{q}_i$ represent the (j,k) pair [(i,j,k)=(1,2,3) et cycl.].

The kinematic factor K_{n_γ} can be written as[47]

$$K_{n_\gamma} = C(1/2,\ell_i,J;\mu_i 0\mu_i)\left(\frac{2\ell_i+1}{4\pi}\right)^{1/2}\left(\frac{4\pi}{2\tilde{\ell}+1}\right)^{1/2} \times \sum_{m=-\tilde{\ell}}^{\tilde{\ell}} [C(1/2,\tilde{\ell},\zeta;\mu_f,m,\mu_f+m)\ C(\zeta,\ell_f,J;\mu_f+m,\mu_i-\mu_f-m,\mu_i) \times Y_{\tilde{\ell},m}(\hat{q}_\gamma)\ Y_{\ell_f,\mu_i-\mu_f-m}(\hat{p}_\gamma)] \ .$$

Here, μ_i and μ_f are respectively the z components of the initial and final nucleon spins, ℓ_i and J are the initial orbital and total angular momenta, ℓ_f and ζ denote the orbital angular momentum between the isobar and the spectator particle and their total spin, respectively, and $\tilde{\ell}$ is the orbital angular momentum of the particles formed by decay of the isobar in their c.m. system.

The Watson final-state interaction theorem[48] was used to evaluate the decay amplitude:

$$D(q_\gamma) = \frac{W_\gamma\ e^{i\delta_{\tilde{\ell}}}\ \sin\delta_{\tilde{\ell}}}{(q_\gamma)^{\tilde{\ell}+1}} \ .$$

Here, W_γ is the isobar subenergy or mass and $\delta_{\tilde{\ell}}$ is the two-body phase shift appropriate for describing the reaction $\alpha\beta\rightarrow\alpha\beta$.

The normalization integrals R are chosen such that the partial-wave cross section has the form[47]

$$\sigma_{n_\gamma} = \frac{2\pi}{Q^2}\ (2J+1)\ |A_{n_\gamma}|^2\ (C_{n_\gamma})^2 \ ,$$

where $\vec{Q}$ is the incident pion momentum in the c.m. system. The required integrals are given by[49]

$$R^2 = \frac{1}{32}\left(\frac{m_N}{W}\right)^2 \frac{Q}{(2\pi)^6} \frac{1}{2\tilde{\ell}+1} \int \frac{\sin^2\delta_{\tilde{\ell}}}{(q_\gamma)^{2\tilde{\ell}+1}} p_\gamma \left(W_\gamma B_{n_\gamma}\right)^2 dW_\gamma ,$$

where the integration limits are $W_{\gamma min} = m_\alpha + m_\beta$ and $W_{\gamma max} = W - m_\gamma$, with m_γ the mass of particle γ.

The c.m. coordinate system used to describe $\pi^-p\to\pi^+\pi^-n$ events is defined by the following unit vectors:

$$\hat{y} = \frac{\vec{Q} \times \vec{p}_3}{|\vec{Q} \times \vec{p}_3|} ,$$

$$\hat{z} = \frac{\vec{Q}}{|\vec{Q}|} ,$$

$$\hat{x} = \hat{y} \times \hat{z} ,$$

where $\vec{Q}$ and $\vec{p}_3$ are the c.m. momenta of the initial pion and final-state nucleon, respectively. For fixed total c.m. energy W, we chose the following kinematic variables to describe a $\pi^-p\to\pi^+\pi^-n$ event:

T_1 = kinetic energy of the final-state π^+ (particle 1),

T_2 = kinetic energy of the final-state π^- (particle 2),

θ = c.m. production angle of the final-state π^+,

β = angle of rotation about the direction of the final-state π^+.

The kinematic variable used by Arndt et al.[14] were:

W_1 = subenergy or mass of the (2,3) isobar,

W_2 = subenergy or mass of the (1,3) isobar,

$z_n = \hat{p}_3 \cdot \hat{z}$,

$z_\phi = \hat{n} \cdot \hat{y}$.

Here, $\hat{n}$ is a unit vector normal to the production plane:

$$\hat{n} = \frac{\vec{p}_1 \times \vec{p}_2}{|\vec{p}_1 \times \vec{p}_2|} .$$

The following equations relate the two sets of kinematic variables:

$$W_1 = [(W - m_\pi)^2 - 2WT_1]^{1/2} ,$$

$$W_2 = [(W - m_\pi)^2 - 2WT_2]^{1/2} ,$$

$$z_n = -(z_{13} \cos\theta + y_{13} \sin\theta \cos\beta) ,$$

$$z_\phi = (y_{13} \cos\theta - z_{13} \sin\theta \cos\beta)/y_n ,$$

where we have introduced:

$$z_{13} = \hat{p}_1 \cdot \hat{p}_3 ,$$

$$y_{13} = [1 - (z_{13})^2]^{1/2} ,$$

$$y_n = [1 - z_n^2]^{1/2} .$$

For completeness, we note that the total c.m. energy W is related to the incident pion kinetic energy in the laboratory T_π by

$$W = [(m_\pi + m_p)^2 + 2m_p T_\pi]^{1/2} .$$

To determine the partial-wave amplitudes from the measured values of $\overline{|M|^2}$, it was necessary to average the square modulus of the T-matrix element over the unobserved spin and kinematic variables. The mean square modulus can be written as

$$\overline{|T|^2} = \frac{\frac{1}{2}\sum_{\text{spins}} \int_0^\pi \int_{T_{2min}}^{T_{2max}} |T|^2 \, dT_2 \, d\beta}{\int_0^\pi \int_{T_{2min}}^{T_{2max}} dT_2 \, d\beta} ,$$

where the integration limits are given by

$$T_{\substack{2max \\ 2min}} = (W - T_1 - m_\pi)[m_\pi(m_\pi + m_n) + W(T_{max} - T_1)] - m_\pi$$

$$\pm \frac{p_1 \{W(T_{max} - T_1)[2m_\pi m_n + W(T_{max} - T_1)]\}^{1/2}}{(m_\pi + m_n)^2 + 2W(T_{max} - T_1)} ,$$

with T_{max} the maximum allowed value of T_1. Integrations over both T_2 and β were performed numerically. The experimental values of $\overline{|M|^2}$ were fitted at each incident energy to

$$\overline{|M|^2} = C_i \overline{C_f} \frac{\overline{|T|^2}}{Q^2}$$

to determine the complex parameters A_{n_γ}. Here, as in Chapter VI, $C_i\overline{C_f}$ is a correction for Coulomb interaction in the initial and final states and the doubly differential cross section for the π^+ in the c.m. system is given by

$$\frac{d^2\sigma}{d\Omega dT} = \overline{|M|^2}\,\frac{d^2\sigma_o}{d\Omega dT} \ .$$

At each incident energy, we calculated the singly differential cross sections $\frac{d\sigma}{dT}$ and $\frac{d\sigma}{d\Omega}$ by numerically integrating values of $\frac{d^2\sigma}{d\Omega dT}$. The integrated reaction cross section σ_R was subsequently found by numerically integrating either of the singly differential cross sections. We estimated that the error introduced in σ_R from numerical integration was about 0.3%.

The isobar model allowed cross-section predictions to be made for the other $\pi N \to \pi\pi N$ charge reactions that are indicated in Table XXXVI and provided a means to determine the elasticities $\eta_{\ell IJ}$ for the initial P11, D13 and D33 waves. We calculated the $\eta_{\ell IJ}$ from the relation

$$\sigma_{\ell IJ} = C_I \frac{\pi}{2Q^2}\,(2J+1)\,[1 - (\eta_{\ell IJ})^2] \ ,$$

where $\sigma_{\ell IJ}$ is the contribution of the (ℓIJ) initial wave to the total inelastic π^-p cross section and C_I is an isospin coefficient with $C_I = 2/3$ for $I = 1/2$ and $C_I = 1/3$ for $I = 3/2$. We made the approximation in calculating the $\sigma_{\ell IJ}$ with the VPI model that T_{CA} contributed only to σ_{P11}.

Comparison with the LBL-SLAC Analysis

Our measurements were compared with the solutions of the LBL-SLAC analysis[13] discussed above. The programs of Arndt et al.[14] were modified to reproduce the LBL-SLAC parametrizations for the barrier-penetration factors and the two-body phase shifts for describing $\pi\pi$ elastic scattering. The following 11 partial waves were included in the LBL-SLAC analysis:

$PS11(\varepsilon N)$,	$SP11(\varepsilon N)$,	$DP13(\varepsilon N)$,
$PP11(\rho_1 N)$,	$PP31(\rho_1 N)$,	$DS13(\rho_3 N)$,
$PP11(\pi\Delta)$,	$PP31(\pi\Delta)$,	$DS13(\pi\Delta)$,
$DS33(\pi\Delta)$,	$DD13(\pi\Delta)$.	

The subscript on ρ refers to the total angular momentum coupling (1/2 or 3/2) of the ρ isobar and the spectator nucleon.

In Table XXXVIII, we present values for the partial-wave amplitudes at incident kinetic energies 292, 331, and 358 MeV that were linearly interpolated from the LBL-SLAC solutions[13] at incident kinetic energies 295, 338, and 381 MeV. The amplitudes in Table XXXVIII are expressed in the phase conventions of Arndt et al., which differ from those of the LBL-SLAC analysis. These phase conventions are related by the following[50]:

$$A_{\varepsilon}(\text{VPI}) = (-1)^{\ell} i\, A_{\varepsilon}(\text{LBL-SLAC}) ,$$

$$A_{\rho_1}(\text{VPI}) = (-1)^{\ell} i^{+1}\, A_{\rho_1}(\text{LBL-SLAC}) ,$$

TABLE XXXVIII. Partial-wave amplitudes in modulus-phase form interpolated from the solutions of the LBL-SLAC analysis. The phase, in radians, is given in parentheses.

Wave	292 MeV	331 MeV	358 MeV
PS11(εN)	0.144 (1.340)	0.132 (1.300)	0.158 (1.160)
SP11(εN)	0.017 (1.950)	0.033 (0.720)	0.045 (0.800)
DP13(εN)	0.070 (0.088)	0.046 (0.400)	0.063 (0.180)
PP11(ρ_1N)	0.011 (1.920)	0.025 (1.890)	0.032 (1.760)
PP31(ρ_1N)	0.031 (0.360)	0.046 (0.340)	0.063 (0.160)
DS13(ρ_3N)	0.032 (0.520)	0.063 (0.660)	0.089 (0.500)
PP11($\pi\Delta$)	0.054 (1.000)	0.083 (1.000)	0.122 (0.820)
PP31($\pi\Delta$)	0.022 (0.320)	0.035 (0.290)	0.051 (0.120)
DS13($\pi\Delta$)	0.098 (-0.080)	0.078 (0.370)	0.100 (0.230)
DS33($\pi\Delta$)	0.041 (0.890)	0.058 (0.900)	0.076 (0.720)
DD13($\pi\Delta$)	0.023 (-0.270)	0.020 (-0.150)	0.047 (-0.350)

$$A_{\rho_3}(\text{VPI}) = (-1)^{\ell_i} A_{\rho_3}(\text{LBL-SLAC}) ,$$

$$A_{\Delta}(\text{VPI}) = (-1)^{\ell_i+1} A_{\Delta}(\text{LBL-SLAC}) .$$

The basis functions X_{n_γ} used in the LBL-SLAC analysis had different parametrizations for the barrier-penetration factors $B_{\ell_f}(p_\gamma)$ and the two-body phase shifts $\delta^{\tilde{I}}_{\ell}$ than those used in the analysis of Arndt et al. We used the LBL-SLAC parametrizations to generate the 11 X_{n_γ}. The form used for the barrier-penetration factors was the low-momentum limit of the Blatt-Weisskopf form[51]:

$$B_{\ell_f}(p_\gamma) = (p_\gamma)^{\ell_f} .$$

The form used for the $\tilde{I} = \tilde{J} = 1$ $\pi\pi$ phase shift was due to Morgan[52]:

$$\frac{q_3^3}{W_3} \cot\delta_\rho = \frac{(m_\pi^2 - 0.1536\ q_3^2)(m_\pi^2 + 0.028\ q_3^2)}{0.070\ m_\pi^2} .$$

The form used for the $\tilde{I} = \tilde{J} = 0$ $\pi\pi$ phase shift can be written as[53]

$$\frac{q_3}{W_3} \cot\delta_\varepsilon = 3.125 - 2.133 \left(\frac{q_3}{m_\pi}\right)^2 + 0.4227 \left(\frac{q_3}{m_\pi}\right)^4 .$$

The basis functions were fairly insensitive to the forms used to parametrize the barrier-penetration factors and phase shifts.

Since the amplitudes in Table XXXVIII were normalized to older, less accurate cross-section measurements, it was necessary to introduce an overall normalization factor N defined by

$$A_{n_\gamma}' = N A_{n_\gamma} ,$$

where A_{n_γ}' represents the renormalized value of the partial-wave amplitude A_{n_γ}.

The VPI Model

Our use of the VPI model to analyze the spectrometer measurements followed closely the procedure used by Arndt *et al.*[14] to analyze bubble-chamber events. Their barrier-penetration factors $B_{\ell_f}(p_\gamma)$ were of the Blatt-Weisskopf form[51] and are summarized in Table XXXIX. The analysis of Arndt *et al.* assumed all ρ production could be described by the background term. T_{CA} has a part which is antisymmetric under interchange of the final-state pion momenta and, therefore, is appropriate for production of P-wave final-state pions. In the VPI model, ρ production is included through this antisymmetric part. The

TABLE XXXIX. Barrier-penetration factors $B_{\ell_f}(p_\gamma)$. Here, $x = p_\gamma R$, where R = 0.25 fm is the radius of interaction.[f]

ℓ_f	$B_{\ell_f}(p_\gamma)$
0	1
1	$x/(1 + x^2)^{1/2}$
2	$x^2/(9 + 3\,x^2 + x^4)^{1/2}$
3	$x^3/(225 + 45\,x^2 + 6\,x^4 + x^6)^{1/2}$

symmetric part of T_{CA} is appropriate for production of S-wave final-state pions and thus contributes to ε production. We evaluated T_{CA} with $\xi = 0$, which is consistent with the result of Chapter VI. However, this choice is not necessarily a limitation because the background is somewhat redundant with partial waves. Since T_{CA} can presumably be expanded into partial waves in a manner analogous to T_{IM}, within the VPI model, the A_{n_γ} must be interpreted, not as the entire amplitudes, but rather as the deviations from current algebra. We used the same forms as Arndt et al. for the two-body phase shifts $\delta_{\tilde{L}}^{\tilde{I}}$. For πN in the $\tilde{I} = \tilde{J} = 3/2$ state, they used the parametrization of Goradia and Arndt.[47] For $\pi\pi$ in the $\tilde{I} = \tilde{J} = 0$ state, they approximated the results of a dispersion relation calculation by Franklin.[6]

Following the treatment of Arndt et al., we considered the following six partial waves:

PS11(εN),	DP13(εN),
PP11($\pi\Delta$),	PP33($\pi\Delta$),
DS13($\pi\Delta$),	DS33($\pi\Delta$).

These choices include all final-state S-waves and the final-state P-waves that arise from resonant initial states (P11, P33, D13). As stated earlier, we used partial-wave amplitudes interpolated from the solutions of Arndt et al. as initial guesses in our fitting routine. When we attempted to vary the waves DS13($\pi\Delta$) and DP13(εN) simultaneously, we found, like Arndt et al., that the two amplitudes could not be clearly separated. This problem is due to the large overlap of

their basis functions. Since those authors proposed that the amplitude for making the P-wave εN transition should be suppressed relative to the amplitude for making the S-wave $\pi\Delta$ transition, we set A(DP13-εN) equal to zero. It follows that the DS13($\pi\Delta$) amplitude determined by our least squares analysis contains a small part representing DP13(εN) production. We also found, along with those authors, that when our analysis included searching of the PP33($\pi\Delta$) wave, the amplitude A(PP33-$\pi\Delta$) searched to a very small value. We concluded that production of this wave was insignificant for the energy range of this experiment and set A(PP33-$\pi\Delta$) equal to zero.

When partial-wave amplitudes were found to be small, their phases were poorly determined. In such cases, it was convenient to fix their phases by making the elastic production phase (EPP) approximation. In this approximation, the phase of the partial-wave amplitude is given by[14]

$$\phi_p = \arctan\left[\frac{\mathrm{Re}(T_e)}{1 - \mathrm{Im}(T_e)}\right] ,$$

where

$$T_e = (\eta e^{2i\delta} - 1)/2i$$

is the πN elastic amplitude for the incident partial wave. Here, δ is the real πN phase shift and η is the elasticity or absorption parameter. In Table XL, we present the elastic production phases used in our analysis. For incident energies above 300 MeV, we graphically

TABLE XL. Elastic production phases (in radians).

T_π(MeV)	P11	D13	D33
203	0.035	0.020	0.000
230	0.076	0.029	0.000
255	0.131	0.040	0.000
280	0.201	0.052	0.000
292	0.245	0.059	0.000
331	0.370	0.053	0.000
357	0.460	0.067	0.000

interpolated the phases from those of Arndt et al.[14] For energies below 300 MeV, the phases were generated with the subroutine SCATPI.[27]

In Table XLI, we present a summary of partial-wave amplitudes at 331 and 358 MeV that were interpolated from the EPP solutions of Arndt et al. These solutions were obtained by using the EPP approximation

TABLE XLI. Partial-wave amplitudes in modulus-phase form interpolated from the EPP solutions of Arndt et al. The phase, in radians, is given in parentheses.

T_π(MeV)	PS11(εN)	PP11($\pi\Delta$)	DS13($\pi\Delta$)	DS33($\pi\Delta$)	χ^2/ν
331	0.190 (1.569)	0.096 (0.370)	0.060 (0.053)	0.029 (0.000)	3.02
358	0.232 (1.504)	0.119 (0.460)	0.087 (0.067)	0.071 (0.000)	4.83

to fix the phases of the PP11($\pi\Delta$), DS13($\pi\Delta$), and DS33($\pi\Delta$) partial waves. The χ^2/ν in this table were obtained by comparing our measurements of $\overline{|M|^2}$ directly with the values predicted by the amplitudes in the table. We also compared our measurements with partial-wave amplitudes that were interpolated from the searched-production-phase (SPP) solutions of Arndt et al. These solutions differed from the EPP solutions in that the phase of the PP11($\pi\Delta$) wave was allowed to vary freely. The interpolated SPP amplitudes and the χ^2/ν obtained by comparing with our measured $\overline{|M|^2}$ are given in Table XLII.

Results

Our production measurements were compared, where possible, with both the LBL-SLAC solutions and the VPI model. Table XLIII presents a summary of the χ^2/ν, normalization factor N, and integrated reaction cross section obtained by renormalizing the interpolated LBL-SLAC solutions at 292, 331, and 358 MeV. The quoted errors include

TABLE XLII. Partial-wave amplitudes in modulus-phase form interpolated from the SPP solutions of Arndt et al. The phase, in radians, is given in parentheses.

T_π(MeV)	PS11(ϵN)	PP11($\pi\Delta$)	DS13($\pi\Delta$)	DS33($\pi\Delta$)	χ^2/ν
331	0.168 (1.437)	0.077 (1.164)	0.047 (0.053)	0.048 (0.000)	3.36
358	0.221 (1.463)	0.105 (1.009)	0.078 (0.067)	0.082 (0.000)	5.31

contributions from systematic uncertainties, mainly from the elastic calibration, that were combined in quadrature with the statistical errors as discussed in Chapter VI. Since the isobar models fit the $\overline{|M|^2}$ with no difficulty, we assumed a 4% systematic uncertainty at 292 MeV, rather than 5% as used for the empirical analysis. The renormalized LBL-SLAC solutions agreed remarkably well with the measurements at 331 and 358 MeV. At these two energies, values for the integrated cross section were about 1% smaller than those obtained with the VPI model, which we discuss below. At 292 MeV, the renormalized solution compared unfavorably with our measurements ($\chi^2/\nu = 3.73$) by predicting larger values of $\overline{|M|^2}$ than measured for the π^+ meson at forward scattering angles and large kinetic energies. To obtain good agreement at 292 MeV, it was necessary to vary at least two real parameters in addition to N. Our best solution, which is also given in Table XLIII, was obtained by varying both the modulus

TABLE XLIII. Integrated reaction cross section for $\pi^-p\to\pi^+\pi^-n$ and normalization factor N determined by comparing LBL-SLAC solutions with spectrometer measurements.

T_π(MeV)	σ_R(μb)	N	χ^2/ν
292[a]	545 ± 31	0.908 ± 0.169	1.10
292	429 ± 22	0.853 ± 0.013	3.73
331	1142 ± 50	1.196 ± 0.011	1.19
358	1856 ± 77	1.165 ± 0.007	1.35

[a]Our best 292 MeV solution was obtained by varying both A(PS11-εN) and the normalization.

and phase of A(PS11-εN). An attractive feature of this solution is the fact that both the normalization and modulus of A(PS11-εN) were within one standard deviation of their initial values. Values for the fitted modulus and phase (in radians) were respectively 0.133 ± 0.018 and 2.384 ± 0.119. This phase was about 60° larger than the initial one. The integrated cross section for this solution was 5% lower than the result obtained by the empirical analysis and 5% higher than the result, discussed below, obtained from the VPI model. Figs. 57-59 present comparisons of our measurements at 292, 331, and 358 MeV with the best renormalized LBL-SLAC solutions. Specifically, these figures show each measured value of $\overline{|M|^2}/(C_i\overline{C_f})$ with the experimental uncertainty given in parentheses. The fitted values are given beneath the measured ones. A peak, which we associate with Δ^- production, is clearly evident for the 331 and 358 MeV measurements at small π^+ kinetic energy and forward angles.

In Table XLIV, we present a summary of our preferred partial-wave amplitudes obtained with the VPI model. Plots of $\overline{|M|^2}/(C_i\overline{C_f})$ that compare our measurements with the fitted values are shown for each incident energy in Figs. 60-66. These plots indicate that the π^+ meson was produced primarily at forward angles in the c.m. system. The largest waves are PS11(εN) and PP11(πΔ). A(PS11-εN) is expected to be large near threshold because conservation of parity and total angular momentum requires the threshold reaction to proceed from an initial P-wave state to a final S-wave state with J = 1/2. We found the amplitude A(DS13-πΔ) to be larger than A(DS33-πΔ) although both amplitudes were small, with the former becoming negligible at about 280 MeV and the latter at about 292 MeV. Therefore, below 280 MeV,

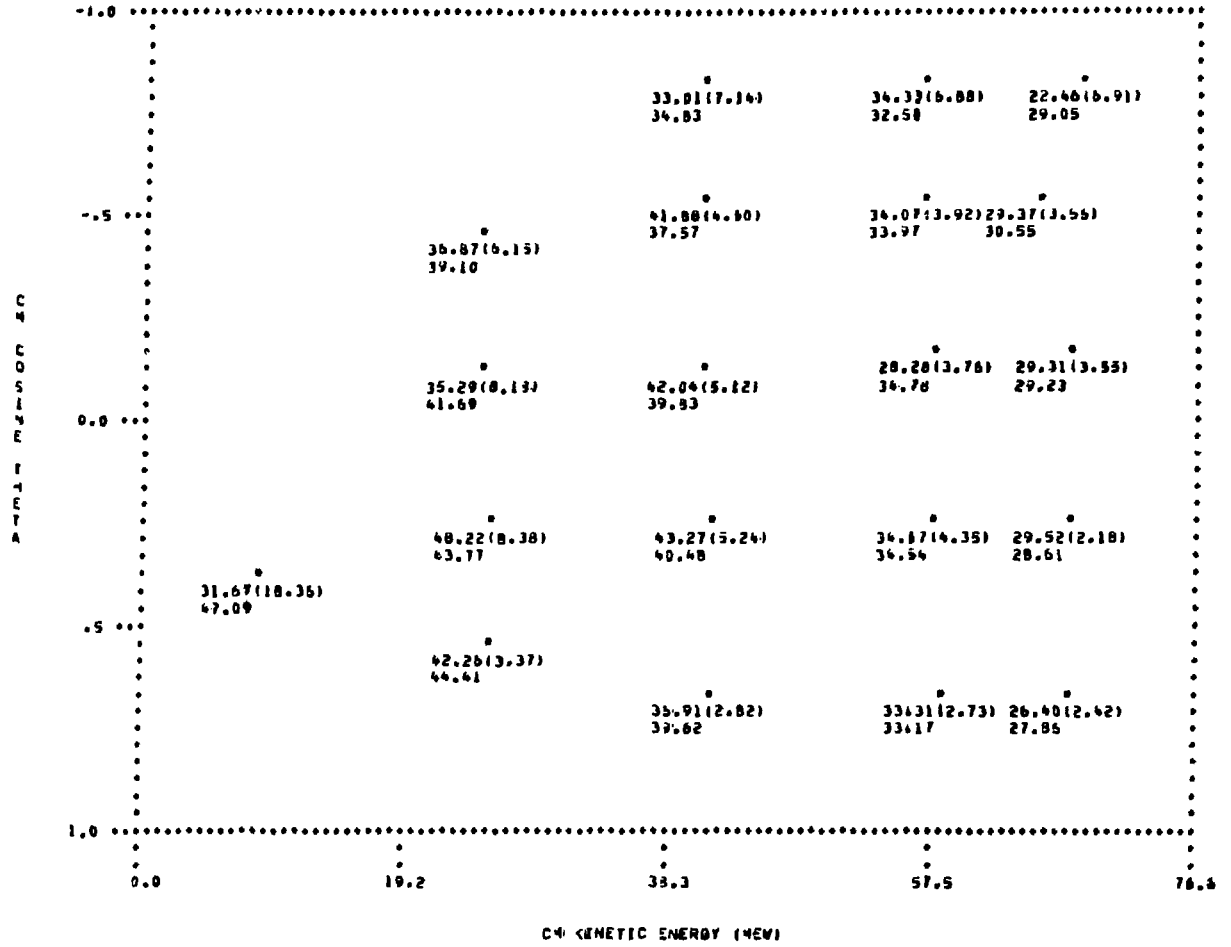

Figure 57. Best comparison of the measured $\overline{|M|^2}/(C_i\overline{C_f})_{10}$ at 292 MeV with the LBL-SLAC solutions. The data were obtained from a previous $\pi^-p\to\pi^+\pi^-n$ experiment.

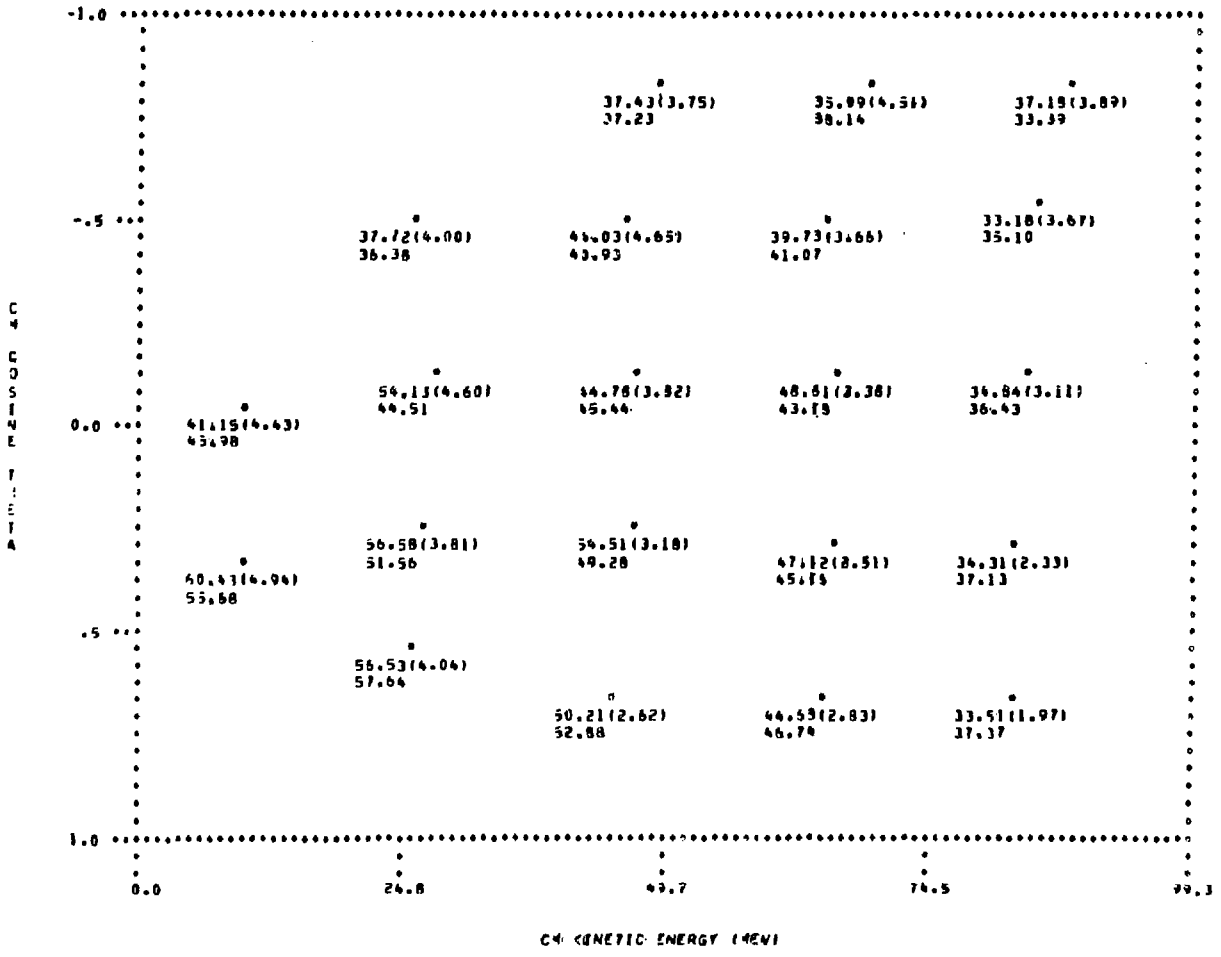

Figure 58. Best comparison of the measured $\overline{|M|^2}/(C_i\overline{C_f})_{10}$ at 331 MeV with the LBL-SLAC solutions. The data were obtained from a previous $\pi^-p\to\pi^+\pi^-n$ experiment.

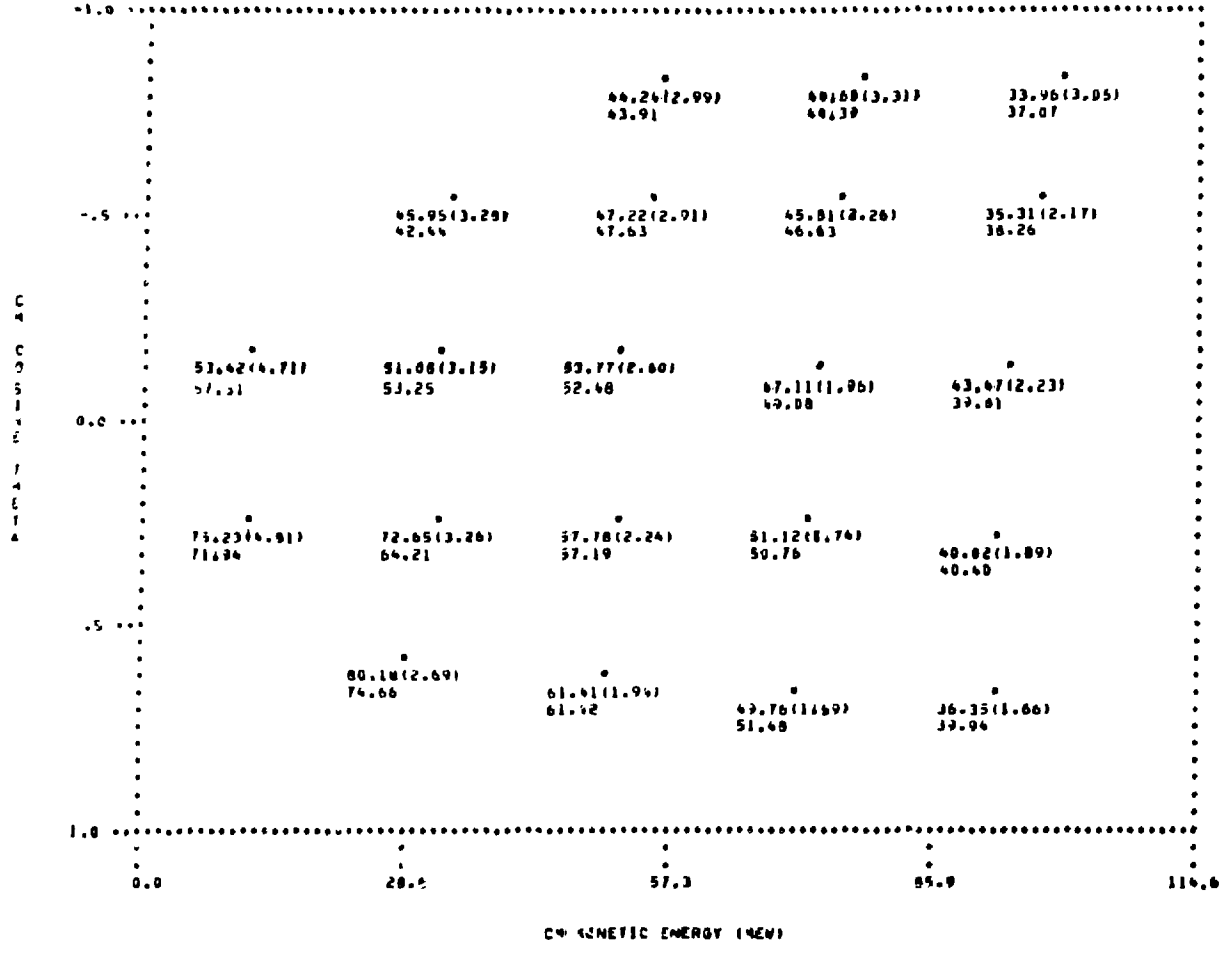

Figure 59. Best comparison of the measured $\overline{|M|^2}/(C_i C_f)$ at 358 MeV with the LBL-SLAC solutions.

TABLE XLIV. Preferred solutions for partial-wave amplitudes in modulus-phase form. The phase, in radians, is given in parentheses.

T_π(MeV)	PS11(ϵN)	PP11($\pi\Delta$)	DS13($\pi\Delta$)	DS33($\pi\Delta$)	χ^2/ν
203	0.013 ± 0.007 (1.477 ± 0.630)	•••	•••	•••	0.58
230	0.031 ± 0.006 (1.447 ± 0.252)	•••	•••	•••	0.67
254	0.063 ± 0.006 (1.571 ± 0.191)	•••	•••	•••	1.60
256	0.058 ± 0.004 (1.452 ± 0.129)	•••	•••	•••	0.86
280	0.101 ± 0.005 (1.516 ± 0.118)	•••	•••	•••	1.25
292	0.079 ± 0.033 (1.605 ± 0.733)	0.068 ± 0.020 (1.361 ± 0.624)	0.049 ± 0.013 (0.059)	0.025 ± 0.014 (0.000)	1.03
331	0.122 ± 0.050 (1.446 ± 0.793)	0.111 ± 0.030 (0.986 ± 0.396)	0.092 ± 0.011 (0.053)	0.023 ± 0.014 (0.000)	1.03
356	0.188 ± 0.033 (1.910 ± 0.384)	0.192 ± 0.047 (0.768 ± 0.286)	0.098 ± 0.018 (0.067)	0.061 ± 0.015 (0.000)	0.89
358	0.185 ± 0.025 (1.647 ± 0.293)	0.147 ± 0.028 (0.856 ± 0.189)	0.113 ± 0.011 (0.067)	0.059 ± 0.012 (0.000)	1.92

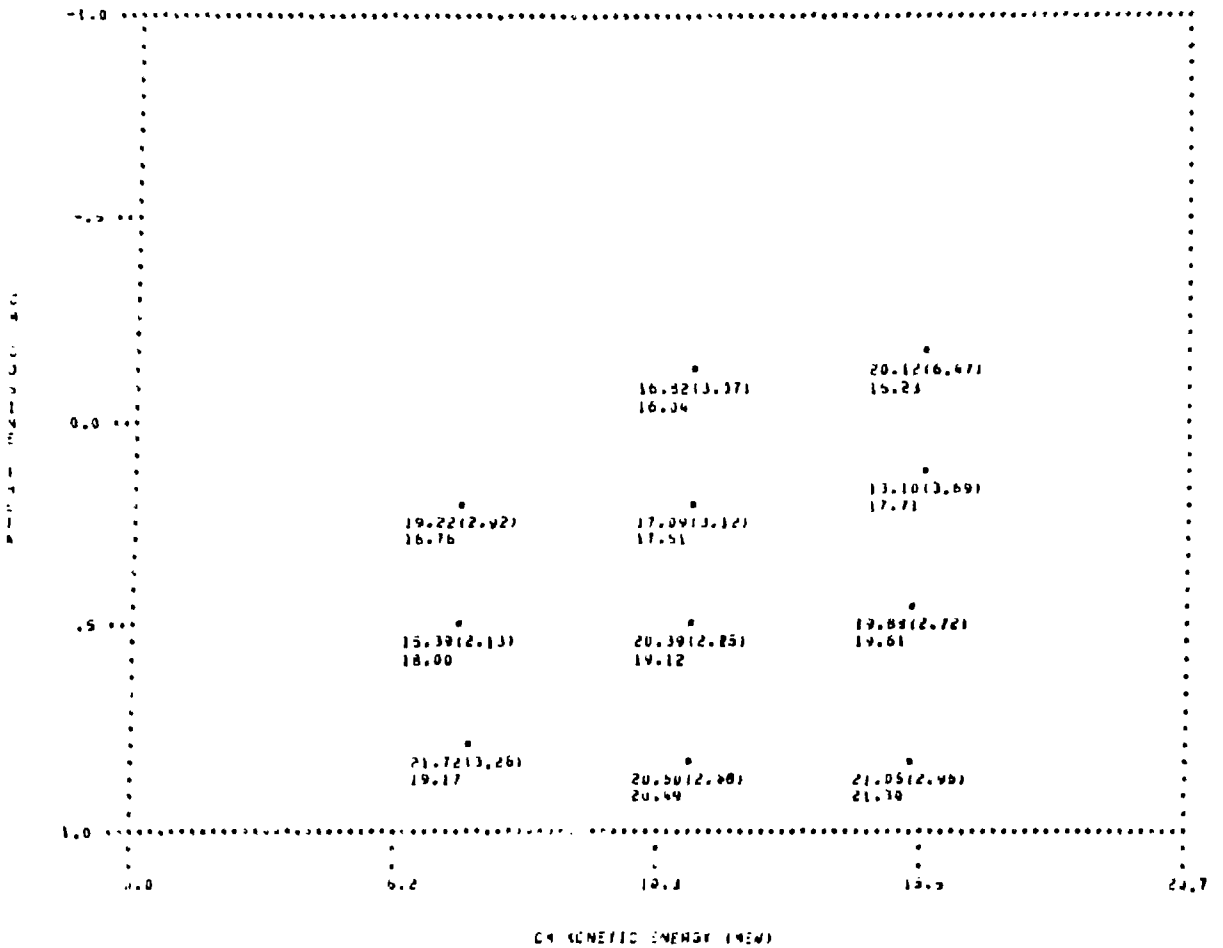

Figure 60. Comparison of the measured $\overline{|M|^2}/(C_i\overline{C_f})$ at 203 MeV with the fitted results of the VPI model.

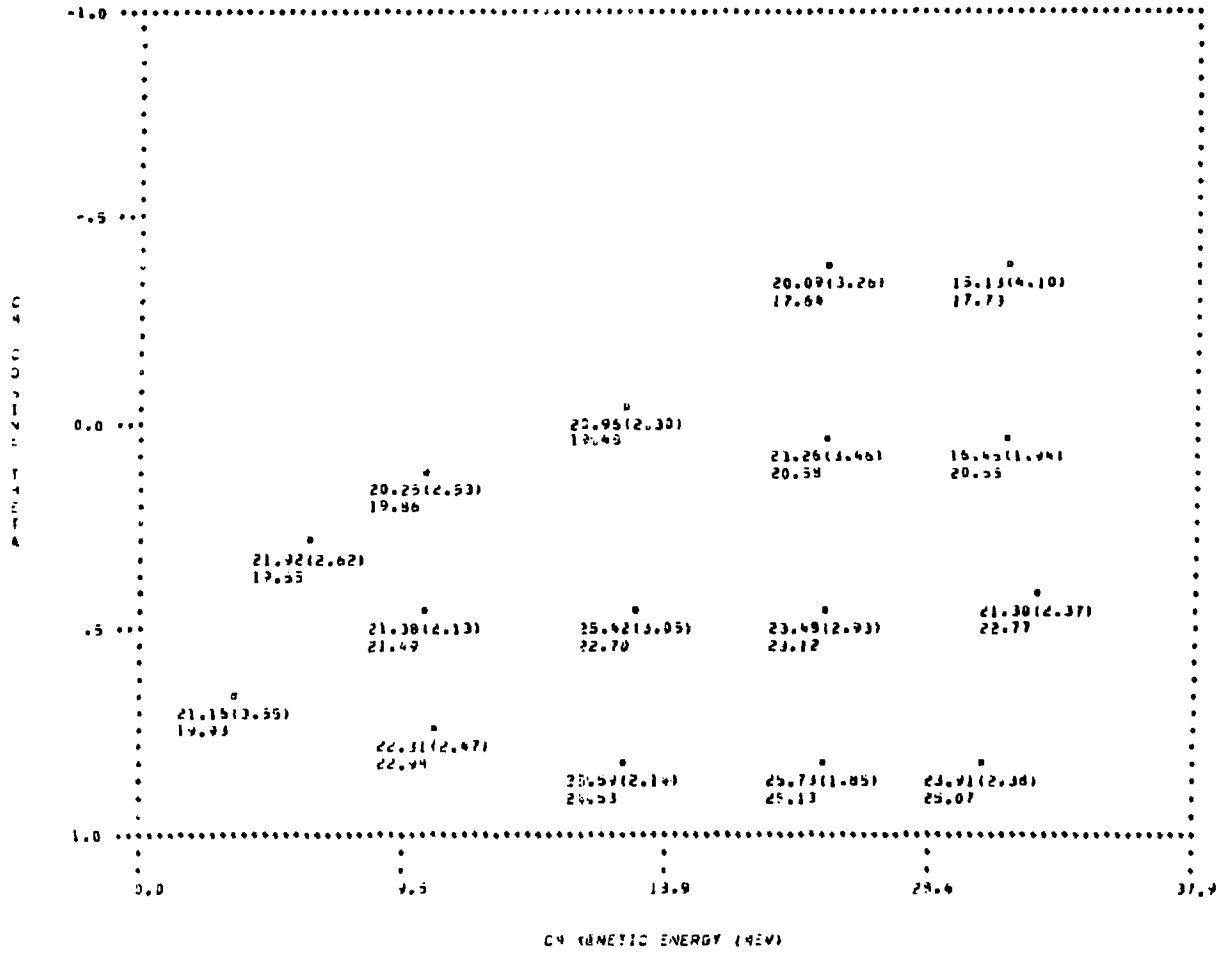

Figure 61. Comparison of the measured $\overline{|M|^2}/(C_i\overline{C_f})$ at 230 MeV with the fitted results of the VPI model.

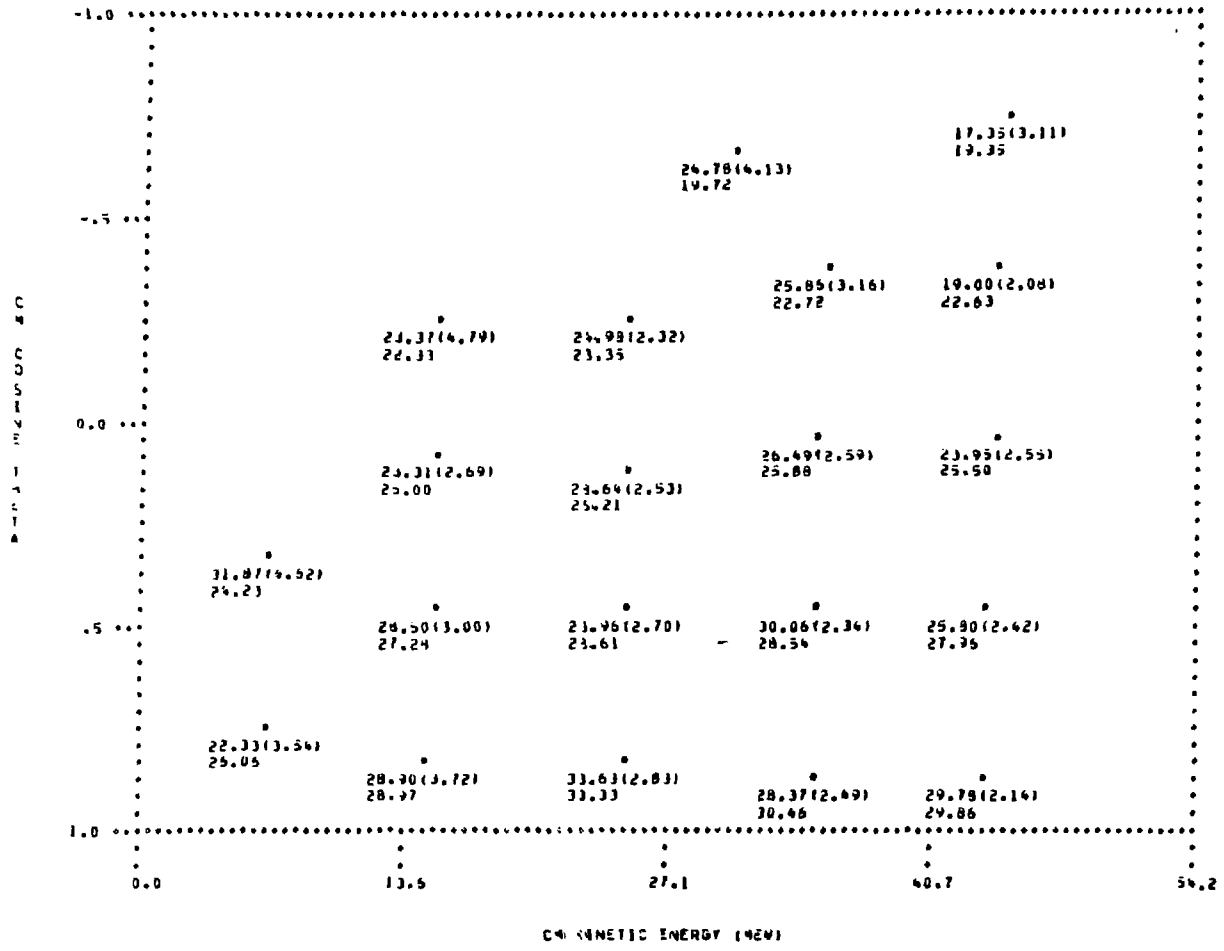

Figure 62. Comparison of the measured $\overline{|M|^2}/(C_i\overline{C_f})$ at 256 MeV with the fitted results of the VPI model.

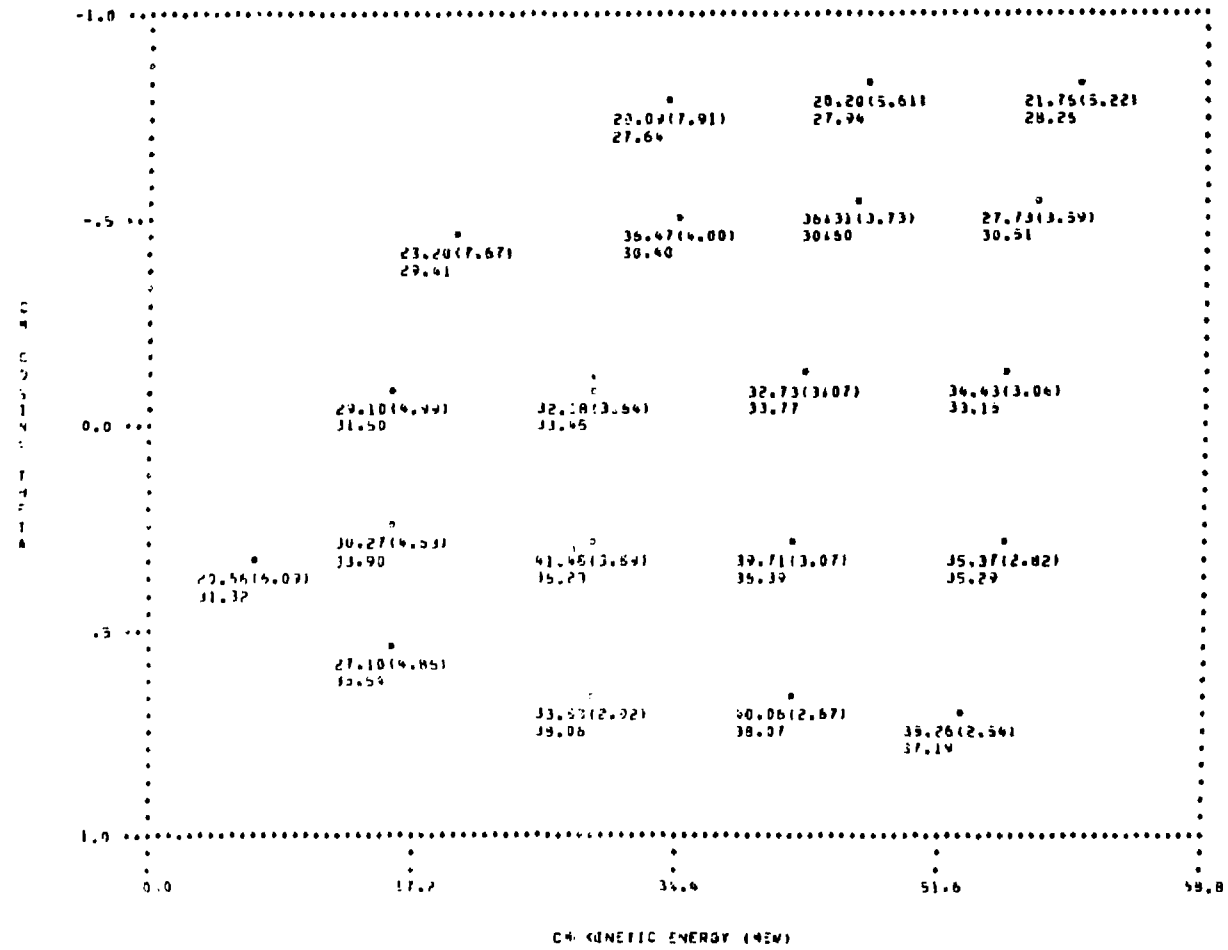

Figure 63. Comparison of the measured $\overline{|M|^2}/(C_i\overline{C_f})$ at 280 MeV with the fitted results of the VPI model. The data were obtained from a previous $\pi^- p \to \pi^+ \pi^- n$ experiment.[10]

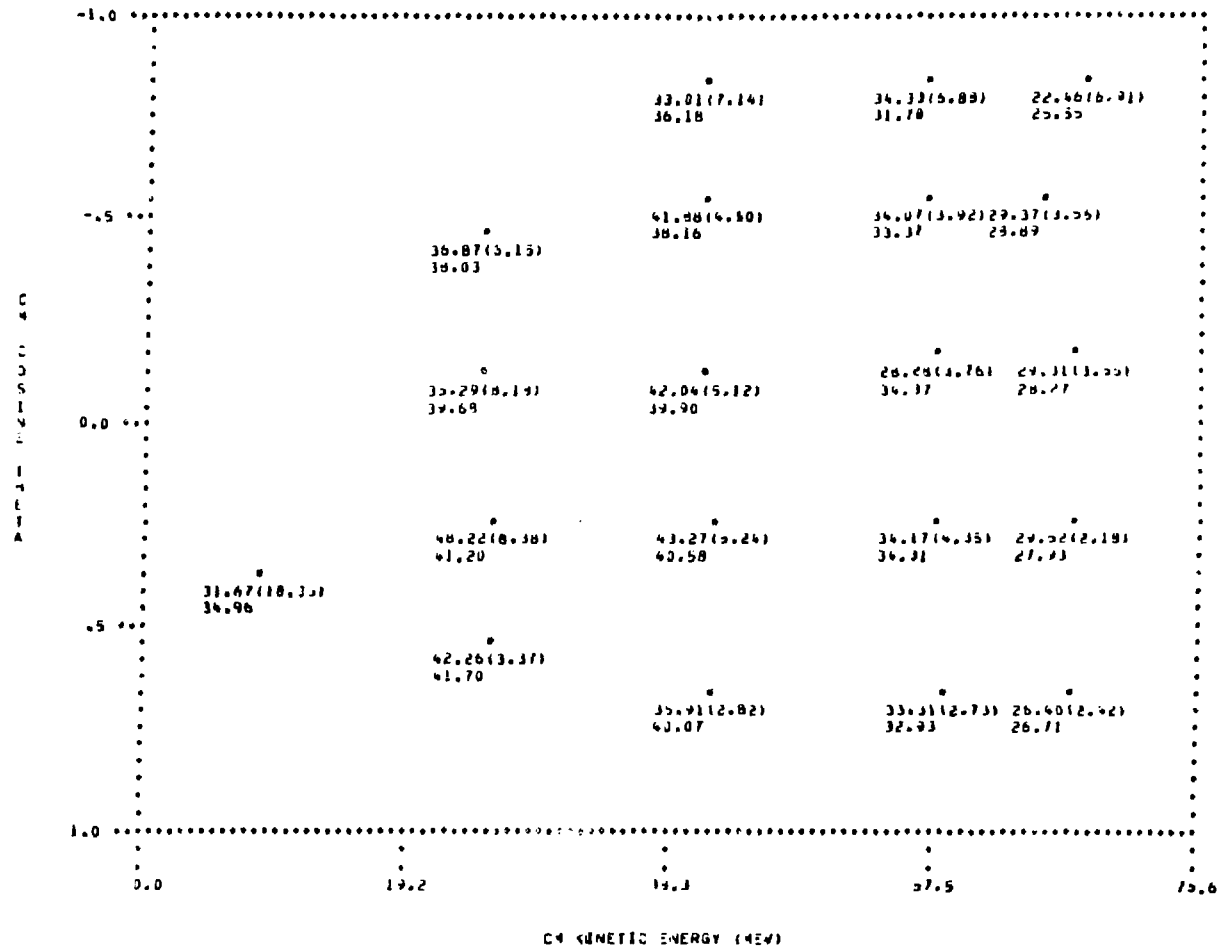

Figure 64. Comparison of the measured $\overline{|M|^2}/(C_i C_f)$ at 292 MeV with the fitted results of the VPI model. The data were obtained from a previous $\pi^- p \to \pi^+ \pi^- n$ experiment.[10]

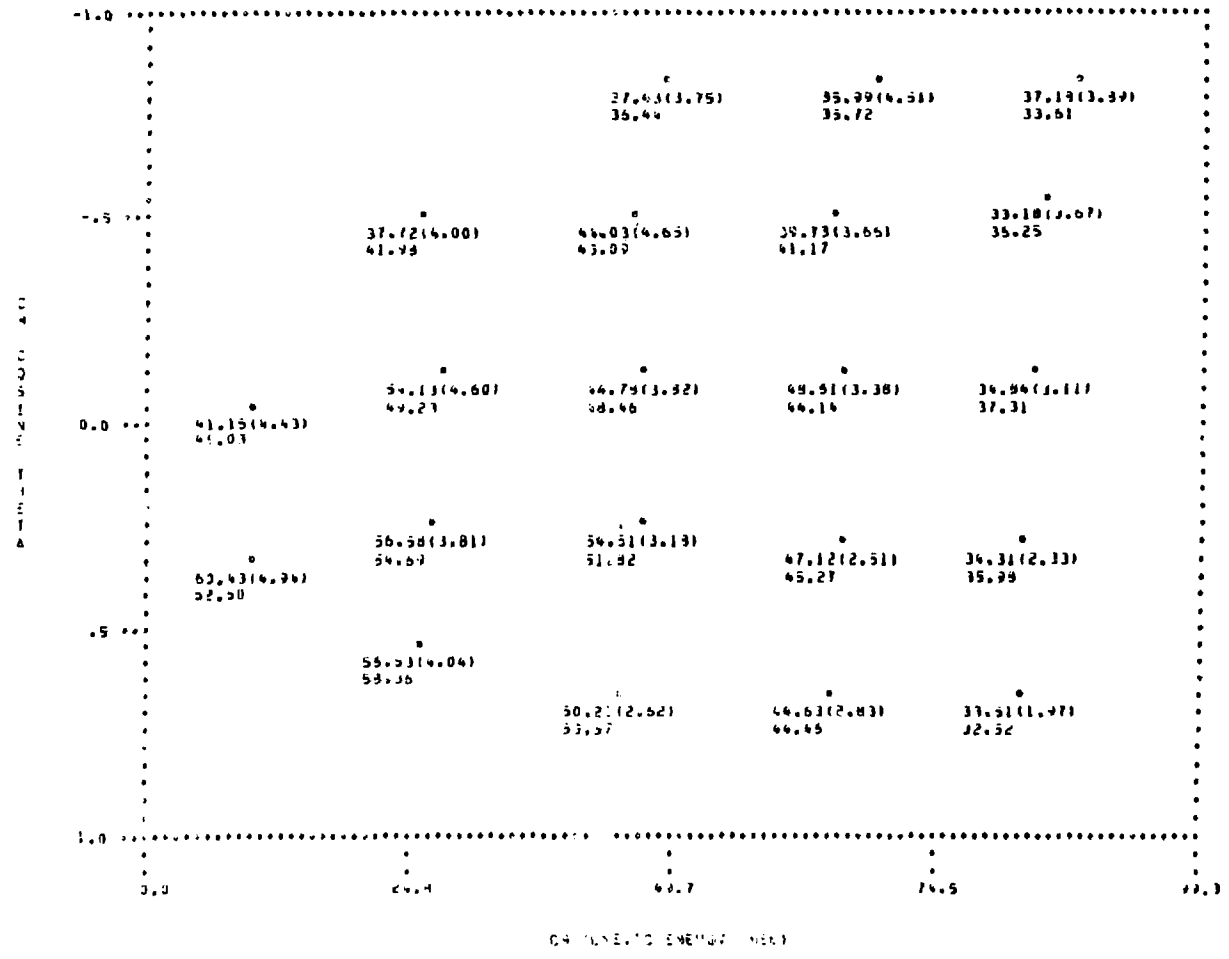

Figure 65. Comparison of the measured $\overline{|M|^2}/(C_i\overline{C_f})$ at 331 MeV with the fitted results of the VPI model. The data were obtained from a previous $\pi^- p \to \pi^+ \pi^- n$ experiment.[10]

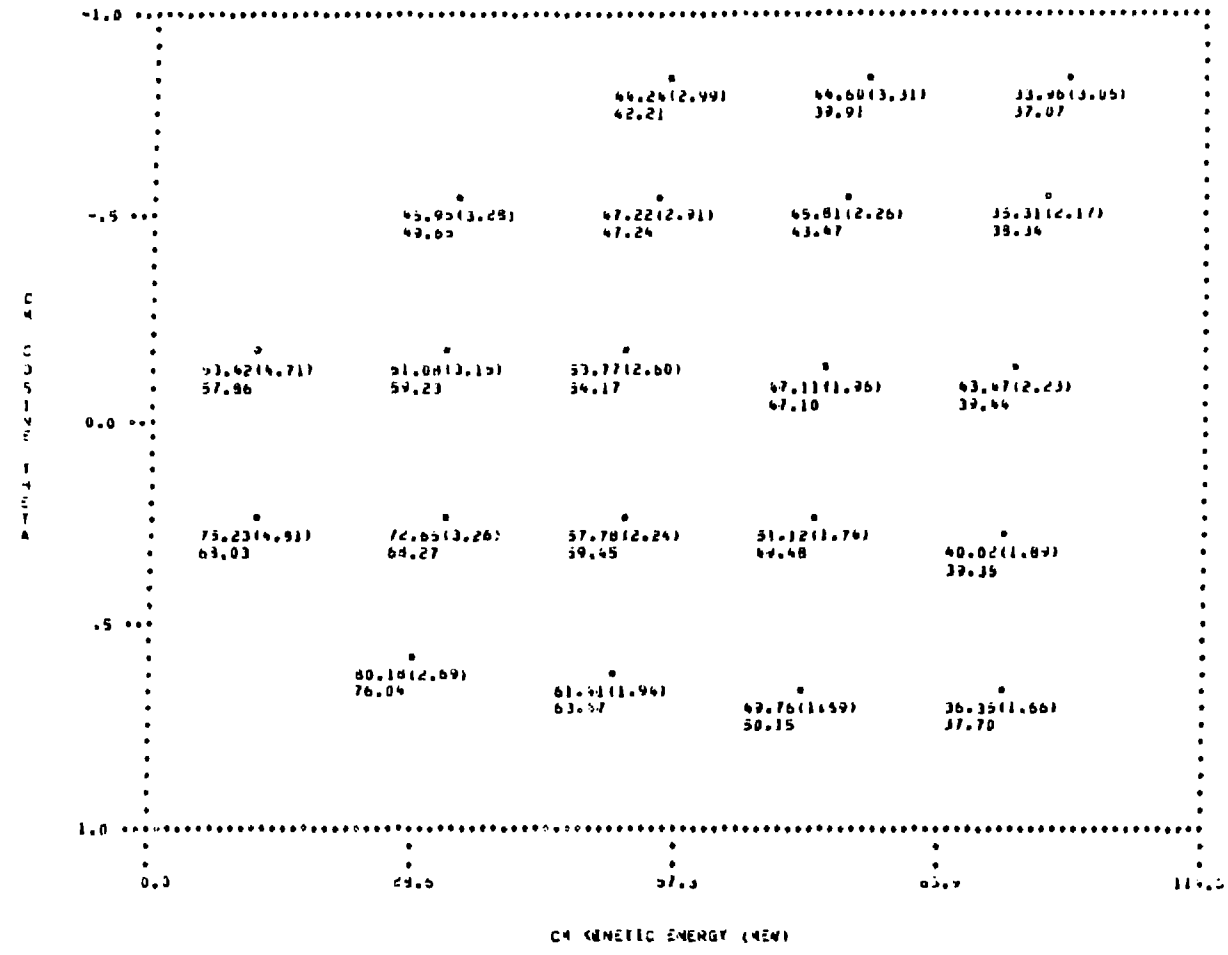

Figure 66. Comparison of the measured $\overline{|M|^2}/(C_i\overline{C_f})$ at 358 MeV with the fitted results of the VPI model.

production proceeds primarily from initial P-wave states. To obtain a good χ^2/ν at 280 MeV and below, only the amplitude A(PS11-εN) and the background were necessary.

Our preferred solutions at the highest two energies agreed well with the searched-production-phase (SPP) solutions of Arndt et al.[14] We found slightly more production of the Δ isobar and slightly less production of the ε isobar. The preferred solution at 358 MeV was fitted with $\chi^2/\nu = 1.92$, which was the smallest χ^2/ν we were able to obtain at this energy. We feel that our measurements were sufficiently precise at this energy to indicate a probable disagreement between the VPI model and our data. When the elastic production phase approximation was used to fix the phase of the PP11(πΔ) wave, we found that the moduli of both A(PP11-πΔ) and A(PS11-εN) increased. In addition, the fitted phase of A(PS11-εN) increased from about 90° to about 130°. We present our EPP solutions at 292, 331, and 357 MeV in Table XLV. These results can be compared with the amplitudes in Table XLI, which were interpolated from the EPP solutions of Arndt et al. Our EPP solutions differ from those of Arndt et al. in two particulars. Whereas the fitted phase of A(PS11-εN) for our EPP solutions was about 130°, the phase determined by Arndt et al. was only about 90°. We also found that the modulus of A(PP11-πΔ) for our EPP solutions was about twice as large as that obtained by Arndt et al. To obtain any appreciable improvement in the χ^2/ν obtained by comparing with the EPP solutions of Arndt et al., it was necessary to free both the modulus of A(PP11-πΔ) and the phase of A(PS11-εN). The solutions that resulted were essentially those in Table XLV.

TABLE XLV. EPP solutions at 292, 331, and 357 MeV in modulus-phase form. The phase, in radians, is given in parentheses.

T_π(MeV)	PS11(εN)	PP11(πΔ)	DS13(πΔ)	DS33(πΔ)	χ^2/ν
292	0.113 ± 0.015 (2.261 ± 0.197)	0.123 ± 0.009 (0.245)	0.029 ± 0.011 (0.059)	0.020 ± 0.015 (0.000)	1.15
331	0.198 ± 0.021 (2.474 ± 0.340)	0.186 ± 0.018 (0.370)	0.076 ± 0.008 (0.053)	0.020 ± 0.016 (0.000)	0.98
356	0.215 ± 0.009 (2.213 ± 0.109)	0.239 ± 0.016 (0.460)	0.083 ± 0.011 (0.067)	0.067 ± 0.017 (0.000)	0.85
358	0.229 ± 0.006 (2.108 ± 0.104)	0.208 ± 0.018 (0.460)	0.092 ± 0.009 (0.067)	0.070 ± 0.013 (0.000)	1.96

We were able to find acceptable alternate solutions at 292 and 331 MeV that involved a smaller number of partial waves than either our preferred or EPP solutions. When we neglected production of the DS33($\pi\Delta$) wave, we obtained the solutions presented in Table XLVI. It is interesting to note that these solutions agree very well, not with our preferred solutions, but rather with our EPP solutions. We present alternate solutions in Table XLVII at 255 and 280 MeV obtained by also considering production of the PP11($\pi\Delta$) wave. For all cases at 280 MeV that involved searching the phase of A(PP11-$\pi\Delta$), the fitting algorithm searched to a very small value without convergence. This kind of behavior was not observed either at higher or lower energies. For this reason, we did not prefer this 280 MeV solution even though inclusion of the PP11($\pi\Delta$) wave resulted in a smaller χ^2/ν.

In Table XLVIII, we summarize values of the integrated reaction cross section determined from the preferred VPI-model amplitudes in Table XLIV. The results in Table XLVIII agree well, except at 292 MeV, with the cross sections obtained by empirical analysis. The

TABLE XLVI. Alternate solutions at 292 and 331 MeV in modulus-phase form. The phase, in radians, is given in parentheses.

T_π(MeV)	PS11(ϵN)	PP11($\pi\Delta$)	DS13($\pi\Delta$)	χ^2/ν
292	0.122 ± 0.026 (2.718 ± 0.603)	0.102 ± 0.034 (1.020 ± 0.257)	0.056 ± 0.027 (0.059)	0.97
331	0.172 ± 0.022 (2.289 ± 0.211)	0.152 ± 0.014 (0.729 ± 0.140)	0.099 ± 0.008 (0.053)	1.01

TABLE XLVII. Alternate solutions in modulus-phase form for the new measurement at 256 MeV and the previous measurements at 254 and 280 MeV. The phase, in radians, is given in parentheses.

T_π(MeV)	PS11(εN)	PP11(πΔ)	χ^2/ν
254	0.046 ± 0.018 (1.449 ± 0.365)	0.032 ± 0.017 (0.832 ± 0.765)	1.77
256	0.045 ± 0.011 (1.503 ± 0.236)	0.026 ± 0.011 (1.694 ± 0.597)	0.71
280	0.056 ± 0.019 (1.067 ± 0.311)	0.071 ± 0.011 (0.201)	0.68

TABLE XLVIII. Integrated reaction cross section for $\pi^-p\to\pi^+\pi^-n$ as determined with the VPI model. Systematic uncertainties are included in the errors.

T_π (MeV)	σ_R (μb)	Error (μb)
203	13.8	1.5
230	58.9	3.3
255	163.0	6.3
280	373	16
292	517	35
331	1152	51
357	1873	78

isobar-model values were consistently smaller, however, differing by about 3% below 292 MeV and by about 1% above. At 292 MeV, the cross section determined with the VPI model was about 10% smaller than the

empirical result. Of the two results, we believe the isobar-model value to be the more reliable. The 10% discrepancy was due to a problem that the empirical function had with fitting the 292 MeV measurements of $\overline{|M|^2}$, which decreased fairly quickly near T_{max}. Since the measurements near T_{max} were better determined than those at lower energies, they were fitted well, whereas the fitted values at lower energies were somewhat high. These overestimated values at lower energies subsequently resulted in an integrated cross section that was too large.

In Figs. 67-69, we display $\frac{d\sigma}{dT}$ and $\frac{d\sigma}{d\Omega}$ at 292, 331, and 358 MeV as determined from our best comparisons with the LBL-SLAC solutions. In Figs. 70-76, we display the singly differential cross sections at each incident energy as calculated from the preferred solutions obtained with the VPI model. Dashed lines indicate the range of experimental uncertainty. The angular distributions for the final-state π^+ mesons were peaked at forward angles, which is consistent with production of a recoiling Δ^- at the higher energies. The forward peaking at lower energies disagrees with the conclusion of Batusov et al.[33] that the π^+ distribution is isotropic below 245 MeV. Our 203 MeV measurements, however, were not inconsistent with an isotropic distribution since, at that energy, we only took measurements at forward angles and these varied in precision between 11% and 32%. Where comparisons were possible between the angular distributions determined from the VPI model and from the LBL-SLAC solutions, we found that they qualitatively differed in their behavior at very forward angles. Values of $\frac{d\sigma}{d\Omega}$ determined with the VPI model did not increase as rapidly at forward angles as those determined from the LBL-SLAC solutions. The

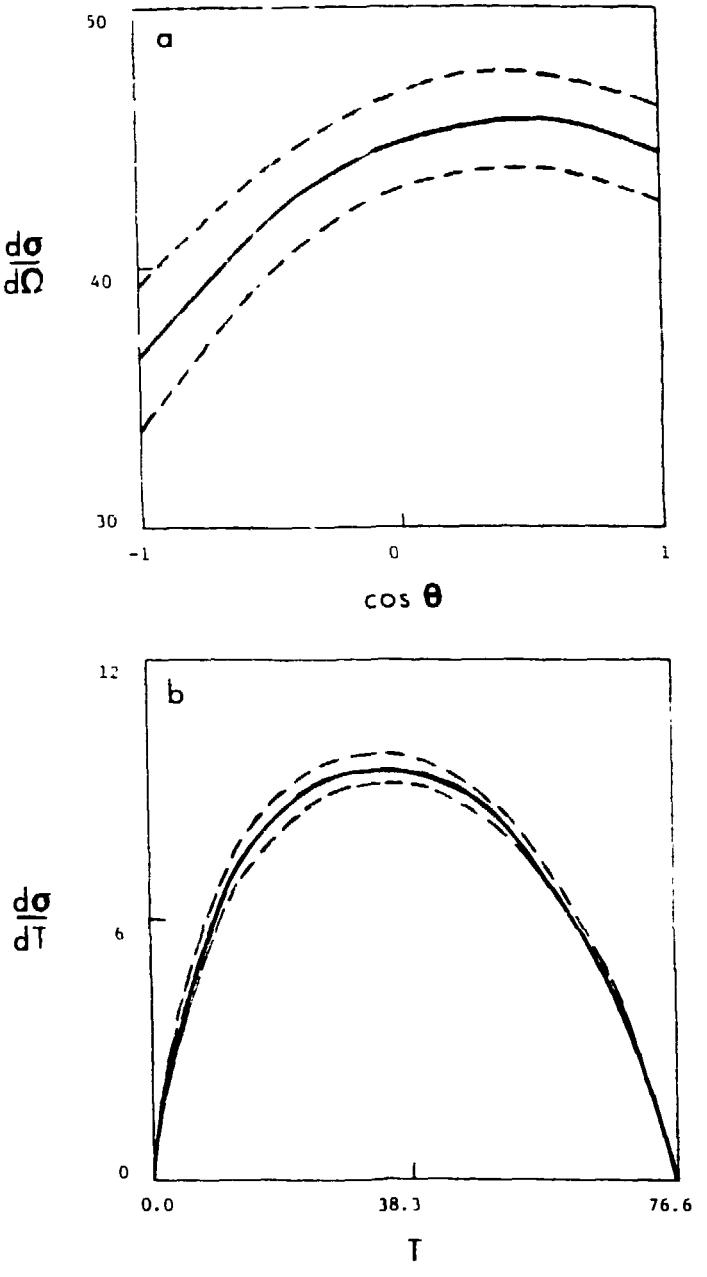

Figure 67. Differential cross sections at 292 MeV obtained from our best comparison with the LBL-SLAC solutions. These are (a) $d\sigma/d\Omega$ in μb/sr and (b) $d\sigma/dT$ in μb/MeV. Dashed lines indicate the range of experimental uncertainty. The data were obtained from a previous $\pi^- p \to \pi^+ \pi^- n$ experiment.[10]

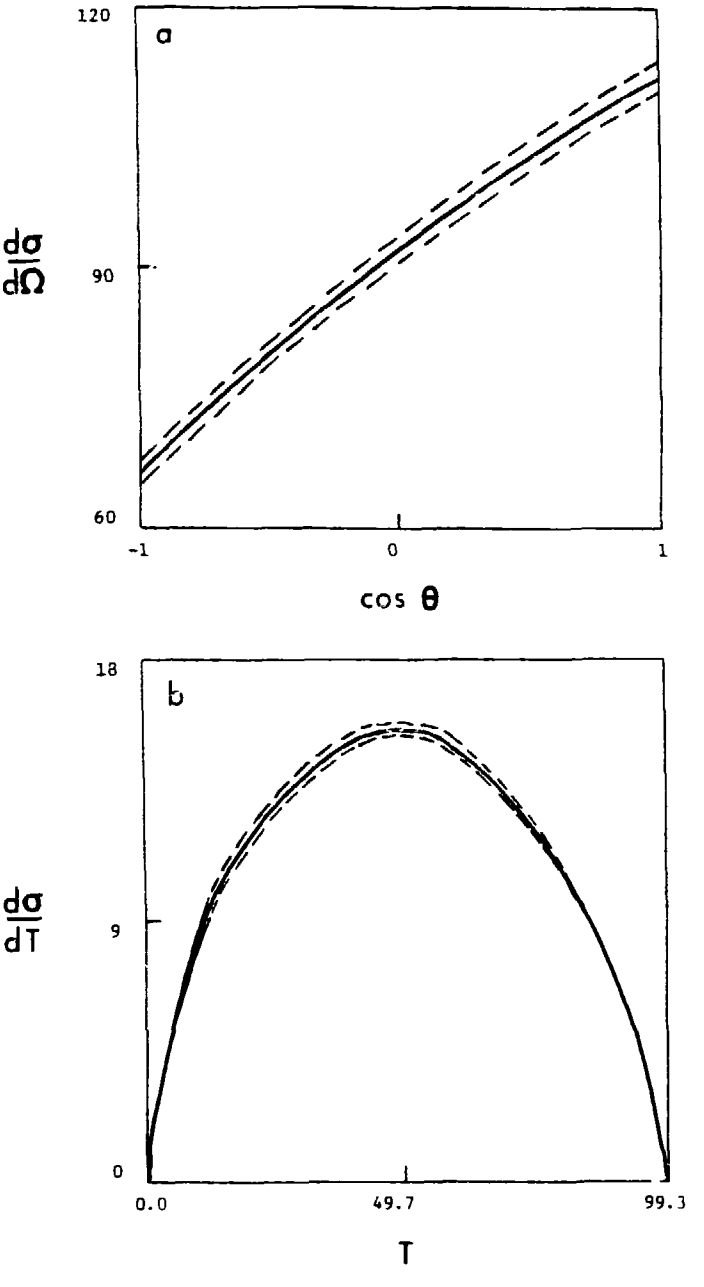

Figure 68. Differential cross sections at 331 MeV obtained from our best comparison with the LBL-SLAC solutions. These are (a) $d\sigma/d\Omega$ in μb/sr and (b) $d\sigma/dT$ in μb/MeV. Dashed lines indicate the range of experimental uncertainty. The data were obtained from a previous $\pi^- p \to \pi^+ \pi^- n$ experiment.[10]

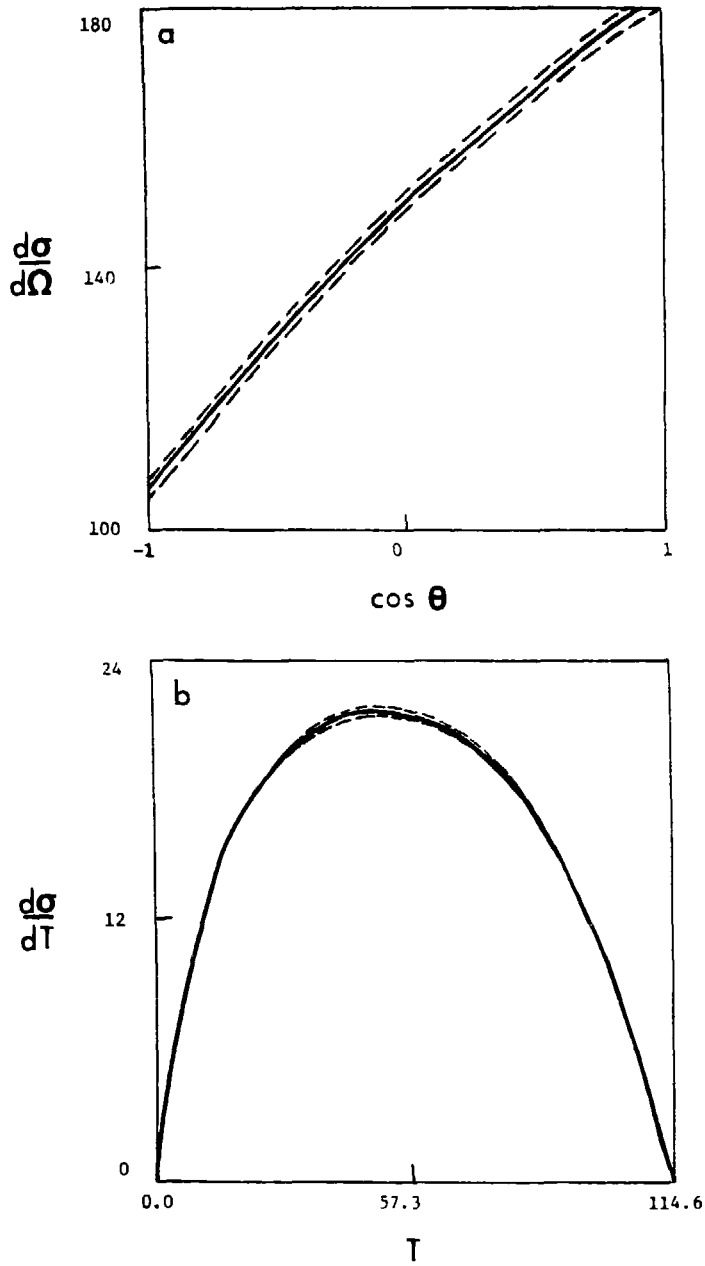

Figure 69. Differential cross sections at 358 MeV obtained from our best comparison with the LBL-SLAC solutions. These are (a) $d\sigma/d\Omega$ in μb/sr and (b) $d\sigma/dT$ in μb/MeV. Dashed lines indicate the range of experimental uncertainty.

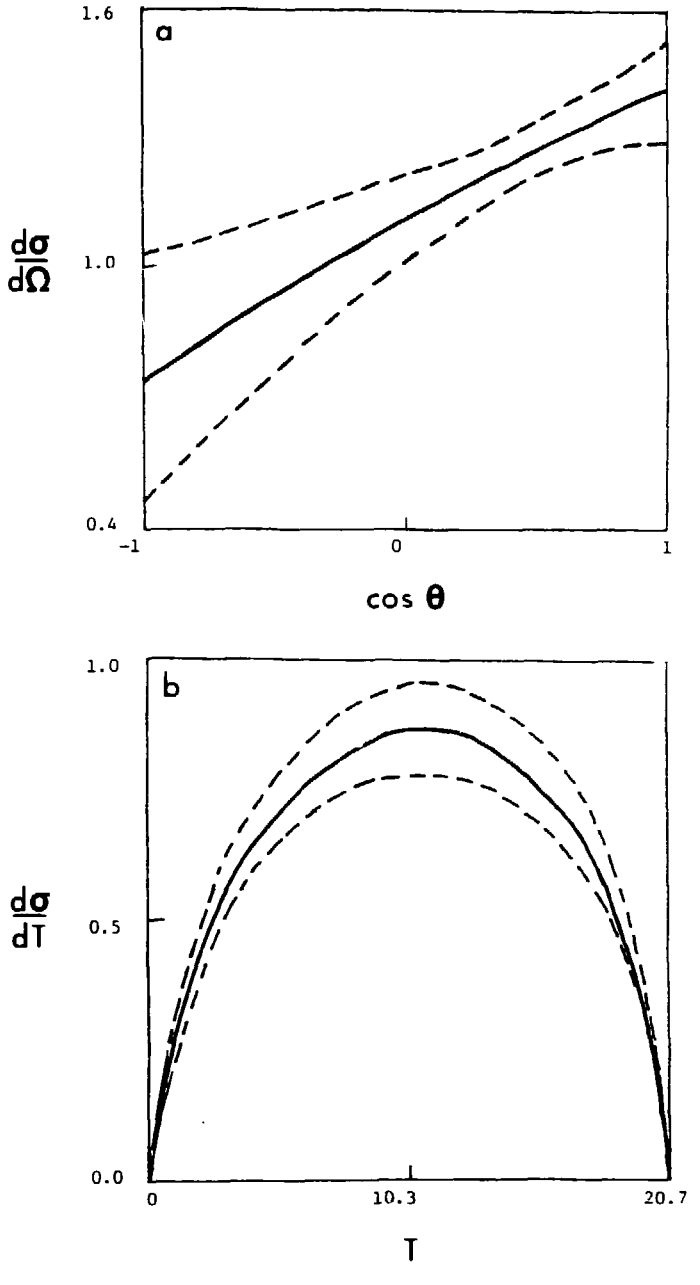

Figure 70. Differential cross sections at 203 MeV obtained with the VPI model. These are (a) $d\sigma/d\Omega$ in μb/sr and (b) $d\sigma/dT$ in μb/MeV. Dashed lines indicate the range of experimental uncertainty.

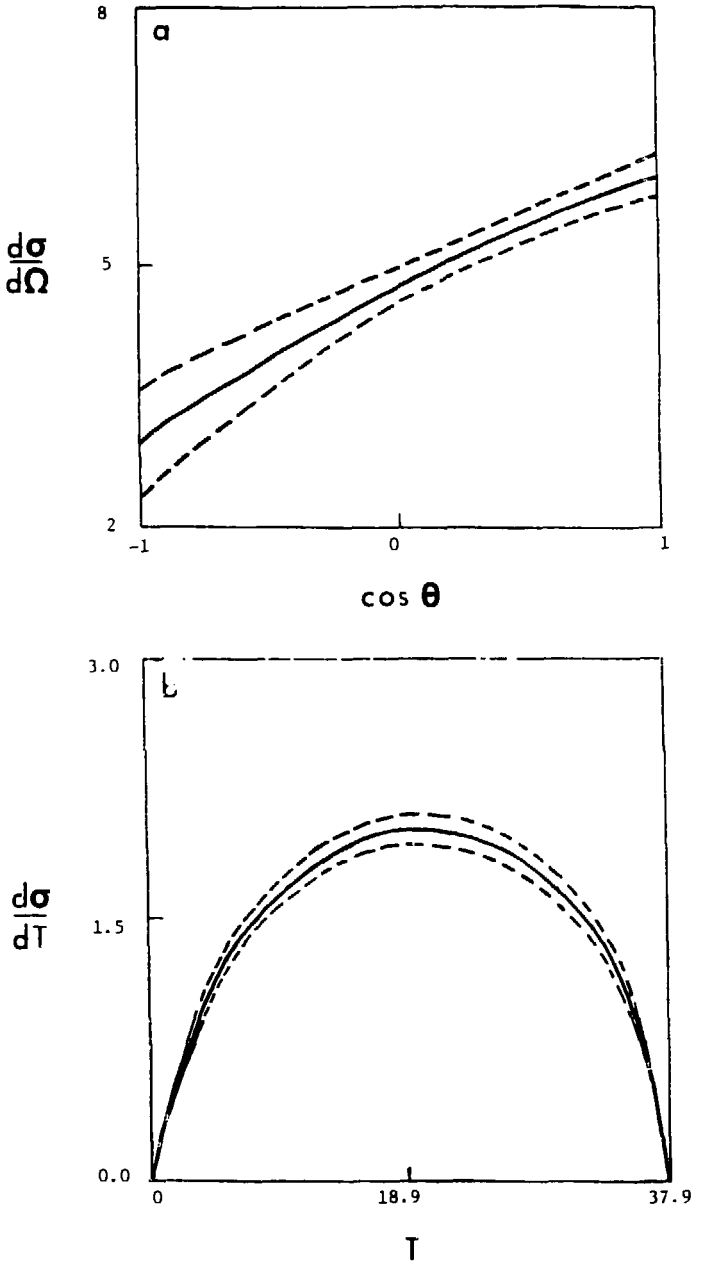

Figure 71. Differential cross sections at 230 MeV obtained with the VPI model. These are (a) $d\sigma/d\Omega$ in μb/sr and (b) $d\sigma/dT$ in μb/MeV. Dashed lines indicate the range of experimental uncertainty.

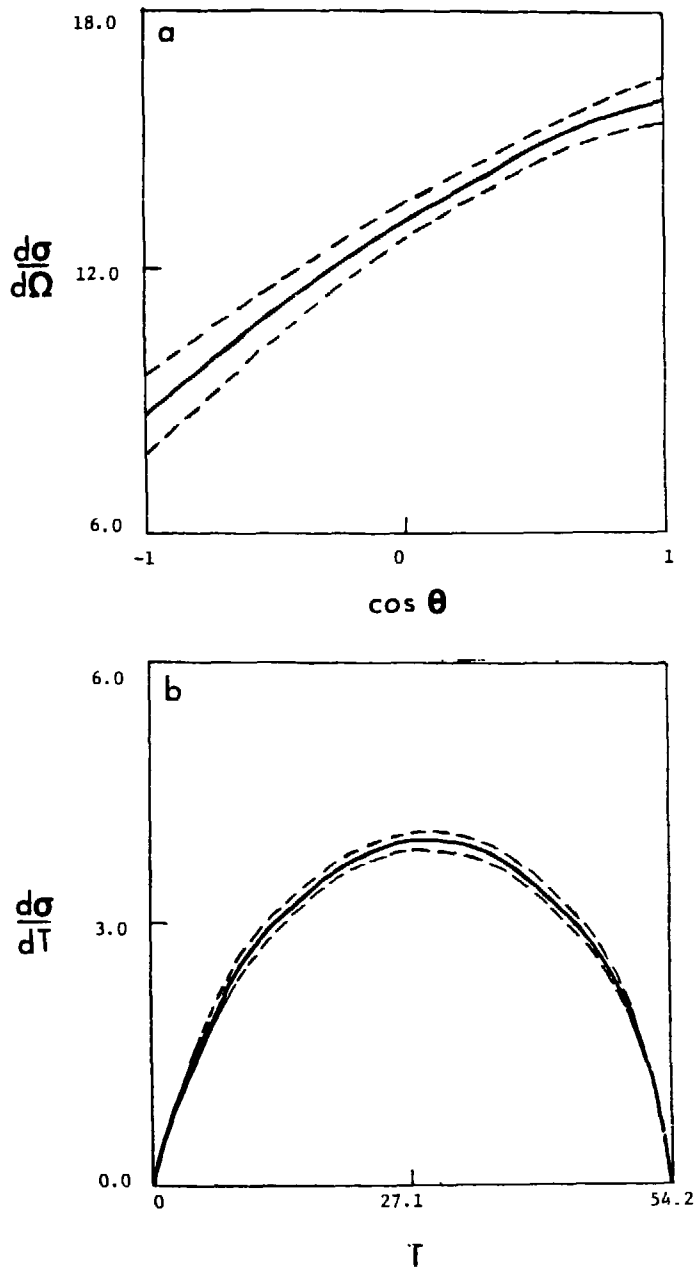

Figure 72. Differential cross sections at 256 MeV obtained with the VPI model. These are (a) $d\sigma/d\Omega$ in μb/sr and (b) $d\sigma/dT$ in μb/MeV. Dashed lines indicate the range of experimental uncertainty.

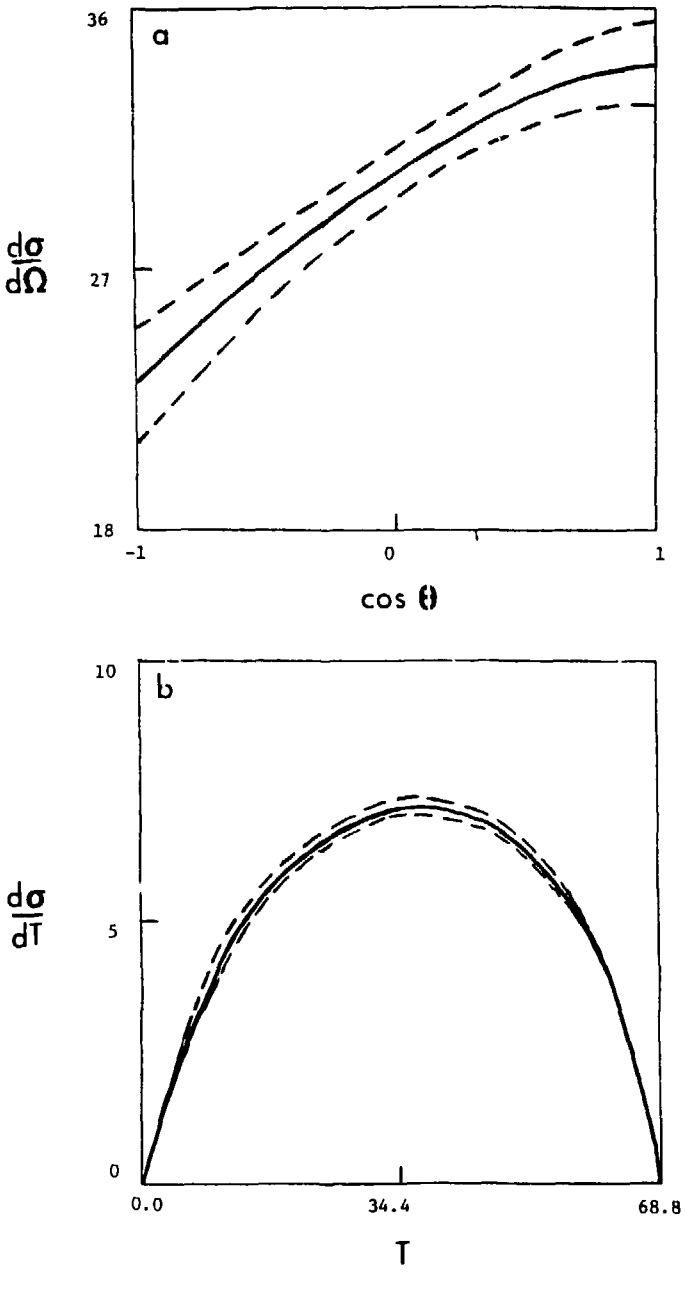

Figure 73. Differential cross sections at 280 MeV obtained with the VPI model. These are (a) $d\sigma/d\Omega$ in μb/sr and (b) $d\sigma/dT$ in μb/MeV. Dashed lines indicate the range of experimental uncertainty. The data were obtained from a previous $\pi^- p \to \pi^+ \pi^- n$ experiment.[10]

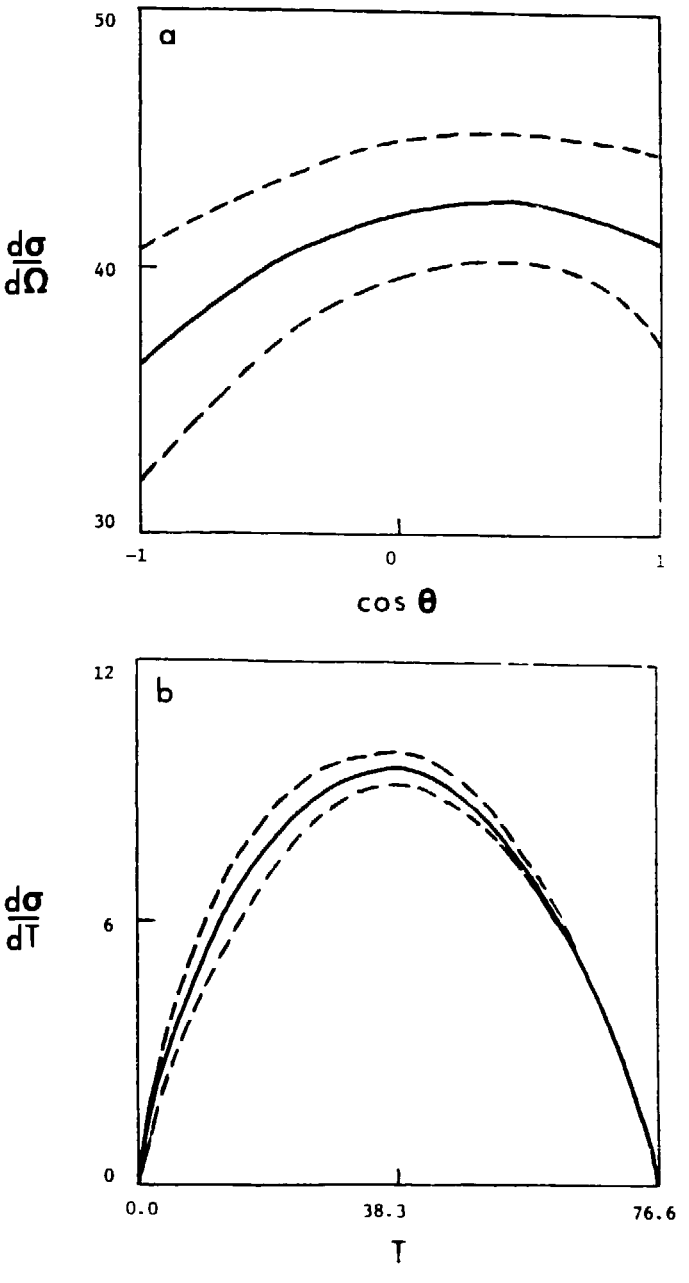

Figure 74. Differential cross sections at 292 MeV obtained with the VPI model. These are (a) $d\sigma/d\Omega$ in μb/sr and (b) $d\sigma/dT$ in μb/MeV. Dashed lines indicate the range of experimental uncertainty. The data were obtained from a previous $\pi^- p \to \pi^+ \pi^- n$ experiment.[10]

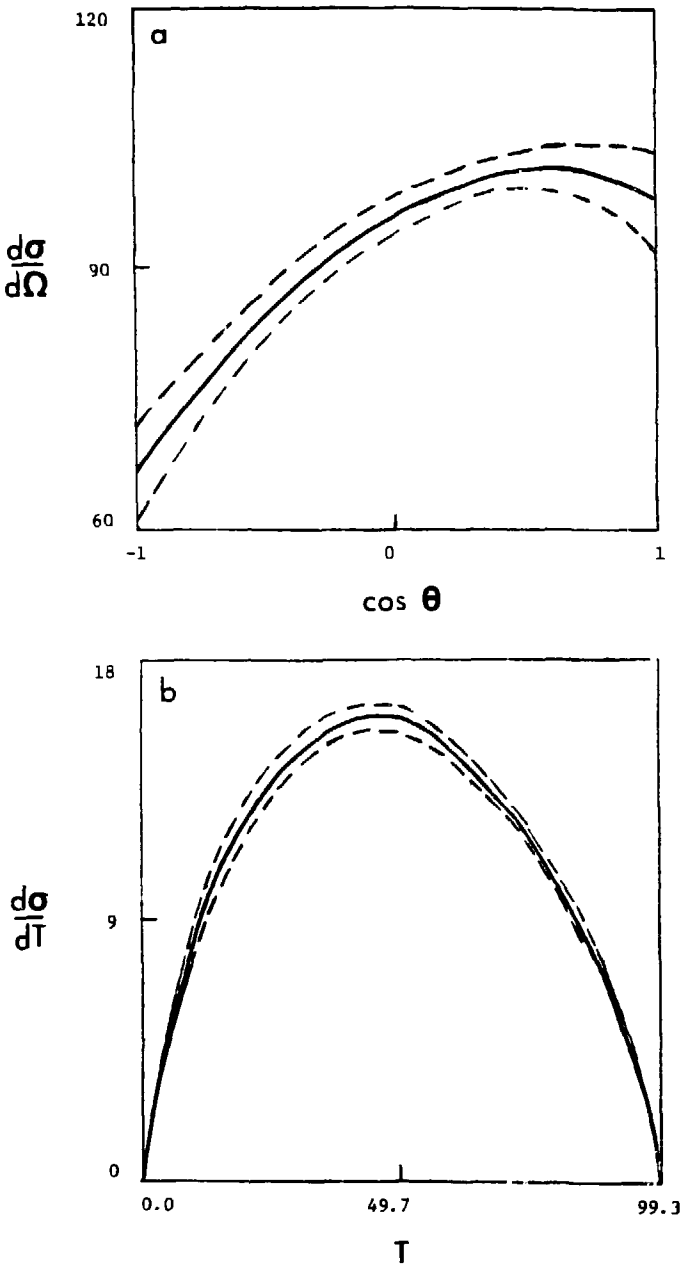

Figure 75. Differential cross sections at 331 MeV obtained with the VPI model. These are (a) $d\sigma/d\Omega$ in $\mu b/sr$ and (b) $d\sigma/dT$ in $\mu b/MeV$. Dashed lines indicate the range of experimental uncertainty. The data were obtained from a previous $\pi^- p \to \pi^+ \pi^- n$ experiment.[10]

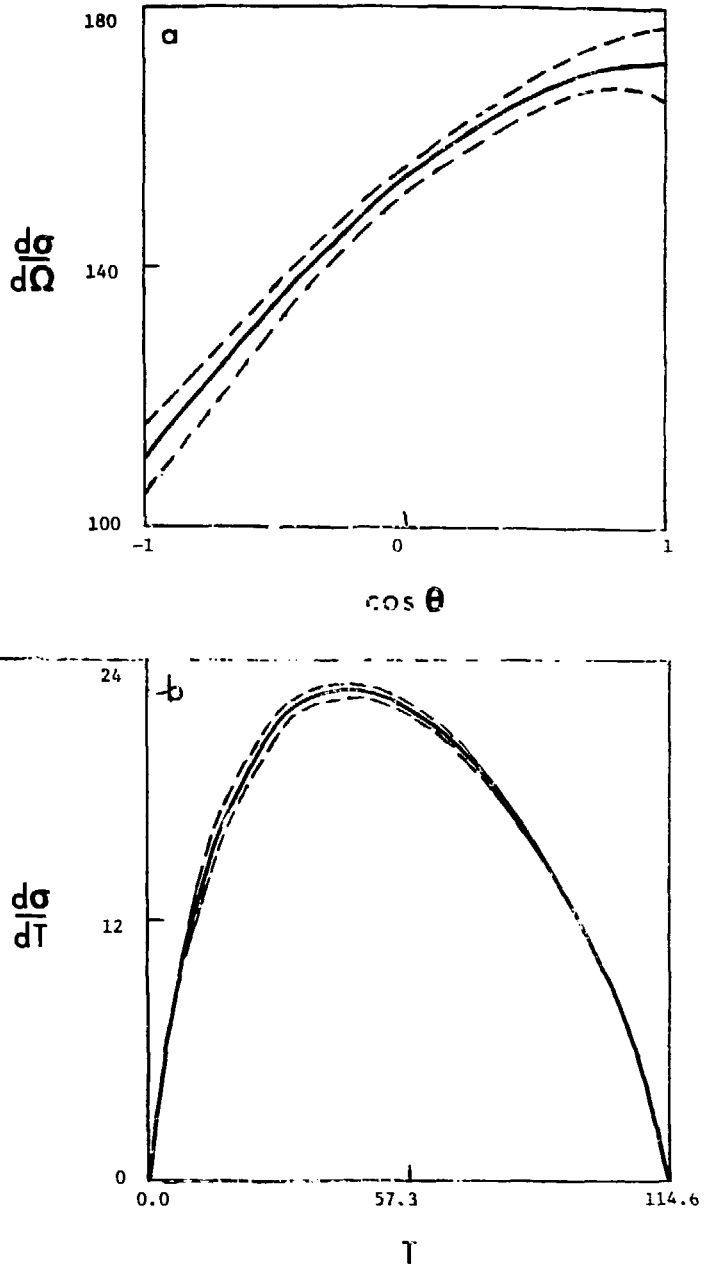

Figure 76. Differential cross sections at 358 MeV obtained with the VPI model. These are (a) dσ/dΩ in μb/sr and (b) dσ/dT in μb/MeV. Dashed lines indicate the range of experimental uncertainty.

energy distributions were dominated by phase space and hence were less sensitive to whatever model was used to fit the measurements.

We obtained values for $\langle|M_c|^2\rangle$ with the isobar models that were extrapolated to threshold, as discussed in Chapter VI, so that our prior value for the chiral-symmetry-breaking parameter ξ could be checked and, possibly, also be better established. The $\langle|M_c|^2\rangle$ obtained from comparisons with the LBL-SLAC solutions are given in Table XLIX and those obtained from the preferred VPI-model amplitudes are given in Table L. Following the procedure discussed in Chapter VI, we fitted the $\langle|M_c|^2\rangle$ obtained from our best comparisons with the LBL-SLAC solutions at the highest three energies and from our preferred VPI-model amplitudes at the lower energies to yield $\chi^2/\nu = 1.53$ and the threshold value

$$\langle|M_c|^2\rangle^{1/2} = 2.362 \pm 0.282\ m_\pi^{-3},$$

TABLE XLIX. Values of $\langle|M_c|^2\rangle$ at 292, 331, and 358 MeV obtained from comparisons with the LBL-SLAC solutions.

T_π (MeV)	$\langle\|M_c\|^2\rangle$ (m_π^{-6})	Error (m_π^{-6})
292[a]	37.5	2.1
292	29.5	1.5
331	43.2	1.9
358	50.2	2.1

[a]This value corresponds to the case in which both A(PS11-εN) and the normalization were varied.

TABLE L. Values of $\langle|M_c|^2\rangle$ for $\pi^-p\to\pi^+\pi^-n$ as determined with the VPI model. Systematic uncertainties are included in the errors.

T_π (MeV)	$\langle\|M_c\|^2\rangle$ (m_π^{-6})	Error (m_π^{-6})
203	16.2	1.8
230	19.2	1.1
255	24.5	0.9
280	32.7	1.4
292	35.6	2.4
331	43.5	1.9
357	51.0	2.1

which is 3% lower than the result of the empirical analysis and corresponds to

$$\xi = 0.03 \pm 0.27 ,$$

$$a_0 = 0.174 \pm 0.017\ m_\pi^{-1},$$

$$a_2 = -0.051 \pm 0.007\ m_\pi^{-1}.$$

This value of ξ is consistent, as before, with zero as required for the Weinberg Lagrangian.[3] We also extrapolated $\langle|M_c|^2\rangle$ to threshold using the VPI-model values at all incident energies. These were fitted with $\chi^2/\nu = 1.27$ to yield, at threshold,

$$\langle|M_c|^2\rangle^{1/2} = 2.310 \pm 0.291\ m_\pi^{-3},$$

which corresponds to

$$\xi = 0.08 \pm 0.27 ,$$

$$a_0 = 0.171 \pm 0.017\ m_\pi^{-1},$$

$$a_2 = -0.052 \pm 0.007\ m_\pi^{-1}.$$

The smaller χ^2 was obtained mainly by replacing the value of $\langle|M_c|^2\rangle$ at 292 MeV obtained from our best comparison with the LBL-SLAC solutions with that obtained from the VPI model. Both sets of parameters obtained by fitting the isobar-model values of $\langle|M_c|^2\rangle$ correspond to $\langle|M_c|^2\rangle = 34.7\ m_\pi^{-6}$ at 292 MeV, which agrees better with the value obtained with the VPI model than that obtained by comparison with the LBL-SLAC solutions. The χ^2/ν for the cases discussed here were larger than that for the empirical analysis because the VPI-model of $\langle|M_c|^2\rangle$ at 203 MeV was less well fitted by the linear function of the total c.m. energy. A plot of the $\langle|M_c|^2\rangle$ obtained with the VPI model showing the extrapolation to threshold is displayed in Fig. 77.

In Table LI, we give our cross-section predictions for other $\pi N \to \pi\pi N$ charge reactions at 292, 331, and 358 MeV obtained from our comparisons with the LBL-SLAC solutions. In Table LII, we present predictions calculated with the VPI model from the preferred partial-wave amplitudes. The predictions for each of the reactions $\pi^- p \to \pi^0\pi^- p$ and $\pi^+ p \to \pi^0\pi^+ p$ agreed roughly with each other and with the available experimental measurements above about 300 MeV. Predictions for $\pi^+ p \to \pi^+\pi^+ n$ calculated from the LBL-SLAC solutions were in good agreement with measurements above 300 MeV, whereas predictions calculated with the VPI model were four to six times high. No measurements of

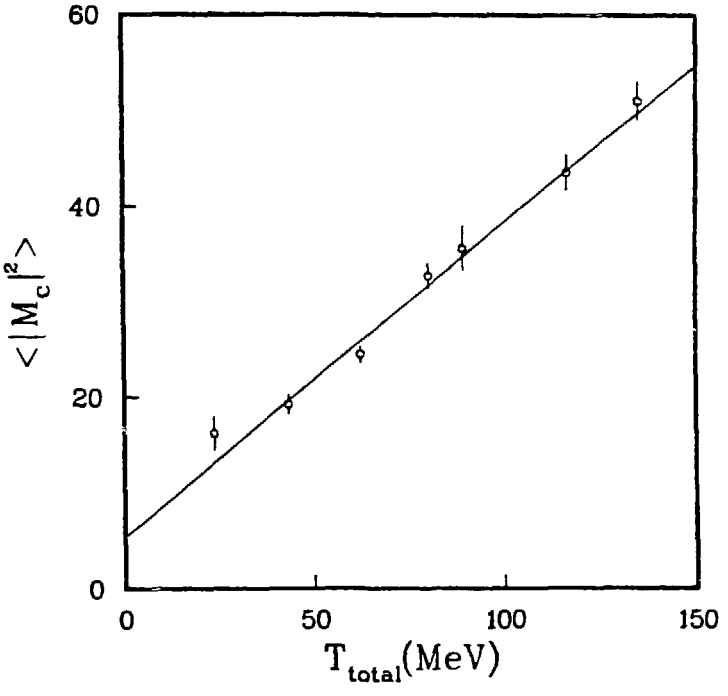

Figure 77. The $\langle |M_c|^2 \rangle$ obtained with the VPI model.

TABLE LI. Cross-section predictions (in μb) at 292, 331, and 358 MeV obtained from comparisons with the LBL-SLAC solutions.

T_π(MeV)	$\pi^-p\to\pi^0\pi^0n$	$\pi^-p\to\pi^0\pi^-p$	$\pi^+p\to\pi^0\pi^+p$	$\pi^+p\to\pi^+\pi^+n$
292[a]	146 ± 9	85 ± 18	138 ± 29	26 ± 6
292	118 ± 6	77 ± 4	125 ± 6	24 ± 1
331	286 ± 13	288 ± 13	418 ± 18	82 ± 4
358	427 ± 18	518 ± 22	644 ± 27	126 ± 5

[a]These predictions correspond to the case in which both A(PS11-εN) and the normalization were varied.

TABLE LII. Cross-section predictions (in μb) for $\pi N\to\pi\pi N$ charge reactions. The predictions are based upon the preferred partial-wave amplitudes obtained with the VPI model.

T_π(MeV)	$\pi^-p\to\pi^0\pi^0n$	$\pi^-p\to\pi^0\pi^-p$	$\pi^+p\to\pi^0\pi^+p$	$\pi^+p\to\pi^+\pi^+n$
203	14 ± 7	3	3	4
230	45 ± 10	10	13	18
256	105 ± 14	26	34	48
280	220 ± 26	51	65	95
292	378 ± 133	125 ± 25	187 ± 89	151 ± 18
331	788 ± 269	337 ± 51	277 ± 82	309 ± 20
358	1236 ± 181	454 ± 46	665 ± 129	529 ± 32

the reaction $\pi^-p\to\pi^0\pi^0n$ were available in our energy range. Predictions for this reaction calculated from the LBL-SLAC solutions were about a factor of three smaller than those calculated with the VPI

model. As discussed below, these differences resulted in different values for η_{P11} at the highest three energies.

Our determinations of the $\eta_{\ell IJ}$ from our comparisons with the LBL-SLAC solutions are summarized in Table LIII and from the preferred amplitudes obtained with the VPI model in Table LIV. The errors include contributions from systematic uncertainties as discussed earlier. The errors quoted for the LBL-SLAC elasticities are probably unrealistic since no uncertainties were associated with the interpolated partial-wave amplitudes. At the three highest energies, the η_{D13} and η_{D33} calculated with the VPI model agree within about one standard deviation of those obtained by comparing with the LBL-SLAC solutions. Because of the larger $\pi^-p\to\pi^0\pi^0n$ cross-section prediction of the VPI model, the η_{P11} for that model at 292, 331, and 358 MeV were respectively 1%, 3%, and 9% lower than the corresponding elasticities determined from the LBL-SLAC solutions. Nevertheless, the

TABLE LIII. Elasticities $\eta_{\ell IJ}$ of the initial P11, D13, and D33 waves at 292, 331, and 358 MeV obtained from comparisons with the LBL-SLAC solutions.

T_π(MeV)	η_{P11}	η_{D13}	η_{D33}
292[a]	0.9675 ± 0.0020	0.9968 ± 0.0001	0.9975 ± 0.0001
292	0.9749 ± 0.0013	0.9971 ± 0.0001	0.9978 ± 0.0001
331	0.9137 ± 0.0040	0.9936 ± 0.0003	0.9912 ± 0.0004
358	0.8533 ± 0.0067	0.9808 ± 0.0008	0.9854 ± 0.0006

[a]These elasticities correspond to the case in which both A(PS11-εN) and the normalization were varied.

TABLE LIV. Elasticities η_{2IJ} of the initial P11, D13, and D33 waves obtained with the VPI model.

T_π(MeV)	η_{P11}	η_{D13}	η_{D33}
203	0.9989 ± 0.0003	1.000	1.000
230	0.9955 ± 0.0005	1.000	1.000
256	0.9867 ± 0.0008	1.000	1.000
280	0.9673 ± 0.0019	1.000	1.000
292	0.9535 ± 0.0177	0.9947 ± 0.0043	0.9989 ± 0.0018
331	0.8861 ± 0.0442	0.9813 ± 0.0115	0.9990 ± 0.0024
358	0.7859 ± 0.0462	0.9718 ± 0.0143	0.9936 ± 0.0062

η_{P11} calculated with the VPI model were in reasonable agreement, considering their errors, with the values determined from the LBL-SLAC solutions.

In elastic phase shift analyses below 300 MeV, it has been customary to set $\eta_{D13} = \eta_{D33} = 1$ since η_{D13} and η_{D33} are only slightly different from unity in our energy range. Prior estimates of η_{P11} have been based upon integrated cross sections for $\pi^-p \to \pi\pi N$ reactions. As we have seen, such measurements exist below about 300 MeV only for the $\pi^-p \to \pi^+\pi^-n$ charge channel. Thus, contributions to η_{P11} from other charge channels have either had to be neglected or estimated from an assumption, such as dominance of $\pi^-p \to \rho n$, which implies[15]:

$$\frac{\sigma(\pi^-p \to \pi^0\pi^0 n)}{\sigma(\pi^-p \to \pi^+\pi^- n)} = \frac{1}{2} .$$

Our η_{P11} below 300 MeV are in good agreement with those of Carter et al.,[15] although our values are very slightly smaller. This result is to be expected since their elasticities were mainly based on the $\pi^-p \to \pi^+\pi^-n$ cross-section measurements of Batusov et al.,[33,34] which, as stated earlier, were 1.3-1.5 times smaller than ours. Since our estimates of η_{P11} are based upon cross sections with several times the accuracy of previous measurements, we suggest that our elasticities be considered in future elastic phase shift analyses.

CHAPTER VIII

SUMMARY AND CONCLUSIONS

We have measured the doubly differential cross section $\frac{d^2\sigma}{d\Omega dT}$ for π^+ mesons produced in the reaction $\pi^-p\rightarrow\pi^+\pi^-n$ at 203, 230, 256, and 358 MeV. The doubly differential cross section was measured at 11 points at 203 MeV, 16 points at 230 MeV, 20 points at 256 MeV, and 21 points at 358 MeV. We also reanalyzed data from a previous experiment[10] that had measured $\frac{d^2\sigma}{d\Omega dT}$ at 254, 280, 292, 331, and 356 MeV. The $\frac{d^2\sigma}{d\Omega dT}$ were calibrated by measuring π^-p elastic scattering and normalizing the measured angular distributions to known elastic cross sections.

From each measurement of $\frac{d^2\sigma}{d\Omega dT}$, we determined $\overline{|M|^2}$, the square modulus of the matrix element averaged over unobserved kinematic variables and divided by the square of the incident c.m. momentum. The $\overline{|M|^2}$ were fitted to an empirical function of the measured kinematic variables to facilitate extrapolation and integration of the measured $\frac{d^2\sigma}{d\Omega dT}$. By this procedure, we obtained σ_R, the integrated reaction cross section, and $\langle|M_c|^2\rangle$, the square modulus of the matrix element corrected for Coulomb attraction in the initial and final states, averaged over all phase space, and divided by the square of the incident c.m. momentum. The σ_R and $\langle|M_c|^2\rangle$ were combined at 254 and 256 MeV and at 356 and 358 MeV to give greater statistical accuracy. Our σ_R had about twice the accuracy of previous measurements above 300 MeV and about five times the accuracy of previous

measurements below. The total uncertainty in σ_R was about 11% at 203 MeV, 5% at 230 MeV, 4% at 255 MeV, 4% at 280 MeV, 6% at 292 MeV, 4% at 331 MeV, and 4% at 357 MeV. Most of the uncertainty in the 331 and 357 MeV measurements was due to a 4% uncertainty in the normalization to π^-p elastic scattering at those energies. Our measurement at 203 MeV is nearer to the 172.4 MeV threshold than any other now in existence.

The seven $\langle|M_c|^2\rangle$ were extrapolated to threshold where comparisons with soft-pion theory are most straightforward. We established ξ, the chiral-symmetry-breaking parameter of soft-pion theory, and a_0 and a_2, the S-wave isoscalar and isotensor $\pi\pi$ scattering lengths. The ξ obtained was consistent with $\xi = 0$ as required by the phenomenological πN Lagrangian of Weinberg.[3] It was inconsistent with either $\xi = 1$ or $\xi = -2$ required for the two Lagrangians of Schwinger.[12] The a_0 determined by this experiment was small and positive like that obtained from a recent measurement of K_{e4} decay, although our value was somewhat smaller.

We also used our data to investigate isobar models for $\pi N \to \pi\pi N$ reactions. Partial-wave amplitudes were interpolated to 292, 331, and 358 MeV from the 11-wave solutions obtained from a recent isobar-model analysis performed by an LBL-SLAC collaboration.[13] We were successful in obtaining excellent agreement with the data at 331 and 358 MeV simply by renormalizing the interpolated amplitudes. At 292 MeV, we obtained good agreement by varying the PS11(εN) amplitude in addition to the normalization. These results indicate that the standard isobar model for $\pi N \to \pi\pi N$ is a viable method of analysis for single pion production in our energy range.

At each incident energy, we compared our data with the VPI isobar model,[14] which includes a background term calculated from soft-pion theory in the matrix element. Good agreement was reached with the measurements at 280 MeV and below by varying only the PS11(εN) amplitude. For the measurements at the three highest energies, our preferred solutions varied the PP11($\pi\Delta$), DS13($\pi\Delta$), and DS33($\pi\Delta$) amplitudes as well as the PS11(εN) amplitude. Inclusion of the additional partial waves at the highest energies was necessary because the 331 and 358 MeV measurements were within the half width for Δ production.

We redetermined σ_R and $\langle|M_c|^2\rangle$, where possible, from both isobar models. The σ_R estimated with the isobar models were consistently a few percent smaller than those estimated with the empirical analysis. Our prior determination of ξ was checked by repeating the extrapolation to threshold using the isobar-model values of $\langle|M_c|^2\rangle$. The redetermined values of ξ, a_0, and a_2 were consistent with those established by the empirical analysis. The isobar models permitted us to predict cross sections for other $\pi N \to \pi\pi N$ reactions: $\pi^- p \to \pi^0\pi^0 n$, $\pi^- p \to \pi^0\pi^- p$, $\pi^+ p \to \pi^0\pi^+ p$, and $\pi^+ p \to \pi^+\pi^+ n$. Our predictions may be of use to future experiments that attempt precision measurements of these reactions. Finally, the isobar models enabled us to estimate elasticities $\eta_{\ell IJ}$ of the P11, D13, and D33 elastic waves. As a consequence of our precise cross-section measurements, our estimates of η_{P11} should be improvements over previous values.

ACKNOWLEDGEMENTS

I wish to thank the Department of Physics and Astronomy, University of Wyoming, and the Clinton P. Anderson Meson Physics Facility for the services and facilities they provided. I am grateful to the group at the Virginia Polytechnic Institute and State University who provided me with copies of their isobar-model codes.

I would like to extend my sincere appreciation to Professors Glen A. Rebka, Jr. and Raymond Kunselman for their guidance and support. Special thanks are due Dr. Vigdor L. Teplitz for many enlightening discussions regarding the VPI isobar model. I wish to thank Chris Bjork for his guidance and many pleasant discussions during my stay in Los Alamos. I am also indebted to my other collaborators: John Walter, Steven Jones, and Charles Bordner, particularly for their contributions to program development. I thank Robert Carawon for valuable assistance toward preparation for the experiment.

I would like to acknowledge the financial support of the Department of Energy, Division of High Energy and Nuclear Physics, and the Clinton P. Anderson Meson Physics Facility, Experimental Nuclear and Particle Physics Group.

REFERENCES AND FOOTNOTES

1. Lay-Nam Chang, Phys. Rev. 162, 1497 (1967).

2. M. G. Olsson and Leaf Turner, Phys. Rev. Lett. 20, 1127 (1968).

3. Steven Weinberg, Phys. Rev. Lett. 18, 188, (1967).

4. M. G. Olsson and Leaf Turner, Phys. Rev. 181, 2141 (1969); Leaf Turner, Ph.D. dissertation, University of Wisconsin, 1969 (unpublished).

5. J. Iliopolous, Nuovo Cimento 52A, 192 (1967); J. Iliopolous, Nuovo Cimento 53A, 552 (1968); P. Grassberger, Bonn preprint, p.12-125 (1972).

6. J. Franklin, Phys. Rev. D11, 513 (1975).

7. R. Arnowitt, M. H. Friedman, and P. Nath, Phys. Rev. Lett. 19, 812 (1967); R. Arnowitt, M. H. Friedman, and P. Nath, Phys. Rev. 174, 1999, 2008; 175, 1802 (1968); S. G. Brown and G. B. West, Phys. Rev. 168, 1605; 174, 1777, 1786 (1968); T. Das, V. Mathur, and S. Okubo, Phys. Rev. Lett. 19, 900 (1967); D. Geffen, Phys. Rev. Lett. 19, 770 (1967); I. S. Gerstein and H. J. Schnitzer, Phys. Rev. 170, 1638 (1968); H. J. Schnitzer and S. Weinberg, Phys. Rev. 164, 1828 (1967).

8. Several useful reviews of methods for calculating corrections to simple current-algebra results have been presented by the following: R. Arnowitt, Proceedings of the Conference on $\pi\pi$ and $K\pi$ Interactions, Argonne National Laboratory, p.619, 1969; P. Nath, Proceedings of the IVth International Conference on Experimental Meson Spectroscopy, Boston, Mass., U.S.A., April, 1974; B. R. Martin, D. Morgan, and G. Shaw, Pion-Pion Interactions in Particle Physics (Academic, New York, 1976).

9. M. Gell-Mann and M. Lévy, Nuovo Cimento 16, 705 (1960).

10. John B. Walter, Ph.D. dissertation, University of Wyoming, 1979 [Los Alamos Scientific Laboratory report LA-8377-T, 1980].

11. Before January 1, 1981, the laboratory was named Los Alamos Scientific Laboratory (LASL).

12. J. Schwinger, Phys. Lett. 24B, 473 (1967); Proceedings of the Seventh Hawaii Topical Conference on Particle Physics, 1977, editted by J. Okada (Univ. of Hawaii, Honolulu, 1977).

13. David J. Herndon, Paul Söding, and Roger J. Cashmore, Phys. Rev. D11, 3165 (1975); D. J. Herndon, R. Longacre, L. R. Miller, A. H. Rosenfeld, G. Smadja, P. Söding, R. J. Cashmore, and D. W. G. S. Leith, Phys. Rev. D11, 3183 (1975).

14. R. A. Arndt, J. B. Cammarata, Y. N. Goradia, R. H. Hackman, V. L. Teplitz, D. A. Dicus, R. Aaron, and R. S. Longacre, Phys. Rev. D20, 651 (1979).

15. J. R. Carter, D. V. Bugg, and A. A. Carter, Nucl. Phys. B58, 378 (1973).

16. R. D. Werbeck and R. J. Macek, IEEE Trans. Nucl. Sci. NS-22, 1598 (1975); H. H. Howard, B. Storms, and S. P. Slatkin, LAMPF Users Handbook, (Los Alamos Scientific Laboratory, Medium Energy Physics Division, Los Alamos, NM 1974).

17. Karl L. Brown, "A First- and Second-Order Matrix Theory for the Design of Beam Transport Systems and Charged Particle Spectrometers," Stanford Linear Accelerator Center report SLAC-75, 1972.

18. Alden T. Oyer, Ph.D. dissertation, University of Wyoming, 1976 [Los Alamos Scientific Laboratory report LA-6599-T, 1976].

19. Christopher Morris, private communication.

20. The computer code for data acquisition was based on one written by W. K. McFarlane, Temple University, Philadelphia, PA.

21. The library of routines KLTAPE.OLB was written by Richard Thomas for use on LAMPF PDP-11 computers.

22. Particle Data Group, Rev. Mod. Phys. 50, No. 2, Part II (April 1978).

23. B. Rossi, High Energy Particles, (Prentice Hall, Englewood Cliffs, NJ 1961).

24. For most of the single pion production measurements of Ref. 10, the value of e_0 was redetermined to be 0.831 ± 0.034. For several measurements at 292 MeV, the value was 0.654 ± 0.27.

25. The minimizing algorithm is based on the procedure implemented at the laboratory in 1965 by Joel Trussell and described by Moore and Zeigler. R. H. Moore and R. K. Zeigler, "The Solution of the General Least Squares Problem with Special Reference to High Speed Computers," Los Alamos Scientific Laboratory report LA-2367, 1960.

26. K. L. Brown and Ch. Iselin, "DECAY TURTLE (Trace Unlimited Rays Through Lumped Elements), A Computer Program for Simulating Charged Particle Beam Transport Systems, Including Decay Calculations," CERN report 74-2, 1974.

27. J. B. Walter and G. A. Rebka, Jr., "SCATPI, A Subroutine for Calculating πN Cross Sections and Polarizations for Incident Pion Kinetic Energies Between 90 and 300 MeV," Los Alamos Scientific Laboratory report LA-7731-MS, 1979.

28. P. M. Ogden, D. E. Hagge, J. A. Helland, M. Banner, J. F. Detoeaf, and J. Teiger, Phys. Rev. 137, B1115 (1965).

29. H. R. Rugge and O. T. Vik, Phys. Rev. 129, 2300 (1963).

30. P. J. Bussey, J. R. Carter, D. R. Dance, D. V. Bugg, A. A. Carter, and A. M. Smith, Nucl. Phys. B58, 363 (1973).

31. The σ_0 defined here, unlike that of Ref. 10, does not include the factor $8(G/2m_N)^6(g_V/g_A)^4$. Olsson and Turner (Refs. 2 and 4) call this quantity $Q^2\times$phase space.

32. The metric, normalization of states, and conventions for matrix elements, gamma matrices, phase space, and flux factor are those of J. D. Bjorken and S. D. Drell, Relativistic Quantum Fields (McGraw-Hill, New York, 1965).

33. Yu. A. Batusov, S. A. Bunyatov, V. M. Sidorov, and V. A. Yarba, Yad. Fiz. 1, 526 (1965) [Sov. J. Nucl. Phys. 1, 374 (1965)].

34. Yu. A. Batusov, N. P. Bogachev, V. M. Sidorov, and V. A. Yarba, Dokl. Akad. Nauk SSSR 133, 52 (1960) [Sov. Phys. Dokl. 5, 731 (1961)].

35. J. A. Jones, W. W. M. Allison, and D. H. Saxon, Nucl. Phys. B83, 93 (1974).

36. Walton A. Perkins, III, John C. Caris, Robert W. Kenney, and Victor Perez-Mendez, Phys. Rev. 118, 1364 (1960).

37. D. H. Saxon, J. H. Mulvey, and W. Chinowsky, Phys. Rev. D2, 1790 (1970).

38. T. D. Blokhintseva et al., in Proceedings of the Twelfth Annual International Conference on High Energy Physics, Dubna, U.S.S.R., 1964 (Atomizdat., Moscow, U.S.S.R., 1965).

39. Barry C. Barish, Richard J. Kurz, Victor Perez-Mendez, and Julius Solomon, Phys. Rev. 135, B416 (1964).

40. Janos Kirz, Joseph Schwartz, and Robert D. Tripp, Phys. Rev. 130, 2481 (1963).

41. R. Koch and E. Pietarinen, Nucl. Phys. A336, 331 (1980).

42. Particle Data Group, Rev. Mod. Phys. 52, No. 2, Part II (April 1980).

43. M. L. Goldberger and S. B. Treiman, Phys. Rev. 110, 1178 (1958).

44. L. Rosselet, P. Extermann, J. Fischer, O. Guisan, R. Mermod, R. Sachot, A. M. Diamant-Berger, P. Bloch, G. Bunce, B. Devaux, N. Do-Duc, G. Marel, and R. Turlay, Phys. Rev. D15, 574 (1977).

45. R. M. Sternheimer and S. J. Lindenbaum, Phys. Rev. 123, 333 (1961); D. Z. Freedman, C. Lovelace, and J. M. Namyslowski, Nuovo Cimento 43A, 218 (1966); M. G. Olsson and G. B. Yodh, Phys. Rev. 145, 1309 (1966); D. Morgan, Phys. Rev. 166, 1731 (1968); J. M. Namyslowski, M. S. K. Razmi, and R. G. Roberts, Phys. Rev. 157, 1328 (1967); R. J. Glauber, Lectures in Theoretical Physics (Interscience, New York, 1959), Vol. I.

46. Three-body unitarity implies that the partial-wave amplitudes have a dependence on the subenergy or isobar mass. We assume the dependence is weak enough that the partial-wave amplitudes can be approximated as constants for a given incident energy.

47. Y. Goradia and R. A. Arndt, Phys. Rev. D19, 2057 (1979).

48. Kenneth M. Watson, Phys. Rev. 88, 1163 (1952).

49. R. Aaron, R. D. Amado, R. A. Arndt, Y. Goradia, D. C. Teplitz, and V. L. Teplitz, Phys. Rev. D16, 50 (1977).

50. Vigdor L. Teplitz and Ronald Aaron, private communication. The relationship between phase conventions given in Ref. 14 is incorrect for the ρ isobar.

51. J. M. Blatt and V. F. Weisskopf, Theoretical Nuclear Physics (Wiley, New York, 1952).

52. David Morgan, Phys. Rev. D2, 520 (1970).

53. David J. Herndon, Ph.D. dissertation, University of California, Berkeley, 1972 [Lawrence Berkeley Laboratory report LBL-544, 1972].

54. R. M. Steinheimer, Phys. Rev. 115, 137 (1959).

55. E. Segrè, Experimental Nuclear Physics (Wiley, New York, 1953).

56. H. J. Bhabha, Proc. Roy. Soc. London A164, 257 (1937).

57. Joseph F. Janni, Air Force Weapons Laboratory report AFWL-TR-65-150 (1966).

58. Murray Gell-Mann, Phys. Rev. 125, 1067 (1962).

59. Yoichiro Nambu, Phys. Rev. Lett. 4, 380 (1960).

60. J. J. Sakurai, Currents and Mesons (University of Chicago, Chicago, 1969); M. Ericson and M. Rho, Phys. Reports 5, 57 (1972).

61. S. L. Adler and R. F. Dashen, Current Algebras and Applications to Particle Physics (W. A. Benjamin, Inc., New York, 1968).

62. Schwinger has shown that additional terms (called Schwinger terms) must be added to the righthand sides of the current commutation relations if they are to be consistent with Lorentz invariance and the positive definiteness of probability. J. Schwinger, Phys. Rev. Lett. 3, 296 (1959).

63. M. M. Nagels, Th. A. Rijken, J. J. DeSwart, G. C. Oades, J. L. Petersen, A. C. Irving, C. Jarlskog, W. Pfeil, H. Pilkuhn, and H. P. Jakob, Nucl. Phys. B147, 189 (1979). The f_π used by these authors differs by a factor of $\sqrt{2}$ from that in the text.

64. Steven Weinberg, Phys. Rev. 112, 1375 (1958).

65. Steven Weinberg, Phys. Rev. 166, 1568 (1968).

66. Leaf Turner and M. G. Olsson, Phys. Rev. D6, 3522 (1972).

APPENDIX A

MODEL FOR AN ELASTIC PEAK AT THE FOCAL PLANE

This appendix discusses details of how the width and centroid of the momentum distribution for each incident pion beam were inferred from an analysis of the momentum distribution of pions elastically scattered from the liquid hydrogen target.

It is useful to first summarize some of the kinematic formulae involved in describing the individual contributions to the centroid and width of the distribution of scattered pions. The velocity of the c.m. system relative to the laboratory is given by

$$\beta = p_{in}/(E_{in} + m_p) ,$$

where p_{in} is the incident pion momentum in the laboratory and E_{in} is the total incident pion energy. The total energy of the scattered pion in the c.m. system is given by

$$E = (W^2 + m_\pi{}^2 - m_p{}^2)/(2W) ,$$

where

$$W = [(E_{in} + m_p)^2 - p_{in}{}^2]^{1/2}$$

is the total c.m. energy of the two-body system. The momentum of the scattered pion in the laboratory is related to the incident pion momentum by

$$p_{out} = \frac{(E/\gamma)\beta\ \overline{\cos\theta_{lab}} + \{(E/\gamma)^2 - m_\pi{}^2[1 - (\beta\ \overline{\cos\theta_{lab}})^2]\}^{1/2}}{1 - (\beta\ \overline{\cos\theta_{lab}})^2},$$

where $\gamma = (1 - \beta^2)^{-1/2}$ and $\overline{\cos\theta_{lab}}$ is the mean cosine of the laboratory scattering angle, which differed from $\cos\theta_{lab}$, the cosine of the nominal scattering angle. Terms of the form $\overline{\cos^n\theta_{lab}}$, with n an integer, and other quantities discussed below were generated for various scattering angles by a Monte Carlo program that has been discussed by Oyer.[18] Table LV presents a summary of the parameters that describe the distribution of angles observed by the spectrometer for nominal scattering angles of interest. The cosine of the scattering angle in the c.m. system was calculated as

$$\cos\vartheta = \frac{E_{out} - \gamma E}{\beta \gamma p},$$

with

$$E_{out} = (p_{out}{}^2 + m_\pi{}^2)^{1/2}$$

and

$$p = (E^2 - m_\pi{}^2)^{1/2}.$$

Several of the formulae discussed below require the quantities

$$\frac{dp_{out}}{d\cos\theta_{lab}} = \frac{\beta \gamma E_{out} p_{out}{}^2}{E E_{out} - \gamma m_\pi{}^2}$$

and

$$\frac{dp_{out}}{dp_{in}} = \frac{p_{in}\,(m_p^2 - m_\pi^2) + (m_\pi^2 + m_p\,E_{in})\,p_{out}\,\overline{\cos\theta_{lab}}}{E_{in}\,(E_{in} + m_\pi)^2\,[(p_{out}/E_{out}) - \beta\,\overline{\cos\theta_{lab}}]} .$$

The incident pion beam suffered momentum loss in the liquid hydrogen target as a result of collisions with atomic electrons. The centroid of the incident momentum distribution was corrected for this effect by the term

TABLE LV. Deviations of scattering angles observed by the spectrometer.

θ_{lab}	$(\overline{\cos\theta_{lab}} - \cos\theta_{lab})$	$(\overline{\cos^2\theta_{lab}} - \overline{\cos\theta_{lab}}^2)$
30	-0.00221	0.000218
40	-0.00187	0.000358
50	-0.00155	0.000507
60	-0.00118	0.000646
70	-0.00079	0.000761
80	-0.00036	0.000835
90	-0.00008	0.000861
100	0.00052	0.000835
110	0.00094	0.000761
120	0.00133	0.000647
130	0.00162	0.000507

$$-p_{loss} = \overline{S_{in}} \frac{dp_{in}}{dx} \frac{dp_{out}}{dp_{in}} + \overline{S_{out}} \frac{dp_{out}}{dx} .$$

$\overline{S_{in}}$ and $\overline{S_{out}}$ represent the average path lengths traveled into and out of the target, before and after scattering, respectively. $\overline{S_{in}}$ and $\overline{S_{out}}$, together with higher-order terms, were also calculated by a Monte Carlo program. Table LVI summarizes the parameters that describe the distributions of path lengths in the liquid hydrogen target for scattering angles of interest. In this table, $\overline{(\Delta S_{in})^2} = (\overline{S_{in}^2} - \overline{S_{in}}^2)$, $\overline{(\Delta S_{out})^2} = (\overline{S_{out}^2} - \overline{S_{out}}^2)$, and

TABLE LVI. Averages of path lengths in the liquid hydrogen target.

θ_{lab}	$\overline{S_{in}}$ (cm)	$\overline{S_{out}}$ (cm)	$\overline{(\Delta S_{in})^2}$ (cm^2)	$\overline{(\Delta S_{out})^2}$ (cm^2)	$\overline{(\Delta S_{in})(\Delta S_{out})}$ (cm^2)
30	1.119	1.104	0.451	0.431	-0.350
40	1.121	1.090	0.446	0.413	-0.312
50	1.118	1.080	0.443	0.395	-0.266
60	1.115	1.071	0.439	0.378	-0.211
70	1.111	1.063	0.436	0.364	-0.149
80	1.109	1.058	0.435	0.355	-0.081
90	1.106	1.056	0.434	0.352	-0.008
100	1.105	1.058	0.434	0.355	0.066
110	1.104	1.063	0.436	0.364	0.141
120	1.103	1.070	0.439	0.378	0.213
130	1.101	1.077	0.442	0.395	0.280

$\overline{(\Delta S_{in})(\Delta S_{out})} = (\overline{S_{in}\, S_{out}} - \overline{S_{in}}\ \overline{S_{out}})$. Terms of the form dp/dx, which represent the decrease with distance of the mean momentum p, were calculated from the Bethe-Bloch equation[23,54-56]:

$$-\frac{dE}{dx} = \frac{2\pi\, n\, e^4}{m_e \beta^2}\left\{\ln\left[\frac{2m_e\beta^2 W_{max}}{I^2(1-\beta^2)}\right] - 2\beta^2 - \delta - U\right\} .$$

Here, $dp/dx = \beta^{-1}dE/dx$ where β is the velocity of the particle, m_e and e are the electronic mass and charge, and $n = \rho(N_A/A)$ is the number density of electrons in the target. N_A is Avogadro's number, A is the molecular weight of hydrogen, and ρ is the mass density of liquid hydrogen. W_{max} is the maximum energy that can be transferred to an electron in a single collision:

$$W_{max} = \frac{2\beta^2\gamma^2 m_e}{1 + 2\gamma(m_e/m_\pi) + (m_e/m_\pi)^2} ,$$

with $\gamma = (1-\beta^2)^{-1/2}$. The ionization potential I of liquid hydrogen is 18.30 eV.[57] The density correction δ was evaluated from the formulae described by Sternheimer.[54] The shell correction U, which is unimportant at energies of interest, was neglected.

We considered seven contributions to the width of the momentum distribution of scattered pions. The largest of these contributions was due to the finite angular acceptance of the spectrometer:

$$\sigma^2_{ang} = (\overline{\cos^2\theta_{lab}} - \overline{\cos\theta_{lab}}^2)(\frac{dp_{out}}{d\cos\theta_{lab}})^2 .$$

Another large source of broadening resulted from variation of path lengths in the target and the concomitant variation in the energy loss. This contribution to the momentum width was calculated as

$$\sigma^2_{loss} = (\overline{S_{in}^2} - \overline{S_{in}}^2)(\frac{dp_{in}}{dx})^2(\frac{dp_{out}}{dp_{in}})^2 + (\overline{S_{out}^2} - \overline{S_{out}}^2)(\frac{dp_{out}}{dx})^2$$

$$+ 2(\overline{S_{in}\,S_{out}} - \overline{S_{in}}\;\overline{S_{out}})(\frac{dp_{in}}{dx})(\frac{dp_{out}}{dp_{in}})(\frac{dp_{out}}{dx}) .$$

We included a contribution to the width from the vertical height of the beam at the target. The height of the beam spot and the magnification of the spectrometer determined the size H of the beam spot at the focal plane. The contribution is given by

$$\sigma^2_{spot} = (p_c \delta\, H)^2 ,$$

where p_c is the central momentum of the spectrometer and $\delta = (4.327 \pm 0.010)\times10^{-3}$/cm is the spectrometer dispersion. Multiple small-angle Coulomb scattering with nuclei introduced a mean square deviation in the scattering angle θ_{lab}. The contribution from this source can be written as[57]

$$\sigma^2_{coul} = (\frac{E_s}{p\beta})^2 (\frac{\overline{S_{out}}\,\rho}{X_o}) (\frac{dp_{out}}{d\theta_{lab}})^2 ,$$

where $E_s = m_e(4\pi/e^2)^{1/2}$ and $X_o = 63.05\ g/cm^2$ is the radiation length in liquid hydrogen.[42] A final source of broadening was caused by the phenomenon known as straggling. Because of the statistical nature of collisions within the target, all particles that entered the target with the same momentum did not have exactly the same momentum after traveling the same distance through the target. The contribution to the width from this effect can be written as

$$\sigma^2_{strag} = \overline{S_{in}} \frac{d\langle p_{in}^2\rangle}{dx} \left(\frac{dp_{out}}{dp_{in}}\right)^2 + \overline{S_{out}} \frac{d\langle p_{out}^2\rangle}{dx} ,$$

where $\langle p^2\rangle$ is the mean square momentum. The variation of $\langle p^2\rangle$ with distance is given by[23]

$$\frac{d\langle p^2\rangle}{dx} = \frac{2\pi\ n\ e^4}{m_e \beta^2} \left(1 - \frac{\beta^2}{2}\right) W_{max} .$$

APPENDIX B

REVIEW OF SOFT-PION THEORY

Soft-pion theories aim at a description of processes involving pions and other particles in which the pions have small kinetic energy. In the limit in which the four-momentum of the pion is zero, the description is thought to be exact. The fundamental ingredients of soft-pion theory are the Gell-Mann current-algebra hypothesis[58] and the partial conservation of the axial-vector current (PCAC) hypothesis.[59] These hypotheses are reviewed in this appendix with a discussion of phenomenological πN Lagrangians that are useful for describing the reaction $\pi^- p \to \pi^+ \pi^- n$ near threshold. The presentation here follows that of several other authors.[4,60,61]

Current Commutation Relations

We begin by using the free-field SU(3) quark model as a guide in deriving the algebraic properties of hadronic currents. The free-field quark Lagrangian is assumed to be[32]

$$L = \bar{q}(i\gamma\cdot\partial - m - \delta m\, \lambda_8)q \ ,$$

with $-\delta m\ \bar{q}\lambda_8 q$ a symmetry-breaking term that removes the mass degeneracy of the quarks under SU(3). λ_8 is one of the generators of the group SU(3). The standard representation and properties of the λ

matrices are discussed, for example, in Refs. 60 and 61. The vector current J_a^μ is generated by the transformation

$$q \to \exp\left(-\frac{i\lambda_a \varepsilon_a}{2}\right) q \ ,$$

where ε_a (a = 1,•••,8) is a real parameter. We obtain

$$J_a^\mu = \frac{\delta L}{\delta(\partial_\mu \varepsilon_a)} = \bar{q}\gamma^\mu \frac{\lambda_a}{2} q \ .$$

From the Gell-Mann--Lévy equation,[9]

$$\partial_\mu \frac{\delta L}{\delta(\partial_\mu \varepsilon_a)} = \frac{\delta L}{\delta \varepsilon_a} \ ,$$

we find the divergence relation

$$\partial_\mu J_a^\mu = f_{a8b}\ \delta m\ \bar{q}\lambda_b q \ ,$$

where the f_{abc} are the structure constants of the group SU(3). Note that the vector current is conserved in the absence of the symmetry-breaking term in the Lagrangian. The axial-vector current $J_a^{5\mu}$ is generated by the transformation

$$q \to \exp\left(-\frac{i\gamma_5 \lambda_a \varepsilon_a}{2}\right) q.$$

Such a transformation is called a chiral transformation because γ_5 can

distinguish the spin components of a fermion field. The axial-vector current is found to be

$$J_a^{5\mu} = \frac{\delta L}{\delta(\partial_\mu \varepsilon_a)} = \bar{q}\gamma^\mu\gamma_5 \frac{\lambda_a}{2} q \ .$$

$J_a^{5\mu}$ satisfies the divergence relation

$$\partial_\mu J_a^{5\mu} = im\bar{q}\gamma_5\lambda_a q + \frac{i}{2}\delta m\, \bar{q}\gamma_5\{\lambda_a,\lambda_8\}q \ .$$

Hence, $J_a^{5\mu}$ is not conserved even in the absence of the symmetry-breaking term. We can form chiral currents from linear combinations of the vector and axial-vector currents:

$$J_a^{L\mu} = \frac{1}{2}(J_a^\mu - J_a^{5\mu}) = \bar{q}\gamma^\mu\left(\frac{1-\gamma_5}{2}\right)\frac{\lambda_a}{2} q \ ,$$

$$J_a^{R\mu} = \frac{1}{2}(J_a^\mu + J_a^{5\mu}) = \bar{q}\gamma^\mu\left(\frac{1+\gamma_5}{2}\right)\frac{\lambda_a}{2} q \ .$$

Chiral currents are so-named because of the presence of the helicity projection operators $(1 \pm \gamma_5)/2$.

We can determine commutation relations for the vector and axial-vector currents from the equal-time commutation relations for the quark fields:

$$\{q_a(x),q_b(y)\}_{x_0=y_0} = \{q_a^\dagger(x),q_b^\dagger(y)\}_{x_0=y_0} = 0 \ ,$$

$$\{q_a(x),q_b^\dagger(y)\}_{x_0=y_0} = \delta_{ab}\,\delta^3(\vec{x}-\vec{y}) \ .$$

We find[61]:

$$[J_a^0(x),J_b^\mu(y)]_{x_0=y_0} = i\delta^3(\vec{x}-\vec{y})\, f_{abc}\, J_c^\mu(x) ,$$

$$[J_a^{50}(x),J_b^\mu(y)]_{x_0=y_0} = i\delta^3(\vec{x}-\vec{y})\, f_{abc}\, J_c^{5\mu}(x) ,$$

$$[J_a^0(x),J_b^{5\mu}(y)]_{x_0=y_0} = i\delta^3(\vec{x}-\vec{y})\, f_{abc}\, J_c^{5\mu}(x) ,$$

$$[J_a^{50}(x),J_b^{5\mu}(y)]_{x_0=y_0} = i\delta^3(\vec{x}-\vec{y})\, f_{abc}\, J_c^\mu(x) .$$

These are the famous Gell-Mann current commutation relations.[58] The essence of the current-algebra hypothesis is that these commutation relations are characteristic of the group SU(3) and that they should by valid even if the SU(3) symmetry is badly broken. Although these commutation relations have been derived from the quark model, they are assumed to be valid even for the more complex particles that are characterized by the group SU(3). We can use the current commutation relations for the vector and axial-vector currents to obtain:

$$[J_a^{L0}(x),J_b^{L\mu}(y)]_{x_0=y_0} = i\delta^3(\vec{x}-\vec{y})\, f_{abc}\, J_c^{L\mu}(x) ,$$

$$[J_a^{R0}(x),J_b^{R\mu}(y)]_{x_0=y_0} = i\delta^3(\vec{x}-\vec{y})\, f_{abc}\, J_c^{R\mu}(x) ,$$

$$[J_a^{L0}(x),J_b^{R\mu}(y)]_{x_0=y_0} = [J_a^{R0}(x),J_b^{L\mu}(y)]_{x_0=y_0} = 0 .$$

These commutation relations for the chiral currents are a mathematical statement that each of the chiral currents forms an independent SU(3) algebra and, since the chiral currents commute, they form together the algebra of chiral SU(3)×SU(3).

PCAC and the Goldberger-Treiman Relation

From this point, we will only be concerned with the SU(2) isospin subgroup of SU(3) which is appropriate for describing the nucleon field, and thus we will discuss the simpler SU(2)×SU(2). Any theory that attempts to correctly describe the interactions of pions and nucleons must allow for pion decay. The most general form of the matrix element for charged pion decay allowed by Lorentz invariance and parity is given by the axial-vector current taken between the pion state and the vacuum:

$$\langle 0|J_a^{5\mu}(0)|\pi_b\rangle = \frac{i\, f_\pi\, p^\mu\, \delta_{ab}}{\sqrt{(2\pi)^3\, 2\omega_p}}\,.$$

Here, p^μ and ω_p are respectively the pion four-momentum and total energy, f_π is the charged pion decay constant, and a and b are isospin indices (a,b = 1,2,3). The remaining factors come from the normalization of the pion state. The matrix element of the divergence of the axial-vector current, taken between the same states, follows by translational invariance:

$$\langle 0|\partial_\mu J_a^{5\mu}(0)|\pi_b\rangle = \frac{f_\pi\, m_\pi^{\,2}\, \delta_{ab}}{\sqrt{(2\pi)^3\, 2\omega_p}}\,.$$

This matrix element suggests an equation known as the PCAC relation:

$$\partial_\mu J_a^{5\mu} = f_\pi\, m_\pi^{\,2}\, \phi_a\,.$$

Here, ϕ_a is an isovector, pseudoscalar field appropriate for the creation of a pion with isospin index a. If the axial-vector current were precisely conserved, the divergence of the current would vanish. The matrix element for pion decay would then falsely imply either $f_\pi = 0$ or $m_\pi = 0$. The idea that the axial-vector current might be almost or "partially" conserved was motivated, in part, by the smallness of the pion mass by hadronic standards. The value of the pion decay constant obtained from measurement of the $\pi^+ \to \mu^+ \nu_\mu$ decay width,[61]

$$\Gamma = \frac{f_\pi^2}{4\pi} (G_\mu \cos\theta_c)^2 \, m_\pi^3 \, (\frac{m_\mu}{m_\pi})^2 \, [1 - (\frac{m_\mu}{m_\pi})^2] \ ,$$

is $f_\pi = 93.2 \pm 0.1$ MeV.[63] Here, G_μ is the muon decay constant, $\theta_c = 0.231 \pm 0.004$ radians[63] is the Cabibbo angle, and m_μ is the mass of the muon.

We now consider the hadronic matrix element of the axial-vector current appropriate for describing neutron beta decay. Taking the isospin-raising part of the axial-vector current $J_+^{5\mu} = J_1^{5\mu} + iJ_2^{5\mu}$ between neutron and proton states, we obtain

$$\langle p(p_2)|J_+^{5\mu}(0)|n(p_1)\rangle = \frac{1}{(2\pi)^3} (\frac{m_p m_n}{E_1 E_2})^{1/2} \bar{u}_p(p_2)[-F_A(q^2)\gamma^\mu + F_P(q^2)q^\mu]\gamma_5 u_n(p_1) \ ,$$

with $q = p_2 - p_1$. Here, p_1 and p_2 are the four-momenta of the neutron and proton, respectively. $F_A(q^2)$ and $F_P(q^2)$ are, respectively, the axial-vector and pseudoscalar form factors. At $q^2 = 0$, we have[42]

$$F_A(0) = -\frac{g_A}{g_V} = 1.254 \pm 0.007 \ ,$$

the axial-vector renormalization constant. Note that G parity rules out a term in the matrix element of the form

$$\bar{u}_p(p_2)\sigma^{\mu\nu}q_\nu\gamma_5 u_n(p_1) \ ,$$

which is an example of what Weinberg has called a second-class current.[64] The hadronic matrix element of the divergence of $J_+^{5\mu}$ is given by

$$\langle p(p_2)|\partial_\mu J_+^{5\mu}(0)|n(p_1)\rangle = i\,\frac{1}{(2\pi)^3}\left(\frac{m_p m_n}{E_1 E_2}\right)^{1/2}\bar{u}_p(p_2)[-(m_p + m_n)F_A(q^2) + q^2 F_p(q^2)]\gamma_5 u_n(p_1) \ ,$$

where we have made use of the Dirac equation:

$$(i\gamma\cdot\partial - m)u(p) = 0 \ .$$

By taking the matrix element of the isospin-raising parts of the PCAC relation between neutron and proton states, we obtain

$$\langle p(p_2)|\partial_\mu J_+^{5\mu}(0)|n(p_1)\rangle = \sqrt{2}\, f_\pi\, m_\pi^2\, \langle p(p_2)|\phi_+(0)|n(p_1)\rangle \ .$$

The righthand side of this expression can be evaluated by taking the

matrix element of both sides of a Klein-Gordon equation for the pion field $\vec{\phi}$:

$$(\partial^\mu \partial_\mu + m_\pi{}^2)\vec{\phi} \simeq - \frac{G}{2m_N} \partial^\mu(\bar{\psi}\gamma_\mu\gamma_5\vec{\tau}\psi) \ ,$$

where G is the πN coupling constant, ψ is the nucleon field, and $\vec{\tau}$ is the usual isospin matrix. The source term expresses the contribution from the πN vertex shown in Fig. 78. We obtain:

$$\langle p(p_2)|\phi_+(0)|n(p_1)\rangle \simeq \frac{1}{(2\pi)^3}\left(\frac{m_p m_n}{E_1 E_2}\right)^{1/2}\left[\frac{\sqrt{2}\ G}{q^2 - m_\pi{}^2}\ \bar{u}_p(p_2) i\gamma_5 u_n(p_1)\right] .$$

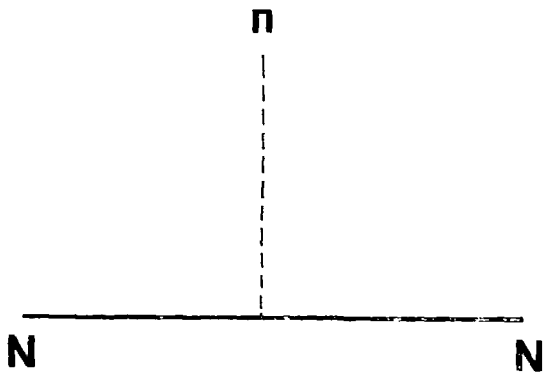

Figure 78. The pion-nucleon vertex diagram.

By comparing both expressions for the neutron beta decay matrix element, we find

$$-(m_p + m_n)F_A(q^2) + q^2F_p(q^2) \simeq 2f_\pi G \frac{m_\pi^2}{q^2 - m_\pi^2} ,$$

where the approximation indicates our neglect of other diagrams. Taking the soft-pion limit in which $q^2 \to 0$, we find

$$f_\pi = \left|\frac{g_A}{g_V}\right| \frac{m_p + m_n}{2G} ,$$

which is the Goldberger-Treiman relation.[43] The value of f_π predicted from the Goldberger-Treiman relation is $f_\pi^{GT} = 87.8 \pm 0.8$ MeV, which agrees within 6 ± 1 % of the value obtained from the direct measurement of pion decay.

Phenomenological πN Lagrangian

The interactions of nucleons and low-energy pions can be described in terms of a phenomenological Lagrangian that, by design, is consistent with the hypotheses of PCAC and current algebra for the isospin subgroup of SU(3). Conservation of isospin in strong interactions implies conservation of the vector current, which is generated by isospin gauge transformations. Thus, the πN Lagrangian must be invariant under global (constant) isospin gauge transformations. In the limit $m_\pi \to 0$, PCAC implies conservation of the axial-vector current; consequently, in this limit, the πN Lagrangian must also be invariant

under global chiral transformations. When a πN Lagrangian satisfies both of these criteria, it is said to possess symmetry under chiral SU(2)×SU(2).

The form of the Lagrangian is restricted by the requirement that the resulting vector and axial-vector currents obey the current algebra appropriate for the SU(2) isospin subgroup of SU(3). It can be shown that such a chiral-invariant Lagrangian is[2,4,65]

$$L_I = \bar{\psi}(i\gamma\cdot D - m_N)\psi + \frac{1}{2} D^\mu \vec{\phi}\cdot D_\mu \vec{\phi} + \frac{G}{2m_N} \bar{\psi}\gamma_\mu\gamma_5 \vec{\tau}\psi\cdot D^\mu\vec{\phi} \ ,$$

where ψ and $\vec{\phi}$ are, respectively, the physical nucleon and pion fields. $D_\mu\psi$ and $D_\mu\vec{\phi}$ are Weinberg covariant derivatives[65]:

$$D_\mu\psi = \partial_\mu\psi + \frac{i}{(2f_\pi^{GT})^2} \frac{\vec{\tau}\cdot(\vec{\phi}\times\partial_\mu\vec{\phi})\psi}{1 + (\frac{\vec{\phi}}{2f_\pi^{GT}})^2} \ ,$$

$$D_\mu\vec{\phi} = \frac{\partial_\mu\vec{\phi}}{1 + (\frac{\vec{\phi}}{2f_\pi^{GT}})^2} \ ,$$

with

$$f_\pi^{GT} = \left|\frac{g_A}{g_V}\right| \frac{m_N}{G} \ .$$

The covariant derivatives are defined such that any isospin-invariant function of ψ, $D_\mu\psi$, and $D_\mu\vec{\phi}$ will be chiral invariant. In the limit

$D_\mu \to \partial_\mu$, L_I becomes the usual gradient-coupling Lagrangian for describing the interactions of nucleons and massless bosons.

Chiral-Symmetry Breaking

To describe the interactions of nucleons with physical pions, it is necessary to violate the chiral SU(2)×SU(2) symmetry of the Lagrangian. We assume that the πN Lagrangian can be written as a sum $L = L_I + L_N$, where L_N is a symmetry-breaking term that vanishes in the soft-pion limit. L_N was first investigated by Weinberg[65] who assumed that it was a function $L_N(\phi^2)$ which transforms according to the (N/2,N/2) representation of SU(2)×SU(2); that is, like a traceless symmetric tensor of rank N. This assumption implies that $L_N(\phi^2)$ must satisfy a second-order differential equation,[65]

$$x(1 + x)^2 L_N'' + \frac{1}{2}(1 + x)(3 + x)L_N' + N(N + 2)L_N = 0 ,$$

where the prime denotes differentiation with respect to the argument $x = (\phi/2f_\pi^{GT})^2$. By introducing the variable $z = 4x/(1 + x)^2$, we obtain an ordinary hypergeometric differential equation,

$$z(1 - z)\frac{d^2L_N}{dz^2} + \frac{1}{2}(3 - 4z)\frac{dL_N}{dz} + \frac{1}{4}N(N + 2)L_N = 0 .$$

Olsson and Turner[66] obtained this equation, with a different argument, by generalizing the Gell-Mann--Lévy σ model.[9] The normalized solution, which is regular at the origin, is given by

$$L_N = \frac{3(m_\pi f_\pi^{GT})^2}{N(N+1)(N+2)} \frac{\sin(N+1)\theta}{\sin\theta} ,$$

where $z = \sin^2\theta$ and $x = \tan^2(\theta/2)$. The symmetry-breaking term was later investigated by Olsson and Turner[2,4] who assumed PCAC in the form

$$\partial_\mu J_a^{5\mu} = f_\pi m_\pi^2 \phi_a F(\xi^2) ,$$

where $F(0) = 1$. By invoking current algebra, they determined the most general form for the phenomenological πN Lagrangian to fourth order in the pion field. By comparing the $\pi\pi$ scattering lengths calculated by Olsson and Turner[2,4] with those of Weinberg,[65] we find

$$\xi = \frac{2}{5}[3 - N(N+2)] ,$$

where ξ is the chiral-symmetry-breaking parameter introduced by Olsson and Turner. In their early treatment,[2,4] the value of ξ was an arbitrary real number. If we require that N be an integer, then the simplest choices for ξ are $\xi = 0$ (Ref. 3) and $\xi = -2$ (Ref. 12), corresponding to $N = 1$ and $N = 2$, respectively.

Applications

We now expand the πN Lagrangian $L = L_I + L_N$ and retain terms that will contribute "tree" diagrams (diagrams that do not contain loops) for the reactions $\pi\pi \to \pi\pi$, $\pi N \to \pi N$, and $\pi N \to \pi\pi N$. We obtain

$$L \simeq L_o + L_\pi + L_{NN\pi} + L_{NN\pi\pi} + L_{NN\pi\pi\pi} ,$$

with

$$L_o = \bar{\psi}(i\gamma\cdot\partial - m_N)\psi + \frac{1}{2}\,\partial_\mu\vec{\phi}\cdot\partial^\mu\vec{\phi} - \frac{1}{2}\,m_\pi{}^2\,\vec{\phi}^2 ,$$

$$L_\pi = -\left(\frac{G}{2m_N}\right)^2\left(\frac{g_V}{g_A}\right)^2\left[\vec{\phi}^2\partial_\mu\vec{\phi}\cdot\partial^\mu\vec{\phi} - \frac{1}{2}\,(1-\frac{1}{2}\,\xi)m_\pi{}^2\,(\vec{\phi}^2)^2\right] ,$$

$$L_{NN\pi} = \left(\frac{G}{2m_N}\right)\bar{\psi}\gamma_\mu\gamma_5\vec{\tau}\psi\cdot\partial^\mu\vec{\phi} ,$$

$$L_{NN\pi\pi} = -\left(\frac{G}{2m_N}\right)^2\left(\frac{g_V}{g_A}\right)^2\bar{\psi}\gamma_\mu\vec{\tau}\psi\cdot(\vec{\phi}\times\partial^\mu\vec{\phi}) ,$$

$$L_{NN\pi\pi\pi} = -\left(\frac{G}{2m_N}\right)^3\left(\frac{g_V}{g_A}\right)^2\bar{\psi}\gamma_\mu\gamma_5\vec{\tau}\psi\cdot(\partial^\mu\vec{\phi})\vec{\phi}^2 .$$

The S-wave $\pi\pi$ scattering lengths can be calculated solely from L_π whereas calculation of the πN scattering lengths requires only $L_{NN\pi}$ and $L_{NN\pi\pi}$. To calculate matrix elements for $\pi N \to \pi\pi N$ reactions, one needs L_π, $L_{NN\pi}$, $L_{NN\pi\pi}$, and $L_{NN\pi\pi\pi}$. Only tree diagrams are considered in these calculations. Important tree diagrams for single pion production include the "one-point" diagrams in Fig. 79(a), the "two-point" diagrams in Fig. 79(b), and the "three-point" diagram in Fig. 79(c). The matrix elements at single pion production threshold have been calculated by Olsson and Turner.[2,4] While Olsson and Turner considered only contributions from one- and two-point diagrams, the three-point diagram they neglected contributes only about 0.5% of the threshold matrix element for $\pi^- p \to \pi^+\pi^- n$ with $\xi = 0$. Matrix elements

for all possible $\pi p \to \pi\pi N$ reactions, with no threshold approximations, have been summarized by Arndt et al.[14] If we let T_i denote the contribution of the i-point diagram, then the T-matrix amplitude for $\pi^-(Q)+p(p_i)\to\pi^+(q_1)+\pi^-(q_2)+n(p_f)$ used in our isobar-model analysis can be written as $T_{CA} = T_1 + T_2 + T_3$, where the T_i are given by the following expressions[14]:

$$T_1 = -2\sqrt{2}\, i \left(\frac{G}{2m_N}\right)^3 \left(\frac{g_V}{g_A}\right)^2 m_N$$

$$\times \bar{u}(p_f)\left[2 + \frac{\not{q}_2}{m_N} + \frac{8Q\cdot q_1 - 4m_\pi{}^2\xi}{(p_f - p_i)^2 - m_\pi{}^2}\right]\gamma_5 u(p_i) \ ,$$

$$T_2 = 2\sqrt{2}\, i \left(\frac{G}{2m_N}\right)^3 \left(\frac{g_V}{g_A}\right)^2 m_N$$

$$\times \bar{u}(p_f)\left[2 + \frac{3\not{q}_2}{m_N} - \frac{\not{q}_1(\not{q}_2 + \not{Q})}{(p_f + q_1)^2 - m_N{}^2} - \frac{(\not{q}_2 + \not{Q})\not{q}_1}{(p_i - q_1)^2 - m_N{}^2}\right.$$

$$\left. + \frac{\not{Q}(\not{q}_2 - \not{q}_1)}{(p_f - Q)^2 - m_N{}^2} + \frac{(\not{q}_2 - \not{q}_1)\not{Q}}{(p_i + Q)^2 - m_N{}^2}\right]\gamma_5 u(p_i) \ ,$$

and

$$T_3 = 2\sqrt{2}\, i \left(\frac{G}{2m_N}\right)^3 m_N$$

$$\times \bar{u}(p_f)\left\{\frac{2\not{q}_2}{m_N} + \frac{2\not{q}_2\not{Q}}{(p_i + Q)^2 - m_N^2} + \frac{2\not{Q}\not{q}_2}{(p_f - Q)^2 - m_N^2}\right.$$

$$- \frac{2\not{q}_2\not{q}_1}{(p_i - q_1)^2 - m_N^2} - \frac{2\not{q}_1\not{q}_2}{(p_f + q_1)^2 - m_N^2}$$

$$- \frac{4m_N\not{Q}\not{q}_2\not{q}_1}{[(p_f - Q)^2 - m_N^2][(p_i - q_1)^2 - m_N^2]}$$

$$\left. - \frac{4m_N\not{q}_1\not{q}_2\not{Q}}{[(p_i + Q)^2 - m_N^2][(p_f + q_1)^2 - m_N^2]}\right\}\gamma_5 u(p_i) \,.$$

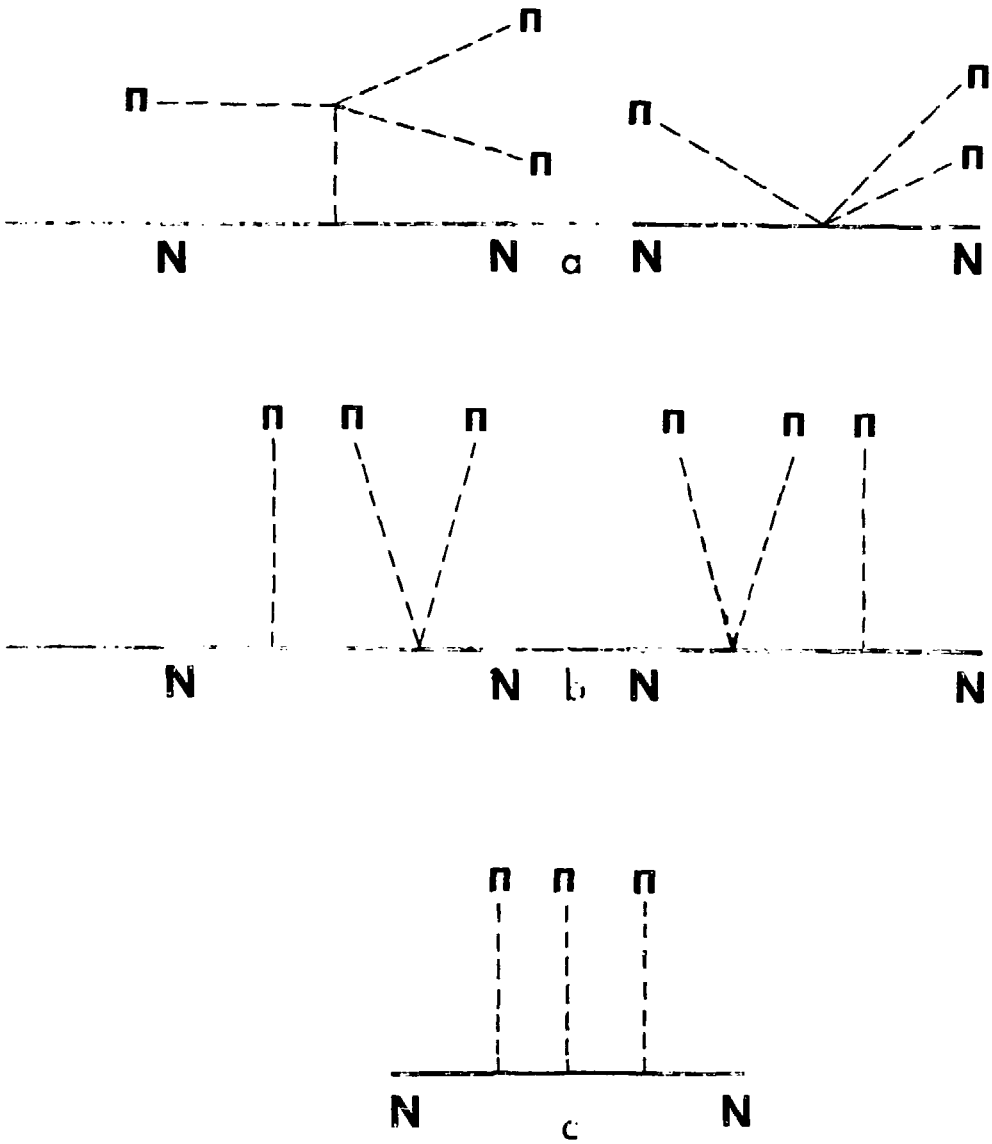

Figure 79. Important tree diagrams that contribute to $\pi N \to \pi\pi N$. These include (a) the "one-point" diagrams, (b) the "two-point" diagrams, and (c) the "three-point" diagram.

★ U.S. GOVERNMENT PRINTING OFFICE: 1981-0-576-020/168